

Changes in Stratospheric Circulation: Evidence and Possible Explanations

—

Änderungen der stratosphärischen Zirkulation: Evidenz und Erklärungsansätze

Zur Erlangung des akademischen Grades eines

DOKTORS DER NATURWISSENSCHAFTEN

von der Fakultät für

Bauingenieur-, Geo- und Umweltwissenschaften

des Karlsruher Instituts für Technologie (KIT)

genehmigte

DISSERTATION

von

Ellen Eckert

aus Telgte

Tag der mündlichen Prüfung:

18. Dezember 2017

Referent: PD Dr. Thomas von Clarmann

Korreferent: Prof. Dr.-Ing. Stefan Hinz

Karlsruhe 2017

Eidesstattliche Erklärung

Eidesstattliche Versicherung gemäß § 6 Abs. 1 Ziff. 4 der Promotionsordnung des Karlsruher Instituts für Technologie für die Fakultät für Bauingenieur-, Geo- und Umweltwissenschaften.

1. Bei der eingereichten Dissertation zu dem Thema "*Changes in Stratospheric Circulation: Evidence and Possible Explanations*" handelt es sich um meine eigenständig erbrachte Leistung.
2. Ich habe nur die angegebenen Quellen und Hilfsmittel benutzt und mich keiner unzulässigen Hilfe Dritter bedient. Insbesondere habe ich wörtlich oder sinngemäß aus anderen Werken übernommene Inhalte als solche kenntlich gemacht.
3. Die Arbeit oder Teile davon habe ich bislang nicht an einer Hochschule des In- oder Auslands als Bestandteil einer Prüfungs- oder Qualifikationsleistung vorgelegt.

Titel der Arbeit: *Changes in Stratospheric Circulation: Evidence and Possible Explanations*.

Hochschule und Jahr: Karlsruher Institut für Technologie (KIT), 2017.

Art der Prüfungs- oder Qualifikationsleistung: Wissenschaftliche Abhandlung und mündliche Promotionsprüfung.

4. Die Richtigkeit der vorstehenden Erklärungen bestätige ich.
5. Die Bedeutung der eidesstattlichen Versicherung und die strafrechtlichen Folgen einer unrichtigen oder unvollständigen eidesstattlichen Versicherung sind mir bekannt. Ich versichere an Eides statt, dass ich nach bestem Wissen die reine Wahrheit erklärt und nichts verschwiegen habe.

12. Januar, 2018

Ort und Datum



Unterschrift

“The noblest pleasure is the joy of understanding.”

Leonardo da Vinci

Abstract

Changes in the Brewer-Dobson circulation (BDC) were identified using data of ozone measurements of Michelson Interferometer for Passive Atmospheric Sounding (MIPAS). CCl_3F (CFC-11), CCl_2F_2 (CFC-12) and carbon tetrachloride (CCl_4), long-lived trace gases in the atmosphere, were then used to improve the understanding of these changes.

Evidence of changes in the BDC was found when calculating and examining the temporal development (trends) of the ozone concentration in the stratosphere. These trends cover the entire MIPAS measurements period, from Juli 2002 to April 2012. For trend estimation, the quasi biennial oscillation (QBO), annual oscillation (AO) and semi-annual oscillation (SAO) were taken into account, as well as several overtones of these variations. MIPAS measurements cover the periods of July 2002 to March 2004 (full spectral resolution) and January 2005 to April 2012 (reduced spectral resolution). The full data error covariance matrix was used and the unknown bias between the data subsets was accounted for by consideration of a fully correlated block in the covariance matrix for one of the periods. The distribution of the resulting trends hints at changes in the BDC. In particular, negative ozone trends were found between 25 and 35 km in the tropics, as well as positive trends just above the tropical tropopause and an overall hemispheric asymmetry, which was not expected. These patterns could, however, be explained by a shift of the subtropics mixing barriers, which are closely linked to the BDC.

To further look into these changes, long-lived trace gases, such as CFC-11, CFC-12 and CCl_4 can be used. Since these reside in the stratosphere for approximately 60, 110 and 44 years, respectively, they are excellent tracers for large circulation patterns, such as the BDC. Thus, the already existing data products of CFC-11 and CFC-12 were reviewed in an extensive validation. Good agreement with other instruments was found for both trace gases. However, a slight high bias of approximately 5% exists in CFC-11 below ~ 15 km. Studies of consecutive profiles in a quiescent atmosphere showed that MIPAS error estimates are presumably accurate for the full spectral resolution CFC-12 product. For the reduced spectral resolution CFC-12 product and both CFC-11 product the errors are underestimated by approximately one quarter to one third. While temporal stability is very good for CFC-11, large drifts ranging from -50 to 50%/decade were found in CFC-12 measurements above 30 km.

Since a CCl_4 product had not yet been derived from MIPAS, a retrieval strategy has been developed for this gas, and global distributions were retrieved using the scientific level-2 processor run by Karlsruhe Institute of Technology (KIT), Institute of Meteorology and Climate Research (IMK) and Consejo Superior de Investigaciones Cientificas (CSIC), Instituto de Astrofísica de Andalucía (IAA). Various other trace

gases and the temperature had to be taken into account. In addition, line-mixing of the CO₂ Q-branch at 792 cm⁻¹ had to be considered. Using a new spectroscopic data set for CCl₄ improved the results significantly, as it lead to lower volume mixing ratios which agree better with values reported in recent literature. Comparisons with other instruments also show very good agreement with MIPAS results.

Finally, the retrieved and validated data products of CCl₄, CFC-11 and CFC-12 were used in an inverse 2D transport model based on the continuity equation. The results show that including newly assessed trace gases in the inverse model could significantly reduce uncertainties in the derived quantities.

Zusammenfassung

Die Brewer-Dobson Zirkulation ist eine großräumige, meridionale Zirkulation in der Atmosphäre, die Luft vom Äquator in höhere Breiten transportiert. Sie beeinflusst somit die Verteilung von Spurengasen in der Atmosphäre. Die Konzentrationen diverser Spurengase können mit Messgeräten, wie beispielsweise dem Michelson Interferometer for Passive Atmospheric Sounding (MIPAS), welches eine Nutzlast des europäischen Satelliten Envisat war, gemessen werden.

Im Rahmen dieser Arbeit konnte gezeigt werden, dass sich die räumliche Verteilung des Spurengases Ozon während des MIPAS-Messzeitraums (Juli 2002 bis April 2012) aufgrund von Änderungen in der Brewer-Dobson Zirkulation verändert. Hierbei wurde eine multivariate Regressionsmethode verwendet, um lineare Variationen (Trends) der Ozonkonzentrationen über den gesamten MIPAS-Messzeitraum zu bestimmen. Bei der Trendbestimmung wurden, neben dem linearen Term, auch die quasi-biennale Oscillation (QBO), der Jahresgang und die halbjährige Oszillation berücksichtigt, ebenso wie diverse Obertöne dieser Variationen. MIPAS-Messungen setzen sich aus dem “full spectral resolution” Zeitraum (Juli 2002 bis März 2004) und dem “reduced spectral resolution” Zeitraum (Januar 2005 bis April 2012) zusammen. Die komplette Fehlerkovarianzmatrix wurde verwendet und der unbekanntes Versatz zwischen den Teildatensätzen wurde berücksichtigt, indem ein voll korrelierter Block zum Kovarianzmatrixteil eines der beiden Zeiträume addiert wurde. In den Tropen zwischen 25 und 35 km wurden negative Ozontrends gefunden, sowie positive Trends direkt oberhalb der tropischen Tropopause und eine generelle hemisphärische Asymmetrie. Diese Strukturen waren so nicht zu erwarten. Sie konnten jedoch mit einer Verschiebung der subtropischen Mischungsbarrieren, welche direkt mit der Brewer-Dobson Zirkulation zusammenhängen, erklärt werden und weisen somit auf Änderungen in der Brewer-Dobson Zirkulation hin.

Mithilfe der Inversion der Kontinuitätsgleichung, welche im Programm zur “Analysis of the Circulation of the Stratosphere using Spectroscopic Measurements” (ANCISTRUS-SPEC) umgesetzt wurde, können Änderungen in der Brewer-Dobson Zirkulation in kleinen zeitlichen Schritten (Monaten) verfolgt werden. Diese Methode verwendet Spurengaskonzentrationen aufeinanderfolgender Monate um daraus 2D-Transportgeschwindigkeiten und Mischungskoeffizienten zwischen den jeweiligen Monaten zu berechnen. Als Eingabe werden monatlich gemittelte Konzentrationsverteilungen langlebiger Spurengase verwendet. Diese können mithilfe von MIPAS bereitgestellt werden.

Der zweite Teil dieser Arbeit befasst sich mit der Bereitstellung entsprechender Daten für das ANCISTRUS-SPEC Programm. Geeignete Spurengase sind CFC-11, CFC-12 und CCl_4 . Diese Gase haben atmosphärische Lebensdauern von etwa 60, 110

und 44 Jahren. Die bereits existierenden Datenprodukte für CFC-11 und CFC-12 wurden einer umfassenden Validierung unterzogen. Für beide Spurengase wurden gute Übereinstimmungen mit den Ergebnissen anderer Instrumente gefunden. Jedoch zeigte sich für CFC-11 unterhalb von 15 km eine leichte Tendenz zu erhöhten Werten. Untersuchungen zu direkt aufeinanderfolgenden Profilen in einer ruhigen Atmosphäre zeigten, dass die Fehlerabschätzung nur für das “full spectral resolution” CFC-12 Produkt als realistisch angesehen werden können. Für das “reduced spectral resolution” CFC-12 Produkt, sowie beide Produkte von CFC-11 werden die Fehler um ein Viertel bis ein Drittel unterschätzt. Während CFC-11 eine sehr gute zeitliche Stabilität aufweist wurden für CFC-12 oberhalb von 30 km starke Drifts, die von -50 bis +50% pro Dekade reichen, gefunden. Die Daten eignen sich jedoch dennoch für die Verwendung durch das ANCISTRUS-SPEC Programm, da hier kleine Zeitschritte von Monaten betrachtet werden. Für solch kleine Zeitschritte ist die gefundene Drift irrelevant.

Da CCl_4 noch nicht auf MIPAS Messungen abgeleitet worden war, wurde eine Retrievalstrategie entwickelt, und globale Verteilungen wurden mithilfe des MIPAS-Datenprozessors am Karlsruher Institut für Technologie, Institut für Meteorologie und Klimaforschung abgeleitet. Dabei mussten diverse interferierende Spurengase und die Temperatur berücksichtigt werden. Zudem musste der Einfluss von Line-Mixing aufgrund des CO_2 Q-Zweigs bei 792 cm^{-1} beachtet werden. Die Verwendung eines neuen spektroskopischen Datensatzes für CCl_4 führte zu niedrigeren Mischungsverhältnissen, welche besser mit der aktuellen Literatur übereinstimmen. Auch Vergleiche mit anderen Messgeräten zeigten sehr gute Übereinstimmungen mit MIPAS Ergebnissen. CCl_4 eignet sich somit hervorragend für eine Verwendung im ANCISTRUS-SPEC Programm.

Abschließend wurden die neu bereitgestellten Datenprodukte von CFC-11, CFC-12 und CCl_4 als Eingabe für das ANCISTRUS-SPEC Programm verwendet. Die daraus resultierenden Ergebnisse zeigen eindeutig, dass eine Hinzunahme der neu verfügbaren Datenprodukte zu einer signifikanten Reduzierung der Unsicherheiten der abgeleiteten Zirkulationsgeschwindigkeiten führt.

Contents

Eidesstattliche Erklärung	i
Abstract	v
Zusammenfassung	vii
List of Figures	xiii
List of Tables	xv
Acronyms	xvii
1 Introduction	1
2 Ozone and Ozone Depleting Substances in the Atmosphere	7
2.1 The Atmosphere of the Earth	7
2.2 Ozone	7
2.2.1 Influence of the Brewer-Dobson Circulation on the Ozone Dis- tribution	11
2.3 Ozone Depleting Substances	12
2.3.1 Influence of the Brewer-Dobson Circulation on the Lifetimes of Ozone Depleting Substances	13
2.3.2 Catalytic Ozone Destruction through Ozone Depleting Substances	13
2.3.3 The Ozone Hole	15
3 The Michelson Interferometer for Passive Atmospheric Sounding (MIPAS)	17
3.1 Scanning Geometry	18
3.2 Principle of Measurement	18
3.3 Scientific Publications	22
4 Retrieval Procedure and Fundamentals of Atmospheric Radiation	23
4.1 Data Processing	23
4.2 Spectroscopy	25

4.2.1	Rotational Transitions	26
4.2.2	Vibrational Transitions	27
4.2.3	Vibration/rotation spectra	27
4.2.4	Line Shape and Line Mixing	28
4.3	Retrieval of Atmospheric Constituents	29
4.3.1	Radiative Transfer in the Atmosphere and Forward Modelling	29
4.3.2	Retrieval Theory	33
	I: Least Squares Fit	34
	II: Optimal Estimation	36
	III: The Tikhonov Approach	37
4.3.3	Error Estimation	39
5	First Author Publications	41
5.1	Drift-corrected trends and periodic variations in MIPAS IMK/IAA ozone measurements	41
5.2	MIPAS IMK/IAA CFC-11 (CCl_3F) and CFC-12 (CCl_2F_2) measurements: accuracy, precision and long-term stability	45
5.3	MIPAS IMK/IAA Carbon Tetrachloride (CCl_4) Retrieval and first Comparison with other Instruments	50
6	Co-Authored related publications	53
6.1	Technical Note: Trend estimation from irregularly sampled, correlated data	53
6.2	Global CFC-11 (CCl_3F) and CFC-12 (CCl_2F_2) measurements with the Michelson Interferometer for Passive Atmospheric Sounding (MIPAS): retrieval, climatologies and trends	55
6.3	Reassessment of MIPAS age of air trends and variability	58
7	Analysis of the Circulation of the Stratosphere using Spectroscopic Measurements (ANCISTRUS-SPEC)	61
7.1	Forward Modelling	61
7.2	Inversion of the Model	62
8	Results of Analyses with ANCISTRUS-SPEC	65
9	Conclusions	69

A Copies of all First Author Publications	73
A.1 Drift-corrected trends and periodic variations in MIPAS IMK/IAA ozone measurements	73
A.2 MIPAS IMK/IAA CFC-11 (CCl ₃ F) and CFC-12 (CCl ₂ F ₂) measure- ments: accuracy, precision and long-term stability	93
A.3 MIPAS IMK/IAA Carbon Tetrachloride (CCl ₄) Retrieval and first Com- parison with other Instruments	129
B Copies of Co-Authored Publications relevant for this Thesis	147
B.1 Technical Note: Trend estimation from irregularly sampled, correlated data	147
B.2 Global CFC-11 (CCl ₃ F) and CFC-12 (CCl ₂ F ₂) measurements with the Michelson Interferometer for Passive Atmospheric Sounding (MIPAS): retrieval, climatologies and trends	159
B.3 Reassessment of MIPAS age of air trends and variability	179
C List of other Co-Authored Publications	197
Bibliography	199
Acknowledgements	209

List of Figures

1.1 Schematic display of the Brewer-Dobson circulation	1
1.2 Turnaround Latitudes: mean residual velocities	3
2.1 Ozone distribution the stratosphere	8
2.2 Vertical ozone distribution in the tropics	9
3.1 Schematic display of MIPAS scanning geometry	17
3.2 Schematic of a Michelson Interferometer	19
3.3 Schematic of constructive and destructive interference	19
3.4 Schematic display of MIPAS	20
3.5 Rectangular function and its Fourier transform	21
4.1 Schematic display of the IMK/IAA retrieval processor	24
4.2 MIPAS Spectrum	25
4.3 Sketch: Optical Path	31
4.4 Sketch: MIPAS limb geometry	33
5.1 Comparison of MIPAS ozone trends with simulation of mixing barrier shift	43
5.2 Relative trends of CFC-11 and CFC-12	48
5.3 Trends of CCl ₄	52
6.1 MIPAS trends of CFC-11 and CFC-12 minus age of air corrected HATS trends	56
8.1 Wind speeds and directions assessed running Ancistrus with 4 vs. 6 tracers	66
8.2 Standard deviation of vertical wind speeds assessed running Ancistrus with 4 vs. 6 tracers	67
8.3 Standard deviation of horizontal wind speeds assessed running An- cistrus with 4 vs. 6 tracers	67
9.1 Drift-corrected trends of MIPAS Ozone	70

List of Tables

2.1 Emissions and ozone depleting potential of ozone depleting substances	14
3.1 Scan sequences of MIPAS - FR and RR nominal mode	18
5.1 Vertical resolution of MIPAS and comparison instruments	46
5.2 MIPAS CCl₄ retrieval characteristics	51

Acronyms

Abbreviations

ACE-FTS	Atmospheric Chemistry Experiment Fourier Transform Spectrometer
ANCISTRUS-SPEC	Analysis of the Circulation of the Stratosphere using Spectroscopic Measurements
AO	Annual oscillation
ASF	Atmospheric Trace Gases and Remote Sensing
ATMOS	Atmospheric Trace Molecule Spectroscopy
BDC	Brewer-Dobson circulation
CCl₄	Carbon tetrachloride
CCM	Chemistry-climate model
CFC	Chlorofluorocarbon
CH₃CCl₃	Methyl chloroform
Cl	Chlorine atoms
ClO	Chlorine monoxide
ClONO₂	Chlorine nitrate
ClO_x	Chlorine radicals
CO	Carbon monoxide
CO₂	Carbon dioxide
CSIC	Consejo Superior de Investigaciones Científicas
Envisat	Environmental Satellite
EOS	Earth Observing System
ERA-Interim	European Centre for Medium-range Weather Forecasts (ECMWF) Interim Reanalysis
ESA	European Space Agency
CFC-11	CCl ₃ F
CFC-113	C ₂ CCl ₃ F ₃
CFC-12	CCl ₂ F ₂
FOV	Field of view
FR	Full spectral resolution
FWHM	Full width at half maximum
GCM	General circulation model
GHG	Greenhouse gas
CBrClF₂	Halon-1211
CBrF₃	Halon-1301
HCFC-22	Chlorodifluoromethane

HCl	Hydrogen chloride
HNO₃	Nitric acid
HOCl	Hypochlorous acid
HO_x	Hydrogen oxide radicals
IAA	Instituto de Astrofísica de Andalucía
IMK	Institute of Meteorology and Climate Research
IR	Infrared
JPL	Jet Propulsion Laboratory
JRA-25	Japanese 25-Year Reanalysis
KIT	Karlsruhe Institute of Technology
KOPRA	Karlsruhe Optimized and Precise Radiative transfer Algorithm
LTE	Local thermodynamic equilibrium
CH₄	Methane
MIPAS	Michelson Interferometer for Passive Atmospheric Sounding
MLS	Microwave Limb Sounder
MOPD	Maximum optical path difference
N₂	Molecular nitrogen
N₂O	Nitrous oxide
NCGG7	Seventh International Symposium on Non-CO ₂ Greenhouse Gases
NO_x	Nitrogen oxide radicals
O₂	Oxygen
OCS	Carbonyl sulfide
ODP	Ozone depletion potential
ODS	Ozone-depleting substances
PSC	Polar stratospheric cloud
QBO	Quasi biennial oscillation
RR	Reduced spectral resolution
SAO	Semi-annual oscillation
SAT	Satellite-borne Remote Sensing of Trace Gases
SF₆	Sulfur hexafluoride
TEM	Transformed Eulerian-mean
TTL	Tropical tropopause layer
UTLS	Upper troposphere/lower stratosphere
UV	Ultraviolet
vmr	Volume mixing ratio
ZOPD	Zero optical path difference

Nomenclature

\mathbf{A}	Averaging kernel matrix
B	Rotational constant
$B_\nu(T)$	Planck's law
c	Speed of light
χ^2	Cost function
ρ	Density
$\delta(x)$	Dirac delta function
h	Planck constant
\hbar	Dirac constant (reduced Planck constant)
I	Moment of inertia
\mathbf{I}	Identity matrix
J	Rotational quantum number
j_ν	Emission coefficient
$j_{\nu,sc}$	Contribution to emission by scattering
$\tilde{J}(T_i, \nu)$	Source function
K	Vibrational quantum number
\mathbf{K}	Jacobian matrix
k_B	Boltzmann constant
$k_{\nu,a}$	Mass absorption coefficient
$k_{\nu,sc}$	Mass scattering coefficient
ν	Frequency
\mathbf{R}	Regularization matrix
T	Temperature
τ_ν	Optical path
t_ν	Transmission
u_{ig}	Column density for the gas g in layer i

1. Introduction

The distribution of trace constituents in the atmosphere is regulated by chemical processes and atmospheric transport and mixing, as well as surface and ocean sinks on the boundaries. Chemical processes include reactions between trace gases and photochemical reactions due to the absorption of e.g., ultraviolet (UV) radiation. However, chemical processes are only one factor influencing trace gas distributions in the atmosphere. Depending on altitude and latitude, the distribution of trace gas concentrations in the atmosphere is predominantly controlled by atmospheric transport and mixing. A particularly prominent transport process in the stratosphere is the Brewer-Dobson circulation (BDC) (Fig. 1.1). Tropospheric air masses to enter the

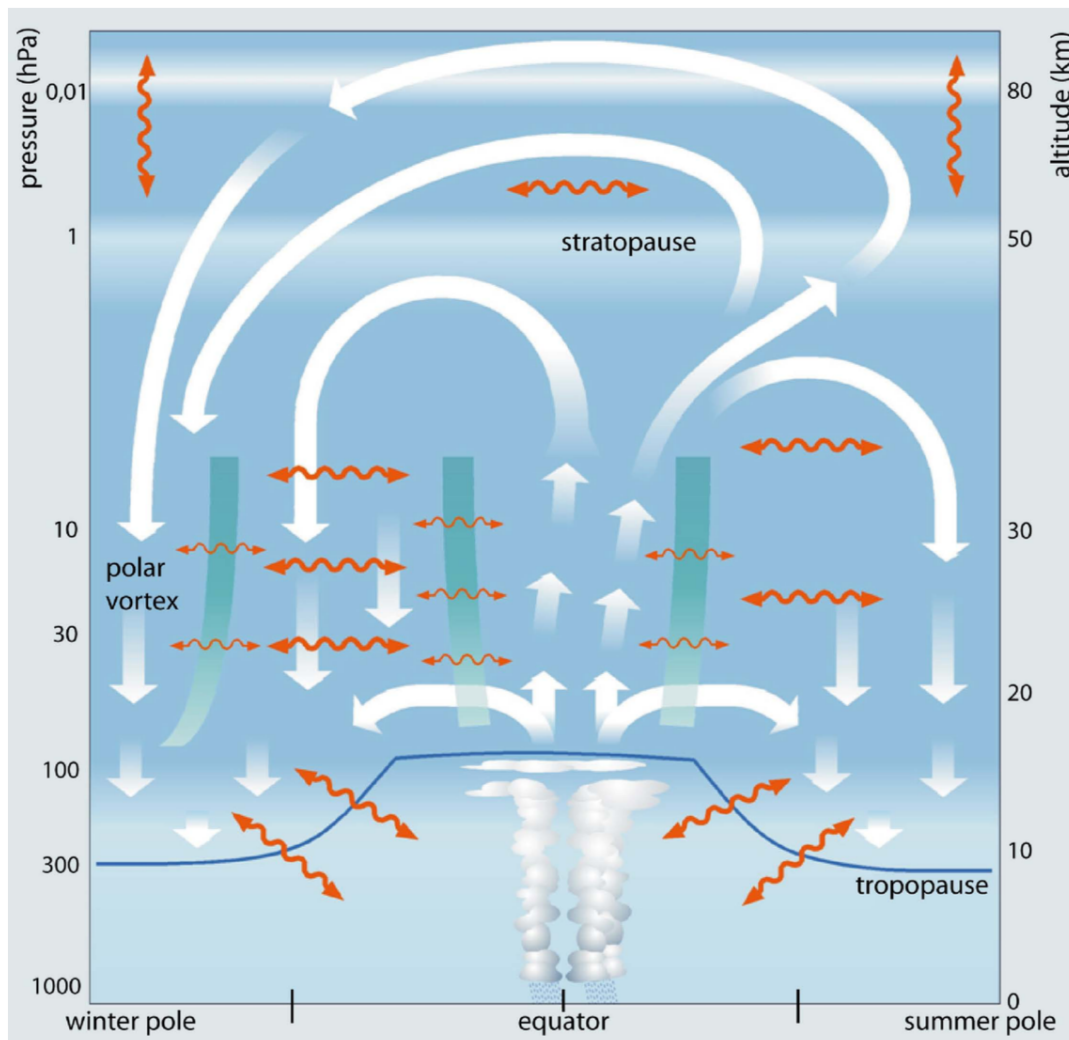


FIGURE 1.1: Schematic display of the Brewer-Dobson circulation and the transport processes in the middle atmosphere - Source: Bönisch et al. (2011) - CC BY 3.0 License.

stratosphere in the region of the tropical tropopause. After ascending further and also traveling polewards, the air subsides at middle and high latitudes. The subtropical mixing barriers (Fig. 1.1: indicated by thick green lines close to the equator) prevent most two-way mixing processes (Fig. 1.1: red wiggling arrows) between the tropics and mid-latitudes. During wintertime, a mixing barrier also forms close to the respective pole (Fig. 1.1: thick green line near the winter pole) due to strong potential vorticity gradients associated with the polar vortex.

The possibility of such a long-range, global circulation was mentioned by Dobson as early as 1929, who stated that “*The only way in which we could reconcile the observed high ozone concentration in the Arctic in spring and the low concentration within the Tropics, with the hypothesis that the ozone is formed by the action of sunlight, would be to suppose a general slow poleward drift in the highest atmosphere with a slow descent of air near the Pole. Such current would carry ozone formed in low latitudes to the Pole and concentrate it there.*” (Dobson et al., 1929), referring to observed ozone values in the tropics which were lower than expected, compared to higher than expected ozone values over high latitudes. However, information on the vertical distribution of ozone was sparse then and global measurements, e.g., from satellites, were not available yet. The term "Brewer-Dobson circulation" was already used in the early 1960's. Yet, it took until the late 1970's for a sound theoretical concept to be developed in terms of the "Transformed Eulerian-mean" (TEM) (Andrews and McIntyre, 1976, 1978) which was later refined by Plumb (2002). The BDC is a global circulation phenomenon between the tropics and the poles. It consists of a "deep branch" in the middle and upper stratosphere and a shallow branch in the lower stratosphere. The deep branch exhibits a pronounced annual cycle and is particularly pronounced in the respective winter hemisphere.

The BDC is driven by waves propagating upwards from the troposphere, e.g., planetary- and synoptic-scale Rossby waves, as well as buoyancy waves that dissipate higher up in the atmosphere and deposit angular momentum when they break. However, drag from planetary-scale Rossby waves, which are the predominant driver of the deep branch of the BDC, can only be westward. Because of the Earth's rotation, this westward drag results in poleward motion of the air. The deep branch of the BDC is particularly pronounced in the winter hemisphere, because planetary-scale Rossby waves can only propagate into the stratosphere when the mean underlying flow is eastward. The thermal wind balance implies an eastward flow in the winter hemisphere and a westward flow in the summer hemisphere. Due to this, planetary-scale Rossby waves can only drive a deep branch in the respective winter hemisphere. Two-way mixing induced by breaking waves is strong within the surf-zone, but weak around the subtropical and polar mixing barriers due to the steep potential vorticity gradients being present there. The surf-zone is located in the mid-latitudinal stratosphere and is defined as the zone where planetary-scale Rossby waves break.

The shallow branches of the BDC are also driven by Rossby waves, but other than for the deep branch, these waves are at the synoptic scale. These synoptic-scale Rossby

waves propagate into the subtropical lower stratosphere of both hemispheres year-round and induce a poleward motion in both hemispheres at altitudes of the lower stratosphere and upper troposphere.

Beside the stratospheric circulation, there exists an overturning circulation in the mesosphere that is driven mainly by buoyancy and gravity waves and enables mass transport from the summer to the winter pole.

A prominent means for diagnosing the BDC, more precisely its strength, is the so-called Downward-Control Principle (Haynes et al., 1991). It states that the mass flux across a particular altitude (or pressure) level can be identified solely from the zonal forces above that level.

It is often used to estimate changes in the BDC from multi-year model runs. In particular, the integrated tropical upwelling mass flux in the lower stratosphere has been used for quantifying the strength of the BDC. The general agreement is to use the mean mass flux at 70 hPa between the so-called turnaround latitudes, which are the latitudes at which the residual-mean velocities \bar{w}^*

change sign from upwards to downwards. It is particularly important not to use a fixed latitude to determine the flux, because the turnaround latitudes vary considerably throughout a year (Fig. 1.2). The pressure level of 70 hPa excludes most of the two-way mixing of the shallow branches, while including most of the deep branch of the BDC.

Another possibility to take a closer look at changes in the BDC is based on the age of stratospheric air. It is defined as the time lag since the air parcel observed had passed the tropopause (Hall and Plumb, 1994). Changes in the age of air over time hint at changes in the BDC. Engel et al. (2009) estimated age of air from 27 balloon flights using of carbon dioxide (CO_2) and sulfur hexafluoride (SF_6). Stiller et al. (2012) derived age of air from global vertical profile measurements of SF_6 of the Michelson Interferometer for Passive Atmospheric Sounding (MIPAS). The fact however, that Hall and Plumb (1994) did not consider the existence of the tropical tropopause layer (TTL) in their definition, gave rise to an ambiguity in the interpretation of where the

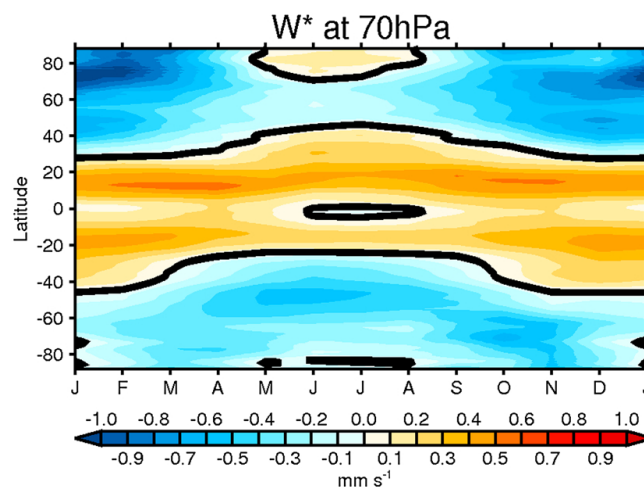


FIGURE 1.2: Mean residual vertical velocities \bar{w}^* from ERA-Interim reanalysis at 70 hPa for 1989–2009. The position of the turnaround latitudes are indicated by thick black lines where the residual-mean vertical velocities, \bar{w}^* , change sign from upward to downward. - Source: Butchart (2014) - CC BY-NC-ND 3.0 License.

age of air is zero. Stiller et al. (2012) calculate the age of air relative to the lower boundary of the TTL, because the atmosphere is well mixed below and thus mixing ratios of long-lived trace gases there can be assumed to equal those at the surface. This unambiguity in the point of zero leads to age estimates which are up to half a year older than those derived from models which commonly use the tropopause as a reference point, for which no measurements are available.

Unfortunately, using long-lived tracers can lead to large uncertainties in the resulting ages and trend estimates of changing ages. However, diagnosing the BDC using age of air has the advantage that mixing and stirring are taken into account.

Reanalyses, such as the European Centre for Medium-range Weather Forecasts (ECMWF) Interim Reanalysis (ERA-Interim), were also used to study the BDC using their wind and temperature estimates, but except from ERA-Interim and the Japanese 25-Year Reanalysis (JRA-25), the zonal-mean vertical velocities in the lower stratosphere exhibited rather large standard deviations.

Since several years, general circulation models (GCMs) and chemistry-climate models (CCMs) have been used to study the BDC in further detail, e.g., to estimate the tropical upwelling, location of the turnaround latitudes and possible changes due to a changing climate. Rind et al. (1990) found that doubling the CO₂ amount in their model lead to a significantly stronger residual-mean circulation. These findings are consistent with multi-model projections within the SPARC Report No. 5 (Eyring et al., 2010) and of the work of Hardiman et al. (2013).

However, Stiller et al. (2012) could only partly confirm these findings: They found decreasing age of air for the lowermost and upper tropical stratosphere in addition to some areas in southern mid-latitudes and northern polar regions. These findings agree with model estimates of increased tropical upwelling, which is associated with the speeding up of the BDC. Increasing age of air, which they found for the southern polar and most of the southern mid-latitudes as well as the lower to middle tropical stratosphere, rather hints at the BDC slowing down. The results of Stiller et al. (2012) were confirmed in the study of Haenel et al. (2015), except for the northern polar stratosphere and the middle tropical troposphere. The findings of Haenel et al. (2015) are based on a slightly longer and improved set of SF₆ data from the MIPAS. As a result of these complex patterns and seemingly partly contradicting findings, the need for further tools and analyses of the BDC is obvious and this thesis originates from the need to provide more reliable input data for one of these tools: the Analysis of the Circulation of the Stratosphere using Spectroscopic Measurements (ANCISTRUS-SPEC) model (von Clarmann and Grabowski, 2016).

In several model studies concentrations of ozone and ozone-depleting substances (ODS), e.g., chlorofluorocarbons (CFCs), in the atmosphere were found to change due to climate change induced changes in the BDC. Details on these changes in ozone and CFC distributions will be described in Section 2.2 and Section 2.3, respectively. While modelling changes in the concentration of these atmospheric constituents due

to climate change's influence on the BDC using CCMs and GCMs is common practice, the reverse way is also possible. Wind speeds and mixing coefficients can be derived using measurements of concentrations of atmospheric trace species as input in an inverse model. This is not surprising, since the BDC was partly discovered because of unexpected ozone concentrations (higher than expected concentrations in middle and high latitudes and lower than expected concentrations at tropical latitudes). The ANCISTRUS-SPEC model was developed to derive wind speeds and mixing coefficients from measurements of long-lived atmospheric constituents. It is a 2D model (latitude-altitude grid) and employs the inversion of the continuity equation. Concentrations of long-lived atmospheric trace gases serve as an input for the model. Further details on ANCISTRUS-SPEC will be given in Section 7.

This thesis relies heavily on measurements of atmospheric constituents performed with MIPAS. The instrument, its basic concept of measurement and its measurement geometry are introduced in Section 3. The underlying concepts of atmospheric radiative transfer, retrieval theory and their applications in the case of MIPAS, e.g., the Karlsruhe Optimized and Precise Radiative transfer Algorithm (KOPRA) (Stiller, 2000) and the MIPAS retrieval processor (both of which were developed at Karlsruhe Institute of Technology (KIT) Institute of Meteorology and Climate Research (IMK) - Atmospheric Trace Gases and Remote Sensing (ASF) - Satellite-borne Remote Sensing of Trace Gases (SAT)), are described in Section 4.3.

After a section on the scientific publications which contribute to this thesis and overviews of how these publications fit into the overall context of this thesis (Sec. 5 and 6), the results obtained with ANCISTRUS-SPEC are presented (Sec. 8) and final conclusions are drawn. All first author and co-author publications relevant to this thesis are appended for further reading.

2. Ozone and Ozone Depleting Substances in the Atmosphere

2.1 The Atmosphere of the Earth

The atmosphere of the Earth consists of several layers which are associated with characteristic temperature profiles. The lowermost layer of the atmosphere is the troposphere. It extends up to ~ 18 km in the tropics, to usually less than ~ 8 km at polar latitudes and to around 10 km at mid-latitudes. The troposphere is the layer of the atmosphere, where all phenomena associated with synoptic meteorology (most of what we commonly call weather) take place, e.g., clouds and cloud formation, surface pressure systems such as lows and highs, precipitation of all kinds and weather fronts. About 75 % of the total mass of the atmosphere is contained in the troposphere and almost all water vapour (about 99 %). In this atmospheric layer, the temperature decreases with altitude at a rate of approximately 9.8 K/km for dry air and about 5.5 K/km for saturated air, while the average is usually around 6.5 K/km. The boundary between the troposphere and the ensuing stratosphere is called the tropopause which exhibits a vertical temperature gradient of close to zero. Its temperature is about -55°C on global average, but can easily get as low as -80°C in the tropics where it exhibits the lowest temperature due to strong convection. This so-called cold point (in the tropical tropopause) causes almost all water vapour to "freeze out" when air crosses the tropopause on its way up. From the tropopause up to approximately 50 km follows the stratosphere, a layer in which the temperature increases with altitude, mainly due to absorption of ultraviolet (UV) radiation by ozone. This is the layer, in which the Brewer-Dobson circulation (BDC) mainly takes place. The stratopause is the boundary between the stratosphere and the mesosphere and marks the point of the temperature gradient reversal. The mesosphere extends up to about 90 km with decreasing temperature as altitude increases, again. It is followed by the mesopause and the thermosphere, a region in which temperatures can rise to as high as 1500°C , depending on solar activity.

This thesis focuses on processes in the stratosphere, but, as the layers are not strictly independent of each other, changes in the stratosphere also influence the troposphere and thus are important for changes in weather, climate and our natural habitat.

2.2 Ozone

Ozone (O_3) is a trace gas in the atmosphere and its molecule consists of three oxygen atoms. The gas has a distinct smell (Greek: $\acute{\omicron}\zeta\epsilon\iota\nu$ - pronounced *ozein* - "to smell") and is colorless in its gaseous phase, e.g., in the atmosphere. It was first isolated and

named by Christian Friedrich Schönbein in 1839 (Schönbein, 1840), while its chemical formula wasn't determined until 1863, when Jacques-Louis Soret suggested ozone's, later confirmed, composition. Atmospheric measurements of ozone were performed starting in 1853 and the column density was first reliably estimated by Fabry and Buisson (1921). Shortly afterwards, Dobson used a Féry spectrograph (Dobson, 1931; Götz et al., 1934) to measure vertically integrated ozone concentration at Oxford and subsequently established a network of column ozone measurements, first in Europe and later on even in the Southern hemisphere (Christchurch, New Zealand) (Dobson, 1968). Instruments similar to the one Dobson used back then are still used today but measurements are now complemented by balloon, aircraft and satellite measurements as well as ground-based techniques.

Figure 2.1 shows a distribution of ozone in the stratosphere (between 10 and 50 km) for the year 2012. This distribution was derived applying the trend estimation method introduced by von Clarmann et al. (2010) to data from the MIPAS (Chap. 3). Using the trend estimation method helps avoiding distortion of the distribution due

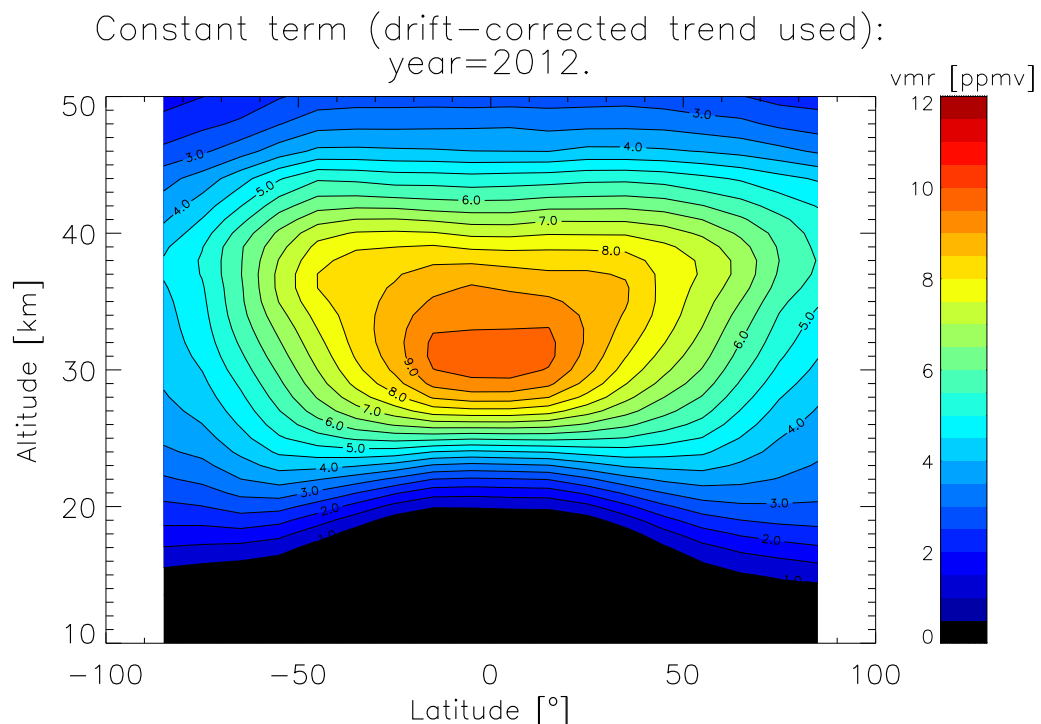


FIGURE 2.1: Altitude-latitude cross-section of ozone distribution in the stratosphere for the year of 2012. The Michelson Interferometer for Passive Atmospheric Sounding (MIPAS) data were deseasonalized using the trend estimation method by von Clarmann et al. (2010). - Source: Eckert et al. (2014) - CC BY 3.0 License.

to, e.g., atmospheric oscillations mapping onto the ozone. Figure 2.1 shows that the mixing ratio maximum (ppmv = parts per million volume) of ozone is centred roughly between 30 and 35 km, while it would rather be around 25 km if displayed in number density

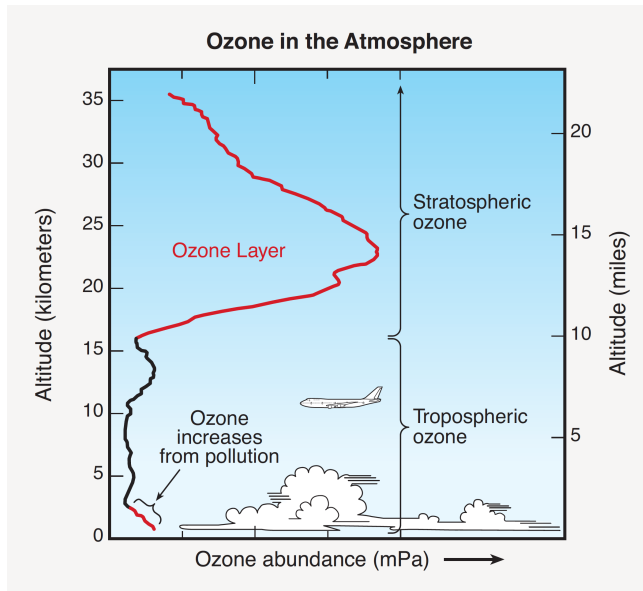
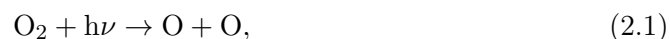


FIGURE 2.2: Vertical distribution of ozone in the tropics in number density. - Source: Hegglin et al. (2015) - public domain.

In other words, the ozone layer prevents most of this radiation reaching Earth's surface where it can increase risk of skin cancer and cataracts and can also impair the human immune system. Thus, ozone in the stratosphere is vital for life on Earth and its careful monitoring is very important. On the other hand, excess tropospheric ozone can pose health problems. Higher than natural amounts of the gas residing close to the ground are strongly associated with anthropogenic pollution, e.g., in the downstream of urban areas during warm periods. They can lead to respiratory issues and negatively affect already existing heart and lung conditions, as well as fauna and flora. In addition, ozone is a greenhouse gas (GHG), which is another good reason for minimizing its emissions at ground level.

In the stratosphere, ozone is formed by UV radiation. When an oxygen molecule absorbs wavelengths of less than 242.4 nm it photo-dissociates into two oxygen atoms (Chapman, 1930):

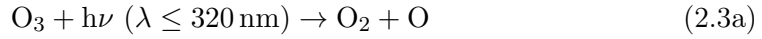


with the Planck constant (h) and the frequency (ν). When these oxygen atoms then react with molecular oxygen, they form ozone (Eq. 2.2):



(Fig. 2.2). Number density and the mixing ratio are related by pressure and temperature through the ideal gas law ($PV = nRT$; P : pressure of the gas, V : Volume of the gas, n : amount of the gas in moles, R : ideal/universal gas constant, T : temperature of the gas). No matter which measure you chose, mixing ratio or number density, most of the ozone resides in the stratosphere, about 90% to be precise. It is commonly known as the ozone layer and it absorbs most of the UV radiation coming from the Sun.

where M is a third body, e.g., an atom or molecule (Brasseur and Solomon, 2005) that does not chemically react in the given situation, but e.g., carries off excess energy. Since this mechanism requires sunlight, the largest amount of ozone is produced in the tropical stratosphere. While ozone is continually formed whenever sunlight is present, absorption of UV radiation and subsequent recombination with atomic oxygen reduce its amount in the atmosphere:

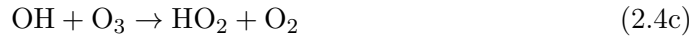


Numerous reactions with other constituents of the atmosphere also add to the budget, namely catalytic losses through hydrogen oxide radicals (HOx) (OH and HO₂) (Eqs. 2.4), nitrogen oxide radicals (NOx) (NO and NO₂) (Eqs. 2.5) and chlorine radicals (ClOx) (Cl and ClO; Sec. 2.3).

Hydrogen compounds participate in the following catalytic cycles in which ozone is destroyed (Brasseur and Solomon, 2005) :



or



or



or



The first cycle is predominant near the tropopause, because it is the only one which does not involve atomic oxygen, which is only formed to larger extents at higher altitudes, e.g., in the middle and higher stratosphere, where all of the above cycles contribute to catalytic ozone destruction.

Nitrogen compounds also have the potential to catalytically destroy ozone. Possible

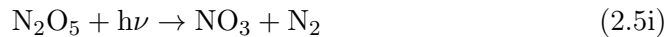
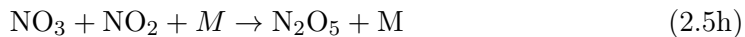
cycles are:



or



or



The first cycle is most efficient one at altitude ranges between 35 and 45 km, while the others are secondary. In the latter two cases, ozone is only destroyed when NO_3 is photolysed to $\text{NO} + \text{O}_2$. When photolysis results in $\text{NO}_2 + \text{O}$, the net destruction of ozone equals zero.

Ozone formation and destruction are in equilibrium. This equilibrium depends on temperature, sunlight, location in the atmosphere and the amount of possible reactants and was found to have shifted to lower ozone amounts in the late 1970s and afterwards due to anthropogenic emissions of chlorofluorocarbons (CFCs) (Sec. 2.3). This led to the formation and annual recurrence of the Antarctic ozone hole and also to, often severe, ozone depletion over the Arctic (Sinnhuber et al., 2011). First evidence of the Antarctic ozone hole through measurements was provided by Chubachi (1985) and Farman et al. (1985).

2.2.1 Influence of the Brewer-Dobson Circulation on the Ozone Distribution

As already mentioned, the BDC also influences the distribution of ozone in the stratosphere significantly. In a model study with doubled carbon dioxide (CO_2) amounts, Mahfouf et al. (1994) found midlatitude column ozone to increase. However, this could not unambiguously be attributed to an accelerated BDC as GHG-induced cooling of the stratosphere might slow down photochemical ozone destruction and it is

difficult to tell from this study how large the contribution of each process is. Nevertheless, photochemical processes are dominant above ~ 10 hPa while transport and chemistry predominate below this level (Butchart, 2014). Shepherd (2008) and Li et al. (2009) were able to distinguish their impact of the different processes further. In both model studies, upper stratospheric ozone was found to increase approximately uniformly with latitude, which can be mostly attributed to changes in photochemistry due to GHG induced cooling of the stratosphere. On the other hand, enhanced poleward transport due to an enhanced BDC causes lower stratospheric ozone to decrease in the Tropics and increase in the Extratropics. These findings were also confirmed by Austin et al. (2010) and Oman et al. (2010). Furthermore, the study by Austin et al. (2010) revealed that, due to the hemispheric asymmetry of the BDC caused by stronger wave-forcing in the Northern winter hemisphere, column ozone in the extratropical Northern hemisphere will recover (to 1980 levels) approximately 10 years faster than in the Southern hemisphere midlatitudes. Unfortunately, they could not find an accelerated BDC to speed up the recovery of Antarctic ozone.

2.3 Ozone Depleting Substances

Ozone-depleting substances (ODS) are anthropogenically produced atmospheric constituents whose decomposition products have the potential to release reactive chlorine and can thus lead to the catalytic destruction of stratospheric ozone. Major ODS are carbon tetrachloride (CCl_4), methyl chloroform (CH_3CCl_3) and CFCs such as CCl_3F (CFC-11), CCl_2F_2 (CFC-12) and $\text{C}_2\text{CCl}_3\text{F}_3$ (CFC-113). They are long-lived species, particularly the CFCs, and thus are excellent tracers for e.g., the BDC. In the troposphere they are almost inert, because UV light strong enough to photolyze them is almost entirely absorbed in the stratosphere.

ODS covered in this thesis are:

- trichlorofluoromethane - CCl_3F (CFC-11)
- dichlorodifluoromethane - CCl_2F_2 (CFC-12)
- carbon tetrachloride - CCl_4

CFC-11 and CFC-12 were widely used as refrigerants and blowing agents during the second half of the 20th century before being banned under the Montreal Protocol in 1987. CCl_4 was additionally commonly used as a refrigerant and as a solvent e.g., for dry cleaning and in fire extinguishers. It was banned under the London Amendment of the Montreal Protocol in 1990. CFC-11 and CFC-12 have atmospheric lifetimes of 60.2 (54.3-66.3) years and 109.5 (102.9-116.1) years (Ko et al., 2013, Tab. 3.7), respectively. The atmospheric lifetime of CCl_4 was recently reassessed to be 44 (36-58) years (Liang et al., 2016). Simply put, the atmospheric lifetime, τ , of an atmospheric constituent is the time the gas resides in the atmosphere, i.e., from its entry through e.g., anthropogenic emission until it is removed from the atmosphere for example by photolysis

or chemical reactions. Lifetimes are calculated, e.g., from model studies, as the global burden of a gas B (total number of molecules of the atmospheric constituent divided by its globally integrated loss L (in molecules/year):

$$\tau = \frac{B}{L} \quad (2.6)$$

2.3.1 Influence of the Brewer-Dobson Circulation on the Lifetimes of Ozone Depleting Substances

As photolysis rates are highly dependent on the gases temporal and spacial distribution in the atmosphere, climate-change induced changes in the BDC were found to influence atmospheric lifetimes of CFCs. In their model study, Rind et al. (1990) found that an accelerated BDC lead to faster removal of CFCs from the atmosphere. Results from Butchart and Scaife (2001) showed that a 3% per decade strengthening of the BDC caused the amounts of CFCs to return to 2050 and 2080 levels approximately 5 and 10 years earlier, respectively. These findings were, however, gained assuming that the efficiency of the photodegradation of CFCs is not altered by climate change or the recovery of stratospheric ozone. Nevertheless, Douglass et al. (2008) confirmed stratospheric loss rates to increase, corresponding to decreasing CFC lifetimes, also when effects of a faster circulation and changes in photodegradation efficiency were accounted for.

2.3.2 Catalytic Ozone Destruction through Ozone Depleting Substances

In 1974 Molina and Rowland¹ published their groundbreaking work on the impact of CFCs from industrial sources. Once ODS, also known as halogen source gases, are photolyzed in the stratosphere, they are converted into so-called reactive halogen gases. Reactive halogen gases is an umbrella term and halogen species under this term can be divided into two categories, so-called reservoir gases:

- hydrogen chloride (HCl)
- chlorine nitrate (ClONO₂)
- hypochlorous acid (HOCl)

and most reactive species:

- chlorine atoms (Cl)
- chlorine monoxide (ClO)

¹Molina and Rowland (1974)

TABLE 2.1: Global emissions of selected ozone-depleting substances (ODS) and their ozone depletion potential (ODP). - Source: Hegglin et al. (2015).

Gas	Global Emissions in 2012 [Kt/yr]	Ozone Depletion Potential (ODP)
<i>Chlorine gases</i>		
CFC-11	46-68	1
CFC-12	16-64	0.73
CCl ₄	40-74	0.72
<i>Bromine gases</i>		
Halon-1301 (CBrF ₃)	1.4-2	15.2
Halon-1211 (CBrClF ₂)	0.3-9.3	6.9

The following cycle of ozone destruction involving chlorine species is particularly effective in the upper stratosphere:



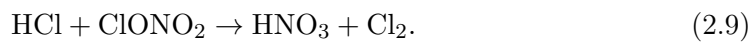
Below 30 km, chlorine species are rather present in the form of reservoir gases. While this limits ozone destruction below 30 km, another cycle is still important at around 20 km:



Similar pathways as pointed out in Eqs. 2.7 and 2.8 also exist for bromine species. Bromine species have even higher ozone depletion potential (ODP) than their chlorine counterparts (Tab. 2.1). The ODP describes the effectiveness of a gas to destroy ozone: the higher the ODP of a gas, the more ozone it can destroy during its atmospheric lifetime. Fortunately, anthropogenically emitted amounts of bromine source gases are considerably smaller than for chlorine species and thus they play a subordinate, even though not negligible, role in ozone depletion through ODS.

2.3.3 The Ozone Hole

Reservoir gases play a significant role in ozone depletion as they can, under certain conditions, be transformed into most reactive species in large quantities which then catalytically destroy ozone. For this to happen, it needs so-called polar stratospheric clouds (PSCs). These form at very low temperatures which only occur inside the polar vortex during the respective hemisphere's winter time. At 195 K (-78 °C), liquid and solid PSCs consisting of nitric acid (HNO₃) form. When temperatures drop as low as 187 K (-85 °C), it is cold enough for the very low amounts of water vapour to freeze and form PSCs consisting of ice particles. Solomon et al. (1986) pointed out that heterogeneous chemistry (Eq. 2.9) occurring on the surface of these clouds



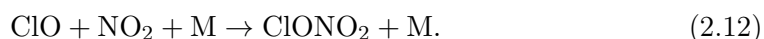
The excess Cl₂ formed this way is then photolyzed (Eq. 2.10) once the sun rises again after polar winter



Through the following catalytic cycle, ozone is then destroyed in large amounts:



The cycle of the so-called ClO dimer is the most effective way of ozone destruction and is responsible for approximately 75 % of the ozone loss within the polar vortex (Solomon, 1999). In addition to providing Cl₂, Eq. 2.9 also generates HNO₃, which remains in the PSCs. This process removes NO_x from the atmosphere and stores it in the liquid and solid phase. Once the cloud particles grow large enough, they sediment and thus permanently remove NO_x from the stratosphere. This is called denitrification. Denitrification prevents active chlorine from returning to reservoirs (Eq. 2.12) and thus significantly increases the amount of ozone destroyed by one chlorine radical as it remains chemically active for a longer time.



Accordingly, formation of PSCs, heterogenous chemistry on their surface and denitrification are the major factors that lead to severe ozone depletion over the poles during late winter and early spring. Because the polar vortex is more stable in the Southern Hemisphere, stratospheric temperatures generally drop lower than in the Northern Hemisphere. As a result, PSCs are more likely to form in the Southern polar vortex,

especially those consisting of water, which barely ever form in the Northern Hemisphere. In the Southern Hemisphere, PSCs also tend to span a wider, more coherent range than in the Northern hemisphere. For these reasons, ozone depletion is more severe in the Southern Hemisphere.

3. The Michelson Interferometer for Passive Atmospheric Sounding (MIPAS)

The Michelson Interferometer for Passive Atmospheric Sounding (MIPAS) was one of ten instruments aboard the Environmental Satellite (Envisat) operated by the European Space Agency (ESA). The satellite was launched into a sun-synchronous polar orbit with an inclination of 98.5° on March 1, 2002. Contact with the satellite was lost on April 8, 2012, which implied the end of the mission. Envisat orbited the Earth 14.4 times a day at an altitude of approximately 800 km. The satellite's orbit ensured global coverage of measurements with equator crossing times of 10:00 and 22:00 local time. Every 35 days the satellite started a new cycle, as it then returned to the same orbit. Due to an instrument failure, MIPAS measurements consist of two periods. The full spectral resolution (FR) period consists of measurements from June 2002 to March 2004 and the reduced spectral resolution (RR) period covers measurements from January 2005 to April 2012. The MIPAS FR and RR period differ in both vertical sampling (Sec. 3.1) and spectral resolution (Sec. 3.2). This can lead to a bias between the FR and the RR product of the same atmospheric constituent, which has to be taken into account, e.g., for trend estimation.

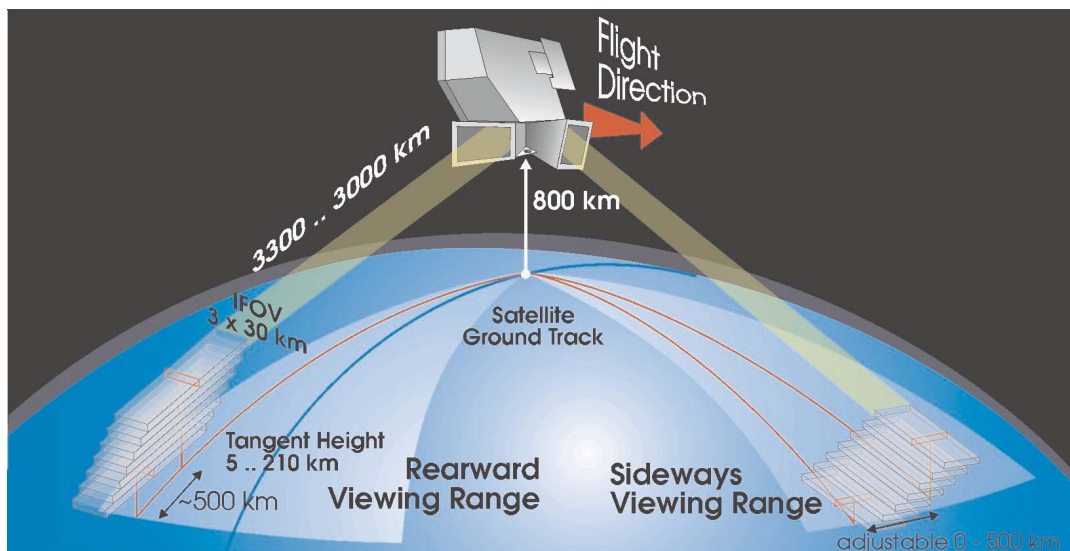


FIGURE 3.1: Schematic display of MIPAS scanning geometry - Source: Fischer et al. (2008) - CC BY 3.0 License.

3.1 Scanning Geometry

MIPAS measured in limb view (Fig. 3.1), meaning that it looked tangentially through the atmosphere, instead of looking straight downward (nadir). It detected mid-infrared radiation emitted along the line of sight and thus originating from all atmospheric layers on the ray path. The point along this path which is closest to the Earth's surface is referred to as the tangent altitude. At the tangent point, the instrument's instantaneous field of view (FOV) is 3 km in the vertical and 30 km in the horizontal domain. While the small extension in the FOV in the vertical domain ensures excellent vertical resolution, the wider range in the horizontal domain improves the signal to noise ratio since more radiation reaches the detector. During the FR period, the vertical scanning pattern of the MIPAS nominal mode consisted of 17 tangent altitudes, changing to 27 tangent altitudes during the RR period (Tab. 3.1). The horizontal spacing of the limb scans changed from 510 to 410 km for the FR and the RR period, respectively, while the number of measurements per day increased from about 1000 to about 1300. However, the price to pay for this improved sampling was a degradation of the spectral resolution (Sec. 3.2).

TABLE 3.1: Scan sequences for the MIPAS FR and RR period (Kellmann et al., 2012). The RR-Nominal mode altitudes are latitude dependent.

Measurement mode	FR	RR
Scan no. 1	68 km	70 km
Scan no. 2	60 km	66 km
Scan no. 3	52 km	62 km
Scan no. 4	47 km	58 km
Scan no. 5	42 km	54 km
Scan no. 6	39 km	50 km
Scan no. 7	36 km	46 km
Scan no. 8	33 km	43 km
Scan no. 9	30 km	40 km
Scan no. 10	27 km	37 km
Scan no. 11	24 km	34 km
Scan no. 12	21 km	31 km
Scan no. 13	18 km	29 km
Scan no. 14	15 km	27 km
Scan no. 15	12 km	25 km
Scan no. 16	9 km	23 km
Scan no. 17	6 km	21 km
Scan no. 18	–	19.5 km
Scan no. 19	–	18 km
Scan no. 20	–	16.5 km
Scan no. 21	–	15 km
Scan no. 22	–	13.5 km
Scan no. 23	–	12 km
Scan no. 24	–	10.5 km
Scan no. 25	–	9 km
Scan no. 26	–	7.5 km
Scan no. 27	–	6 km

3.2 Principle of Measurement

MIPAS is a cryogenic limb emission Fourier transform spectrometer detecting mid-infrared radiation in the range of 685 to 2410 cm^{-1} (14.6 to $4.1 \mu\text{m}$) (Fischer et al., 2008). It consists of eight

detectors measuring in 5 different bands (A-band: $685-970\text{ cm}^{-1}$, AB-band: $1020-1170\text{ cm}^{-1}$, B-band: $1215-1500\text{ cm}^{-1}$, C-band: $1570-1750\text{ cm}^{-1}$ and D-band: $1820-2410\text{ cm}^{-1}$). Measurements of emission, as opposed to solar occultation, allow for observations during day and night, since no background source, like the sun, is needed.

Figure 3.2 shows a schematic of a Michelson Interferometer. It basically consists of two mirrors, a semi-permeable mirror - also called a beamsplitter - and a detector. At least one of the two retroreflecting mirrors of a Michelson Interferometer is a moving mirror, Mirror 2 in Figure 3.2. A beam of radiation - in the case of MIPAS mid-infrared emissions from the atmosphere - enters the Michelson Interferometer.

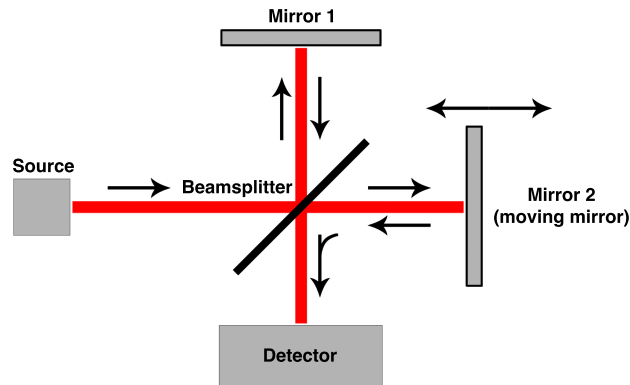


FIGURE 3.2: Schematic of a Michelson Interferometer.

At hitting the beamsplitter, it is split into two parts, each continuing to one of the mirrors. Both parts of the beam are reflected at the mirrors, recombined at the beamsplitter and directed to the detector.

Depending on the difference of the path lengths travelled by each of the beams, the signal is amplified, weakened or even cancelled out entirely. To explain this in detail, we assume a monochromatic (only comprising one wavelength) beam of radiation entering the instrument.

When the two beams, previously split at the beamsplitter, are recombined when the two mirrors

are equally far apart from the beamsplitter and thus cause the two beams to travel the same distance, the detector will receive a maximal signal. If the mirrors are positioned such that the path difference of the two beams is equal to half their wavelength, they cancel out when recombined and the detector receives no signal. To better understand this, we have to assume that light is a wave. The left panel of Figure 3.3 displays the situation, when the two beams travel the same distance or when the path difference is equal to a multiple of the beams' wavelength: $\Delta l = n \cdot \lambda$; with Δl being the

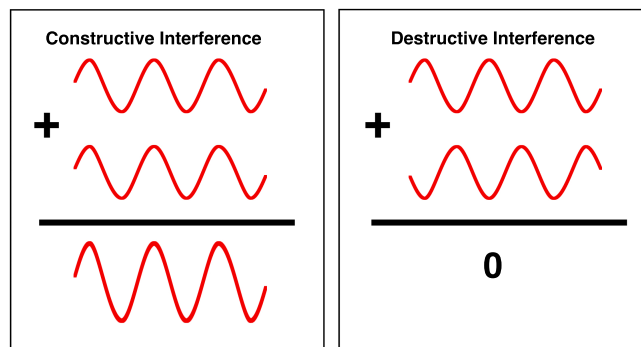


FIGURE 3.3: Schematic of constructive (left) and destructive (right) interference.

are equally far apart from the beamsplitter and thus cause the two beams to travel the same distance, the detector will receive a maximal signal. If the mirrors are positioned such that the path difference of the two beams is equal to half their wavelength, they cancel out when recombined and the detector receives no signal. To better understand this, we have to assume that light is a wave. The left panel of Figure 3.3 displays the situation, when the two beams travel the same distance or when the path difference is equal to a multiple of the beams' wavelength: $\Delta l = n \cdot \lambda$; with Δl being the

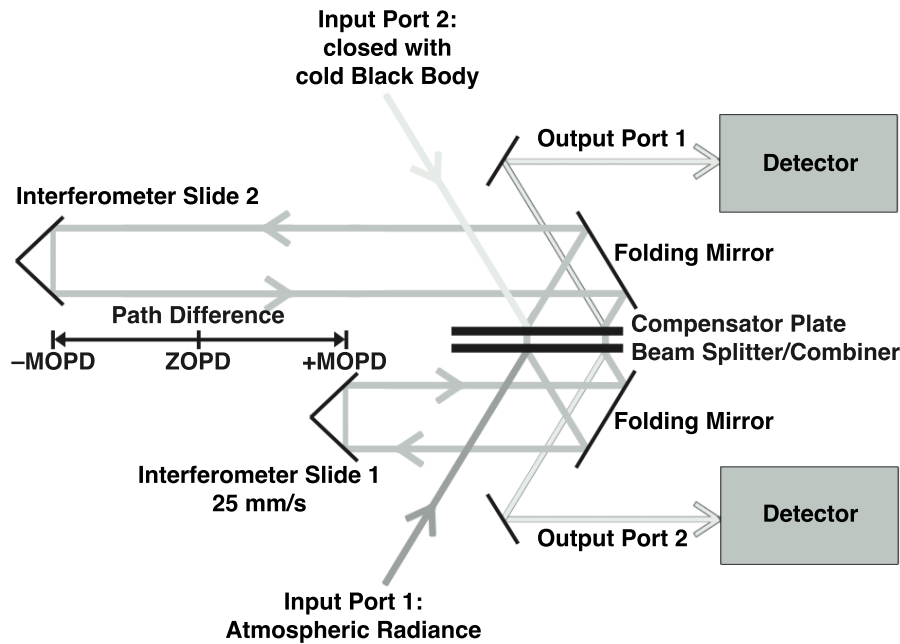


FIGURE 3.4: Schematic display of MIPAS.

path difference, n being an arbitrary integer greater or equal zero and λ being the wavelength of the radiation. The right panel of Figure 3.3 shows what happens when the two beams travel distances with a difference of one half of their wavelength, or $\Delta l = 1/2 + n \cdot \lambda$, before being recombined. During a certain amount of time, the mirror moves from zero path difference to the maximum path difference. This creates a continuous, sinusoidal pattern, since the recombined signal alternates between constructive and destructive interference (coming past any states in between). The result is called an interferogram and for monochromatic radiation looks simply like a sinusoidal wave.

For MIPAS (Fig. 3.4), there are two essential differences compared to this very simple model:

First, in the case of MIPAS, both mirrors moved in opposite directions, but this does not change the measurement principle. It did, however, allow for an efficient use of space inside the instrument while still achieving a maximum optical path difference (MOPD) of 20 cm. The MOPD is the difference of the distances the two beams travel when the mirrors are the furthest apart, while zero optical path difference (ZOPD) is the position of the mirrors when the two beams travel an equally long distance before being recombined. Unfortunately, an instrument failure resulted in reducing the MOPD to 8 cm.

The second difference compared to the previously introduced, very simple model is that MIPAS does not receive only one wavelength, but all wavelengths between 4.1 and 14.6 μm , with certain band gaps where the atmosphere is opaque and no useful information is available. Due to that, interference patterns for all wavelengths are superimposed when reaching the detector. Their signals can, however, be separated by the means of Fourier transformation which results in a radiance spectrum. The spectrum represents the frequency distribution of the incoming radiation. Due to the maximum path difference of the instrument being finite, only a finite number of maxima (from constructive interference) and minima (from destructive interference) is detected for each wavelength. If the maximum path difference was infinite, we would be able to distinguish all wavelengths from each other perfectly and unambiguously. But in reality, this results in the spectral resolution of the instrument being finite as well. However, the longer the MOPD, the better the spectral resolution of the instrument. The spectral resolution of an instrument is calculated as follows:

$$\Delta\nu = \frac{1}{2 \cdot \text{MOPD}} \quad (3.1)$$

Accordingly, the spectral resolution of MIPAS deteriorated from 0.025 cm^{-1} during the FR period to 0.0625 cm^{-1} during the RR period, as MIPAS' ZOPD decreased from 20 cm to 8 cm.

Nevertheless, deriving a spectrum from a finite interferogram using Fourier transformation has its pitfalls. A finite interferogram is equal to an infinite interferogram multiplied with a rectangular function and, according to the convolution theorem $\mathcal{F}\{f * g\} = \mathcal{F}\{f\} \cdot \mathcal{F}\{g\}$ its Fourier transform equals the pointwise product of the Dirac delta function and the so-called sinc function $\text{sinc}(x) = \frac{\sin(x)}{x}$ (right panels in Figure 3.5). The side wiggles of the sinc function cause ambiguities in the attribution of the spectral signal, which is highly undesirable. A often-used work-around for this problem is the so-called apodization: The interferogram is multiplied with a smoothing function - in the case of MIPAS the Norton-Beer "strong" apodization (Norton and Beer, 1976) - leading to

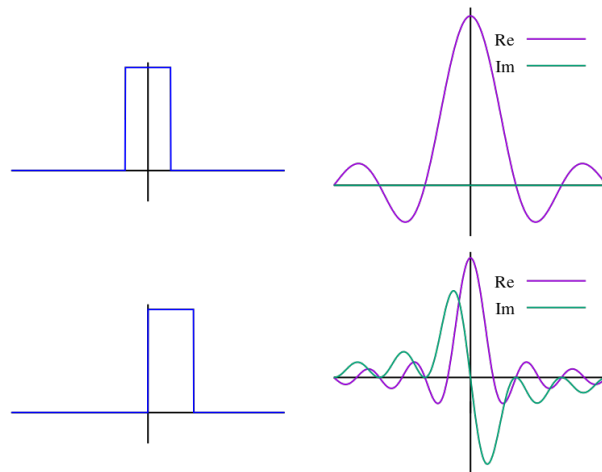


FIGURE 3.5: Rectangular function and its Fourier transform - Source: By Sławomir_Biały, Ikamusu-meFan - Own work, CC BY-SA 4.0, <https://commons.wikimedia.org/w/index.php?curid=42300194>.

a smoother transition at the outer edges of the interferogram. This prevents unwanted side wiggles in the spectrum for the most part. However, it comes at the cost of degraded spectral resolution, because by smoothing the original interferogram we remove some of the information content in there. After apodization, MIPAS spectral resolutions deteriorate to 0.048 cm^{-1} and 0.121 cm^{-1} for the FR and RR period, respectively.

3.3 Scientific Publications

MIPAS measurements were used to derive numerous atmospheric constituents, subdivided into several data products. All IMK MIPAS publications can be found at <https://www.imk-asf.kit.edu/english/298.php>. For most reliable and valuable data products, the precise location of the tangent altitude (von Clarmann et al., 2003) is required as well as knowledge about a possible spectral shift of the spectra. Since MIPAS measures in infrared (IR) emission instead of occultation, the temperature has a major impact on the emitted radiation intensity. Therefore, a calibration of black body radiances at known temperatures is essential. This makes the retrieval somewhat vulnerable, as errors in temperature propagate onto all subsequent retrievals. Nevertheless, the advantage of being independent from a background source like the sun compensate for this downside of IR emission measurements.

Several previously retrieved MIPAS products, including temperature and spectral shift, were used in the retrievals of products validated and/or retrieved within the scope of this thesis. These are:

- ozone (O_3): Gil-López et al. (2005); Glatthor et al. (2006); von Clarmann et al. (2009)
- chlorine nitrate (ClONO_2): Höpfner et al. (2004); von Clarmann et al. (2009)
- chlorine monoxide (ClO): Glatthor et al. (2004); von Clarmann et al. (2009)
- methane (CH_4): Glatthor et al. (2005); von Clarmann et al. (2009)
- nitrous oxide (N_2O): Glatthor et al. (2005); von Clarmann et al. (2009)
- nitric acid (HNO_3): Stiller et al. (2005); von Clarmann et al. (2009)
- CCl_3F (CFC-11): Kellmann et al. (2012)
- ethane (C_2H_6): von Clarmann et al. (2007)
- hydrogen cyanide (HCN): Glatthor et al. (2009)
- peroxyntiric acid (HNO_4): Stiller et al. (2007)

4. Retrieval Procedure and Fundamentals of Atmospheric Radiation

This chapter is dedicated to the description and explanation of the entire retrieval process, which leads from measured radiances to vertical profiles of atmospheric constituents. The processing of the data collected by the Michelson Interferometer for Passive Atmospheric Sounding (MIPAS) is covered in detail, as well as radiative transfer and retrieval theory. These theories lay the foundation for retrieving ozone (O_3), CCl_3F (CFC-11), CCl_2F_2 (CFC-12) and carbon tetrachloride (CCl_4), alongside many others, and thus are essential for this thesis and the scientific conclusions drawn from the data as well as subsequent analyses.

4.1 Data Processing

To successfully derive vertically resolved profiles of atmospheric constituents from the original MIPAS measurements, several steps are necessary. Essentially, MIPAS measures spectrally resolved infrared (IR) radiances emitted by trace gases in the atmosphere (Sec. 4.2 and 4.3.1), which are converted into electronic signals by its detectors. These raw data - the Level 0 data - are checked for missing and erroneous data, which are excluded from further data processing. The Level 0 data are then transmitted to the ground.

The European Space Agency (ESA) transforms the Level 0 data into fully reconstructed interferograms, which are called Level 1a data. Afterwards, the data are further processed into calibrated emission spectra - Level 1b data - by the means of Fourier transformation and calibration (Kleinert et al., 2007).

The Satellite-borne Remote Sensing of Trace Gases (SAT) research group at the Institute of Meteorology and Climate Research (IMK), Karlsruhe Institute of Technology (KIT), receives the Level 1b data from the ESA and use their in-house processor developed specifically for this purpose to gain vertical profiles of the temperature and atmospheric trace gases. Three other MIPAS retrieval processors exist. These are: at the ESA (Raspollini et al., 2013), at Oxford University (The University of Oxford Physics Department, 2008) and in Bologna (Dinelli et al., 2010). For this thesis, only data processed at IMK in Karlsruhe were used. Figure 4.1 shows a schematic of the MIPAS IMK/IAA retrieval processor. Level 1b data provided by ESA serve as input and the final products are vertical profiles of atmospheric constituents, such as CFC-11 or ozone, and temperature.

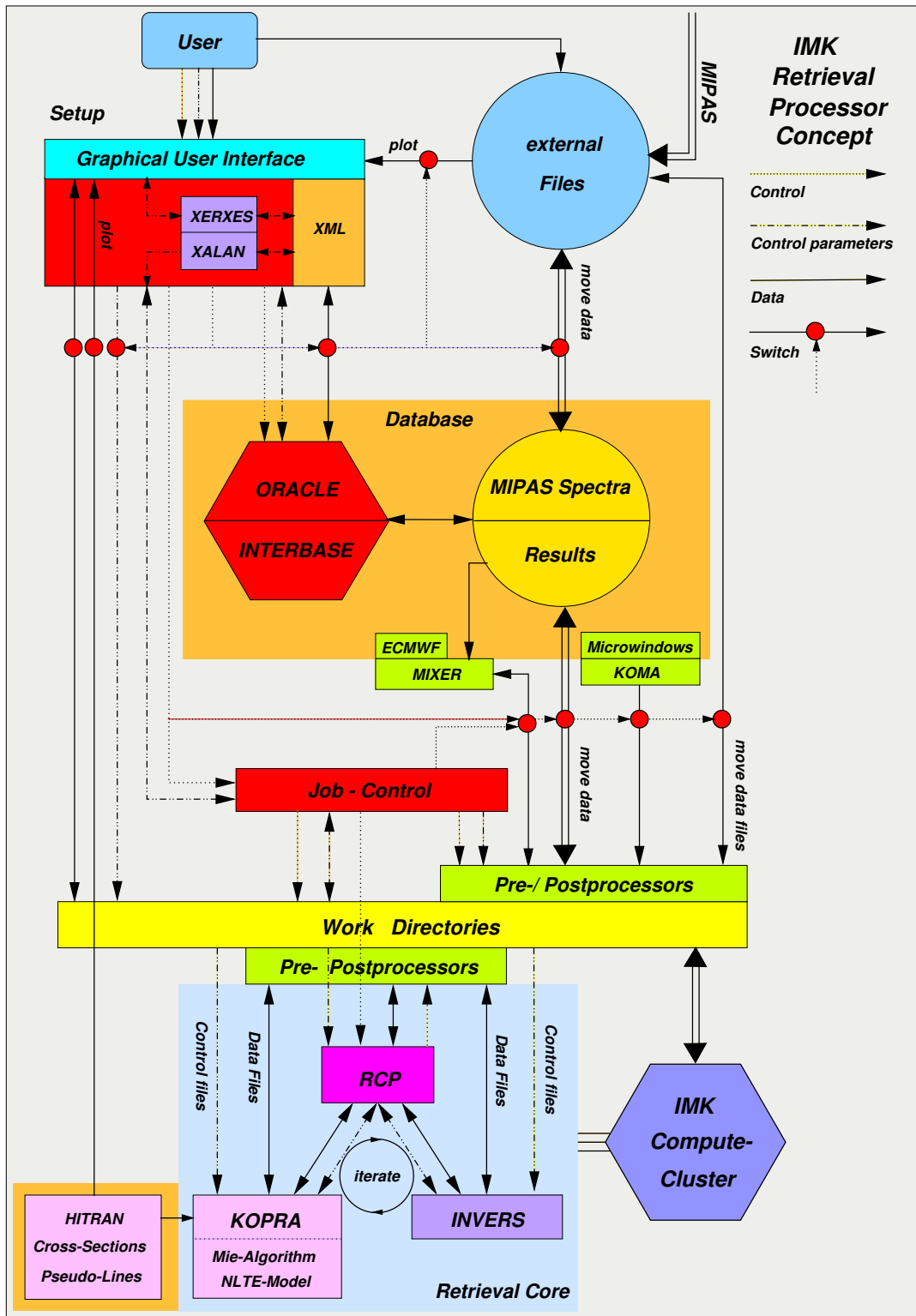


FIGURE 4.1: Schematic display of the IMK/IAA retrieval processor. The upper left corner, as well as the Interbase database and the Oracle database were replaced with MySQL. The Processor Graphical User Interface is not working. This does not impair the functionality of the processor though. - Source: IMK-ASF-SAT research group.

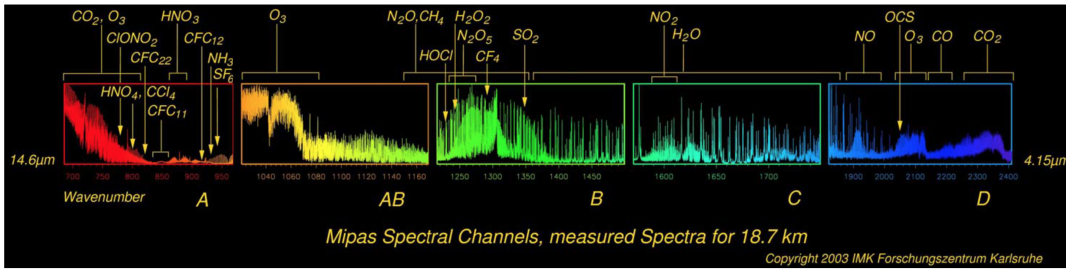


FIGURE 4.2: Entire MIPAS spectrum as detected at 18.7 km with spectral emission lines of numerous trace species. - Source: Fischer et al. (2008) - CC BY 3.0 License.

4.2 Spectroscopy

The basic concept behind MIPAS measurements is spectroscopy. Spectroscopy is based on interactions of electromagnetic waves - IR radiation in the case of MIPAS - with matter, e.g., the molecules in the Earth's atmosphere. The energy (E) of a photon is proportional to its frequency (ν) through the Planck constant (h):

$$E = h\nu. \quad (4.1)$$

This energy can be absorbed by a molecule in the atmosphere, providing that the photon's energy equals the energy difference between two energy states of that molecule before the interaction (E') and after the interaction (E''):

$$E'' - E' = h\nu \quad (4.2)$$

because possible energy states of the molecule are discrete (quantized). Through energy absorption, the molecule will jump from a lower to a higher energy state. The reverse process is called emission, where a molecule drops from a higher to a lower energy state, emitting a photon with the energy equal to the difference of the two energy states of the molecule. When absorption/emission is quantized, like it is when IR radiation interacts with molecules of the atmosphere, the resulting absorption/emission spectra are called line spectra, because they consist of distinct lines characteristic for each molecule, even though certain processes alter the line shape and energy distribution (Sec. 4.2.4). As an example, an emission spectrum, as acquired by MIPAS at 18.7 km, is shown in Figure 4.2. However, the detected signal does not exclusively consist of line spectra because, e.g., clouds and aerosols produce a signal which is only weakly dependent on frequency. This is known as continuum.

Measurements of the absorption/emission spectra of the atmosphere can reveal its molecular composition. In the atmosphere, three different processes are of interest:

- electronic excitation in the ultraviolet (UV) and visible part of the spectrum
- vibrational excitation in the near and mid-IR part of the spectrum
- rotational excitation in the far-IR and microwave part of the spectrum

A photon doesn't only carry a specific energy/frequency but also has a so-called spin. Whenever this photon interacts, its spin has to be conserved, which results in a change of angular momentum of the absorbing molecule. Due to this, usually a combined vibrational-rotational excitation takes place. Exceptions from this occur, when vibrations superimpose in a way that results in net rotation. An example for this is the ν_2 mode of the carbon dioxide (CO_2) molecule. The resulting Q-branch (Sec. 4.2.3) in the spectral region around 792 cm^{-1} caused some problems during the MIPAS CCl_4 retrieval (Eckert et al., 2017).

For MIPAS measurements, only the vibrational and rotational excitation are important and, hence, these are described in more detail in the following.

4.2.1 Rotational Transitions

Like all physical objects (except a point mass, e.g., a single isolated atom in good approximation), molecules have a moment of inertia (I). Similar to the mass in translational acceleration, the moment of inertia of an object indicates the resistance of that object to rotational acceleration applied through an external torque. However, at the molecular level, this moment of inertia is quantized. In addition, electromagnetic radiation can only interact via rotational transition with molecules that have a permanent magnetic or electric dipole moment. Molecules composed of two identical atoms, e.g., molecular nitrogen (N_2) or oxygen (O_2), don't exhibit a permanent dipole moment, but O_2 possesses a permanent magnetic dipole moment. CO_2 and methane (CH_4) have no permanent dipole moments due to their symmetry, which can however be altered by bending vibrational motion. Other molecules which are of interest in IR spectrometry of the atmosphere present permanent electric dipole moments.

The set of discrete rotational energy levels (E_{rot}) of a rotating rigid diatomic molecule, e.g., carbon monoxide (CO), is given by:

$$E_{rot} = \frac{\hbar}{2I} J(J+1) \quad (4.3)$$

with the Dirac constant (reduced Planck constant) $\hbar = \frac{h}{2\pi}$ and the rotational quantum number (J), which is an integer and cannot be negative. Looking at the transition from one rotational energy state to its neighbour we find that the corresponding change in energy is:

$$\begin{aligned} \Delta E &= E_{rot}(J+1) - E_{rot}(J) \\ &= \frac{\hbar}{2I}(J+1)(J+2) - \frac{\hbar}{2I}J(J+1) \\ &= \frac{\hbar}{2I}(2J+2) \\ &= \frac{\hbar}{I}(J+1). \end{aligned} \quad (4.4)$$

Introducing the rotational constant

$$B = \frac{\hbar}{2I}, \quad (4.5)$$

Eq. 4.4 transforms into

$$\Delta E = 2Bh(J + 1). \quad (4.6)$$

With Eq. 4.1 we gain the appropriate photon energies for this transition

$$\nu = 2B(J + 1), \quad (4.7)$$

which form a spectrum of equally spaced lines with the distance of $2B$. However, a diatomic molecule is a very simple case, but similar relationships as shown in the example above exist for more complex molecules as well. These molecules have up to 3 moments of inertia (one for each axis in space/degree of freedom) and rotational quantum numbers. Furthermore, each quantum number has its own set of energy levels and, as in the very simple example above, the spacing of the respective lines depends on their moment of inertia. Accordingly, heavier, more complex molecules have denser lines than simple, light ones with lesser spacial extent.

4.2.2 Vibrational Transitions

When molecules vibrate, their molecular bonds act like springs, e.g., they can contract or stretch parallel to the bond or they can bend orthogonally to the bond. Which vibrations are possible depends on the molecule's geometry. For a diatomic molecule, like O_2 or N_2 , with masses of m_1 and m_2 the set of discrete rotational energy levels is given by:

$$E_{vib} = \left(K + \frac{1}{2} \right) \hbar\omega_v \quad (4.8)$$

with the vibrational quantum number (K) and the resonant frequency $\omega_v = \sqrt{\frac{k(m_1+m_2)}{m_1m_2}}$. k is the spring constant of the covalent bond. Like the rotational quantum number, the vibrational quantum number is an integer and cannot be negative. The more complex a molecule is, the more normal modes of vibrations it has. For molecules with at least 2 atoms, the number of normal modes is $N = 3n - 6$ for nonlinear molecules and $N = 3n - 5$ for linear molecules (Petty, 2006).

4.2.3 Vibration/rotation spectra

In reality, vibrational and rotational transitions are often superimposed. These superpositions are sometimes abbreviated rovibrational transitions. Since rotational transitions are associated with considerably smaller energies than vibrational transitions, the energy of rovibrational transitions is either slightly smaller or slightly larger compared to the frequency associated with a pure vibrational transition. In other words,

rotational transitions superimposing on vibrational transitions form fine structures of closely spaced separate lines in the vibrational spectrum. Depending on whether the rotational quantum number (J) increases ($\Delta J = +1$) or decreases ($\Delta J = -1$), these fine structures belong to the R-branch or the P-branch, respectively (cf. Petty, 2006, Fig. 9.3). When ΔJ equals zero, the respective feature is called the Q-branch. ν_0 is the nominal frequency of the pure vibrational transition. In some molecules, like CO, changes in the vibrational quantum number $\Delta K = \pm 1$ are required to be accompanied by non-zero rotational transitions ($\Delta J = \pm 1$), according to quantum mechanics. In that case, the Q-branch is missing from the spectrum.

4.2.4 Line Shape and Line Mixing

The distinct line shape characteristic for each molecule is altered in the atmosphere mainly by two processes. Since all molecules have a temperature above 0 K they are in motion (Brownian motion). The hotter the gas, the faster the molecules move as their average translational kinetic energy (\bar{E}) in 3D space (with 3 degrees of freedom) is proportional to the temperature (T) as follows:

$$\bar{E} = \frac{3}{2}k_B T \quad (4.9)$$

with the Boltzmann constant (k_B). This motion leads to a Doppler effect - comparable to that known from acoustics - that, in statistical superposition, broadens the line shape and is accordingly called Doppler broadening. Its effect increases with temperature and thus is the predominant mechanism in the high atmosphere, e.g., from the mesosphere upwards.

In addition, molecules in motion collide which leads to a the so-called Lorentz broadening. Because the chance of collision increases when more molecules are present in the a specific volume, Lorentz broadening effects increase with pressure. Therefore, this is the predominant mechanism at lower altitudes, e.g., in the troposphere and lower stratosphere. A graphic comparison of the Doppler and the Lorentz profile can be found in Liou (1980, Figure 1.9).

The Voigt line shape (Eq. 4.10) is a convolution of the Lorentz profile and the Doppler profile and thus describes the overall line shape when the half width of the pressure broadening ($\alpha_{Lorentz}$) is of similar magnitude as the half width of the Doppler broadening ($\alpha_{Doppler}$). This is usually the case for our regions of interest.

$$g_{voigt}(\nu - \nu_0) = \frac{\alpha_{Lorentz}}{\pi\sqrt{\pi}\alpha_{Doppler}} \int_0^\infty \frac{\exp\left(-\left(\frac{\nu-\nu'}{\alpha_{Doppler}}\right)^2\right)}{(\nu' - \nu_0)^2 + \alpha_{Lorentz}^2} d\nu' \quad (4.10)$$

The Voigt line shape behaves similar to the Doppler profile close to the center of the line and more like the Lorentz profile further away from the center.

When molecules collide, angular momentum can be transferred. This leads to

modifications in the molecules' energy levels, which, in turn, can lead to shuffling between proximate transitions. Accordingly, the resulting energy distribution is altered without any interaction of radiation with the molecules. This phenomenon is commonly known as line mixing. Since energy levels of Q-branches are particularly close to each other, line mixing is most prevalent here, e.g., for the spectral region around 792 cm^{-1} where the CO_2 Q-branch influences the retrieval of CCl_4 . The effect of line mixing increases with increasing pressure, which makes sense since collisions are more likely the more molecules are present.

4.3 Retrieval of Atmospheric Constituents

In order to gain information on the composition of the atmosphere from emission spectra, in-depth understanding of radiative transfer processes is crucial (Sec. [4.3.1](#)). Modelling radiative transfer then allows us to solve the inverse problem which links measured irradiance with concentrations of atmospheric constituents. However, it is usually not possible to strictly solve the problem. Hence, we instead look for the most likely solution (Sec. [4.3.2](#)) using powerful computer clusters. All necessary steps to derive vertical profiles from limb emission spectra will be covered in the following.

4.3.1 Radiative Transfer in the Atmosphere and Forward Modelling

The theory of radiative transfer is based on the work of Chandrasekhar ([1960](#)). The equation of transfer describes what happens to radiation when it travels through a medium. The main influencing factors are:

- absorption
- scattering
- emission

which potentially happen at every molecule in the atmosphere. Absorption and scattering are gathered under the term extinction. While so-called Rayleigh scattering covers cases where the scattering particles are much smaller than the wavelength, Mie theory deals with scattering by particles similar to or larger than the wavelength. Scattering plays a very subordinate role in the IR, because the wavelength dependence for Rayleigh scattering is λ^{-4} and and Mie scattering usually only happens when sufficiently large water, ice or aerosol particles are in the atmosphere. However, in the thermal and far IR, water clouds look very similar to black bodies while they are almost transparent for microwaves. Nevertheless, scattering has to be accounted for in the UV and visible part of the spectrum.

While emission is the only "true" source of radiation, smaller portions of radiation can also be scattered into the direction of interest.

Whenever a pencil of radiation travels through a medium, e.g., the atmosphere, it is attenuated by extinction (Chandrasekhar, 1960; Liou, 1980). The respective change in radiance ($dI_{\nu,ext}$) at a specific frequency as a beam of radiation travels through a medium for a certain distance (ds) can be written as:

$$dI_{\nu,ext} = -(k_{\nu,a} + k_{\nu,sc})I_{\nu}\rho ds = -I_{\nu}d\tau \quad (4.11)$$

with the density (ρ) of the medium, the mass absorption coefficient ($k_{\nu,a}$) and the mass scattering coefficient ($k_{\nu,sc}$) for the frequency ν . In turn, the change in radiation due to emission ($dI_{\nu,e}$) can be written as

$$dI_{\nu,em} = (j_{\nu} + j_{\nu,sc})\rho ds \quad (4.12)$$

with the emission coefficient (j_{ν}) and the contribution to emission by scattering ($j_{\nu,sc}$). The overall change in radiance (dI_{ν}) including absorption, scattering and emission is thus

$$dI_{\nu} = dI_{\nu,ext} + dI_{\nu,em} = -(k_{\nu,a} + k_{\nu,sc})I_{\nu} + j_{\nu} + j_{\nu,sc})\rho ds. \quad (4.13)$$

For MIPAS, we can neglect scattering effects, which leads to the simplified equation of

$$dI_{\nu} = (-k_{\nu,a}I_{\nu} + j_{\nu})\rho ds \quad (4.14)$$

Kirchhoff's law of thermal radiation tells us, that for a body in local thermodynamic equilibrium (LTE) emissivity and absorptivity are equal. Thus, on a short path the change in radiation due to emission is equal to its black body absorption:

$$j_{\nu} = k_{\nu,a}B_{\nu}(T) \quad (4.15)$$

with Planck's law

$$B_{\nu}(T) = \frac{2h\nu^3}{c^2} \frac{1}{e^{\frac{h\nu}{k_B T}} - 1} \quad (4.16)$$

with the temperature (T), the speed of light (c) and the Boltzmann constant (k_B). With this, Eq. 4.14 turns into

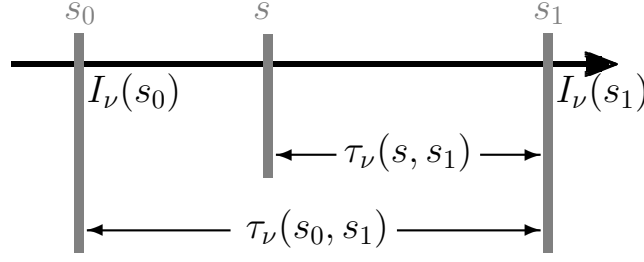
$$dI_{\nu} = [-k_{\nu,a}I_{\nu} + k_{\nu,a}B_{\nu}(T)]\rho ds = [B_{\nu}(T) - I_{\nu}]k_{\nu,a}\rho ds \quad (4.17)$$

or

$$\frac{dI_{\nu}}{k_{\nu,a}\rho ds} = B_{\nu}(T) - I_{\nu} \quad (4.18)$$

which is known as Schwarzschild's equation.

To derive the intensity of radiation measured by a detector looking at the atmosphere remotely, we have to integrate Schwarzschild's equation. For this, we first introduce the optical path (τ_{ν}) between two points (Chandrasekhar, 1960; Liou, 1980;

FIGURE 4.3: Optical path (τ_ν).

Petty, [2006](#)), s and s_1 , as depicted in Figure [4.3](#):

$$\tau_\nu(s, s_1) = \int_s^{s_1} k_{\nu,a}(s')\rho(s')ds' \quad (4.19)$$

with

$$\frac{d\tau_\nu(s, s_1)}{ds} = -k_{\nu,a}(s)\rho(s) \quad (4.20)$$

Accordingly, the transmission (t_ν) is:

$$t_\nu(s, s_1) = e^{-\tau_\nu(s, s_1)} \quad (4.21)$$

Using Eq. [4.20](#) Schwarzschild's equation can be rewritten as:

$$\frac{dI_\nu}{d\tau_\nu(s, s_1)} = I_\nu - B_\nu(T) \quad (4.22)$$

We apply the integrating factor $e^{-\tau_\nu(s, s_1)}$ to Eq. [4.22](#) (Petty, [2006](#)):

$$\frac{dI_\nu}{ds} e^{-\tau_\nu(s, s_1)} = I_\nu e^{-\tau_\nu(s, s_1)} - B_\nu(T) e^{-\tau_\nu(s, s_1)} \quad (4.23)$$

We now use the product rule, according to which

$$\begin{aligned} \frac{d}{d\tau_\nu(s, s_1)} \left(I_\nu e^{-\tau_\nu(s, s_1)} \right) &= \left(\frac{dI_\nu}{d\tau_\nu(s, s_1)} e^{-\tau_\nu(s, s_1)} + I_\nu \frac{d}{d\tau_\nu(s, s_1)} \left(e^{-\tau_\nu(s, s_1)} \right) \right) \\ &= \left(\frac{dI_\nu}{d\tau_\nu(s, s_1)} e^{-\tau_\nu(s, s_1)} + I_\nu e^{-\tau_\nu(s, s_1)} \frac{d}{d\tau_\nu(s, s_1)} (-\tau_\nu(s, s_1)) \right) \\ &= \left(\frac{dI_\nu}{d\tau_\nu(s, s_1)} e^{-\tau_\nu(s, s_1)} - I_\nu \tau_\nu(s, s_1) e^{-\tau_\nu(s, s_1)} \right) \\ &= \left(\frac{dI_\nu}{d\tau_\nu(s, s_1)} - I_\nu \right) e^{-\tau_\nu(s, s_1)}. \end{aligned} \quad (4.24)$$

After transposing Eq. [4.23](#)

$$\left(\frac{dI_\nu}{d\tau_\nu(s, s_1)} - I_\nu \right) e^{-\tau_\nu(s, s_1)} = -B_\nu(T) e^{-\tau_\nu(s, s_1)}, \quad (4.25)$$

we can use Eqs. 4.24 leading to:

$$\frac{d}{d\tau_\nu(s, s_1)} \left(I_\nu e^{-\tau_\nu(s, s_1)} \right) = -B_\nu(T) e^{-\tau_\nu(s, s_1)}. \quad (4.26)$$

We can now integrate from $\tau_\nu(s_1, s_1) = 0$ to $\tau_\nu(s_0, s_1)$ resulting in:

$$\begin{aligned} \int_0^{\tau_\nu(s_0, s_1)} \frac{d}{d\tau_\nu(s, s_1)} \left(I_\nu e^{-\tau_\nu(s, s_1)} \right) d\tau_\nu(s, s_1) &= - \int_0^{\tau_\nu(s_0, s_1)} B_\nu(T) e^{-\tau_\nu(s, s_1)} d\tau_\nu(s, s_1) \\ I_\nu(s_0) e^{-\tau_\nu(s_0, s_1)} - I_\nu(s_1) &= - \int_0^{\tau_\nu(s_0, s_1)} B_\nu(T) e^{-\tau_\nu(s, s_1)} d\tau_\nu(s, s_1). \end{aligned} \quad (4.27)$$

Resolving for $I_\nu(s_1)$ and resubstituting gives:

$$I_\nu(s_1) = I_\nu(s_0) e^{-\tau_\nu(s_0, s_1)} + \int_{s_0}^{s_1} k_{\nu, a}(s) \rho(s) B_\nu(T) e^{-\tau_\nu(s_0, s_1)} ds \quad (4.28)$$

Using Eq. 4.21 on Eq. 4.28 leads to:

$$I_\nu(s_1) = I_\nu(s_0) t_\nu(s_0, s_1) + \int_{s_0}^{s_1} k_{\nu, a}(s) \rho(s) B_\nu(T) t_\nu(s, s_1) ds. \quad (4.29)$$

This is the radiative transfer equation. It tells us how much radiation reaches the point s_1 when $I_\nu(s_0)$ is the radiation at the point s_0 .

Due to its complexity and multi-variable dependency, the radiative transfer equation cannot easily be solved analytically. In order to be able to use it in numeric models, it has to be discretized, as has the space considered by the model. Thus, the atmosphere is divided into spherical layers which are assumed to be homogeneous (Fig. 4.4). One of these radiative transfer models is the Karlsruhe Optimized and Precise Radiative transfer Algorithm (KOPRA) (Stiller, 2000), which is used at IMK in Karlsruhe within the scope of deriving profiles of atmospheric constituents from MIPAS measurements (Sec. 4.3.2). The discrete form of the radiative transfer equation (Eq. 4.29) is given as (Höpfner, 2000):

$$I(\nu) = B(T_{background}) \prod_{i=1}^N t_i + \sum_{i=1}^N \tilde{J}(T_i, \nu) (1 - t_i(\nu)) \prod_{k=i+1}^N t_k(\nu) \quad (4.30)$$

In there, i indicates the layers, with 1 denoting the layer farthest away from the instrument and N that being closest, and $\tilde{J}(T_i, \nu)$ is the source function. The transmission is given as:

$$t_i(\nu) = e^{-\tau_i(\nu)} \quad (4.31)$$

with :

$$\tau_i(\nu) = \tau_{e, aerosol, i}(\nu) + \sum_{g=1}^G \left[k_{ig}(\nu) + \sum_{g=1}^{B_g} \alpha_{igb} k_{a, igb}(\nu) \right] u_{ig} \quad (4.32)$$

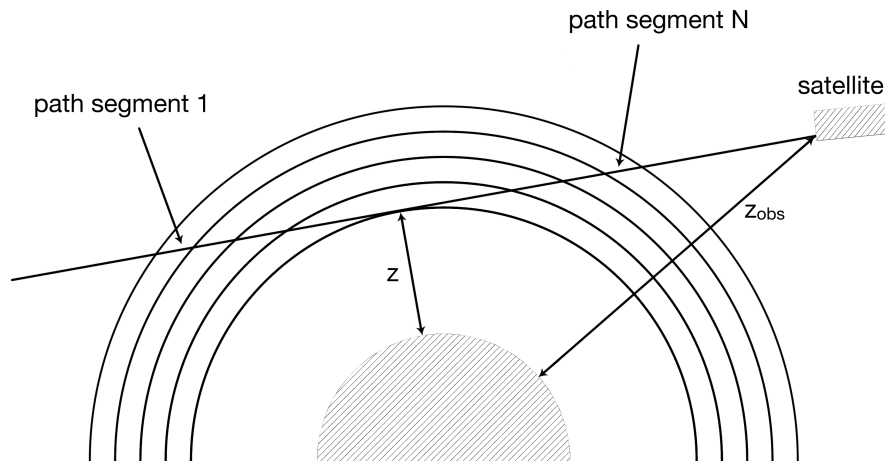


FIGURE 4.4: MIPAS limb geometry for the tangent altitude z .

$\tau_{e,aerosol,i}(\nu)$ is the optical depth with respect to aerosol extinction, $k_{ig}(\nu)$ and $k_{a,igb}(\nu)$ are the absorption coefficients for all local thermodynamic equilibrium (LTE) bands and non-LTE band b for the gas g , respectively, and α_{igb} is the ratio of these coefficients indicating the part of non-LTE compared to LTE absorption. u_{ig} is the column density for the gas g in layer i . In a measurement geometry like that of MIPAS, the background is space, which is very cold (at 2.7 K), and thus the first term on the right hand side of in Eq. 4.30 is negligible. In the simplest cases the source function ($\tilde{J}(T_i, \nu)$) is equal to Planck's law ($B_\nu(T)$) for the temperature of air for layer i , while it becomes considerably more complex under non-LTE conditions (Funke and Höpfner, 2000).

KOPRA is a complex radiative transfer model, which contains all of the important physical effects emerging in the atmosphere from the troposphere up to the thermosphere, including refraction, i.e., bending of rays due to density changes between different layers in the atmosphere (Hase and Höpfner, 2000), and line mixing (Funke, 2000). The numerical approximation of the radiances detected by MIPAS is calculated by KOPRA as the weighted sum of so-called pencil-beams, infinitesimally narrow rays simulated to form the viewing path of the instrument. This is indispensable to tackle the problem of deriving vertical profiles of atmospheric constituents from MIPAS measured radiances, which is an inverse problem.

4.3.2 Retrieval Theory

If used in the context of the retrieval of atmospheric constituents, models like KOPRA are called forward models. This is the case, because they model radiances based on the given state of the atmosphere, while retrieval theory helps us to go the reverse way and estimate the state of the atmosphere (e.g., the amount of atmospheric trace

gases in the atmosphere) based on measured radiances. The simplest formalization to describe a forward model (\mathbf{f}) in principle is:

$$\mathbf{y} = \mathbf{f}(\mathbf{x}; \mathbf{b}), \quad (4.33)$$

in which \mathbf{y} is an m -dimensional vector containing the radiances associated with the tangent altitudes of one scan sequence of the instrument (e.g., MIPAS) and \mathbf{x} is an n -dimensional vector consisting of the amount of an atmospheric trace gas we are interested in (e.g., in our case CCl_4). \mathbf{b} contains additional parameters (e.g., concentrations of other trace gases) that influence the radiances, but are not treated as variables in the inversion but kept constant. However, in order to calculate an appropriate spectrum, all trace gases contributing to the radiances at the examined wavelength range have to be taken into account in the forward model. Their abundances are part of the \mathbf{b} -vector.

The model \mathbf{f} is usually non-linear but can be linearized by considering only the first two terms in the Taylor expansion of \mathbf{f} around \mathbf{x}_0 :

$$\mathbf{f}(\mathbf{x}) \approx \mathbf{f}(\mathbf{x}_0; \mathbf{b}) + \frac{\partial \mathbf{f}}{\partial \mathbf{x}}(\mathbf{x} - \mathbf{x}_0), \quad (4.34)$$

where $\frac{\partial \mathbf{f}}{\partial \mathbf{x}}$ is called the Jacobian matrix (\mathbf{K}) (Rodgers, 2000).

I: Least Squares Fit

In the context of retrieving profiles of atmospheric constituents from measurements of radiances, we would like to go the reverse way to Eq. 4.33 and estimate \mathbf{x} from a known \mathbf{y} . To solve Eq. 4.34 for \mathbf{x} , the Jacobian matrix (\mathbf{K}) has to be inverted, which is only possible when \mathbf{K} is quadratic and not singular (e.g., its determinant must be non-zero, granting full information content of the matrix). \mathbf{x} could then simply be calculated as:

$$\mathbf{x} = \mathbf{x}_0 + \mathbf{K}^{-1}(\mathbf{y} - \mathbf{f}(\mathbf{x}_0; \mathbf{b})). \quad (4.35)$$

In reality, we usually have more measurements (m) than unknowns (n) so that the inverse problem is overdetermined resulting in \mathbf{K} not being quadratic, e.g., not directly invertible. In addition, real measurements always have an error. Accordingly, it will be impossible to find an exact solution for the given problem. However, we can search for the most likely one using the least square approach. It relies on the assumption, that the measurements are normally distributed (Gaussian distribution function). The conditional probability of \mathbf{y} being measured when \mathbf{x} is the actual atmospheric state (Rodgers, 2000) is given by:

$$P(\mathbf{y}|\mathbf{x}) = \frac{1}{\sqrt{(2\pi)^m |\mathbf{S}_y|}} e^{-\frac{1}{2}((\mathbf{y} - \mathbf{f}(\mathbf{x}))^T \mathbf{S}_y^{-1} (\mathbf{y} - \mathbf{f}(\mathbf{x})))}, \quad (4.36)$$

where \mathbf{S}_y is the measurement error covariance matrix, containing the variances of \mathbf{y} as the diagonal of the matrix, and error correlations as off-diagonal elements in the case when the values of \mathbf{y} are not entirely independent from each other. The most likely \mathbf{y} for a given \mathbf{x} is that for which the probability density function, $P(\mathbf{y}|\mathbf{x})$, has its maximum. To find it, we have to maximize $P(\mathbf{y}|\mathbf{x})$. This is done by minimization of $(\mathbf{y} - \mathbf{f}(\mathbf{x}))^T \mathbf{S}_y^{-1} (\mathbf{y} - \mathbf{f}(\mathbf{x}))$, which is the so-called cost function (χ^2). This is called the least squares fit method, because the sum of the squares, of $(\mathbf{y}$ minus $\mathbf{f}(\mathbf{x}))$ in our case, is minimized:

$$\begin{aligned} \frac{d\chi^2}{dx} &= \frac{d}{dx} ((\mathbf{y} - \mathbf{f}(\mathbf{x}))^T \mathbf{S}_y^{-1} (\mathbf{y} - \mathbf{f}(\mathbf{x}))) \\ &\approx \frac{d}{dx} ((\mathbf{y} - \mathbf{f}(\mathbf{x}_0; \mathbf{b}) - \mathbf{K}(\mathbf{x} - \mathbf{x}_0))^T \mathbf{S}_y^{-1} (\mathbf{y} - \mathbf{f}(\mathbf{x}_0; \mathbf{b}) - \mathbf{K}(\mathbf{x} - \mathbf{x}_0))) \\ &= 0; \end{aligned} \quad (4.37)$$

the result is:

$$\hat{\mathbf{x}} = \mathbf{x}_0 + (\mathbf{K}^T \mathbf{S}_y^{-1} \mathbf{K})^{-1} \mathbf{K}^T \mathbf{S}_y^{-1} (\mathbf{y} - \mathbf{f}(\mathbf{x}_0; \mathbf{b})), \quad (4.38)$$

where the $\hat{\cdot}$ -symbol denotes the estimate instead of the true value. This is called the maximum likelihood solution.

As the model \mathbf{f} is usually not linear, which is usually not sufficiently satisfied, Eq. 4.38 has to be solved iteratively:

$$\mathbf{x}_{i+1} \approx \mathbf{x}_i + (\mathbf{K}_i^T \mathbf{S}_y^{-1} \mathbf{K}_i)^{-1} \mathbf{K}_i^T \mathbf{S}_y^{-1} (\mathbf{y} - \mathbf{f}(\mathbf{x}_i; \mathbf{b})) \quad (4.39)$$

For the first iterative step, the respective \mathbf{x}_i equals \mathbf{x}_0 , the so-called initial guess, which can be taken from e.g., a climatology. For each subsequent step, \mathbf{x}_i is taken from the previous iterative step.

In Eq. 4.38

$$\mathbf{G} = (\mathbf{K}^T \mathbf{S}_y^{-1} \mathbf{K})^{-1} \mathbf{K}^T \mathbf{S}_y^{-1} \quad (4.40)$$

is called the gain matrix and describes the sensitivity of the retrieval to the measurement $\left(\frac{\partial \hat{\mathbf{x}}}{\partial \mathbf{y}}\right)$. We can use it to calculate the covariance matrix for \mathbf{x} :

$$\mathbf{S}_x = \mathbf{G} \mathbf{S}_y \mathbf{G}^T. \quad (4.41)$$

Using Eq. 4.40 we get:

$$\begin{aligned} \mathbf{S}_x &= ((\mathbf{K}^T \mathbf{S}_y^{-1} \mathbf{K})^{-1} \mathbf{K}^T \mathbf{S}_y^{-1}) \mathbf{S}_y ((\mathbf{K}^T \mathbf{S}_y^{-1} \mathbf{K})^{-1} \mathbf{K}^T \mathbf{S}_y^{-1})^T \\ &= (\mathbf{K}^T \mathbf{S}_y^{-1} \mathbf{K})^{-1}. \end{aligned} \quad (4.42)$$

It describes the error propagation of \mathbf{y} onto \mathbf{x} (generalized Gaussian error propagation).

II: Optimal Estimation

Previously, we assumed that we have more measurements (m) than unknowns (n) and also that these measurements provide enough information to solve the problem. While we usually do have more measurements than unknowns, in reality, the measurements carry largely redundant information, leading to almost linear dependencies in the lines of $\mathbf{K}^T \mathbf{S}_y^{-1} \mathbf{K}$ making the matrix inversion instable. This is referred to as an ill-posed problem.

Bayes offered a solution to this problem in his "Essay towards Solving a Problem in the Doctrine of Chances" (Bayes and Price, 1763). He suggested that additional information, so-called a priori knowledge, can be used to find the most likely solution, e.g., we can use a climatology to confine \mathbf{x} to a range close to its climatological value. In that case, we assume that \mathbf{x} is less likely the more it deviates from the climatological mean. Explicitly, we assume that \mathbf{x} is normally distributed around the climatological mean:

$$P(\mathbf{x}) = \frac{1}{\sqrt{(2\pi)^m |\mathbf{S}_x|}} e^{-\frac{1}{2}((\mathbf{x}-\mathbf{x}_a)^T \mathbf{S}_a^{-1} (\mathbf{x}-\mathbf{x}_a))} \quad (4.43)$$

where \mathbf{x}_a denotes our a priori knowledge and \mathbf{S}_a is the respective covariance matrix. Bayes' theorem tells us that the probability of \mathbf{x} lying within a certain range ($\mathbf{x}, \mathbf{x}+d\mathbf{x}$) when \mathbf{y} is measured is

$$P(\mathbf{x}|\mathbf{y}) = \frac{P(\mathbf{y}|\mathbf{x})P(\mathbf{x})}{P(\mathbf{y})}. \quad (4.44)$$

Under the conditional probability density function, $P(\mathbf{x}|\mathbf{y})$, the prior probability density function of the measurement, $P(\mathbf{y})$, is only a normalizing factor (cf. Rodgers (2000), Fig. 2.3, which illustrates what the conjoined probability of x and y in the two-dimensional case looks like), so that

$$P(\mathbf{x}|\mathbf{y}) \propto P(\mathbf{y}|\mathbf{x})P(\mathbf{x}). \quad (4.45)$$

Using Eqs. 4.36 and 4.43 this leads to

$$P(\mathbf{x}|\mathbf{y}) \propto e^{-\frac{1}{2}[(\mathbf{y}-\mathbf{f}(\mathbf{x}))^T \mathbf{S}_y^{-1} (\mathbf{y}-\mathbf{f}(\mathbf{x})) + (\mathbf{x}-\mathbf{x}_a)^T \mathbf{S}_a^{-1} (\mathbf{x}-\mathbf{x}_a)]}. \quad (4.46)$$

Minimizing the cost function $\chi^2 = (\mathbf{y}-\mathbf{f}(\mathbf{x}))^T \mathbf{S}_y^{-1} (\mathbf{y}-\mathbf{f}(\mathbf{x})) + (\mathbf{x}-\mathbf{x}_a)^T \mathbf{S}_a^{-1} (\mathbf{x}-\mathbf{x}_a)$ leads to:

$$\hat{\mathbf{x}} = \mathbf{x}_0 + (\mathbf{K}^T \mathbf{S}_y^{-1} \mathbf{K} + \mathbf{S}_a^{-1})^{-1} \mathbf{K}^T \mathbf{S}_y^{-1} (\mathbf{y} - \mathbf{f}(\mathbf{x}_0; \mathbf{b})). \quad (4.47)$$

Again, this can be solved iteratively in case the model is not sufficiently linear:

$$\mathbf{x}_{i+1} = \mathbf{x}_i + (\mathbf{K}_i^T \mathbf{S}_y^{-1} \mathbf{K}_i + \mathbf{S}_a^{-1})^{-1} [\mathbf{K}_i^T \mathbf{S}_y^{-1} (\mathbf{y} - \mathbf{f}(\mathbf{x}_i; \mathbf{b})) - \mathbf{S}_a^{-1} (\mathbf{x}_i - \mathbf{x}_a)]. \quad (4.48)$$

According to the above, the gain matrix in this case is

$$\mathbf{G} = (\mathbf{K}^T \mathbf{S}_y^{-1} \mathbf{K} + \mathbf{S}_a)^{-1} \mathbf{K}^T \mathbf{S}_y^{-1} \quad (4.49)$$

and the covariance matrix for \mathbf{x} can be calculated following Eq. 4.41. Since a priori knowledge brings additional information into the system, the errors will always be smaller than if only measurements were used.

While \mathbf{G} is the sensitivity of the retrieval to the measurement, the averaging kernel matrix (\mathbf{A}) describes the sensitivity of the retrieval to the true state:

$$\mathbf{A} = \frac{\partial \hat{\mathbf{x}}}{\partial \mathbf{x}} = (\mathbf{K}^T \mathbf{S}_y^{-1} \mathbf{K} + \mathbf{S}_a)^{-1} \mathbf{K}^T \mathbf{S}_y^{-1} \mathbf{K} = \mathbf{G} \mathbf{K} \quad (4.50)$$

It describes the smoothing of the retrieved profile of an atmospheric constituent due to the usage of a priori information. Without the usage of a priori information, \mathbf{A} is the identity matrix (\mathbf{I}). Column i of the averaging kernel matrix describes how the system reacts to a Dirac delta function ($\delta(x)$) applied at altitude level i , while row i gives information on the composition of the signal at altitude level i , e.g., how strongly the signal from each altitude level contributes to the signal at altitude level i . The diagonal elements of \mathbf{A} reveal how much a priori information contributes to the solution. The larger they are, the smaller is the portion of the a priori information in the final result and vice versa. It is also possible to estimate the vertical resolution from the averaging kernel matrix. It is most commonly calculated as the full width at half maximum (FWHM) of each row of \mathbf{A} .

The degrees of freedom of the estimated profile can be calculated from the averaging kernel matrix as follows:

$$dgf = tr(\mathbf{A}) \quad (4.51)$$

Since an approach as shown above attempts to find the best estimate for the sum of both contributing terms, is known as “optimal estimation”.

III: The Tikhonov Approach

While optimal estimation allows us to retrieve atmospheric constituents from measured radiances even for underdetermined or ill-posed problems it has its pitfalls. If the state of an the atmosphere, \mathbf{x} , is far away from the a priori, \mathbf{x}_a , it is considered very unlikely and thus the result is drawn towards the a priori. First occurrences are, naturally, not part of the climatology, so that a first occurrence could be missed or at least its effect can be severely underestimated. Even though rare events are part of the climatology, they have very little influence on the climatological mean and thus, rare events can also be overlooked. In addition to that, the covariance matrix of \mathbf{x} (\mathbf{S}_a) is often not known.

In such cases, a variant of the regularization approach suggested by Tikhonov (1963) can be more adequate. Based on the assumption that vertical profiles of atmospheric constituents, as derived by MIPAS, have a certain smoothness, a first order

differential operator, with dimensions $(n - 1) \times n$, is introduced

$$\mathbf{L}_1 = \begin{pmatrix} -1 & 1 & 0 & 0 & 0 \\ 0 & -1 & \cdots & 0 & 0 \\ \vdots & \vdots & \ddots & \vdots & \vdots \\ 0 & 0 & \cdots & -1 & 1 \end{pmatrix} \quad (4.52)$$

resulting in the cost function

$$\chi^2 = (\mathbf{y} - \mathbf{f}(\mathbf{x}))^T \mathbf{S}_y^{-1} (\mathbf{y} - \mathbf{f}(\mathbf{x})) + \gamma \mathbf{x}^T \mathbf{L}_1^T \mathbf{L}_1 \mathbf{x} \quad (4.53)$$

with γ being a scalar weighting factor, so it is possible to control the influence of this term. This leads to the best estimate of

$$\hat{\mathbf{x}} = \mathbf{x}_0 + (\mathbf{K}^T \mathbf{S}_y^{-1} \mathbf{K} + \gamma \mathbf{L}_1^T \mathbf{L}_1)^{-1} \mathbf{K}^T \mathbf{S}_y^{-1} (\mathbf{y} - \mathbf{f}(\mathbf{x}_0; \mathbf{b})). \quad (4.54)$$

Like for the other approaches, we can solve this iteratively following

$$\mathbf{x}_{i+1} = \mathbf{x}_i + (\mathbf{K}_i^T \mathbf{S}_y^{-1} \mathbf{K}_i + \gamma \mathbf{L}_1^T \mathbf{L}_1)^{-1} [\mathbf{K}_i^T \mathbf{S}_y^{-1} (\mathbf{y} - \mathbf{f}(\mathbf{x}_i; \mathbf{b})) - \gamma \mathbf{L}_1^T \mathbf{L}_1 (\mathbf{x}_i - \mathbf{x}_a)]. \quad (4.55)$$

Accordingly, the gain matrix is

$$\mathbf{G} = (\mathbf{K}^T \mathbf{S}_y^{-1} \mathbf{K} + \gamma \mathbf{L}_1^T \mathbf{L}_1)^{-1} \mathbf{K}^T \mathbf{S}_y^{-1} \quad (4.56)$$

and the respective averaging kernel matrix is given by

$$\mathbf{A} = \mathbf{G} \mathbf{K} = (\mathbf{K}^T \mathbf{S}_y^{-1} \mathbf{K} + \gamma \mathbf{L}_1^T \mathbf{L}_1)^{-1} \mathbf{K}^T \mathbf{S}_y^{-1} \mathbf{K}. \quad (4.57)$$

In the case of the MIPAS retrieval, the IMK-ASF-SAT group took the Tikhonov approach even a step further and introduced an altitude dependent γ , so that Eqs. 4.58 and 4.59 transform into

$$\hat{\mathbf{x}} = \mathbf{x}_0 + (\mathbf{K}^T \mathbf{S}_y^{-1} \mathbf{K} + \mathbf{L}_1^T \boldsymbol{\gamma} \mathbf{L}_1)^{-1} \mathbf{K}^T \mathbf{S}_y^{-1} (\mathbf{y} - \mathbf{f}(\mathbf{x}_0; \mathbf{b})). \quad (4.58)$$

and

$$\mathbf{x}_{i+1} = \mathbf{x}_i + (\mathbf{K}_i^T \mathbf{S}_y^{-1} \mathbf{K}_i + \mathbf{L}_1^T \boldsymbol{\gamma} \mathbf{L}_1)^{-1} [\mathbf{K}_i^T \mathbf{S}_y^{-1} (\mathbf{y} - \mathbf{f}(\mathbf{x}_i; \mathbf{b})) - \mathbf{L}_1^T \boldsymbol{\gamma} \mathbf{L}_1 (\mathbf{x}_i - \mathbf{x}_a)]. \quad (4.59)$$

respectively. In there, $\boldsymbol{\gamma}$ is an $(n - 1) \times (n - 1)$ diagonal matrix with the weighting factors for the respective altitudes as diagonal elements.

By using a priori information in the sense of optimal estimation or Tikhonov, the previously irregular matrix in the model becomes regular (and invertible) again. Accordingly, such constraints are commonly known as regularization matrixs (\mathbf{R}). Regularizing reduces the degrees of freedom because the latter is a measure of how many independent data points exist.

4.3.3 Error Estimation

The total error of the modelled solution consists of several error components:

$$\mathbf{S}_{total} = \mathbf{S}_x + \mathbf{S}_{model} + \mathbf{S}_{smoothing} + \sum_b \mathbf{S}_{x,b} \quad (4.60)$$

where \mathbf{S}_x is the noise error, \mathbf{S}_{model} is the model error, $\mathbf{S}_{smoothing}$ is the smoothing error and $\mathbf{S}_{x,b}$ are parameter errors.

The noise error was already introduced within the scope of the least squares fit (Eq. 4.41) and describes the error due to the noise of the measurement. In case a regularization is used, Eq. 4.41 results in

$$\begin{aligned} \mathbf{S}_x &= \mathbf{G}\mathbf{S}_y\mathbf{G}^T \\ &= ((\mathbf{K}^T\mathbf{S}_y^{-1}\mathbf{K} + \mathbf{R})^{-1}\mathbf{K}^T\mathbf{S}_y^{-1}) \mathbf{S}_y ((\mathbf{K}^T\mathbf{S}_y^{-1}\mathbf{K} + \mathbf{R})^{-1}\mathbf{K}^T\mathbf{S}_y^{-1})^T \\ &= (\mathbf{K}^T\mathbf{S}_y^{-1}\mathbf{K} + \mathbf{R})^{-1}\mathbf{K}^T\mathbf{S}_y\mathbf{K}(\mathbf{K}^T\mathbf{S}_y^{-1}\mathbf{K} + \mathbf{R})^{-1} \end{aligned} \quad (4.61)$$

(von Clarmann et al., 2003). Measurement noise is usually randomly distributed and can also lead to negative values, which have no physical meaning. Nevertheless, it is recommendable to tolerate these negative data points, since forcing results to positive values would lead to biases.

Another error component result from uncertainties in parameters in the forward model. These parameters are assumed to be known and held constant during the inversion, e.g., profiles of other trace gases contributing to the spectrum. Uncertainties in a scalar parameter are estimated as follows

$$\Delta_b\hat{\mathbf{x}} = \mathbf{G}(\mathbf{f}(\hat{\mathbf{x}}; b + \Delta b) - \mathbf{f}(\hat{\mathbf{x}}; b)) \quad (4.62)$$

where b is the parameter and Δb is its uncertainty. In matrix notation (in case the parameter is e.g., a profile \mathbf{b}) this leads to

$$\mathbf{S}_{x,b} = \mathbf{G}\mathbf{K}_b\mathbf{S}_b\mathbf{K}_b^T\mathbf{G}^T. \quad (4.63)$$

Here, \mathbf{K}_b denotes the sensitivity of the measurement to a variation in \mathbf{b} and \mathbf{S}_b is the covariance matrix of this parameter.

Since certain simplifications are often used in the model, the influence of these simplifications has to be quantified. Such simplifications include the assumption of local thermodynamic equilibrium (LTE) for all altitudes or not taking line mixing into account, because these processes can be very computationally demanding. In general, assuming LTE for the MIPAS nominal mode is justified (López-Puertas et al., 2003) but becomes less accurate above 50 km. As stated in Section 4.2.4, line mixing becomes more important at higher pressure, i.e., lower altitudes. To estimate the effect of using a simplified model, this model is compared to the simplified model

leading to

$$\Delta_{model}\hat{\mathbf{x}} = \mathbf{G}(\tilde{\mathbf{f}}(\hat{\mathbf{x}}; b) - \mathbf{f}(\hat{\mathbf{x}}; b)) \quad (4.64)$$

where $\tilde{\mathbf{f}}$ is the simplified model and $\Delta_{model}\hat{\mathbf{x}}$ is the resulting uncertainty. While this looks very similar to the scalar parameter error (Eq. 4.62), here, the simplified model is used and the parameters are held constant. However, the algebraic sign of model errors is deterministic and thus the latter add up linearly, while parameter errors add up quadratically. Eq. 4.64 can also be written in matrix notation resulting in

$$\Delta_{model}\hat{\mathbf{x}}\Delta_{model}\hat{\mathbf{x}}^T = \mathbf{S}_{model} = \mathbf{G}\mathbf{S}_f\mathbf{G}^T \quad (4.65)$$

with \mathbf{S}_f being the covariance matrix of the model error.

The last source of error to be mentioned here, is the regularization. In leading to a smoother profile, it introduces an error based on the strength of the regularization. The stronger the regularization, the more the profile is smoothed and thus leads to a larger deviation from the true state. This is characterized by the so-called smoothing error

$$\mathbf{S}_{smoothing} = (\mathbf{I} - \mathbf{A})^T \mathbf{S}_a (\mathbf{I} - \mathbf{A}). \quad (4.66)$$

However, the covariance matrix \mathbf{S}_a is often not known and, in addition to that, von Clarmann (2014), shows that the smoothing error does not comply with Gaussian error propagation. Thus, it is questionable whether including the smoothing error in the total error budget is desirable. It might be better to characterize the influence of the a priori information just by the \mathbf{A} itself.

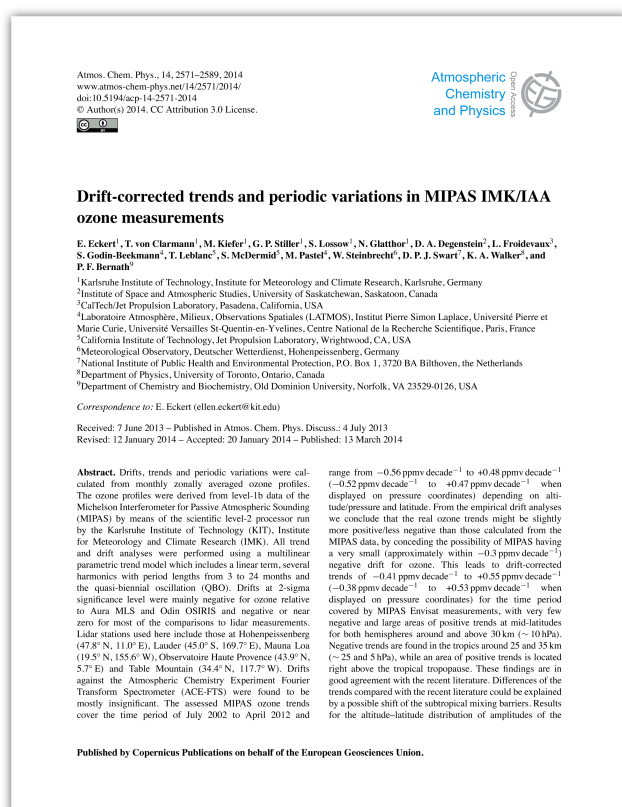
Nevertheless, smoothing differences have to be taken into account, when comparing measurements with noticeably different vertical resolutions.

5. First Author Publications

5.1 Drift-corrected trends and periodic variations in MIPAS IMK/IAA ozone measurements

Authors: E. Eckert, T. von Clarmann, M. Kiefer, G. P. Stiller, S. Lossow, N. Glatthor, D. A. Degenstein, L. Froidevaux, S. Godin-Beekmann, T. Leblanc, S. McDermaid, M. Pastel, W. Steinbrecht, D. P. J. Swart, K. A. Walker, and P. F. Bernath

In: Atmos. Chem. Phys., 14, 2571–2589, 2014 www.atmos-chem-phys.net/14/2571/2014/
doi:10.5194/acp-14-2571-2014



Authorship Statement

My first publication as a first author lays the foundation for this thesis. For this publication, I estimated trends and periodic variations in stratospheric ozone (between 10 and 50 km) from data collected by the Michelson Interferometer for Passive Atmospheric Sounding (MIPAS) from Juli 2002 to April 2012. I used the multilinear parametric trend estimation method introduced by von Clarmann et al. (2010), which is more closely discussed in Chap. 6 since I made a significant contribution to that publication. As MIPAS was expected to have an instrument drift, which could introduce a superimposed, artificial trend, I also estimated drifts by comparison to other instruments, including satellite borne and ground-based lidar measurements. For this, I first selected coincident measurements among MIPAS and each of the comparison instruments complying with pre-selected coincidence criteria, depending of the coverage of the comparison instruments. I then calculated the difference between MIPAS and each comparison for each profile pair. I made sure to take the different vertical resolution of the instruments

into account by applying the respective MIPAS averaging kernel.

Michael Kiefer provided his expertise on convolution with the MIPAS averaging kernel following a concept first applied during the extensive validation of the MOHAVE-2009 campaign (Stiller et al., 2012). Doug Degenstein (University of Saskatchewan, mission Principal Investigator of the Odin-OSIRIS instrument), Lucien Froidevaux (Jet Propulsion Laboratory (JPL), Pasadena, California, USA, Deputy Principle Investigator of the Earth Observing System (EOS) Microwave Limb Sounder (MLS)), Sophie Godin-Beekmann (Observatoire de Versailles Saint-Quentin-en-Yvelines, Director of Observatoire de Haute Provence (OHP)), Thierry Leblanc (JPL, Principal Investigator for the JPL atmospheric lidar measurement programs initiated at the JPL Table Mountain Facility), Wolfgang Steinbrecht (Meteorological Observatory, Deutscher Wetterdienst, Hohenpeissenberg, Germany, Principal Investigator for lidar measurements at Hohenpeissenberg), and Kaley Walker (University of Toronto, Atmospheric Chemistry Experiment Fourier Transform Spectrometer (ACE-FTS)) provided data and valuable information about their instruments. Thomas von Clarmann und Gabriele Stiller initiated and supervised the paper.

Abstract

Drifts, trends and periodic variations were calculated from monthly zonally averaged ozone profiles. The ozone profiles were derived from level-1b data of the Michelson Interferometer for Passive Atmospheric Sounding (MIPAS) by means of the scientific level-2 processor run by Karlsruhe Institute of Technology (KIT), Institute for Meteorology and Climate Research (IMK). All trend and drift analyses were performed using a multilinear parametric trend model which includes a linear term, several harmonics with period lengths from three to twenty four months and the quasi-biennial oscillation (QBO). Drifts at 2-sigma significance level were mainly negative for ozone relative to Aura MLS and Odin OSIRIS and negative or near zero for most of the comparisons to Lidar measurements. Lidar stations used here include those at Hohenpeissenberg (47.8°N, 11.0°E), Lauder (45.0°S, 169.7°E), Mauna Loa (19.5°N, 155.6°W), Observatoire Haute Provence (43.9°N, 5.7°E) and Table Mountain (34.4°N, 117.7°W). Drifts against ACE-FTS were found to be mostly insignificant. The assessed MIPAS ozone trends cover the time period of July 2002 to April 2012 and range from -0.56 ppmv/decade to +0.48 ppmv/decade (-0.52 ppmv/decade to +0.47 ppmv/decade when displayed on pressure coordinates) depending on altitude/pressure and latitude. From the empirical drift analyses we conclude that the real ozone trends might be slightly more positive/less negative than those calculated from the MIPAS data, by conceding the possibility of MIPAS having a very small (approx. within -0.3 ppmv/decade) negative drift for ozone. This leads to drift-corrected trends of -0.41 ppmv/decade to +0.55 ppmv/decade (-0.38 ppmv/decade to +0.53 ppmv/decade when displayed on pressure coordinates) for the time period covered by MIPAS Envisat measurements with very few negative and large areas

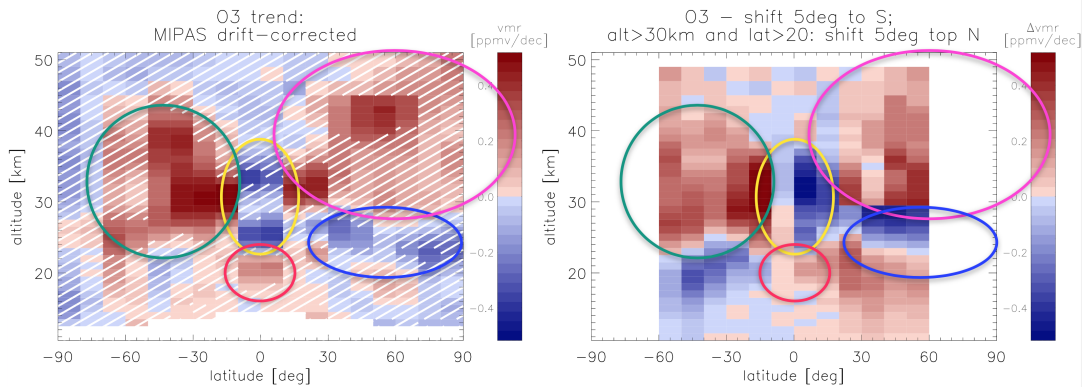


FIGURE 5.1: Comparison of the results of the ozone trend estimation (left) with a simulation of the subtropical mixing barrier shift (right). Red areas indicate increasing concentrations of ozone, while blue areas indicate decreasing concentrations. Hatching in the left panel shows where no trend at 2σ significance level could be found. In the right panel, altitudes beyond 60°S and 60°N were omitted to avoid interference with the polar mixing barriers. - Source: Eckert et al. (2014) - CC BY 3.0 License.

of positive trends at mid-latitudes for both hemispheres around and above 30 km (~ 10 hPa). Negative trends are found in the tropics around 25 and 35 km (~ 25 and 5 hPa), while an area of positive trends is located right above the tropical tropopause. These findings are in good agreement with recent literature. Differences of the trends compared with recent literature could be explained by a possible shift of the subtropical mixing barriers. Results for the altitude-latitude distribution of amplitudes of the quasi-biennial, annual and the semi-annual oscillation are overall in very good agreement with recent findings.

The full article is reprinted in Appendix [A](#).

Relevance within the scope of this thesis

In this study, pronounced hemispherically asymmetric distributions of ozone trends were found (left panel in Figure [5.1](#)) which were not expected from what we knew from model predictions in recent literature (World Meteorological Organization, [2011](#)). Particularly interesting are positive ozone trends in the regions around the tropical tropopause (red outline) and the negative ozone trends in tropical mid-stratospheric regions (yellow outline). From model calculations in recent literature, we expected positive ozone trends throughout the stratosphere, but negative ozone trends in the region around the tropical tropopause. The latter was expected due to an postulated increase of the Brewer-Dobson circulation (BDC) due to climate change and increased tropical upwelling of air with lower amounts of ozone from tropospheric altitudes (s. Fig. [2.1](#)), which would thus result in negative trends in this region.

The right panel of Figure 5.1 show the result of a simple test: here, an ozone distribution from the beginning of the MIPAS measurement period was shifted by 5° to the south at altitudes below 30 km and expanded by 5° above that altitude to simulate a shift of the subtropical mixing barriers (s. Fig. 1.1). Latitudes beyond 60°S and 60°N were omitted to avoid interfering effects by the polar mixing barriers. This simulation (Fig. 5.1: right) resembles the estimated trends (left) very well. Accordingly, a shift of the subtropical mixing barriers can sufficiently explain differences to results that could be expected from recent literature. This effect is discussed in Stiller et al. (2017).

In this publication, I was able to show clearly that changes in the BDC occurred during the 10-year measurement period of MIPAS. Furthermore, it showed need of investigation on the topic and my following first author publications, together with the development of the ANCISTRUS-SPEC inverse model, facilitate a closer, more sophisticated outlook.

5.2 MIPAS IMK/IAA CFC-11 (CCl₃F) and CFC-12 (CCl₂F₂) measurements: accuracy, precision and long-term stability

Authors: E. Eckert, A. Laeng, S. Lossow, S. Kellmann, G. Stiller, T. von Clarmann, N. Glatthor, M. Höpfner, M. Kiefer, H. Oelhaf, J. Orphal, B. Funke, U. Grabowski, F. Haenel, A. Linden, G. Wetzel, W. Woiwode, P. F. Bernath, C. Boone, G. S. Dutton, J. W. Elkins, A. Engel, J. C. Gille, F. Kolonjari, T. Sugita, G. C. Toon, and K. A. Walker

In: Atmos. Meas. Tech., 9, 3355–3389, 2016 www.atmos-meas-tech.net/9/3355/2016/ doi:10.5194/amt-9-3355-2016



Authorship Statement

This first author article of mine originates from the need of additional long lived trace gases as input for the ANCISTRUS-SPEC inverse to better constrain its results and, in the longer run, to better understand the Brewer-Dobson circulation (BDC). While the data products for CCl₃F (CFC-11) and CCl₂F₂ (CFC-12) already existed at the time this study was undertaken, they had not been systematically compared to other instruments to detect biases yet, nor had their temporal stability been assessed.

Within the scope of an extensive validation study, I com-

pared both the full spectral resolution (FR) and the reduced spectral resolution (RR) data sets of both trace gases with various instruments, including satellite borne, airplane borne, balloon borne and ground-based measurements. I performed most of the comparisons using coincident profile pairs. Since the vertical resolution of some of the comparison instruments was significantly different from that of Michelson Interferometer for Passive Atmospheric Sounding (MIPAS) (s. Table 5.1), I convolved each profile of the better resolving instruments with the respective MIPAS averaging kernel.

TABLE 5.1: Vertical resolution of MIPAS RR (FR) period and those of comparison instruments used for the validation study on CFC-11 and CFC-12.

Instrument	Vertical Resolution CFC-11	Vertical Resolution CFC-12
MIPAS Envisat	(3-7 km) 2-6 km	(3-8 km) slightly better
ACE-FTS	3-4 km	3-4 km
HIRDLS	1-1.2 km	1-1.2 km
ILAS-II	1.5-2.5 km	1.5-2.5 km
MkIV	2-4 km	2-4 km
Cryosampler	1-2 km	1-2 km
MIPAS-B	2-5 km	2-5 km
HATS	none → ground-based	none → ground-based
MIPAS-STR	1-2 km	1-2 km

The vertical resolutions given in Table [5.1](#) are average estimates. For all instruments except MIPAS Envisat these estimates are approximately the same for CFC-11 and CFC-12. However, averaging kernels differ from measurement to measurement. Thus, I had to use the respective MIPAS averaging kernel for every collocated profile pair instead of using an average MIPAS averaging kernel for all of them.

Alexandra Laeng provided IDL routines for this validation exercise, which I extended or changed according to the needs of my study and she also prepared figures on comparisons of MkIV and Cryosampler with MIPAS and a figure to determine how realistic the MIPAS error estimates are. Gerald Wetzel provided figures of the comparison with MIPAS-B. Similar to my first study - regarding stratospheric ozone - the instrument PI's of the comparison instruments contributed by providing data and answering instrument-specific questions. Thomas von Clarmann und Gabriele Stiller initiated and supervised the paper.

Abstract

Profiles of CFC-11 (CCl_3F) and CFC-12 (CCl_2F_2) of the Michelson Interferometer for Passive Atmospheric Sounding (MIPAS) aboard the European satellite Envisat have been retrieved from versions MIPAS/4.61 to MIPAS/4.62 and MIPAS/5.02 to MIPAS/5.06 level-1b data using the scientific level-2 processor run by Karlsruhe Institute of Technology (KIT), Institute of Meteorology and Climate Research (IMK) and Consejo Superior de Investigaciones Científicas (CSIC), Instituto de Astrofísica de Andalucía (IAA). These profiles have been compared to measurements taken by the balloon borne Cryosampler, Mark IV (MkIV) and MIPAS-Balloon (MIPAS-B), the airborne MIPAS-STRatospheric aircraft (MIPAS-STR), the satellite borne Atmospheric Chemistry Experiment Fourier transform spectrometer (ACE-FTS) and the High Resolution Dynamic Limb Sounder (HIRDLS) as well as the ground based Halocarbon and other Atmospheric Trace Species (HATS) network for the reduced spectral resolution period (RR: Jan. 2005 - April 2012) of MIPAS. ACE-FTS, MkIV and HATS also provide measurements during the high spectral resolution period (FR:

July 2002 - March 2004) and were used to validate MIPAS CFC-11 and CFC-12 products during that time, as well as profiles from the Improved Limb Atmospheric Spectrometer ILAS-II. In general, we find that MIPAS shows slightly higher values for CFC-11 at the lower end of the profiles (below ~ 15 km) and in a comparison of HATS ground-based data and MIPAS measurements at 3 km below the tropopause. Differences range from approximately 10 to 50 pptv (~ 5 -20 %) during the RR period. In general, differences are slightly smaller for the FR period. An indication of a slight high-bias at the lower end of the profile exists for CFC-12 as well, but this bias is far less pronounced than for CFC-11 and is not as obvious in the relative differences between MIPAS and any of the comparison instruments. Differences at the lower end of the profile (below ~ 15 km) and in the comparison of HATS and MIPAS measurements taken at 3 km below the tropopause mainly stay within 10 to 50 pptv (corresponding to ~ 2 -10 % for CFC-12) for the RR and the FR period. Between ~ 15 and 30 km, most comparisons agree within 10 to 20 pptv (10 to 20 %), apart from ILAS-II, which shows large differences above ~ 17 km. Overall, relative differences are usually smaller for CFC-12 than for CFC-11. For both species - CFC-11 and CFC-12 - we find that differences at the lower end of the profile tend to be larger at higher latitudes than in tropical and subtropical regions. In addition, MIPAS profiles have a maximum in their mixing ratio around the tropopause, which is most obvious in tropical mean profiles. Comparisons of a the standard deviation in a quiescent atmosphere (polar summer) show that only the CFC-12 FR error budget can fully explain the observed variability, while for the other products (CFC-11 FR and RR and CFC-12 RR) only two thirds to three quarters can be explained. Investigations regarding the temporal stability show very small negative drifts in MIPAS CFC-11 measurements. These instrument drifts vary between ~ 1 -3 %/decade. For CFC-12, the drifts are also negative and close to zero up to ~ 30 km. Above that altitude larger drifts of up to ~ 50 %/decade appear which are negative up to ~ 35 km and positive, but of a similar magnitude, above.

The full article is reprinted in Appendix [A](#).

Relevance within the scope of this thesis

Since my study on stratospheric ozone, alongside other IMK-ASF-SAT group publications, clearly showed that further investigation of changes in the stratospheric circulation was necessary. Thomas von Clarmann and Udo Grabowski had already developed a first version of the ANCISTRUS-SPEC inverse model, and the next step towards reliable scientific results was to provide validated data sets of atmospheric trace gases that could reduce uncertainty in the model's results. Trace gases appropriate for this purpose have the following characteristics:

- They are long-lived and are thus transported through the entire stratosphere.

- They either have well-known, finite stratospheric lifetimes **OR** they have lifetimes which can be regarded as infinite compared to the short measurement period of MIPAS (e.g., SF₆ with a stratospheric lifetime of about 8000 years) and their well-known abundance in the troposphere is monotonically increasing or decreasing.
- Ideally, their sources and sinks are known and not complex - e.g., only a sink due to being photolyzed when travelling through the stratosphere.
- They should show different features, e.g., in terms of stratospheric lifetimes and their vertical gradient to provide independent information about stratospheric circulation processes.

Taking these criteria into account, CFC-11 and CFC-12 are ideal candidates to further increase precision in ANCISTRUS-SPEC results: CFC-11 and CFC-12 have atmospheric lifetimes of approximately 60 and 110 years, respectively. CFC-11's most likely decomposition scheme in the atmosphere is photolytic decomposition by ultraviolet (UV) light of 226 nm. While photolytic destruction at 215 nm is the primary path of destruction for CFC-12, reaction with the electronically excited oxygen atom O(¹D) also takes place (Brasseur and Solomon, 2005). CFC-12 reaches far higher up in the stratosphere and its gradient is less steep compared with CFC-11, so the information these two gases give about stratospheric circulation processes is not redundant. Since CFC-11 and CFC-12 had already been derived from MIPAS measurements, the main task was to ensure their quality, possible biases and instrument drifts, which is the purpose of this study. Hemispheric asymmetries of stratospheric trends could also be confirmed (Fig. 5.2) and the estimated drifts showed that, up to 30 km, these trends are real and not an artifact introduced by e.g., temporally unstable detectors.

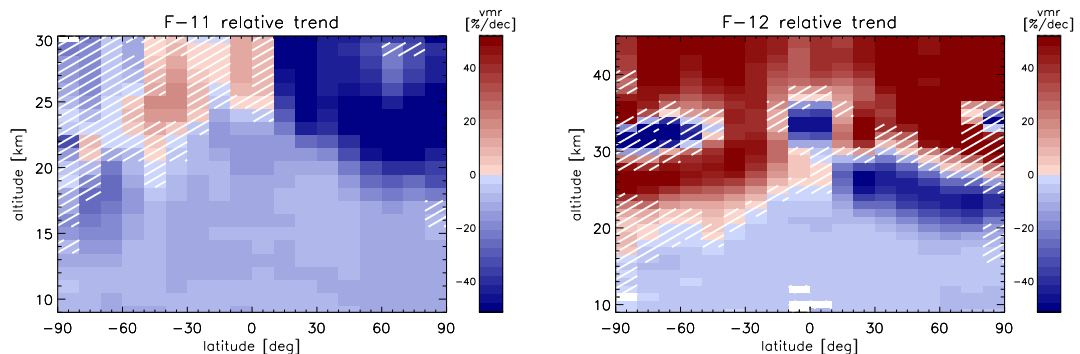


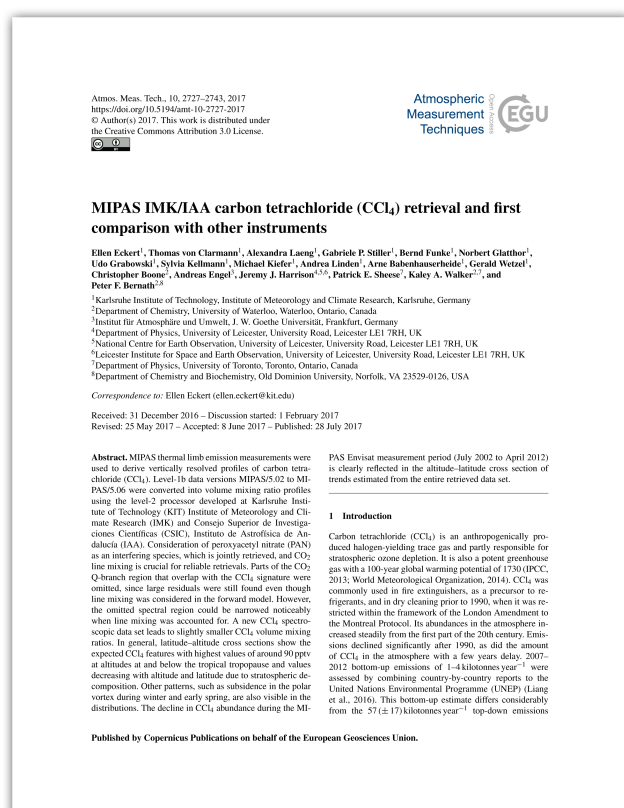
FIGURE 5.2: Altitude-latitude cross-sections of relative trends in CFC-11 (left) and CFC-12 (right) for the entire MIPAS measurement period from July 2002 to April 2012. Color coding and hatching are similar to the left panel of Figure 5.1. - Source: Eckert et al. (2016) - CC BY 3.0 License.

According to this study, CFC-11 and CFC-12 can be used with ANCISTRUS-SPEC and were expected to improve the reliability of its results.

5.3 MIPAS IMK/IAA Carbon Tetrachloride (CCl₄) Retrieval and first Comparison with other Instruments

Authors: E. Eckert, T. von Clarmann, A. Laeng, G. P. Stiller, B. Funke, N. Glatthor, U. Grabowski, S. Kellmann, M. Kiefer, A. Linden, A. Babenhauserheide, G. Wetzel, C. Boone, A. Engel, J. J. Harrison, P. E. Sheese, K. A. Walker, and P. F. Bernath

In: Atmos. Meas. Tech., 10, 2727–2743, 2017 <https://doi.org/10.5194/amt-10-2727-2017>



Authorship Statement

I conducted research on the topic of deriving carbon tetrachloride (CCl₄) from measurements of the Michelson Interferometer for Passive Atmospheric Sounding (MIPAS), which lead to this first author publication. For this purpose, I decided which spectral regions were suitable for a retrieval of CCl₄ (s. Table 5.2) and was able to narrow the gap between the two regions further by considering line-mixing in the retrieval setup. I selected previously retrieved species should be used in the CCl₄ retrieval so they would not be mis-interpreted for CCl₄. Together with Christopher Boone from Waterloo University I determined further potential interfering species and I implemented the usage of a new spectroscopic dataset with support of Norbert Glatthor. I then compared the results of the CCl₄ retrieval with those of other measurements, both historic and simultaneously taken ones. Arne Babenhauserheide supported the comparison with the Atmospheric Trace Molecule Spectroscopy (ATMOS) by extracting data directly from Zander et al. (1996). I also estimated stratospheric trends and I have provided an extensive error budget of the MIPAS CCl₄ dataset. Alexandra Laeng contributed to the study by preparing a figure to determine how

phosphorus from the MIPAS dataset. I also estimated stratospheric trends and I have provided an extensive error budget of the MIPAS CCl₄ dataset. Alexandra Laeng contributed to the study by preparing a figure to determine how

Alexandra Laeng contributed to the study by preparing a figure to determine how

TABLE 5.2: Retrieval details on the spectroscopic region, species imported from preceding retrieval steps and variables fitted jointly during the retrieval process. Brackets denote mixing ratios. - Source: Eckert et al. (2017).

Spectral regions	Imported from preceding retrieval steps	Jointly fitted variables
772.0 - 791.0 cm^{-1}	Shift(z_{tangent})	[PAN](z)
792.0 - 805.0 cm^{-1}	T(z)	[CH_3CCl_3](z)
	$T_{\text{grad}}(z)$	[HCFC-22](z)
	[HNO_3](z)	[O_3](z)
	[ClO](z)	[H_2O](z)
	[CFC-11](z)	[C_2H_2](z)
	[C_2H_6](z)	[COF_2](z)
	[HCN](z)	Continuum(z)
	[ClONO_2](z)	offset
	[HNO_4](z)	

realistic the MIPAS error estimates are and by generating a figure of a comparison of MIPAS CCl_4 with that of Cryosampler. Gerald Wetzel and Patrick Sheese provided figures of the comparison of MIPAS CCl_4 measurements with those of MIPAS-B and ACE-FTS, respectively. Thomas von Clarmann und Gabriele Stiller initiated and supervised the paper.

Abstract

MIPAS thermal limb emission measurements were used to derive vertically resolved profiles of carbon tetrachloride (CCl_4). Level-1b data versions MIPAS/5.02 to MIPAS/5.06 were converted into volume mixing ratio profiles using the level-2 processor developed at Karlsruhe Institute of Technology (KIT) Institute of Meteorology and Climate Research (IMK) and Consejo Superior de Investigaciones Científicas (CSIC), Instituto de Astrofísica de Andalucía (IAA). Consideration of peroxyacetyl nitrate (PAN) as interfering species, which is jointly retrieved, and CO_2 line mixing is crucial for reliable retrievals. Parts of the CO_2 Q-branch region that overlap with the CCl_4 signature were omitted, since large residuals were still found even though line mixing was considered in the forward model. However, the omitted spectral region could be narrowed noticeably when line mixing was accounted for. A new CCl_4 spectroscopic dataset leads to slightly smaller CCl_4 volume mixing ratios. In general, latitude-altitude cross-section show the expected CCl_4 features with highest values of around 90 pptv at altitudes at and below the tropical tropopause and values decreasing with altitude and latitude due to stratospheric decomposition. Other patterns, such as subsidence in the polar vortex during winter and early spring, are also visible

in the distributions. The decline in CCl_4 abundance during the MIPAS Envisat measurement period (July 2002 to April 2012) is clearly reflected in the altitude-latitude cross-section of trends estimated from the entire retrieved data set.

The full article is reprinted in Appendix [A](#).

Relevance within the scope of this thesis

CCl_4 is another long-lived atmospheric trace gas. Its atmospheric lifetime is currently estimated to be approximately 44 years (Liang et al., [2016](#)). This gas is decomposed in the stratosphere by photolysis (Brasseur and Solomon, [2005](#)). Its vertical gradient is even steeper than that of CCl_3F (CFC-11) and thus the gas can provide additional information on transport processes in the stratosphere. Conclusively, CCl_4 is an additional great candidate to decrease uncertainty and consequently improve the reliability of ANCISTRUS-SPEC results. For the given reasons, it was desirable to derive CCl_4 from MIPAS measurements. This work also supports the hypothesis of changes in the Brewer-Dobson circulation (BDC), as a hemispheric asymmetry is visible in the CCl_4 trends (Fig. [5.3](#)).

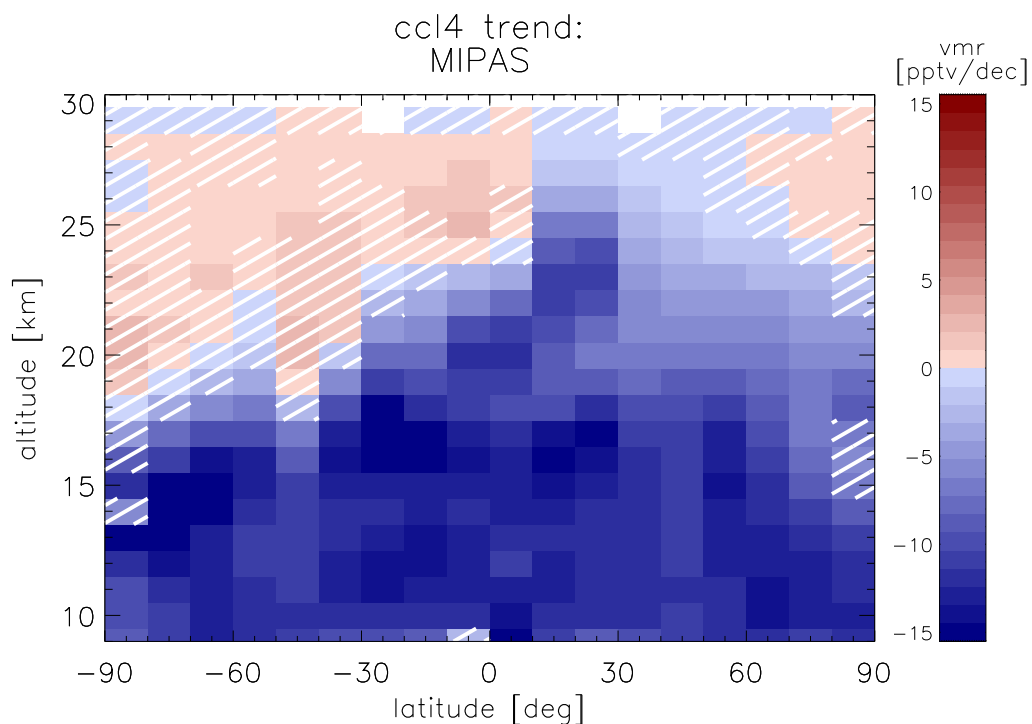


FIGURE 5.3: Altitude-latitude cross-sections of trends in CCl_4 for the entire MIPAS measurement period. Color coding and hatching are similar to the left panel of Figure [5.1](#). - Source: Eckert et al. ([2017](#)) - CC BY 4.0 License.


6. Co-Authored related publications

6.1 Technical Note: Trend estimation from irregularly sampled, correlated data

Authors: T. von Clarmann, G. Stiller, U. Grabowski, E. Eckert, and J. Orphal

In: Atmos. Chem. Phys., 10, 6737–6747, 2010 www.atmos-chem-phys.net/10/6737/2010/
doi:10.5194/acp-10-6737-2010

Atmos. Chem. Phys., 10, 6737–6747, 2010
www.atmos-chem-phys.net/10/6737/2010/
doi:10.5194/acp-10-6737-2010
© Author(s) 2010. CC Attribution 3.0 License.



Technical Note: Trend estimation from irregularly sampled, correlated data

T. von Clarmann, G. Stiller, U. Grabowski, E. Eckert, and J. Orphal
Karlsruhe Institute of Technology, Institute for Meteorology and Climate Research, Karlsruhe, Germany

Received: 16 November 2009 – Published in Atmos. Chem. Phys. Discuss.: 21 December 2009
Revised: 12 July 2010 – Accepted: 12 July 2010 – Published: 22 July 2010

Abstract. Estimation of a trend of an atmospheric state variable is usually performed by fitting a linear regression line to a set of data of this variable sampled at different times. Often these data are irregularly sampled in space and time and clustered in a sense that error correlations among data points cause a similar error of data points sampled at similar times. Since this can affect the estimated trend, we suggest to take the full error covariance matrix of the data into account. Superimposed periodic variations can be jointly fitted in a straightforward manner, even if the shape of the periodic function is not known. Global data sets, particularly satellite data, can form the basis to estimate the error correlations. State-dependent amplitudes of superimposed periodic corrections result in a non-linear optimization problem which is solved iteratively.

1 Introduction

Correct trend estimation is a key question in the discussion of climate change (IPCC, 2007). While fitting a straight line to a sample of data is an almost trivial task, errors in the data set and non-representativeness of the sample add some difficulty to the problem. Assuming normally distributed errors which are uncorrelated over the sample, each data point is simply weighted by the inverse of its variance to obtain a best linear unbiased estimate of the trend (Aitken, 1935). Methods applicable to least squares fitting of data where both the dependent and the independent variables are affected by errors have recently been reviewed by Cantrell (2008).

If the assumption of normal error distribution is questionable, robust linear regression methods help to reduce the sensitivity of the trend to outliers in the sample (Mühlbauer

et al. 2009 and references therein). Another cure against non-normality of distributions of residuals are bootstrap methods, introduced by Efron (1979) as a variant to jackknife methods and applied to atmospheric trend analysis by, e.g. Cox et al. (2002), Gardiner et al. (2008) or Vigouroux et al. (2008).

Besides non-normality of the distribution of residuals, correlations between the sampled data are another class of problems. When using multisite means to infer a trend, the standard errors of the means σ_{mean} which determine the weight of each mean in the regression analysis are not the standard deviation σ of the sample over the sites divided by the square root of the number of sites M but


$$\sigma_{\text{mean}} = \sqrt{\sigma^2 \left(\frac{1 + (M-1)r_{\text{inter}}}{M} \right)}, \quad (1)$$

where r_{inter} is the average intersite correlation coefficient (Jones et al., 1997). This can easily be verified by multiplication of the averaging operator from the left and right to the intersite covariance matrix S_{inter} according to multivariate Gaussian error propagation:

$$\sigma_{\text{mean,inter}}^2 = \frac{1}{M^2} \frac{1}{M} S_{\text{inter}} \begin{pmatrix} 1 \\ \vdots \\ 1 \end{pmatrix}. \quad (2)$$

where the element at position (i,k) of S_{inter} is $r_{\text{inter},i,k}\sigma^2$. This approach solves the problem of intersite correlations and is applicable, e.g., if measurements of the same set of sites are used over the whole period. σ_{mean} calculated under consideration of r_{inter} accounts for the fact that the available sites do not fully represent the population, i.e., the sample mean at a given time is not necessarily identical to the global mean. Since the same set of stations is used over the whole period, the measurements at the given sites are not a random sample.

Weatherhead et al. (1998) discuss how autocorrelations of noise in the data affect the precision of the estimated trend.

 Correspondence to: T. von Clarmann (thomas.clarmann@kit.edu)

Published by Copernicus Publications on behalf of the European Geosciences Union.

Authorship Statement

This article was written by Thomas von Clarmann to introduce his method of trend estimation, which incorporates the full error covariance matrix to account for dependencies between data points of a time series. In there, he gives various examples of different application of his trend estimation method.

I contributed by calculating case studies for all of these examples, demonstrating the versatility of the trend method, and thoroughly reviewed the manuscript.

Abstract

Estimation of a trend of an atmospheric state variable is usually performed by fitting a linear regression line to a set of data of this variable sampled at different times. Often these data are irregularly sampled in space and time and clustered in a sense that error correlations among data points cause a similar error of data points sampled at similar times. Since this can affect the estimated trend, we suggest to take the full error covariance matrix of the data into account. Superimposed periodic variations can be jointly fitted in a straightforward manner, even if the shape of the periodic function is not known.

Global data sets, particularly satellite data, can form the basis to estimate the error correlations. State-dependent amplitudes of superimposed periodic corrections result in a non-linear optimization problem which is solved iteratively.

The full article is reprinted with the kind permission of the first author in Appendix [B](#).

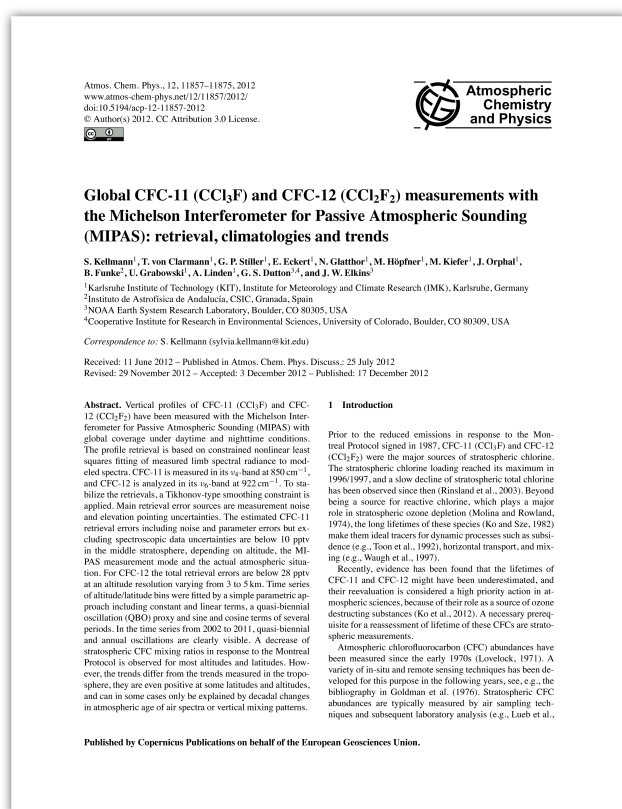
Relevance within the scope of this thesis

The method published in this manuscript for the first time lays the foundation for my extensive study on ozone trends (Eckert et al., [2014](#)) and all subsequent estimations of trends in the abundance of atmospheric constituents. Assisting Thomas von Clar-mann within the scope of his publication allowed me to gain profound understanding of his method of trend estimation and to comprehend the advantages of taking the full error covariance matrix into account to consider dependencies between the data points, e.g., biases between the full spectral resolution (FR) and reduced spectral resolution (RR) period as well as autocorrelations the data points. It further enabled me to interpret the results of the studies I undertook using his method of trend estimation and thus I could avoid possible pitfalls, e.g., I was able to distinguish an artificially introduced trend from a real trend.

6.2 Global CFC-11 (CCl₃F) and CFC-12 (CCl₂F₂) measurements with the Michelson Interferometer for Passive Atmospheric Sounding (MIPAS): retrieval, climatologies and trends

Authors: S. Kellmann, T. von Clarmann, G. P. Stiller, E. Eckert, N. Glatthor, M. Höpfner, M. Kiefer, J. Orphal, B. Funke, U. Grabowski, A. Linden, G. S. Dutton, and J. W. Elkins

In: Atmos. Chem. Phys., 12, 11857–11875, 2012 www.atmos-chem-phys.net/12/11857/2012/
doi:10.5194/acp-12-11857-2012



Authorship Statement

Sylvia Kellmann published this paper to document the Michelson Interferometer for Passive Atmospheric Sounding (MIPAS) retrieval of CCl₃F (CFC-11) and CCl₂F₂ (CFC-12) and to present climatologies and other applications such as trends of these trace gases. In addition, CFC-11 and CFC-12 trends found in MIPAS measurements between 10 and 30 km (35 km for CFC-12) were compared with trends assessed by using the mean age of air on ground based trends of these gases to simulate what the ground-based trends would look like if transported to the stratosphere. This publication also gives an overview of

various error compounds of the MIPAS CFC-11 and CFC-12 retrieval. My responsibilities in this project covered all aspects of trend estimation. Further, I reviewed the manuscript in detail and presented the results at the Seventh International Symposium on Non-CO₂ Greenhouse Gases (NCGG7) on behalf of Sylvia Kellmann.

Abstract

Vertical profiles of CFC-11 (CCl_3F) and CFC-12 (CCl_2F_2) have been measured with the Michelson Interferometer for Passive Atmospheric Sounding (MIPAS) with global coverage under daytime and nighttime conditions. The profile retrieval is based on constrained nonlinear least squares fitting of measured limb spectral radiance to modeled spectra. CFC-11 is measured in its ν_4 -band at 850 cm^{-1} , and CFC-12 is analyzed in its ν_6 -band at 922 cm^{-1} . To stabilize the retrievals, a Tikhonov-type smoothing constraint is applied. Main retrieval error sources are measurement noise and elevation pointing uncertainties. The estimated CFC-11 retrieval errors including noise and parameter errors but excluding spectroscopic data uncertainties are below 10 pptv in the middle stratosphere, depending on altitude, the MIPAS measurement mode and the actual atmospheric situation. For CFC-12 the total retrieval errors are below 28 pptv at an altitude resolution varying from 3 to 5 km. Time series of altitude/latitude bins were fitted by a simple parametric approach including constant and linear terms, a quasi-biennial oscillation (QBO) proxy and sine and cosine terms of several periods. In the time series from 2002 to 2011, quasi-biennial and annual oscillations are clearly visible. A decrease of stratospheric CFC mixing ratios in response to the Montreal Protocol is observed for most altitudes and latitudes. However, the trends differ from the trends measured in the troposphere, they are even positive at some latitudes and altitudes, and can in some cases only be explained by decadal changes in atmospheric age of air spectra or vertical mixing patterns.

The full article is reprinted with the kind permission of the first author in Appendix [B](#).

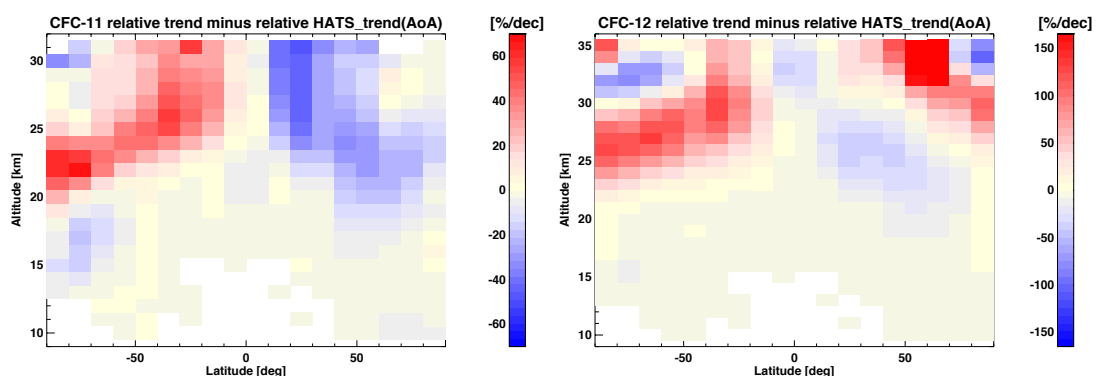


FIGURE 6.1: Relative trends of CFC-11 and CFC-12 calculated from age of air corrected HATS ground-based data subtracted from relative MIPAS trends of these species. Red colors indicate that the MIPAS trends increase stronger or decrease less strong than the age of air corrected HATS trends. The reverse is denoted by blue colors. - Source: Kellmann et al. (2012) - CC BY 3.0 License.

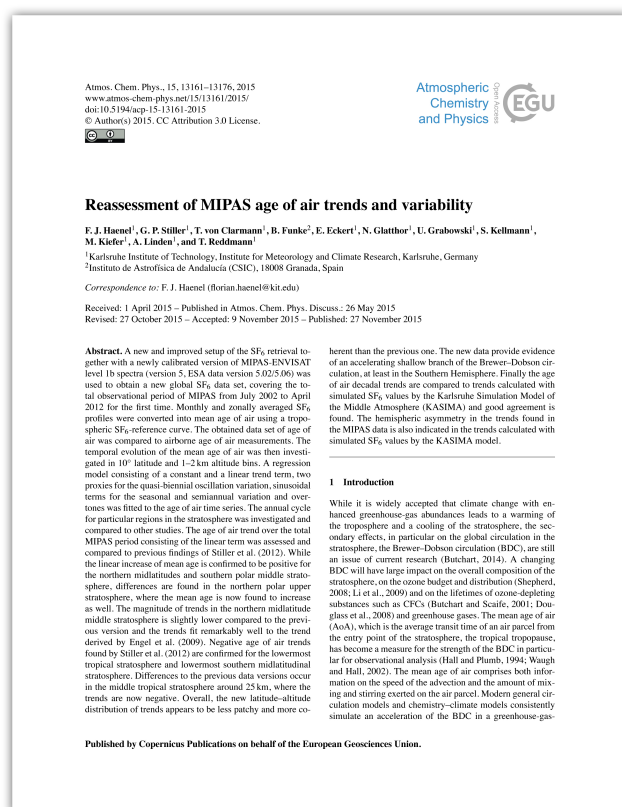
Relevance within the scope of this thesis

The relevance of this paper for my project is twofold. Firstly, this paper describes the retrieval and characterizes the results of stratospheric CFC-11 and CFC-12 from MIPAS. These data products play an important role in my analysis of stratospheric circulation. Secondly, this paper provides additional evidence of changes in the stratospheric circulation and thus motivates my further work in this area. In particular, trends of CFC-11 and CFC-12 are presented in this paper. It is shown that these trends cannot be fully explained by trends of ground-based CFC-11 and CFC-12 measurements. To make ground-based trends comparable to stratospheric ones, the time-lag caused by stratospheric transport times is considered by using age of air data provided by Stiller et al. (2012). Furthermore, trends are analyzed in relative (percentage) units because decomposition rates are proportional to the active amount of a trace gas in the atmosphere. If stratospheric circulation was stationary, e.g., if it did not change during the measurement period, the percentage trends of stratospheric mixing ratios would equal those in the troposphere after correcting the time-lag. Our analysis, however, disproved this expectation and thus furnishes evidence of changes in stratospheric circulation.

6.3 Reassessment of MIPAS age of air trends and variability

Authors: F. Haenel, G. P. Stiller, T. von Clarmann, B. Funke, E. Eckert, N. Glatthor, U. Grabowski, S. Kellmann, M. Kiefer, A. Linden, and T. Reddmann

In: Atmos. Chem. Phys., 15, 13161–13176, 2015 www.atmos-chem-phys.net/15/13161/2015/
doi:10.5194/acp-15-13161-2015



Authorship Statement

In this publication, Florian Haenel introduced the updated and improved data product of SF₆ from the Michelson Interferometer for Passive Atmospheric Sounding (MIPAS) and presented the results of age of air calculations and age of air trends from this new data set, as well as validating his findings. He also compared his results with the previously presented MIPAS SF₆ data and its applications by Stiller et al. (2012).

Again, my responsibilities in this project covered issues in the field of trend estimation.

Abstract

A new and improved setup of the SF₆ retrieval together with a newly calibrated version of MIPAS-ENVISAT level 1b spectra (version 5, ESA data version 5.02/5.06) was used to obtain a new global SF₆ data set, covering the total observational period of MIPAS from July 2002 to April 2012 for the first time. Monthly and zonally averaged SF₆ profiles were converted into mean age of air using a tropospheric SF₆-reference curve. The obtained data set of age of air was compared to airborne age of air measurements. The temporal evolution of the mean age of air was then investigated in 10° latitude and 1–2 km altitude bins. A regression model consisting of a constant

and a linear trend term, two proxies for the quasi-biennial oscillation variation, sinusoidal terms for the seasonal and semiannual variation and overtones was fitted to the age of air time series. The annual cycle for particular regions in the stratosphere was investigated and compared to other studies. The age of air trend over the total MIPAS period consisting of the linear term was assessed and compared to previous findings of Stiller et al. (2012). While the linear increase of mean age is confirmed to be positive for the northern midlatitudes and southern polar middle stratosphere, differences are found in the northern polar upper stratosphere, where the mean age is now found to increase as well. The magnitude of trends in the northern midlatitude middle stratosphere is slightly lower compared to the previous version and the trends fit remarkably well to the trend derived by Engel et al. (2009). Negative age of air trends found by Stiller et al. (2012) are confirmed for the lowermost tropical stratosphere and lowermost southern midlatitudinal stratosphere. Differences to the previous data versions occur in the middle tropical stratosphere around 25 km, where the trends are now negative. Overall, the new latitude–altitude distribution of trends appears to be less patchy and more coherent than the previous one. The new data provide evidence of an accelerating shallow branch of the Brewer–Dobson circulation, at least in the Southern Hemisphere. Finally the age of air decadal trends are compared to trends calculated with simulated SF₆ values by the Karlsruhe Simulation Model of the Middle Atmosphere (KASIMA) and good agreement is found. The hemispheric asymmetry in the trends found in the MIPAS data is also indicated in the trends calculated with simulated SF₆ values by the KASIMA model.

The full article is reprinted with the kind permission of the first author in Appendix B.

Relevance within the scope of this thesis

SF₆ is an excellent tracer for determination the age of stratospheric air since its abundance increased monotonically and almost linearly at ground level. In addition, the gas itself has no sources or sinks in the stratosphere leading to an atmospheric lifetime of approximately 8000 years. The only pitfall arises from a sink in the mesosphere which can lead to artefacts in the estimated age of air. The age of air is the time it took an air parcel to travel from the top of the troposphere to a certain point in the stratosphere. Since air parcels can travel on different paths and two-way mixing occurs on its way, the age of air at a certain point in the atmosphere is always a spectrum, while the mean age of air is the mean age of the spectrum of age of air. Thus, if changes over time are detectible in age of air this is a hint at changes in the large-scale circulation, including mixing patterns. In addition, this publication shows a hemispheric asymmetry in the distribution of trends in age of air derived from the improved MIPAS SF₆ dataset as have also been seen in trends of atmospheric trace gases. Thus, this study on SF₆ supports the need of taking a closer look at the Brewer–Dobson circulation (BDC).

7. Analysis of the Circulation of the Stratosphere using Spectroscopic Measurements (ANCISTRUS-SPEC)

The idea for the Analysis of the Circulation of the Stratosphere using Spectroscopic Measurements (ANCISTRUS-SPEC) inverse model was triggered by the need for a tool for diagnosing the Brewer-Dobson circulation (BDC) using measurements of atmospheric constituents without the detour through the age of air. As discussed in Section 1, using age of air in the context of diagnosing the BDC has its limitations: Due to the SF₆ tropospheric growth not being strictly linear, the age spectrum of SF₆ has to be considered. The age spectrum, however, requires some assumption on its own, which causes uncertainties in the age determination. While SF₆ is the most suitable tracer for age of air estimations to date, it still has a sink in the mesosphere which, through subsidence in the polar vortex, influences stratospheric SF₆ mixing ratios and thus draws age of air estimates to older ages in this region. In addition to the above, a point in the atmosphere at which the time is zero has to be defined. Practical reasons suggest this point to be top of the well mixed part of the troposphere (Stiller et al., 2012) so that ground based measurements of SF₆ can be used, since measurements are not available at the upper boundary of the tropical tropopause layer (TTL). The latter would have been necessary to follow the original suggestion of age of air being the time lag since the air parcel had passed the tropopause (Hall and Plumb, 1994). Different definitions challenge unambiguity of the results and make comparison tricky.

In the following, the ANCISTRUS-SPEC inverse model is introduced. Since it is of high complexity, only the major ideas are outlined. A detailed, equation by equation description of the model can be found in von Clarmann and Grabowski (2016).

7.1 Forward Modelling

ANCISTRUS-SPEC aims at the determination of zonal mean atmospheric circulation vectors from measured distributions of air density and volume mixing ratios of trace gases by inversion of the continuity equation. Similar inverse techniques as introduced for the retrieval of trace species abundances from spectra (Sec. 4.3) are used. ANCISTRUS-SPEC is set up on a 2D altitude-latitude grid. The forward model makes use of the continuity equation to estimate a later state of the atmosphere from a given atmospheric state. The state of the atmosphere is characterized by the density of air (ρ) and the volume mixing ratios of different atmospheric constituents (vmr). Despite the model's complexity, von Clarmann and Grabowski (2016) figured out a

way to integrate all necessary equations into a prediction operator, such that the forward model can be written as

$$\begin{pmatrix} \rho_I \\ \mathbf{vmr}_I \end{pmatrix} = \left(\prod_{i=1}^I \mathbf{D}_i \right) \begin{pmatrix} \rho_0 \\ \mathbf{vmr}_0 \end{pmatrix} \quad (7.1)$$

where \mathbf{D}_i is the prediction operator of each so-called micro time step (denoted by i). The subscript of 0 is associated with the initial atmospheric state which the prediction is made from. I denotes the end of the full (macro) time step.

The idea behind the concept of micro time steps is explained in the following: For each grid point on the altitude-latitude grid, the later state of the atmosphere includes contributions from its surrounding grid points. To ensure that transport is possible over longer distances, e.g., not just from the directly neighbouring grid points, micro time steps were introduced. These split the macro time step into smaller parts and for each micro time step transport and mixing are simulated. Since the boundary conditions of the later state of the atmosphere (e.g., at the lower and upper end of the altitude range) cannot be simulated using this method, they are calculated for each micro time step from a linear interpolation of the initial state of the atmosphere and the final state of the atmosphere. If this was not done, the area of the calculated atmospheric state would shrink with each micro time step.

The concise notation possible due to the design of the prediction operator makes error estimation for the prediction pretty straightforward

$$\mathbf{S}_I = \left(\prod_{i=1}^I \mathbf{D}_i \right) \mathbf{S}_0 \left(\prod_{i=1}^I \mathbf{D}_i \right)^T \quad (7.2)$$

where \mathbf{S}_I is the covariance matrix of the final state of the atmosphere and \mathbf{S}_0 is the covariance matrix of the initial state of the atmosphere.

7.2 Inversion of the Model

For the inversion of the previously described model, \mathbf{f} , the desired quantities of the vertical and meridional wind components (\mathbf{v} and \mathbf{w} , respectively) and respective the mixing coefficients (\mathbf{K}_Φ and \mathbf{K}_z) are condensed into one vector

$$\mathbf{q} = \begin{pmatrix} \mathbf{v} \\ \mathbf{w} \\ \mathbf{K}_\Phi \\ \mathbf{K}_z \end{pmatrix}. \quad (7.3)$$

\mathbf{q} is of the dimension of $N = 4J$ with $J = \sum_0^{gases} J_g$ (four unknowns at each grid point). In analogy to Section [4.3.2](#), the Jacobian matrix (\mathbf{F}) can be calculated as the derivative of the model to each element in \mathbf{q} . Using the Jacobian matrix (\mathbf{F}) it is now

possible to linearize the prediction with regard to the vertical and meridional winds and the mixing coefficients

$$\mathbf{x}_I = \mathbf{x}_0 + \mathbf{F}(\mathbf{q} - \mathbf{q}_0). \quad (7.4)$$

Under the assumption that \mathbf{x} is normally distributed, the probability density function of the atmospheric state is

$$P(\mathbf{x}) \propto e^{-\frac{1}{2}((\mathbf{x}_{m,I} - \mathbf{x}_I)^T \mathbf{S}_r^{-1} (\mathbf{x}_{m,I} - \mathbf{x}_I))} \quad (7.5)$$

with $\mathbf{x}_{m,I}$ being the measured final state and \mathbf{S}_r being the covariance matrix of the residual. Under the assumption that the errors of the measured final state of the atmosphere and the errors of the prediction are uncorrelated, the covariance matrix of the residual can be calculated according to

$$\mathbf{S}_r = \mathbf{S}_{m,I} + \mathbf{S}_p. \quad (7.6)$$

\mathbf{S}_p consists of those elements of \mathbf{S}_I that are associated with \mathbf{x}_I and $\mathbf{S}_{m,I}$ is the covariance matrix of the measured final state of the atmosphere. Eq. 7.5 leads to the cost function

$$\begin{aligned} \chi^2 &= (\mathbf{x}_{m,I} - \mathbf{x}_I)^T \mathbf{S}_r^{-1} (\mathbf{x}_{m,I} - \mathbf{x}_I) \\ &\approx (\mathbf{x}_{m,I} - \mathbf{x}_0 + \mathbf{F}(\mathbf{q} - \mathbf{q}_0))^T \mathbf{S}_r^{-1} (\mathbf{x}_{m,I} - \mathbf{x}_0 + \mathbf{F}(\mathbf{q} - \mathbf{q}_0)) \end{aligned} \quad (7.7)$$

which is minimal for the most likely \mathbf{q} . Here, linearity was assumed so that Eq. 7.4 could be used. According to the above, the most likely estimate $\hat{\mathbf{q}}$ is given as

$$\hat{\mathbf{q}} = \mathbf{q}_0 + (\mathbf{F}^T \mathbf{S}_r \mathbf{F})^{-1} \mathbf{F} \mathbf{S}_r^{-1} (\mathbf{x}_{m,I} - \mathbf{x}_I). \quad (7.8)$$

As stated in Section 4.3.2, the problem might be under-determined or ill-posed. Accordingly, a regularizing term was introduced transforming Eq. 7.8 to

$$\hat{\mathbf{q}} = \mathbf{q}_a + (\mathbf{F}^T \mathbf{S}_r \mathbf{F} + \mathbf{R})^{-1} \mathbf{F} \mathbf{S}_r^{-1} (\mathbf{x}_{m,I} - \mathbf{x}_I). \quad (7.9)$$

with \mathbf{q}_a containing prior information on the winds and mixing coefficients. For the winds a first order Tikhonov regularization was chosen, while for the mixing coefficients an optimal estimation approach was used. Again, Eq. 7.9 is only valid under the assumption of linearity. Non-linearity tackled by iterating the solution

$$\mathbf{q}_{it+1} = \mathbf{q}_{it} + (\mathbf{F}^T \mathbf{S}_r \mathbf{F} + \mathbf{R})^{-1} (\mathbf{F}_{it}^T \mathbf{S}_r^{-1} (\mathbf{x}_{m,I} - \mathbf{x}_{I,it}) - \mathbf{R}(\mathbf{q}_{it} - \mathbf{q}_a)) \quad (7.10)$$

In strong analogy to Section 4.3.2 the uncertainties of estimated winds and mixing coefficients are accumulated in the respective covariance matrix:

$$\mathbf{S}_q = (\mathbf{F}^T \mathbf{S}_r \mathbf{F} + \mathbf{R})^{-1} \mathbf{F}^T \mathbf{S}_r^{-1} \mathbf{F} (\mathbf{F}^T \mathbf{S}_r \mathbf{F} + \mathbf{R})^{-1} \quad (7.11)$$

The respective averaging kernels relating the estimated winds and mixing coefficients to the true ones are given by

$$\mathbf{A} = \frac{\partial \hat{\mathbf{q}}}{\partial \mathbf{q}} = (\mathbf{F}^T \mathbf{S}_r \mathbf{F} + \mathbf{R})^{-1} \mathbf{F}^T \mathbf{S}_r^{-1} \mathbf{F}. \quad (7.12)$$

Using the above concept, it is possible to infer vertical and meridional winds as well as mixing coefficients in the vertical and meridional direction from MIPAS measurements.

8. Results of Analyses with ANCISTRUS-SPEC

To investigate the influence of different numbers and types of trace gases on the inference of the stratospheric circulation, the Analysis of the Circulation of the Stratosphere using Spectroscopic Measurements (ANCISTRUS-SPEC) inverse model was run with two different sets of trace gas measurements from the Michelson Interferometer for Passive Atmospheric Sounding (MIPAS). In each case, the monthly mean altitude-latitude distributions of September and October, 2010, were used as the boundary conditions of the macro time step and ten micro time steps were performed. The strengths of the regularization was the same in both test runs as were the densities of air that were used. For the first run, the set consisted of only four trace gases:

- CCl_2F_2 (CFC-12)
- sulfur hexafluoride (SF_6)
- methane (CH_4)
- nitrous oxide (N_2O)

while the second run was performed with the initial set of four trace gases plus

- CCl_3F (CFC-11)
- carbon tetrachloride (CCl_4)

As everything else was held constant, changes in the results can unambiguously be attributed to the information content of the distributions of the two additional trace gases introduced in the second test run.

The resulting 2D altitude-latitude velocity fields for the test runs performed with sets of four and six trace gases are shown in Figure [8.1](#) top and bottom, respectively. The direction and strength of the wind at each grid point was calculated from its respective vertical and meridional component. For clarity, the wind speed is displayed in arrow length (the longer the arrow, the higher the wind speed) and color. Higher wind speeds are associated with reddish coloring, while blueish coloring indicates rather low wind speeds.

On first glance, the velocities derived in the two test runs (top and bottom of Fig. [8.1](#)) look very similar. The overall pattern of the mesospheric circulation, transporting air from the South to the North pole, is clearly visible. Subsidence over the North pole is also observable, which is presumably associated with the polar vortex that is already starting to form. Only small details hint at the fact that these are actually two different runs of the model, e.g., slightly stronger winds in the tropical

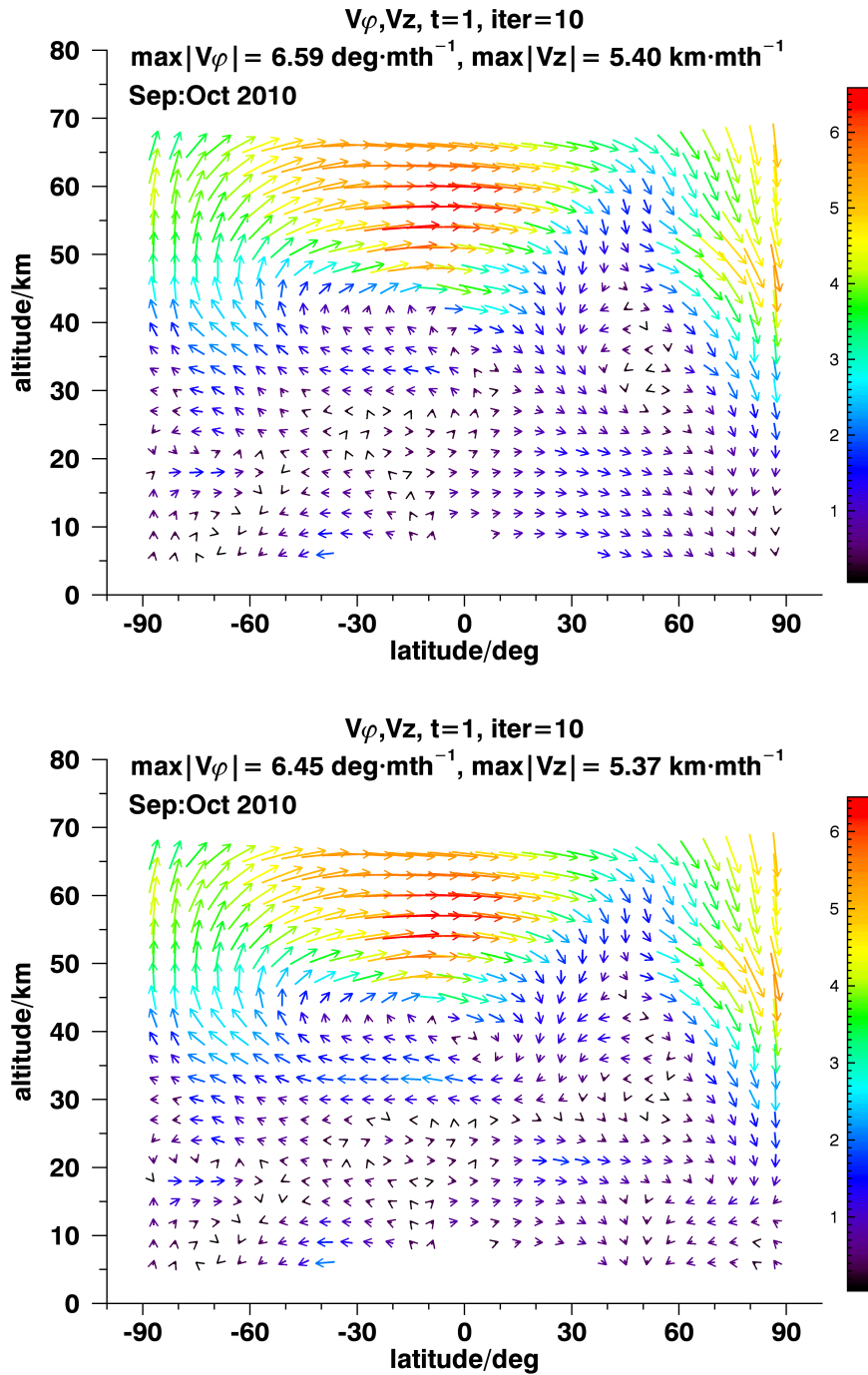


FIGURE 8.1: Altitude-latitude cross-section of wind directions and speeds assessed running ANCISTRUS-SPEC with four input trace gases (top) versus six input trace gases (bottom).

middle stratosphere (close to 35 km) or changes in direction of the winds in the northern mid-latitude and polar upper troposphere/lower stratosphere (UTLS).

While including two additional trace gases does not seem to have any major effects on the the 2D velocity field, the error estimates of the vertical and meridional wind components change significantly (Fig. [8.2](#) and [8.3](#), respectively). In there, red and orange

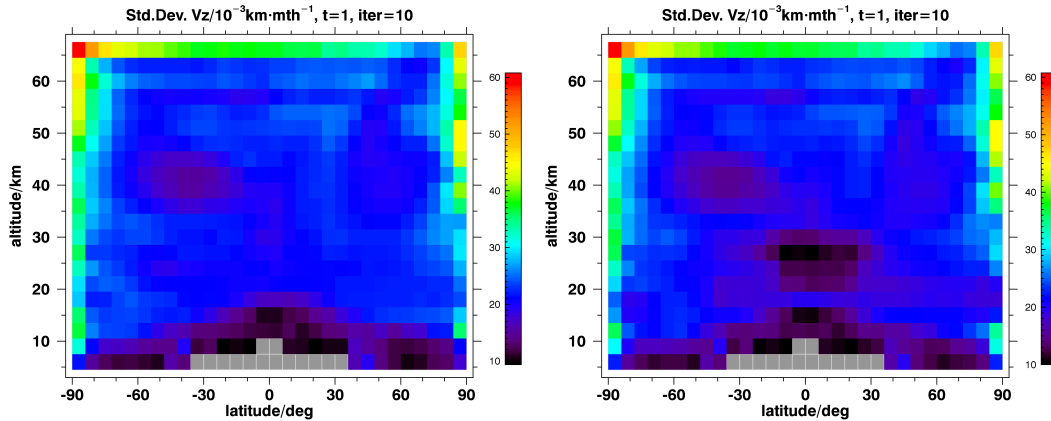


FIGURE 8.2: Altitude-latitude cross-section of the standard deviation of vertical wind speeds assessed running Ancistrus with four input trace gases (left) versus six input trace gases (right).

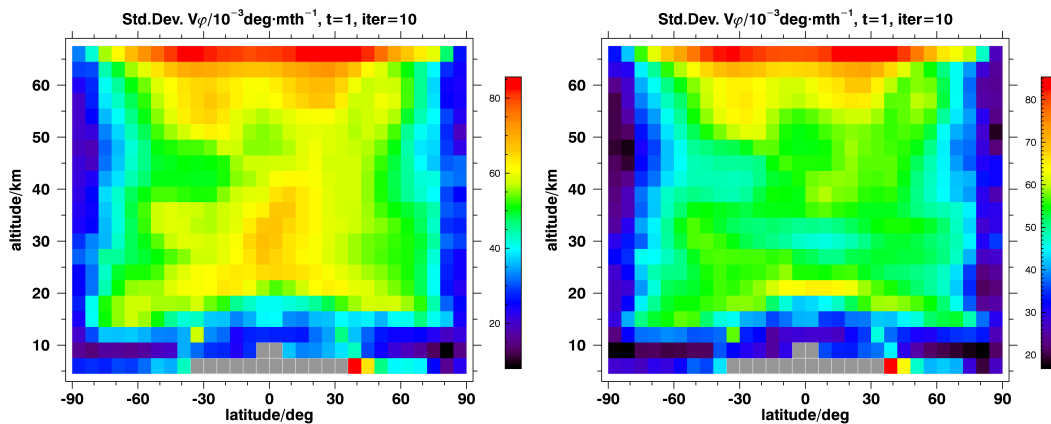


FIGURE 8.3: Altitude-latitude cross-section of the standard deviation of horizontal wind speeds assessed running Ancistrus with four input trace gases (left) versus six input trace gases (right).

coloring is associated with large standard deviations, while blue and turquoise coloring indicates small standard deviations. While the scale is slightly different for the standard deviations of the vertical wind component, the overall impression remains unchanged: Particularly below 40 km, the standard deviations of the wind (both in vertical and meridional direction) decrease considerably when CFC-11 and CCl_4 are used in addition to the original set of trace gases. This makes perfect sense, because basically all CFC-11 and CCl_4 resides below this altitude. Accordingly, these two trace add significant information to the system.

These findings are very promising, as they are solid proof that the results derived with ANCISTRUS-SPEC become more reliable when the trace gases investigated in this study (CFC-11: validated; CCl_4 : newly retrieved) are included to better constrain

the inverse transport problem.

9. Conclusions

Evidence of changes in stratospheric circulation have been found in measurements of the Michelson Interferometer for Passive Atmospheric Sounding (MIPAS). Within the scope of this thesis, a study on the temporal evolution of ozone (ozone trends) in the stratosphere was performed using MIPAS data (Eckert et al., 2014) and these trends were displayed on an altitude-latitude grid with a resolution of 1 km and 10° (Fig. 9.1). Red colors indicate increasing ozone, while blue colors denote decreasing ozone for the time period of the MIPAS measurements (July 2002 to April 2012). Hatching indicates that no trend could be found at 2σ confidence level. The distribution of the trends showed prominent hemispheric asymmetries, with positive ozone trends between ~ 25 and 45 km and ~ 10 to 50°S , while in the Northern hemisphere an area of positive trends is rather centred around 40 km with a band of negative trends lying underneath. The feature that raised most questions however, are the negative trends in the tropics at and above 25 km and particularly the small area of positive trends around the tropical tropopause. While slightly positive or near zero trends are expected for the stratosphere, models predicted negative ozone trends around the tropical tropopause due to a speedup of the Brewer-Dobson circulation (BDC). A shift of the subtropical mixing barriers was able to explain most of the peculiar features in the ozone trend distribution, which is a strong hint at changing stratospheric circulation changes. Hints at changes of the stratospheric circulation were also found by Kellmann et al. (2012) (CFCs), Chirkov et al. (2016) (HCFC-22), Glatthor et al. (2017) (carbonyl sulfide (OCS)) and Stiller et al. (2017). The latter investigated the mixing barrier shift in detail and found that it was able to explain the hemispheric asymmetry in age of air, while previously having found good agreement of this hypothesis in the distribution of other MIPAS trace gases (Stiller et al., 2013).

Using age of air had so far been the only way of diagnosing the BDC from measurements, with sulfur hexafluoride (SF_6) being the most suitable tracer to date. However, this approach has its limitations. Since the tropospheric growth of SF_6 is not strictly linear, the age spectrum of SF_6 has to be considered, which in turn introduces further uncertainty. In addition, SF_6 has a mesospheric sink which leads to overestimation of age of air in polar regions due to subsidence in the polar vortex in winter. Furthermore, a point of zero has to be defined, which leads to different estimates from measurements versus models.

While the need of diagnosing the BDC persists, it is desirable to avoid the detour through age of air, due to the above reasons. From this need, the idea of the Analysis of the Circulation of the Stratosphere using Spectroscopic Measurements (ANCISTRUS-SPEC) inverse model arose (von Clarmann and Grabowski, 2016). With this tool it is possible to derive vertical and meridional winds, as well as the respective mixing coefficients, from measurements of atmospheric constituents. While it

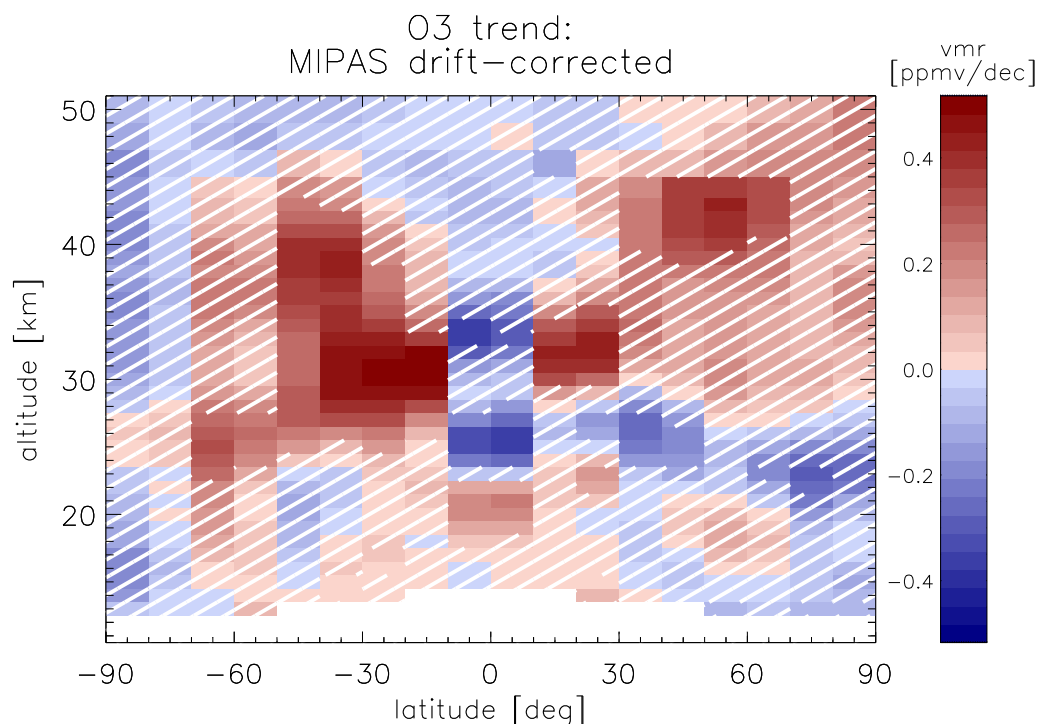


FIGURE 9.1: Drift-corrected ozone trends as derived from MIPAS measurements. - Source: Eckert et al. (2014) - CC BY 3.0 License.

was assumed that the predictions of ANCISTRUS-SPEC would become more reliable the more input data were used to constrain the problem, this point still had to be evaluated.

Further studies within the scope of this thesis, thus, focused on providing and validating additional datasets of trace gases suitable for being used with ANCISTRUS-SPEC. These had to be long-lived enough to travel to and through the stratosphere. Ideal candidates thus were CCl_3F (CFC-11), CCl_2F_2 (CFC-12) and carbon tetrachloride (CCl_4) due to their atmospheric lifetimes of 60.2 (54.3-66.3) years, 109.5 (102.9-116.1) years (Ko et al., 2013, Tab. 3.7) and 44 (36-58) years (Liang et al., 2016), respectively. While CFC-11 and CFC-12 had already been derived from MIPAS measurements a thorough validation study had not yet been carried out. This task was performed within the scope of this thesis (Eckert et al., 2016). The results supported good agreement of MIPAS CFC-11 and CFC-12 with other instruments, even though MIPAS CFC-11 showed a slight high bias below 15 km. While temporal stability was found to be very good for the CFC-11 product, large relative drifts were found in CFC-12 above 35 km. Error estimates were found to be slightly underestimated (or miss an error source), except for the CFC-12 product for the first period of MIPAS measurements where they seem to be realistic. None of the above,

however, affects suitability of MIPAS CFC-11 and CFC-12 distributions for the usage with ANCISTRUS-SPEC as performed for this thesis.

Since a MIPAS CCl_4 product did not yet exist, the gas was retrieved and first comparisons with CCl_4 data from other instruments were carried out (Eckert et al., 2017). Our CCl_4 distributions were found to be in very good agreement with those of other instruments. Hence, the conclusion is that the newly generated CCl_4 data are adequate to be used as additional input of ANCISTRUS-SPEC.

To estimate the influence of additional trace gases in ANCISTRUS-SPEC, two test runs from September to October, 2010, were performed. The first test run used a set of four MIPAS data products, CFC-12, SF_6 , methane (CH_4) and nitrous oxide (N_2O). The second test run was set up with six data products, which consisted of the initial four plus those of CFC-11 and CCl_4 .

The resulting velocities were very similar for both runs, with only minor changes in wind directions or speeds. This furnishes evidence of the consistency of the MIPAS tracer distributions. However, the error estimates of the velocities differed significantly. Below ~ 40 km, the standard deviation in both vertical and meridional winds were considerably smaller. Since CFC-11 and CCl_4 are only present in the atmosphere in significant amounts below ~ 40 km, they contribute most information in this altitude range.

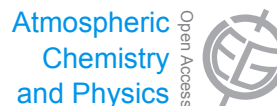
These findings are solid proof that reliability of the ANCISTRUS-SPEC results increases significantly when using two additional trace gases.

Since chemical sinks had not yet been implemented when these test runs were performed, future work could be to test the effects of that implementation. In addition, longer periods of time than just from September to October could be examined to get an overall picture of changes in the BDC during the MIPAS measurement period.

A. Copies of all First Author Publications

A.1 Drift-corrected trends and periodic variations in MIPAS IMK/IAA ozone measurements

Atmos. Chem. Phys., 14, 2571–2589, 2014
www.atmos-chem-phys.net/14/2571/2014/
doi:10.5194/acp-14-2571-2014
© Author(s) 2014. CC Attribution 3.0 License.



Drift-corrected trends and periodic variations in MIPAS IMK/IAA ozone measurements

E. Eckert¹, T. von Clarmann¹, M. Kiefer¹, G. P. Stiller¹, S. Lossow¹, N. Glatthor¹, D. A. Degenstein², L. Froidevaux³, S. Godin-Beekmann⁴, T. Leblanc⁵, S. McDermid⁵, M. Pastel⁴, W. Steinbrecht⁶, D. P. J. Swart⁷, K. A. Walker⁸, and P. F. Bernath⁹

¹Karlsruhe Institute of Technology, Institute for Meteorology and Climate Research, Karlsruhe, Germany

²Institute of Space and Atmospheric Studies, University of Saskatchewan, Saskatoon, Canada

³CalTech/Jet Propulsion Laboratory, Pasadena, California, USA

⁴Laboratoire Atmosphère, Milieux, Observations Spatiales (LATMOS), Institut Pierre Simon Laplace, Université Pierre et Marie Curie, Université Versailles St-Quentin-en-Yvelines, Centre National de la Recherche Scientifique, Paris, France

⁵California Institute of Technology, Jet Propulsion Laboratory, Wrightwood, CA, USA

⁶Meteorological Observatory, Deutscher Wetterdienst, Hohenpeissenberg, Germany

⁷National Institute of Public Health and Environmental Protection, P.O. Box 1, 3720 BA Bilthoven, the Netherlands

⁸Department of Physics, University of Toronto, Ontario, Canada

⁹Department of Chemistry and Biochemistry, Old Dominion University, Norfolk, VA 23529-0126, USA

Correspondence to: E. Eckert (ellen.eckert@kit.edu)

Received: 7 June 2013 – Published in Atmos. Chem. Phys. Discuss.: 4 July 2013

Revised: 12 January 2014 – Accepted: 20 January 2014 – Published: 13 March 2014

Abstract. Drifts, trends and periodic variations were calculated from monthly zonally averaged ozone profiles. The ozone profiles were derived from level-1b data of the Michelson Interferometer for Passive Atmospheric Sounding (MIPAS) by means of the scientific level-2 processor run by the Karlsruhe Institute of Technology (KIT), Institute for Meteorology and Climate Research (IMK). All trend and drift analyses were performed using a multilinear parametric trend model which includes a linear term, several harmonics with period lengths from 3 to 24 months and the quasi-biennial oscillation (QBO). Drifts at 2-sigma significance level were mainly negative for ozone relative to Aura MLS and Odin OSIRIS and negative or near zero for most of the comparisons to lidar measurements. Lidar stations used here include those at Hohenpeissenberg (47.8° N, 11.0° E), Lauder (45.0° S, 169.7° E), Mauna Loa (19.5° N, 155.6° W), Observatoire Haute Provence (43.9° N, 5.7° E) and Table Mountain (34.4° N, 117.7° W). Drifts against the Atmospheric Chemistry Experiment Fourier Transform Spectrometer (ACE-FTS) were found to be mostly insignificant. The assessed MIPAS ozone trends cover the time period of July 2002 to April 2012 and

range from -0.56 ppmv decade⁻¹ to $+0.48$ ppmv decade⁻¹ (-0.52 ppmv decade⁻¹ to $+0.47$ ppmv decade⁻¹ when displayed on pressure coordinates) depending on altitude/pressure and latitude. From the empirical drift analyses we conclude that the real ozone trends might be slightly more positive/less negative than those calculated from the MIPAS data, by conceding the possibility of MIPAS having a very small (approximately within -0.3 ppmv decade⁻¹) negative drift for ozone. This leads to drift-corrected trends of -0.41 ppmv decade⁻¹ to $+0.55$ ppmv decade⁻¹ (-0.38 ppmv decade⁻¹ to $+0.53$ ppmv decade⁻¹ when displayed on pressure coordinates) for the time period covered by MIPAS Envisat measurements, with very few negative and large areas of positive trends at mid-latitudes for both hemispheres around and above 30 km (~ 10 hPa). Negative trends are found in the tropics around 25 and 35 km (~ 25 and 5 hPa), while an area of positive trends is located right above the tropical tropopause. These findings are in good agreement with the recent literature. Differences of the trends compared with the recent literature could be explained by a possible shift of the subtropical mixing barriers. Results for the altitude–latitude distribution of amplitudes of the

2572

E. Eckert et al.: Drifts, trends and periodic variations in MIPAS ozone

quasi-biennial, annual and the semi-annual oscillation are overall in very good agreement with recent findings.

1 Introduction

Stratospheric ozone depletion has been an important issue for more than the past three decades. Although ozone can cause health problems when being present close to the surface in unnaturally large amounts, e.g. downstream of urban areas during warm periods, its presence is very important at higher altitudes. Most of the ozone is located in the stratosphere, where it absorbs ultraviolet light coming from the Sun. Light at these wavelengths can lead to e.g. increased risk of skin cancer; hence the careful monitoring of stratospheric ozone abundances is mandatory.

After Hartley's approximate measurements of the absorption of ozone in the ultraviolet Fabry and Buisson were the first to estimate the vertical thickness of ozone in the atmosphere (Dobson, 1968). Shortly afterwards, during the 1920s, Dobson measured column ozone at Oxford using a Féry spectrograph (Dobson, 1931; Götz et al., 1934). Subsequently further Féry spectrographs were set up at several other locations in Europe. As a second step the measurements were expanded beyond Europe during the late 1920s, including a southern hemispheric site at Christchurch, New Zealand. Over the years, many different instruments and measurement techniques were developed so that nowadays data are collected by ground-based instruments like lidars, airborne observations including instruments carried by airplanes or balloons, and spaceborne limb sounders like MIPAS (Michelson Interferometer for Passive Atmospheric Sounding) Envisat, the Microwave Limb Sounder on the Aura satellite (Aura MLS), the Optical Spectrograph and Infrared Imaging System (Odin OSIRIS) and the Atmospheric Chemistry Experiment Fourier Transform Spectrometer (ACE-FTS). Measurements from the latter satellite instruments are used in the analyses that follow.

All measurements show that the largest abundance of ozone can be found in the stratosphere, forming the ozone layer. This layer protects the Earth's flora and fauna from most of the harmful solar ultraviolet radiation. Molina and Rowland (1974) discovered that some anthropogenically produced chemicals could lead to the depletion of stratospheric ozone. The discovery of the Antarctic ozone hole by Farman et al. (1985) indicated that ozone depletion due to anthropogenic emission of e.g. chlorofluorocarbons (CFC) had the potential of a global threat. These findings led to the restriction of major ozone-depleting substances (ODSs) via the Montreal Protocol in 1987, but since most of these substances are long-lived their amounts continued to increase in the stratosphere until the mid-1990s (WMO, 2011). Consequently a negative global trend in ozone was observed for the same time period, reaching minimum total ozone val-

ues during 1996–1997. Even though a decrease of stratospheric ODS concentrations was noted from the mid-1990s on, ozone did not recover consistently. Trends after 1995 were found to be either nonexistent or slightly positive (Steinbrecht et al., 2009a; WMO, 2011).

In this paper, linear variations of ozone calculated from zonal monthly means are shown, which were derived from MIPAS Envisat IMK/IAA level-2 V5H_O3_20, V5R_O3_220 and V5R_O3_221 data. The analyses cover the altitude range from 10 to 44 km in steps of one kilometre and continue in 2 km steps up to 50 km. For some cases the analyses were additionally performed on the pressure grid used for Aura MLS and cover a range from 215.44 to 0.68 hPa. Beyond this, altitude–latitude distributions of the amplitude of periodic variations with period lengths of 6 (semi-annual oscillation – SAO) and 12 (annual oscillation – AO) months were assessed, as well as the quasi-biennial oscillation (QBO). These results were obtained using MIPAS data from July 2002 to April 2012. MIPAS measurement data exhibit a gap between March 2004 and January 2005, during which no data could be collected by the instrument due to technical problems. This also led to an altered operation mode for the second time period, with different spectral and horizontal resolution and tangent height pattern.

In order to support the trend analyses, drifts are estimated via comparison with several coincident measurements of spaceborne instruments, namely ACE-FTS, Aura MLS and Odin OSIRIS. We also calculated drifts by comparing MIPAS profiles to coincident measurements of the Network for the Detection of Atmospheric Composition Change (NDACC) lidars at Hohenpeissenberg, Mauna Loa, Lauder, Observatoire Haute Provence and Table Mountain. Our conclusions from the drift analyses were used to correct trends derived from the MIPAS data. The instruments used for this study are introduced and characterized in Sect. 2, followed by a detailed description of the method of trend estimation and additional scientific tools in Sect. 3. While the results are presented in Sect. 4, we provide a closing overview in the conclusions (Sect. 5), putting the findings of this work into an overall context and point out possible future work.

2 Instruments

2.1 MIPAS Envisat

MIPAS was one of the core payload atmospheric chemistry instruments aboard the European satellite Envisat (Fischer et al., 2008). The satellite was launched into a Sun-synchronous polar orbit at approximately 800 km, with 98.55° inclination, by the European Space Agency (ESA) in March 2002. The instrument setup allows global coverage from pole to pole. Envisat crossed the Equator at approximately 10:00 and 22:00 local time and performed about 14.4 orbits per day. However it ceased sending data on 8 April

E. Eckert et al.: Drifts, trends and periodic variations in MIPAS ozone

2573

Table 1. Overview of the instruments, important characteristics and time spans used for the drift analyses.

Instrument	Version	Vertical resolution	Period used for analyses
MIPAS Envisat	V5H_O3_20	~2–6 km	07/2002–03/2004
MIPAS Envisat	V5R_O3_220 & V5R_O3_221	~2.5–5 km; largest values around ~30–35 km	01/2005–04/2012
ACE-FTS	v3.0	~3–4 km	01/2005–09/2009
Aura MLS	v2.2	~2.5–3.0 km	01/2005–04/2012
Lidar: Hohenpeissenberg	V5.60 MOHP3	~1–2 km below 30 km; degrading to ~9 km above 40 km	07/2002–03/2012
Lidar: Lauder	v8.2	~1.8–3 km up to 30 km; degrading above	07/2002–06/2011
Lidar: Mauna Loa	v05.15	~2–3 km up to 40 km; degrading above	07/2002–03/2012
Lidar: Observatoire Haute Provence	v4	~0.6–2.4 km up to 30 km; degrading to ~6.5 km at 45 km	07/2002–01/2012
Lidar: Table Mountain	LidAna v05.4x to v6.x	~2–4 km up to 30 km; degrading above	07/2002–01/2012
Odin OSIRIS	v5.07	~2.2 km up to about 40 km; degrading above	07/2002–04/2012

2012 and was declared dead shortly afterwards; all in all, MIPAS provided data for a period of about 10 yr.

MIPAS is a Fourier transform limb emission spectrometer which measures the signatures of various trace gases within the spectral range of 4.15 to 14.6 μm . Originally, MIPAS measured one limb scan consisting of 17 tangent altitudes from 6 to 68 km and about 75 profiles per orbit in its nominal mode, which results in approximately 1000 profiles per day. The spectral resolution of MIPAS during this first time period (2002–2004) was 0.025 cm^{-1} unapodized (0.035 cm^{-1} apodized). This period is referred to as the high spectral resolution period. The data version used in this study is associated with this time period is the V5H_O3_20 data set. The retrieval grid width in all MIPAS data versions is 1 km for altitudes below 44 km and 2 km above, independent of the tangent altitudes of the measurements. The vertical resolution of the V5H_O3_20 ozone data product varies between 2 and 6 km. For the second time period we chose to use the combination of the V5R_O3_220 (1541474 profiles) and V5R_O3_221 (331287 profiles) MIPAS ozone product, both of which were derived from version 5.0 and later level-1b data. The V5R_O3_221 data ozone set consistently extends the V5R_O3_220 product after April 2011. These versions of the ozone product are closely linked with version V4O_O3_202 (deduced from version 4.67 level-1b data) as characterized by von Clarmann et al. (2009) and validated by Stiller et al. (2012). The thorough validation of the V5R_O3_220 (and V5R_O3_221) is currently in progress (Laeng et al. (2012) and paper submitted). Differences in the setup from version V4O_O3_202 to both V5R_O3_220 versions are major changes in level-1b data used (calibrated spectra) and the preceding temperature retrieval of which the results are used for the subsequent ozone retrieval. An empirical continuum emission signal was retrieved up to altitudes of 50 km instead of only 33 km in the preceding version. From version V5R_O3_220 to V5R_O3_221 only minor technical changes of the retrieval setup were applied which do not appreciably change the results for ozone in the investigated altitude range. The vertical resolution of the version V5R_O3_220 and V5R_O3_221 data product ranges from about 2.5 to 5 km, exhibiting the worst vertical resolu-

tion around 30 to 35 km. Recent investigations of this feature showed that the vertical resolution in this altitude range would be significantly improved by activating microwindows in the MIPAS AB band (1020–1170 cm^{-1}) at and above 33 km instead of 36 km and above as performed for the data set used here, at the cost of a higher positive bias, however. The combined data set of V5H_O3_20, V5R_O3_220 and V5R_O3_221 contains 2359706 ozone profiles in total.

2.2 Aura MLS

The Microwave Limb Sounder (MLS) is one amongst four instruments currently operating on the Earth Observing System (EOS) Aura satellite, which was launched into a Sun-synchronous, near-polar orbit at about 705 km by NASA on 15 July 2004. The Aura satellite is dedicated to chemical constituents of the atmosphere, while the other satellites of the EOS program, Aqua and Terra, focus on the hydrological cycle and land processes, respectively (Schoeberl et al., 2006). Aura MLS records microwave emissions in spectral regions centred at approximately 118, 190, 240 and 640 GHz and additionally 2.5 THz (Waters et al., 2006). With a vertical resolution of 2.5 to 3 km it measures atmospheric constituents in the upper troposphere, stratosphere and mesosphere, while achieving nearly pole-to-pole coverage (82° S to 82° N).

Mainly focusing on tropospheric and stratospheric processes concerning ozone chemistry, Aura MLS provides data on several atmospheric chemical species linked to ozone destruction, including various reservoir gases. With approximately 240 profiles per orbit (nearly 3500 profiles per day) Aura MLS provides a large number of profiles (day and night) and is thus a very good candidate for drift estimation by means of coinciding profiles. In this study the ozone version v2.2 of the Aura MLS data was used. The standard ozone product, which is used in this study, is derived from the 240 GHz region (main line at 235.7 GHz and lines at 243.45 and 244.16 GHz; Froidevaux et al., 2008). This Aura MLS data set is recommended for pressure levels between 215 and 0.02 hPa, after necessary data screening is applied (Froidevaux et al., 2008). Since the application of the MIPAS averaging kernel, as described in Sect. 3.3.2, was originally

performed on the MIPAS altitude grid, we interpolated the Aura MLS data from its pressure grid to an adequate altitude grid using coincident ECMWF temperatures and pressure to calculate pressure–altitude relations. However, using this approach is prone to the risk that the temperatures used for conversion (here from ECMWF analysis) map onto the ozone drift. In order to avoid the related artefact, the drift analysis has in addition also been performed on the Aura MLS pressure grid as explained in Sect. 3.3.3.

2.3 ACE-FTS

The Fourier transform spectrometer (FTS) of the Atmospheric Chemistry Experiment (ACE) is one of the two instruments aboard the Canadian satellite SCISAT-1. It was launched into a circular low Earth orbit at approximately 650 km from an airplane on 12 August 2003, and the routine measurements were started in February 2004. ACE typically measures in the altitude range from 10 to 100 km, depending on the measurement and the strength of the spectral lines, although the high-resolution (0.02 cm^{-1}) infrared FTS can generally start at the cloud tops and reach up to about 150 km. The vertical resolution of the FTS is approximately 3–4 km (Dupuy et al., 2009). While using a similar wavelength region (2.2 to $13.3\ \mu\text{m}$) as MIPAS, ACE-FTS measures in solar occultation. For this study, version v3.0 of the ACE-FTS ozone data was used for comparison. Due to the fact that some of the profiles seemed to show very unrealistic values, the following rejection criteria were applied: first, the criteria provided at the data issue page (https://database.scisat.ca/validation/data_issues_table.php), where certain peculiarities are reported, were used to sort out some profiles. In addition, we used only data points of each profile for which all of the following criteria were fulfilled:

- The data value has to be larger than the error.
- The error has to be larger than 1 % of the data value.

Since this approach still left some suspicious profiles in the data sets, we also removed those for which the ozone mixing ratios were outside of the range –10 to 20 ppmv. This range was suggested by Dupuy et al. (2009) during the validation of the ACE-FTS ozone product. The profiles were rejected if their values were outside these ranges at any point, which was valid according to the other filter criteria.

2.4 Odin OSIRIS

The Optical Spectrograph and InfraRed Imaging System (OSIRIS) is a Canadian instrument aboard the Swedish satellite Odin and has been collecting data since February 2001 (Degenstein et al., 2009). It orbits Sun-synchronously at about 600 km with northward Equator-crossing time at 18:00 local time and 98° inclination. Since OSIRIS is an instrument which measures scattered sunlight, measurements are only

possible during June, July, August and September (November, December, January and February) in the Northern Hemisphere (Southern Hemisphere) because sunlight is imperative for the instrument's observations. While the optical spectrograph (OS) records spectra of limb-scattered sunlight from 280 to 800 nm and has a spectral resolution of about 1 nm, the second part of the instrument, the infrared imager (IRI), measures scattered sunlight as well as airglow emissions (Llewellyn et al., 2004). The altitudinal coverage of OSIRIS is generally from 10 to 100 km and scans from 7 to 70 km tangent altitude in normal operation mode (Degenstein et al., 2009). In this study we use version v5.07 of the OSIRIS ozone data retrieved by means of the SaskMART multiplicative algebraic reconstruction technique. The retrieved profiles have a vertical resolution of approximately 2.2 up to 40 km, degrading slightly above.

2.5 Lidars

All lidar data used in this study were provided by the NDACC community (www.ndacc.org; see also Steinbrecht et al., 2009a, b; McDermid et al., 1990, 1995; Brinksma et al., 2000). These lidars (at Hohenpeissenberg, Lauder, Mauna Loa, Haute Provence and Table Mountain) use the differential absorption lidar (DIAL) Technique (Megie et al., 1977) to derive stratospheric ozone profiles from atmospheric measurements. Light at two different wavelengths is emitted. One wavelength is 308 nm for all lidars, while the reference wavelength is 353 nm at Hohenpeissenberg and Lauder and 355 nm for the other lidars during the investigated time period. Lidar measurements become less reliable with altitude, which is reflected in deteriorating precision from approximately 1 % up to 30 km through about 2–5 % around 40 km to up to 25 % at 50 km (Nair et al., 2012). Most lidars have vertical resolutions of around 2 km for altitudes below 30 km, which then increases rapidly above. More detailed information about the lidar characteristics and the measurement technique can be found in Nair et al. (2012); Megie et al. (1977). Since the recorded data are provided in terms of number density, ECMWF data were used for conversion to volume mixing ratio.

3 Methods

3.1 Method of trend estimation

The multilinear parametric trend model used in this study consists of a constant and a linear term, annual and semi-annual oscillation terms, as well as several harmonic overtones. Others, like Kirgis et al. (2013), fit the Ozone Depleting Gas Index (ODGI) instead of a linear term and find that the value of total explained variance is increased compared to using a linear term. However, for the time series used here (2002–2012) the ODGI does not differ noticeably from the linear term, which justifies using a simple linear term here.

E. Eckert et al.: Drifts, trends and periodic variations in MIPAS ozone

2575

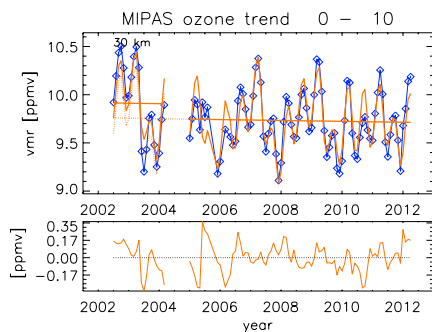


Fig. 1. Trend fit for 0 to 10° N, showing the monthly mean data (blue diamonds), the calculated fit and the related trend (orange lines) for MIPAS ozone measurements at 30 km. The dotted orange line represents the linear component of the regression function for times affected by bias correction. The bottom panel shows the residual of the fit and the data points.

The QBO was implemented using the Singapore winds at 30 and 50 hPa as a proxy, which are approximately phase-shifted by a quarter period and can thus be treated equivalently to sine and cosine functions of the same period length. Equation (1) is the basic function applied here, similar to Stiller et al. (2012).

$$\hat{y}(x) = a + bx + c_1 \text{qbo}_1 + d_1 \text{qbo}_2 + \sum_{n=2}^m \left(c_n \sin \frac{2\pi x}{l_n} + d_n \cos \frac{2\pi x}{l_n} \right) \quad (1)$$

Here x is the time, whereas qbo_1 and qbo_2 refer to the Singapore winds at 30 and 50 hPa. The sum comprises 8 sine and cosine functions with the period length l_n , including the annual and semi-annual oscillation as well as 6 overtones with period lengths of 3, 4, 8, 9, 18 and 24 months. a and b represent the constant term and the slope of the fit, respectively. c_n and d_n are parameters which have to be found to fit amplitude and phase of the oscillations. The method is based on a concept introduced by von Clarmann et al. (2010) in order to estimate trends of combined data sets which have a potential bias. By using the full covariance matrix when minimizing the cost function (cf. von Clarmann et al., 2010) an arbitrary bias can be accounted for during the regression process and thus makes the model resistant to such biases. The scheme is equivalent to fitting the trends in each data subset individually and ignoring any jump between the subsets. The final trend then corresponds to a weighted mean of the trends of each subset. Coefficients associated with periodic and quasi-periodic variations refer to the entire data set.

In order to account for the autocorrelative nature of the atmosphere and to get realistic error estimates, the autocorrelations among the data points were considered in the co-

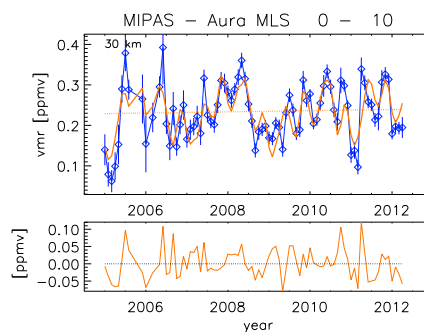


Fig. 2. Trend fit for 0 to 10° N, showing the monthly mean data (blue diamonds), the calculated fit and the related trend (orange lines) for the differences in the ozone measurements of MIPAS and Aura MLS at 30 km. The first subset of data is missing in the plot compared to Fig. 1 because Aura MLS and MIPAS have no overlap time within the first period of the MIPAS mission (cf. Table 1). The bottom panel shows the residual of the fit and the data points.

variance matrix of the data set, and a model error component was assessed iteratively and added to the covariance matrix such that χ^2 of the fit approaches unity. The parameters a , b , c_n and d_n of Eq. (1) were fitted to zonal monthly means of 10° latitude bands of the MIPAS ozone time series covering 1 July 2002 to 8 April 2012 to assess the linear variation during that period. An example of the fit is shown in Fig. 1, showing the ozone monthly means as well as the fit and linear variation at 0 to 10° N and 30 km altitude. The bias between the two data blocks is quite obvious and it is reasonably accounted for during the fit process. A semi-annual oscillation and a QBO signal can also be identified in the data, which are satisfactorily reproduced by the fit.

Before analysing derived trends, a potential drift in MIPAS ozone data must be identified and accounted for. To estimate the drifts against other instruments, the difference of MIPAS minus the reference instrument was calculated for each data point and the related time series were fitted by the same method as just introduced. The linear term of the variation of these differences is the drift.

3.2 Drifts

In our definition, drifts are trend-like artificial linear variations of a signal due to less-than-perfect instrument stability. In order to assess a clean natural trend from the measurements, possible drifts are analysed in a preceding step. This is realized by calculating the difference of the MIPAS measurement and that of another instrument at every valid altitude grid point of each coinciding profile pair, establishing monthly means of these differences and applying the trend method as introduced in Sect. 3.1. Figure 2 shows an example

2576

E. Eckert et al.: Drifts, trends and periodic variations in MIPAS ozone

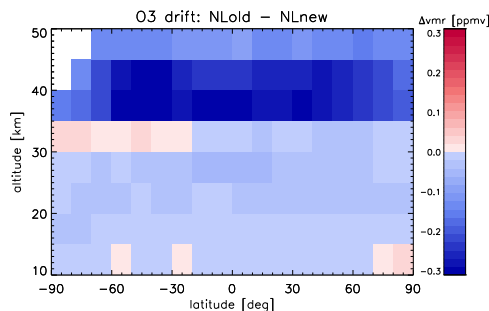


Fig. 3. Altitude–latitude cross-section of absolute drifts resulting from nonlinearity correction. On the basis of a limited number of spectra, ozone analyses based on spectra generated with a time-dependent nonlinearity correction are compared to those of a standard nonlinearity correction. The linear component of the temporal development is shown.

of the fit for the differences of Aura MLS and MIPAS. As can be seen here, there are still some oscillations in the differences, which we first expected to cancel out. When we discovered that this assumption was not justified, we decided to use the full multilinear parametric regression model for drift estimation as well, including the whole set of oscillations, instead of just using a linear and a constant term. This is to account for possible dependence of the differences on the atmospheric state.

To improve comparability with e.g. Nair et al. (2012), we also assessed relative drifts by using the relative difference (vmr_{rel}) of each coinciding profile pair consistently with their paper as follows

$$\begin{aligned} \text{vmr}_{\text{rel}} &= \frac{\text{vmr}_M - \text{vmr}_{\text{RF}}}{\text{vmr}_{\text{RF}}} \cdot 100\% \\ &= A \cdot 100\%. \end{aligned} \quad (2)$$

vmr_M and vmr_{RF} are the volume mixing ratios of MIPAS and the reference instrument, respectively. The respective error was estimated accounting for Gaussian error propagation and with respect to Eq. (2).

3.3 Expected MIPAS drifts

Recent studies (Kiefer et al., 2013) have raised doubts about the stability of the MIPAS instrument. During the calibration of the spectra, a correction accounting for the nonlinearity of the detector is performed. The coefficients of the nonlinearity correction function were determined prior to the launch of Envisat, but it is believed that ageing makes the detectors more linear and the preflight coefficients might no longer be valid for later MIPAS measurements. The drift possibly introduced by this detector ageing effect is shown in Fig. 3.

The expected artificial drift of ozone due to detector ageing has been the subject of a sensitivity study and is largest above 35 to 40 km. Preliminary results show drifts down to maximum values of $-0.3 \text{ ppmv decade}^{-1}$ for ozone. The drifts are far smaller than $-0.3 \text{ ppmv decade}^{-1}$ at lower altitudes and seem to become slightly more negative with altitude. At shorter wavelengths, a larger ageing effect is predicted. This explains the sudden increase of the effect above 35 km. In the data version used, ozone lines of the MIPAS AB band ($1120\text{--}1170 \text{ cm}^{-1}$) were used in addition to the A band ($685\text{--}970 \text{ cm}^{-1}$) above 33 km, while below only lines from the A band were used.

3.3.1 Coincidence criteria

To account for varying data coverage, two different coincidence criteria were used, depending on the availability of data from the respective instrument. For instruments with dense data coverage, measurements which are closer than 250 km radial spatial distance and 6 h temporal difference to the MIPAS measurements are taken into account. Weaker criteria of 1000 km and 24 h were applied to instruments with sparser coverage and/or fewer measurements to still obtain a sufficiently large number of measurements to compare in the drift analyses. In both cases the distance is calculated relative to the nominal geolocation of the MIPAS profile, which is the tangent point of the 30 km tangent altitude limb view. Table 2 summarizes these criteria for the different instruments and lists the total number of profiles which matched these criteria. For some instruments which originally cover the whole MIPAS mission period we additionally performed the analysis for a reduced time series, meaning that we only took coincidences of the second MIPAS period into account. This was done in order to assure that the results exhibit only minor changes when the first MIPAS period is omitted due to lack of data, e.g. for instruments like Aura MLS or ACE-FTS.

In cases with more than one measurement fulfilling the coincidence criteria, only the closest profile was chosen. This was done by normalizing the distance and time criteria as shown in Eq. (3), such that the pair with the lowest C_{comb} value is considered to be the best coincidence.

$$C_{\text{comb}} = \left(\frac{d}{d_{\text{max}}} \right)^2 + \left(\frac{t}{t_{\text{max}}} \right)^2, \quad (3)$$

where d is the spatial distance between the two profiles, d_{max} is the maximum allowed distance, t is the time difference between the profiles and t_{max} is the maximum allowed time difference. In the case of two MIPAS profiles matching the same profile of the other instrument a selection process was undertaken such that the loss of profiles pairs was minimized and the entirety of the pairs fulfilled the criteria best.

Table 2. Summary of coincidence criteria and the total number of coinciding profiles (reduced time periods – January 2005 to April 2012 – in parenthesis) for the reference instruments with MIPAS, showing the maximal time and spatial distance allowed between the measurements.

Instrument	Time criteria [hours]	Distance criteria [km]	Number of coinciding profiles
ACE-FTS	24	1000	14 190
Aura MLS	6	250	401 251
Lidar: Hohenpeissenberg (2005–2012)	24	1000	652 (509)
Lidar: Lauder	24	1000	243
Lidar: Mauna Loa (2005–2012)	24	1000	693 (503)
Lidar: Observatoire Haute Provence	24	1000	753
Lidar: Table Mountain	24	1000	539
Odin OSIRIS (2005–2012)	6	250	109 820 (94 274)

3.3.2 Application of the MIPAS averaging kernel: on an altitude grid

In most cases the vertical resolution of the reference instrument was better than that of MIPAS in certain altitude regions. For the lidars this region is rather the lower end of the profile. Their vertical resolution is certainly not better than that of MIPAS above 40 km, but as already mentioned measurements above approximately this altitude should be treated with care. The reason for applying the MIPAS averaging kernels is primarily the vertical resolution peak around 30 to 35 km in version V5R_O3_220 and V5R_O3_221 of MIPAS data from the second time period of the MIPAS mission. In the case of ACE-FTS the worst-case assumption on the vertical resolution, based on the field of view, is about 3–4 km, which is very similar to that of MIPAS. Sensitivity studies showed that application of the MIPAS averaging kernels to ACE-FTS profiles does not exhibit any major differences compared to ACE-FTS profiles to which no averaging kernels were applied. Thus, for all instruments except ACE-FTS the MIPAS averaging kernel was applied according to Eq. (4).

$$\tilde{x}_{fM} = \mathbf{A}_{MIPAS} \mathbf{V} x_f + (\mathbf{I} - \mathbf{A}_{MIPAS}) x_a \quad (4)$$

In this equation, x_f is the initially finer profile (e.g. that of Aura MLS). \tilde{x}_{fM} is that profile transferred to the MIPAS grid under consideration of the MIPAS averaging kernel \mathbf{A}_{MIPAS} . \mathbf{I} is unity and x_a is the a priori profile used for MIPAS. \mathbf{V} is a transformation matrix relating the fine profile x_f to the coarser grid. It is inferred as follows (cf., e.g. Rodgers, 2000): let \mathbf{W} be an interpolation matrix which transforms a profile originally sampled on a coarse grid onto a finer grid. The transformation from the fine to the coarse grid then uses the transformation matrix $\mathbf{V} = (\mathbf{W}^T \mathbf{W})^{-1} \mathbf{W}^T$.

In the case of ozone a zero a priori profile is used for the MIPAS retrievals, simplifying Eq. (4) to

$$\tilde{x}_{fM, O_3} = \mathbf{A}_{MIPAS, O_3} \mathbf{V} x_{f, O_3}. \quad (5)$$

More detailed information on the methodology may be found in Stiller et al. (2012).

3.3.3 Application of the MIPAS averaging kernel: on a pressure grid

As mentioned above, the conversion of ozone profiles from a pressure grid to an altitude grid relies on ECMWF temperatures which might have a drift in themselves. This would cause an artificial drift in ozone at a given altitude. In order to avoid related problems, for instruments whose native altitude coordinate is pressure (MLS, ACE-FTS), the drift analysis has also been performed on pressure coordinates. Even for MIPAS, whose profiles are usually reported on an altitude grid, the representation on a pressure grid is more robust, since the MIPAS altitudes are based on the hydrostatic approximation involving one ECMWF data triple (altitude, pressure, temperature) per profile. While the altitude resolution of MIPAS and ACE-FTS ozone profiles is comparable over a wide altitude range, a direct comparison is justified (cf. Sect. 3.3.2). Aura MLS ozone profiles, however, have a finer altitude resolution than those of MIPAS, and thus have to be smoothed using the MIPAS averaging kernels. These are provided on an altitude grid; but for all MIPAS altitude grid points, pressure values are also available. We use the following procedure: MLS ozone profiles are interpolated onto the MIPAS pressure grid, for which corresponding altitudes are available. There the MIPAS averaging kernel is applied. The result is transformed back to the Aura MLS pressure grid. This step is necessary because the drift analysis is only meaningful on a fixed grid while the MIPAS pressure grid (contrarily to its altitude grid) varies from profile to profile. For this purpose we need both transformation matrices.

Similar to the previous section, transformation matrices are needed, where the subscript p indicates that the matrices refer to the pressure grid. \mathbf{W}_p performs the transformation from the Aura MLS pressure grid to the MIPAS pressure grid, while the reverse transformation is performed using the matrix $\mathbf{V}_p = (\mathbf{W}_p^T \mathbf{W}_p)^{-1} \mathbf{W}_p^T$. The latter transforms the finer sampled MIPAS profile to the coarser Aura MLS grid. The MIPAS profile can be represented as (cf. Rodgers, 2000)

$$\tilde{x}_{MIPAS} = \mathbf{A}_{MIPAS} x_{true} + \varepsilon_{MIPAS}. \quad (6)$$

2578

E. Eckert et al.: Drifts, trends and periodic variations in MIPAS ozone

where \mathbf{x}_{true} is the true state of the atmosphere and $\varepsilon_{\text{MIPAS}}$ is the measurement error. Using the transformations introduced above, the MIPAS profile on the Aura MLS pressure grid can be written as

$$\mathbf{V}_p \hat{\mathbf{x}}_{\text{MIPAS}} = \mathbf{V}_p \mathbf{A}_{\text{MIPAS}} \mathbf{x}_{\text{true}} + \mathbf{V}_p \varepsilon_{\text{MIPAS}}. \quad (7)$$

We use Aura MLS as a reference instrument and replace \mathbf{x}_{true} with the Aura MLS profile transformed to the MIPAS grid:

$$\mathbf{x}_{\text{MLS}_{\text{MIPAS}}} = \mathbf{W}_p \mathbf{x}_{\text{MLS}}. \quad (8)$$

Since MLS is not an ideal instrument either, we replace $\varepsilon_{\text{MIPAS}}$ by the combined error of the two instruments, which leads to

$$\mathbf{V}_p \hat{\mathbf{x}}_{\text{MIPAS}} = \mathbf{V}_p \mathbf{A}_{\text{MIPAS}} \mathbf{W}_p \mathbf{x}_{\text{MLS}} + \mathbf{V}_p \varepsilon_{\text{combined}}. \quad (9)$$

Solving this equation for $\mathbf{V}_p \varepsilon_{\text{combined}}$ gives

$$\mathbf{V}_p \varepsilon_{\text{combined}} = \mathbf{V}_p \hat{\mathbf{x}}_{\text{MIPAS}} - \mathbf{V}_p \mathbf{A}_{\text{MIPAS}} \mathbf{W}_p \hat{\mathbf{x}}_{\text{MLS}}, \quad (10)$$

where $\mathbf{V}_p \varepsilon_{\text{combined}}$ is the difference profile of the MIPAS and the Aura MLS ozone profile represented on the Aura MLS pressure grid. The linear component of temporal regression of these differences $\frac{d\mathbf{V}_p \varepsilon_{\text{combined}}}{dt}$ is what we call a drift.

3.4 Drift-corrected trend

Since we were interested in how the drift would influence the MIPAS ozone trend, we calculated a so-called drift-corrected trend $b_{\text{corrected}}$ (Eq. 11).

$$b_{\text{corrected}} = b_{\text{MIPAS}} - b_{\text{Drift, MIPAS vs REF}} \quad (11)$$

For this purpose we used the drift estimates and calculated the difference of the MIPAS trend b_{MIPAS} and the drift versus the reference instrument $b_{\text{Drift, MIPAS vs REF}}$ for every altitude–latitude grid point. The associated error was simply calculated as the combined error of the MIPAS trend and the drift established in comparison to the respective instrument, both of which were assessed within the respective regression process. Here we assume the difference to be caused by a MIPAS drift to a large extent, not by a possible drift of the other instrument for reasons discussed in Sect. 3.3. The resulting errors can be considered as a conservative estimate, because we did not account for possible correlations between the single instrument errors. If these errors were treated as positively correlated to some extent, the resulting error would decrease. Not expecting any correlation is justified here for the following reasoning: we assume that natural variability should mostly be cancelled out by calculating differences, which is the main contributor to the basic errors. Even though this is not entirely true, as shown in Sect. 3.2, this approximation is valid to a good extent, since the oscillations in the differences are considerably smaller than those in the time series of the measurements themselves. In addition, the data sets used for drift estimation are at least six times smaller than the data set used for trend estimation (MIPAS), because only coinciding measurements are considered.

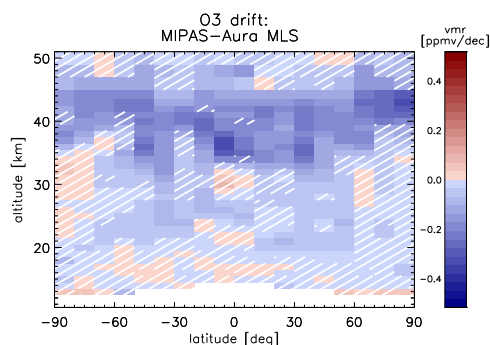


Fig. 4. Altitude–latitude cross-section of absolute drifts of MIPAS vs. Aura MLS ozone measurements. Hatched areas mean that the significance is less than 2 sigma.

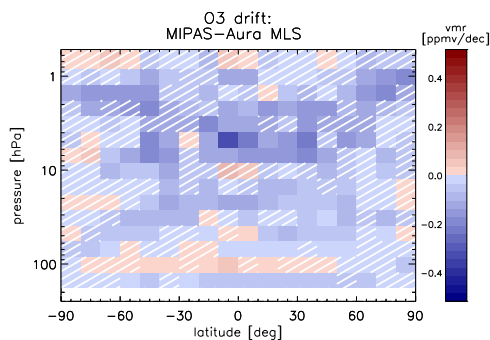


Fig. 5. Same as in Fig. 4 but represented on the Aura MLS pressure grid.

4 Results

4.1 Drifts

For the set of comparison instruments chosen, the resulting drifts cover a wide range of values. Comparisons with instruments which offer global or near-global coverage are displayed as altitude–latitude cross-sections of the linear term of the drift analysis. In these plots, hatched areas denote that the significance of the estimated drifts is less than 2 sigma. We have performed MIPAS drift estimations versus Aura MLS, ACE-FTS and Odin OSIRIS (Figs. 4–8). Estimates versus lidars are displayed in drift panels showing the linear term of the drift analysis as well as a 2-sigma uncertainty at each altitude grid point. In the following we will focus on discussing only drifts with 2-sigma significance or better. Blue colors in Figs. 4–8 indicate that the linear variation for the MIPAS data decreases more strongly than that of

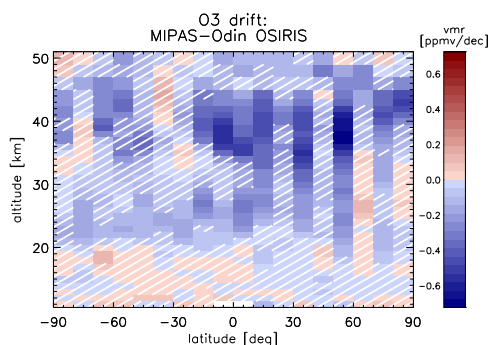


Fig. 6. Same as in Fig. 4 but for comparison versus Odin OSIRIS.

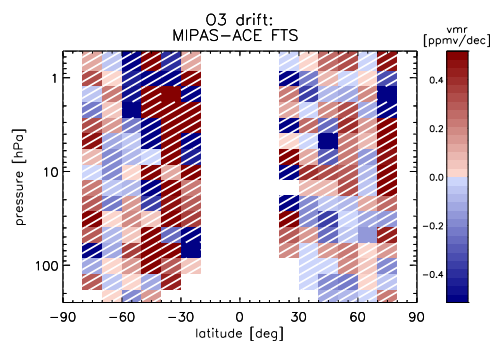


Fig. 8. Same as in Fig. 7 but represented on the Aura MLS pressure grid.

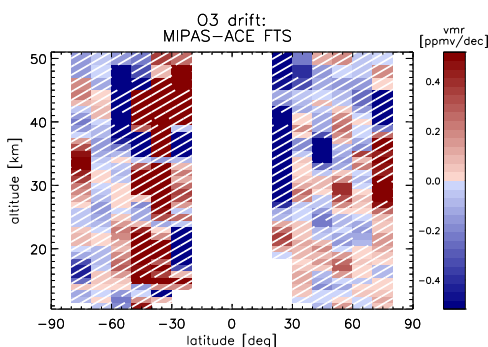


Fig. 7. Same as in Fig. 4 but for comparison versus ACE-FTS.

the reference instrument, while red colors denote a stronger increasing linear variation for the MIPAS data.

For the comparison versus Aura MLS the drift estimations on the altitude (Fig. 4) and on the pressure (Fig. 5) grid show very similar results. The distribution as well as the magnitude of the drifts are very alike. This means that the influence of a possible drift in ECMWF temperatures on the ozone drifts is quite small. The results exhibit only negative drifts, except from very few values at lower latitudes. The negative drifts range from near zero to approximately $-0.33 \text{ ppmv decade}^{-1}$ on the altitude grid and $-0.31 \text{ ppmv decade}^{-1}$ on the pressure grid and seem to become slightly more negative with altitude up to $\sim 40 \text{ km}$ ($\sim 3 \text{ hPa}$). For Odin OSIRIS (Fig. 6) we find a similar pattern, but the absolute values range down to about $-0.55 \text{ ppmv decade}^{-1}$ at several grid points and even reach values around $-0.7 \text{ ppmv decade}^{-1}$ in a few cases. The plots of ACE-FTS (Figs. 7–8) look a bit different, mainly because we found very few significant drifts overall. This is presumably due to the fact that we find very few months (around

35 at the best) for which coincident measurements of MIPAS with ACE-FTS exist. Thus the trend estimation is based on far fewer monthly data points than for example the trend estimation versus the lidars (around 55 at the worst – e.g. for Lauder – up to more than 90 for other lidars), although their total number of measurements is a lot smaller than that of ACE-FTS. This might also explain the patchiness of the drifts estimated in the comparison with ACE-FTS. In the Northern Hemisphere the drifts are much smaller than for most of the Southern Hemisphere. Here the largest numbers of monthly data point occur, which allows a better fit. The large white area in the tropics, where no drifts could be calculated, results from ACE-FTS focusing on higher latitudes. Due to this, there are simply not enough months during which ACE-FTS measured at low latitudes, resulting in under-determination of the system of the multilinear parametric trend model. The remaining drifts do not seem to have a positive or negative majority in sign.

Aura MLS and Odin OSIRIS do not cover the same time period. In order to assess if including the first measurement period of MIPAS makes a difference, we also analysed the drifts of MIPAS versus Odin OSIRIS only for the low-resolution period of MIPAS (Fig. A2). It is obvious from these plots that differences compared to the drift analyses for the combined high and low spectral resolution time period of MIPAS are negligible.

Considering the lidars (Fig. 9) we assessed insignificant or negative drifts in most cases (Hohenpeissenberg, Table Mountain, Mauna Loa and Lauder). Only the comparison of MIPAS versus the lidar at Haute Provence shows positive drifts above $\sim 25 \text{ km}$, which increase with altitude and even exceed $1.0 \text{ ppmv decade}^{-1}$ around 40 km . While the calculated drifts for the comparison of MIPAS with Mauna Loa and Lauder lidars are insignificant except for very few cases, we found significant negative drifts versus the lidar measurements at Hohenpeissenberg and Table Mountain above

2580

E. Eckert et al.: Drifts, trends and periodic variations in MIPAS ozone

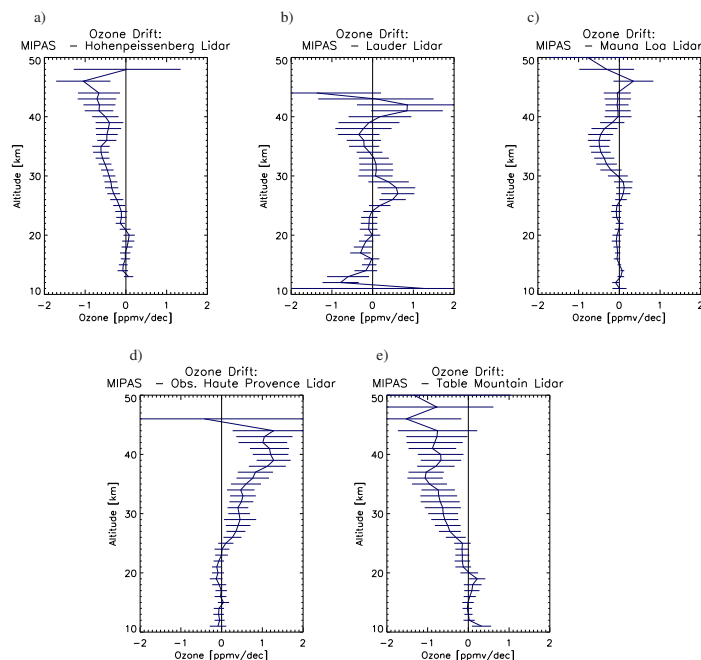


Fig. 9. Absolute drifts of MIPAS vs. (a) Hohenpeissenberg, (b) Louder, (c) Mauna Loa, (d) Observatoire Haute Provence and (e) Table Mountain lidar ozone measurements. The error bars are the 2-sigma uncertainties of the estimated drifts.

~ 20 km. As already observed for the analyses for MIPAS versus Aura MLS and Odin OSIRIS, these drifts seem to increase with altitude; but since the lidar data are not very reliable above 40 km, it is difficult to verify maximum drift values at and above 40 km, which are apparently present in the satellite–satellite comparisons. In order to facilitate comparison with recent research (Nair et al., 2012, p. 1310) we also calculated the relative drifts of MIPAS versus these lidars as described in Sect. 3.2 of this paper. The results are shown in Fig. A1. We find a striking resemblance with the findings of the aforementioned authors' comparison of Aura MLS with the lidars. They also find mainly insignificant drifts for comparisons of Aura MLS with the lidar measurements at Mauna Loa and Louder. Drifts versus lidar measurements at Hohenpeissenberg and Table Mountain are predominantly negative above ~ 20 km and increase with altitude, while positive drifts dominate the results found for comparisons with measurements at Haute Provence. Quantitatively our results are also in very good agreement with those which Nair et al. (2012) found for Aura MLS versus the lidars. Negative drifts below 40 km for MIPAS versus Hohenpeissenberg and Table Mountain measurements of down to $-8.2\% \text{ decade}^{-1}$ and $-12.8\% \text{ decade}^{-1}$ correspond to

approximately $-1.0\% \text{ yr}^{-1}$ and $-1.5\% \text{ yr}^{-1}$ for Aura MLS from Nair et al. (2012), respectively. For lidar measurements at Haute Provence positive MIPAS drifts assessed in our study range up to $10\% \text{ decade}^{-1}$ below ~ 35 km and increase above, exceeding $15\% \text{ decade}^{-1}$ close to 40 km, while in the comparison of Aura MLS versus the same lidar measurements Nair et al. (2012) find values smaller than $1.0\% \text{ yr}^{-1}$ up to about 39 km and values close to $1.5\% \text{ yr}^{-1}$ above. This indicates that the drifts are probably (at least in part) related to the lidar instruments and not the satellite instruments, e.g. Aura MLS.

The most likely explanation for the drifts of MIPAS versus the other instruments is the ageing of the MIPAS detectors, which is not considered in the nonlinearity correction of the spectra used for the MIPAS ozone retrievals under investigation. The large number of coincident measurements available for the drift estimation between MIPAS and MLS implies that these drift estimates are the most significant ones, and in tendency these are confirmed by most of the other instruments under consideration. The good agreement between the drifts established from the comparison of MIPAS versus Aura MLS and the theoretically predicted drifts of MIPAS due to detector nonlinearity suggest that it is most likely that

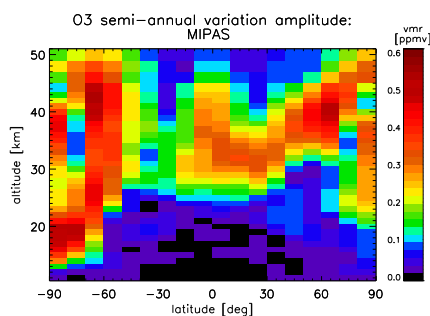


Fig. 10. Altitude–latitude cross-section of the amplitudes in ppmv of the semi-annual oscillation (6-month periodic variation) derived from the MIPAS time series.

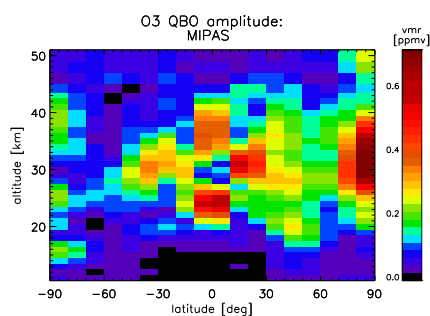


Fig. 11. Same as in Fig. 10 but for the quasi-biennial oscillation (QBO).

the drifts are for the most part originated in MIPAS, not Aura MLS. In addition there has been no indication of a possible drift in the Aura MLS ozone data so far (Hubert et al., 2012; Hubert et al., 2014). For these reasons, we believe that the assumption of an artificial drift of the order of 0 to -0.3 ppmv decade $^{-1}$, depending on altitude, is well justified for MIPAS ozone.

4.2 Amplitudes of the QBO, annual and semi-annual oscillation

Among other quantities like the drifts and trends which were assessed in this work, we took a closer look at the altitude–latitude distribution of the amplitudes of the quasi-biennial (QBO) and semi-annual oscillation (SAO) as well as of the seasonal variation of the MIPAS ozone data. These quantities were also fitted during the trend estimation process.

The amplitude of the SAO (Fig. 10) shows approximately hemispherically symmetric distributions. We find an amplitude maximum of the ozone SAO signal which is centred

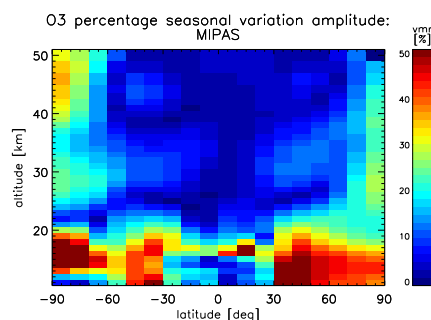


Fig. 12. Percentage amplitude of the seasonal variation of the MIPAS ozone time series (12-month periodic variation).

slightly above 30 km and exhibits maximum amplitudes of 0.5 ppmv. Beyond tropical latitudes the amplitude decreases rapidly to near-zero values, except for polar regions. These findings agree very well with the results of Huang et al. (2008), who analysed QBO and SAO ozone signals based on the Sounding of the Atmosphere using Broadband Emission Radiometry (SABER) satellite measurements for 2002 through 2005 from 20 to 100 km and for latitudes within 48° north and south. They found good agreement with ozone data of the Microwave Limb Sounder on the Upper Atmosphere Research Satellite (UARS MLS) and assess an amplitude maximum of ~ 0.5 ppmv between 30 and 35 km for ozone. This is a result remarkably similar to ours.

The amplitude of the ozone QBO signal A_{QBO} is calculated as in Eq. (12) (cf. Eq. 1).

$$A_{\text{QBO}} = \frac{d_1}{\sin\left(\arctan\left(\frac{d_1}{c_1}\right)\right)} \quad (12)$$

Its distribution, which is displayed in Fig. 11, shows a slightly more complex structure. Beside two tropical maxima around 25 km, with slightly over 0.6 ppmv, and 35 km, with approximately 0.4 ppmv, we find an additional subtropical maximum slightly above 30 km in each hemisphere. Of the latter two areas, the Northern Hemisphere one shows larger amplitudes with values of nearly 0.6 ppmv, while the Southern Hemisphere area is spatially larger but exhibits smaller maximum values of more than 0.3 ppmv for several grid points but none reaching 0.4 ppmv.

The location of these maxima in the QBO ozone amplitude agrees very well with previous findings of e.g. Zawodny and McCormick (1991), who find tropical maxima in SAGE II data located between 20–27 km and 30–38 km; Randel and Wu (1996), who report extra-tropical maxima located close to 30 km in latitude ranges of 10–60° also from SAGE II data; as well as Fadnavis and Beig (2009), who find tropical maxima around 22 hPa (~ 26 km) and 9 hPa (~ 32 km) at equatorial latitudes and weaker extratropical maxima. The

2582

E. Eckert et al.: Drifts, trends and periodic variations in MIPAS ozone

values of the reported maxima are larger though (about 1 ppmv (Randel et al., 1999), up to 1.4–1.6 ppmv (Fadnavis and Beig, 2009)), showing the larger values at the higher tropical maximum. MIPAS amplitudes are smaller, which might partly be due to the coarse vertical resolution especially around the upper maximum in tropical latitudes. The pattern could be understood as a periodic expansion and shrinking of the ozone maximum in the tropics with the QBO phase both in vertical and meridional direction. In this case, the amplitudes would be largest where the ozone gradient in both vertical and meridional direction is largest, which is what we observe (cf. Fig. 17, which is discussed in detail in Sect. 4.3).

We chose to show the seasonal variation in terms of relative values, because otherwise the important regions for this variation, along the tropopause, fade into the background since the absolute ozone values are much smaller in these regions than above. In the tropical tropopause layer (TTL) vertical motion has a great impact on the ozone amplitude, while at higher latitudes meridional mixing plays an important role. Around the tropical tropopause (16–18 km; $\sim 20^\circ$ S to $\sim 20^\circ$ N) an area of strong seasonal variation is visible. Most values of the absolute amplitude in this region are within ~ 0.01 and ~ 0.06 ppmv, with a few outliers reaching up to ~ 0.11 ppmv. In the extratropical upper troposphere–lower stratosphere (UTLS: 10–22 km; 40 – 60° south/north) the signal of the ozone variation is clearly visible around the tropopause and below. The values of the ozone amplitude in this region range from ~ 0.1 to ~ 0.8 ppmv in the Northern Hemisphere and from ~ 0.01 to ~ 0.6 ppmv in the Southern Hemisphere. We also see a signal in polar regions reaching up beyond 40 km with absolute values of up to 1.23 ppmv in the Northern Hemisphere. In the Southern Hemisphere around 30 km we find AO amplitudes of ~ 1.0 and ~ 1.24 ppmv between 40 and 50 km. These results were found to be in very good agreement with recent findings. Eyring et al. (2010) report amplitudes of ~ 0.05 ppmv for NIWA (National Institute of Water and Atmospheric Research) observations between 20° S and 20° N at 100 hPa (~ 16 km), while some models show amplitudes ranging up to ~ 0.1 ppmv. For the extratropical UTLS region in the Northern Hemisphere, ozone AO amplitudes of ~ 0.5 ppmv were deduced from Aura MLS and a multimodel mean at 100 hPa, while at 200 hPa (~ 12 km) ~ 0.3 ppmv were found for the ozone AO amplitude in Aura MLS and a slightly smaller amplitude of ~ 0.2 ppmv was assessed from the multimodel mean. For the Southern Hemisphere amplitudes of ~ 0.4 and ~ 0.1 ppmv were found at pressure levels of 100 and 200 hPa, respectively. These amplitudes are very similar to those we found in the MIPAS ozone data. Tegtmeier et al. (2013) report ozone AO amplitudes of ~ 0.15 ppmv for a multi-instrument mean at 80 hPa (~ 17 km) between 20° north and south for the period of 2005 to 2010. For southern mid-latitudinal regions (40 – 50° S) an amplitude of ~ 0.15 ppmv was deduced from the multi-instrument mean at

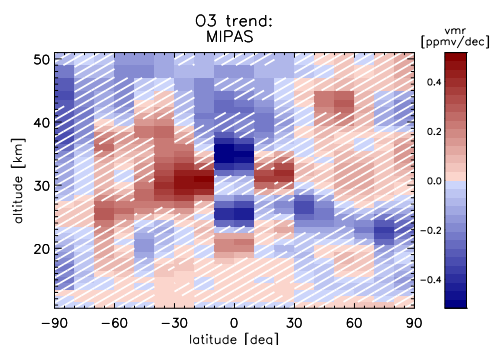


Fig. 13. Altitude–latitude cross-section of the linear variation of the MIPAS time series. As for the drifts, hatched areas indicate trends with less than 2-sigma significance level.

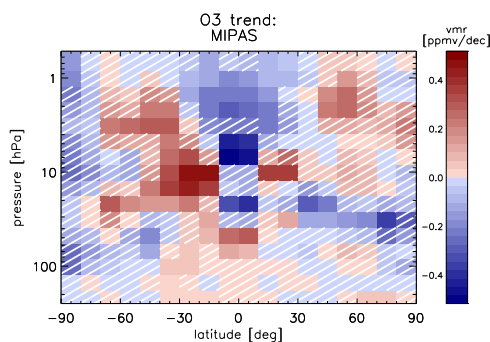


Fig. 14. Same as in Fig. 13 but represented on the Aura MLS pressure grid.

200 hPa for the same time period as mentioned above. In the Northern Hemisphere at 50 hPa the multi-instrument mean shows an amplitude of ~ 1.2 ppmv. Some of these amplitudes are larger than those deduced from MIPAS ozone data during this analyses. However, Tegtmeier et al. (2013) offer the explanation that this might be due to significantly better vertical resolution of some of the instruments used in their analysis.

4.3 Linear variations (short-term trends)

The linear term of the analysis of the MIPAS data estimated with the method described in Sect. 3.1 represents a short-term trend of the evolution of stratospheric ozone during the past 10 yr. Similar to the drifts, we will concentrate on 2-sigma significant trends throughout the following discussion. As can be seen in Fig. 13, this excludes most of the results beyond 60° north and south, where natural variability is large and thus the simple multilinear parametric trend

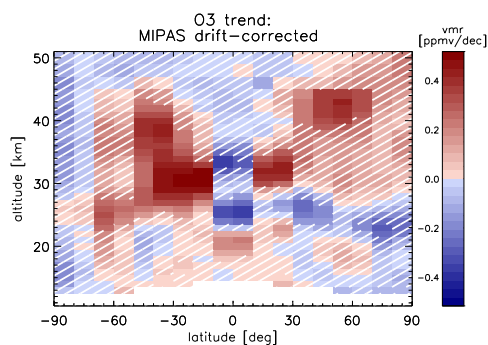


Fig. 15. Same as in Fig. 13 but corrected by the drifts estimated in comparison with Aura MLS. Two-sigma significances are based on the combined error of the trend and the drift.

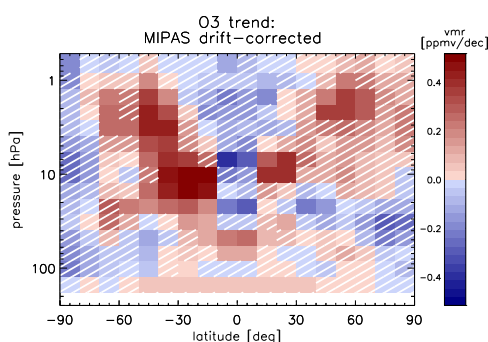


Fig. 16. Same as in Fig. 15 but displayed on the Aura MLS pressure grid.

model can presumably not fit the data properly. However, we should keep in mind that the non-random pattern of the estimated trends is a strong hint that increased significance could be achieved by a reduced spatial resolution of the analysis, both in the vertical and the latitudinal domain. Most of the trends below 20 km are non-significant, probably because ozone values are very small and MIPAS measurements are inhibited by clouds especially at low latitudes.

The results of this part of the trend analysis are displayed in Figs. 13 and 14 by means of an altitude–latitude/pressure–latitude cross-section, respectively. As already observed for the drift estimation versus Aura MLS, the features of both vertical grids look very similar. Both show a northern–southern hemispherically asymmetric pattern, and we found a larger number of 2-sigma-significant trends for Southern Hemisphere latitudes in general. In addition these significant trends exhibit predominantly positive values. A pronounced positive area ranges from the subtropics to near-polar lati-

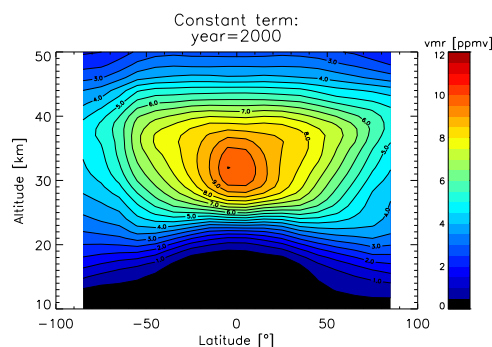


Fig. 17. Values of the MIPAS ozone regression function for the year 2000.

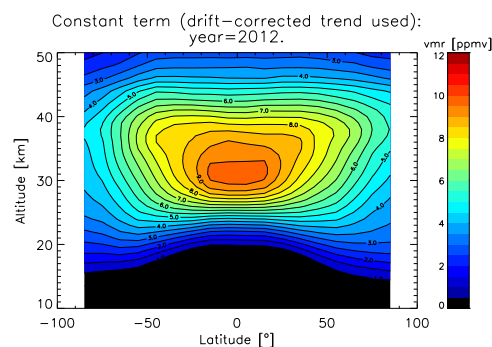


Fig. 18. Same as in Fig. 17 but for the year 2012. The drift-corrected MIPAS trends were used.

tudes centred approximately around 30 km (~ 10 hPa) and with maximum ozone trend values of $+0.48$ ppmv decade $^{-1}$ ($+0.48$ ppmv decade $^{-1}$). Apart from that we find a few smaller areas which also exhibit weaker positive trends, e.g. in the tropics around 20 km (~ 55 hPa), at northern subtropical latitudes slightly above 30 km (~ 10 hPa), at northern mid-latitudes at approximately 45 km (~ 1.5 hPa) and at subtropical latitudes below 20 km (~ 55 hPa) in both hemispheres. Negative trends are observed in the tropics in the form of a double-peak structure with maxima at approximately 25 and 35 km (~ 25 and 5 hPa) which reveal minimum trends of -0.56 ppmv decade $^{-1}$ (-52 ppmv decade $^{-1}$). Considerably smaller values appear at Northern Hemisphere mid-latitudes between 20 and 30 km (~ 55 and 10 hPa).

Negative ozone trends in the tropical middle stratosphere have also been found in SCIAMACHY data (Gebhardt et al., 2014). Generally the trends shown in their paper agree with ours, but not in every detail. In particular the trends provided

2584

E. Eckert et al.: Drifts, trends and periodic variations in MIPAS ozone

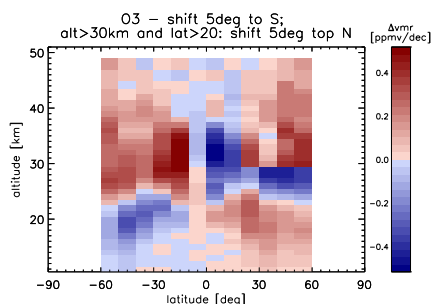


Fig. 19. Altitude–latitude cross-section showing the resulting trends when shifting the tropical mixing barriers below 30 km by 5 degrees to the south and expanding them by 5 degrees above that altitude.

by Gebhardt et al. (2014) for the middle tropics are more negative with only one negative peak.

Kyrölä et al. (2013) see less negative trends in the tropics around 30 to 35 km than Gebhardt et al. (2014). The trends by Kyrölä et al. (2013) are of the order of -2 to -3% decade $^{-1}$. This is even a bit smaller than what we find, but in their paper the time period looked at (1997–2011) is a bit longer than ours and covers a slightly different time span in general. Thus differences can be expected when comparing their results with ours. In the extratropics up to $\sim 50^\circ$ N/S Kyrölä et al. (2013) find predominantly positive or near-zero trends between 25 and 50 km. Their trends are of the order of up to $+2\%$ decade $^{-1}$ in these regions. This agrees considerably well with our results. Comparing our results with others of the post-mid-1990s period we find that the assessed changes are predominantly positive or near zero, except for the lower stratospheric tropics. While column ozone from ground-based and satellite measurements seem to exhibit non-changing ozone values in the mid-latitudes for both hemispheres after 1998 after showing an increase of $\sim 2\%$ from 1996 to 1998, an increase in mid-latitude ozone was found for the Northern Hemisphere for the time period of 1996 to 2009 at altitude ranges of 12–15, 20–25 and 35–45 km with largest increases (6%) at the lowest level and smaller values above. Southern Hemisphere mid-latitude trends were only found to be statistically significant at the highest level (35–45 km), exhibiting an increase of 1–3% for the time period of 1996 to 2009 (cf. WMO (2011, Chapter 2, Table S2-1)). Tropical ozone trends from simulations show negative values right above the tropopause (18–19 km), presumably due to increased upwelling.

In addition to the trends estimated from MIPAS measurements, we also calculated “drift-corrected trends”, again both on an altitude (Fig. 15) as well as on a pressure grid (Fig. 16). The displayed trends and associated errors were calculated as described in Sect. 3.4. We chose the drift estimates versus Aura MLS for correction of the MIPAS trends

for two reasons. First, a drift of the order of magnitude such as the one established by comparison with Aura MLS can mostly be explained by drifts associated with the nonlinearity correction for the MIPAS detector as already mentioned in Sect. 4.1. Second, there has been no indication of a possible drift in Aura MLS ozone data so far. In addition to that the number of coinciding profiles with Aura MLS is the largest compared to all other instruments, even when using strict coincidence criteria, which presumably provides the most reliable analysis. Thus the drift estimate versus Aura MLS seems to be the most suitable candidate for shifting the MIPAS trends towards reality. While one might think that the drift-corrected MIPAS trends using Aura MLS for drift determination actually gives an Aura MLS ozone trend, this is not true: the MIPAS trend is inferred from a much larger data set than that used for drift estimation. For the drift estimation of MIPAS–Aura MLS coincidences had to be used, while the trends have been inferred from the entire MIPAS data set. Most of the negative ozone trends which were significant in the pure MIPAS estimates are no longer significant at 2-sigma level in the corrected version, especially at higher altitudes. In addition, significant areas with positive trends become larger and more significant. These results agree better with recent findings (e.g. WMO, 2011; Steinbrecht et al., 2009a) than the MIPAS trends without any correction. The few negative trends left are the tropical double-peak structure and Northern Hemisphere areas around 20 to 25 km (~ 20 hPa). The latter feature is more pronounced in the altitude–latitude cross-section. A clear hemispherically asymmetric distribution is still visible in both figures. Positive values reach up to $+0.55$ ppmv decade $^{-1}$ ($+0.53$ ppmv decade $^{-1}$) in the Southern Hemisphere and $+0.44$ ppmv decade $^{-1}$ ($+0.41$ ppmv decade $^{-1}$) in the Northern Hemisphere, with the northern hemispheric areas slightly above 40 km (~ 3 hPa) now reaching values of maximum $+0.42$ ppmv decade $^{-1}$ ($+0.37$ ppmv decade $^{-1}$). The tropical negative peaks show minimum values of -0.37 ppmv decade $^{-1}$ and -0.41 ppmv decade $^{-1}$ (-0.28 ppmv decade $^{-1}$ and -0.38 ppmv decade $^{-1}$) for the lower and the upper one, respectively.

A reasonable explanation for negative trends near the Equator is increased tropical upwelling, as has been suggested before (WMO, 2011), but only for altitudes slightly above the tropopause. So upwelling does not provide a sufficient explanation for the negative values in the tropical middle stratosphere. It cannot explain the double-peak structure either. The altitude–latitude cross-section of the amplitude of the QBO shows that the negative peaks in the trends coincide closely with the maxima in QBO amplitude. While the pattern of the QBO amplitude hints towards a periodic expansion and shrinking of the ozone maximum in the tropics (see Sect. 4.2), the trend pattern hints towards a vertical shrinking and latitudinal expansion of the ozone maximum. This is also most pronounced where the gradient in the ozone distribution is largest. According to this it is reasonable for the

maxima of the QBO amplitude and the extrema of the trends to occur in similar areas. Figures 17 and 18 show the zonal ozone distribution calculated from the results of the parametric trend fit for the years 2000 and 2012, respectively. While the value of the MIPAS regression function for the year 2000 is a direct output of the trend fit process, the value for the year 2012 was calculated by extrapolating the ozone volume mixing ratio from the year 2000 to the year 2012 using the drift-corrected trend which was assessed previously. One can see a vertical shrinking and latitudinal expansion of the ozone maximum in the tropics.

The hemispherically asymmetric trend patterns shown in Fig. 15 could be explained by a shift of the subtropical mixing barriers by 5° to the south over the observation period, as first indicated by Stiller et al. (2012). A simple way to mimic this shift is shown in Fig. 19: the zonal mean distribution of ozone as obtained from the constant terms of the parametric fits of the time series for all latitude-altitude bins has been shifted by 5° to the south below altitudes of 30 km. Above 30 km, the Northern Hemisphere (20° to 60° N) has been shifted to the north, simulating a widening of the tropical pipe. The shifts have been applied between 60° S and 60° N only, since a shift of the polar mixing barriers was not expected. The differences between the original and the shifted distribution assumed to appear over a period of 10 yr is shown in Fig. 19. The pattern of the change of the ozone distribution over a decade is stunningly similar to the linear trends observed in the real ozone distributions. Since the main features of the zonal ozone distribution are, to a large extent, ruled by the subtropical mixing barriers a shift of the barriers by 5° to the south (and an expansion of the tropical pipe above 30 km) would be able to explain the observed decadal linear trend to a large degree. We do not claim, however, that this is a climatological trend, but possibly rather a low-frequency natural variability, the causes of which are still unknown.

5 Conclusions

The investigations performed in this work offer an overall coherent picture. We calculated drifts of the MIPAS ozone time series versus several instruments which include satellite as well as ground-based experiments. Most of these analyses suggest that MIPAS ozone data most probably have a small negative drift, and thus trends calculated from the MIPAS data might exhibit values which are less positive (more negative) than in reality. Only a few comparisons suggest that MIPAS ozone data do not reveal a drift, such as the drift estimation versus ACE-FTS, or even hint at positive drifts like the analysis comparing MIPAS with the lidar at Observatoire Haute Provence. Magnitudes of the established negative drifts differ from minimum values of about -0.3 ppmv decade $^{-1}$ for Aura MLS to approximately -0.7 ppmv decade $^{-1}$ for Odin OSIRIS and for some lidars

at high altitudes. Due to recent studies on MIPAS' nonlinearity correction and the analysis versus Aura MLS, which presumably offers the most reliable drift estimates, we assume that a drift in MIPAS ozone data is most likely of a magnitude of 0 to -0.3 ppmv decade $^{-1}$, depending on latitude, and thus we correct our trends estimated from MIPAS data by the drift estimates of the comparison with Aura MLS. The corrected trends agree well with recent findings and offer better agreement with those findings than the non-corrected trends. They range from approximately -0.41 ppmv decade $^{-1}$ in the tropics up to $+0.55$ ppmv decade $^{-1}$ at southern mid-latitudes (-0.38 ppmv decade $^{-1}$ to $+0.53$ ppmv decade $^{-1}$ on the pressure grid). Significant areas exhibiting positive values increase spatially when correcting with the drifts estimated in comparison with Aura MLS, leaving mostly positive values. This is in very good agreement with results shown in WMO (2011). In the aforementioned work there are predominantly positive or close-to-zero trends found for the period after 1996/1997.

We observe a negative double-peak structure around the Equator, with minima at approximately 25 and 35 km, exhibiting extreme values of -0.37 ppmv decade $^{-1}$ and -0.41 ppmv decade $^{-1}$ (-0.28 ppmv decade $^{-1}$ and -0.38 ppmv decade $^{-1}$ on the pressure grid), respectively, which coincide in altitude with the maxima of the amplitude of the ozone QBO. This coincidence of the tropical QBO maxima with the negative ozone trends occurs due to the ozone gradient being largest at these altitudes, so that the periodic vertical expansion and shrinking (in the case of the QBO) and the vertical flattening of the ozone maximum over the measured period (in the case of the trends) both are very obvious here. We find a clear hemispherically asymmetric pattern in the trends with the negative signs in the northern lower stratosphere and positive values in the southern lower stratosphere (20–30 km). This, together with negative trends at tropical mid-stratospheric altitudes can be mimicked by shifting the zonal ozone distribution 30 km by 5° to the south and expanding the tropical pipe by 5° to the north and south above, simulating mainly a respective shift of the subtropical mixing barriers over the observation period. Even the positive trends just above the tropical tropopause can be simulated by the shift of the subtropical mixing barriers to the south. Such a shift is not necessarily a climatological trend, but possibly rather a low-frequency natural variation, the cause of which is still unknown.

The altitude–latitude cross-sections of the amplitudes of the QBO, SAO and the seasonal variation agree well with previous results. In the case of the SAO, both the altitude–latitude distribution as well as the magnitude are very similar to previous findings, while the estimated values of the ozone QBO amplitude are smaller than those found in other studies. Our results for the amplitudes of the seasonal variation show reasonable altitude–latitude distributions and reveal similar magnitudes to previous findings.

2586

E. Eckert et al.: Drifts, trends and periodic variations in MIPAS ozone

Appendix A

Drifts

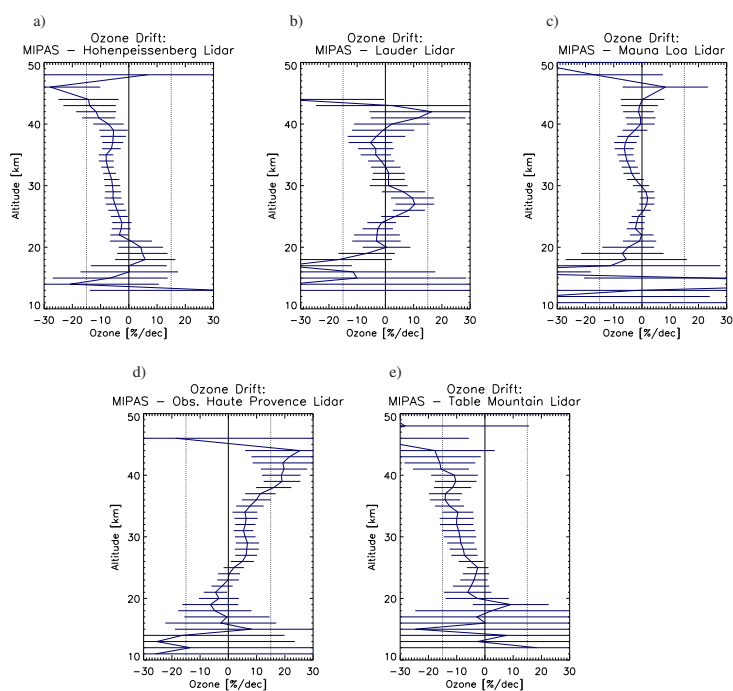


Fig. A1. Same as Fig. 9 but showing relative drifts.

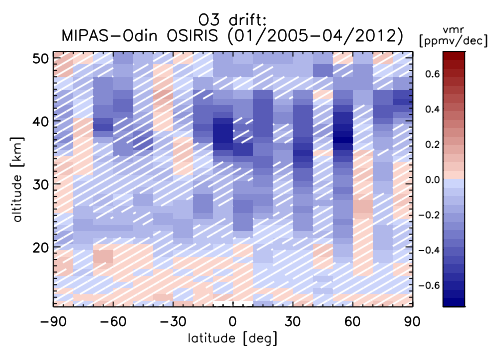


Fig. A2. Altitude–latitude cross-section of absolute drifts of MIPAS vs. Odin OSIRIS ozone measurements only for the time period from January 2005 to April 2012. Hatching as described before.

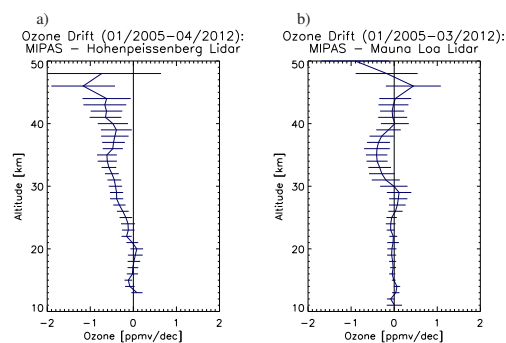


Fig. A3. Same as Fig. 9a and c but only for the time period of 2005 to 2012.

E. Eckert et al.: Drifts, trends and periodic variations in MIPAS ozone

2587

Acknowledgements. The retrievals of IMK/IAA were partly performed on the HP XC4000 of the Scientific Supercomputing Center (SSC) Karlsruhe under project grant MIPAS. IMK data analysis was supported by DLR under contract number 50EE0901. MIPAS level-1b data were provided by ESA. We acknowledge support by Deutsche Forschungsgemeinschaft and Open Access Publishing Fund of Karlsruhe Institute of Technology. The Atmospheric Chemistry Experiment (ACE), also known as SCISAT, is a Canadian-led mission mainly supported by the Canadian Space Agency and the Natural Sciences and Engineering Research Council of Canada. Work at the Jet Propulsion Laboratory, California Institute of Technology, was carried out under contract with the National Aeronautics and Space Administration.

The service charges for this open access publication have been covered by a Research Centre of the Helmholtz Association.

Edited by: R. Eckman

References

- Brinksma, E. J., Bergwerff, J. B., Bodeker, G. E., Boersma, K. F., Boyd, I. S., Connor, B. J., de Haan, J. F., Hogervorst, W., Hovenier, J. W., Parrish, A., Tsou, J. J., Zawodny, J. M., and Swart, D. P. J.: Validation of 3 years of ozone measurements over Network for the Detection of Stratospheric Change station Lauder, New Zealand, *J. Geophys. Res.*, 105, 17291, doi:10.1029/2000JD900143, 2000.
- Degenstein, D. A., Bourassa, A. E., Roth, C. Z., and Llewellyn, E. J.: Limb scatter ozone retrieval from 10 to 60 km using a multiplicative algebraic reconstruction technique, *Atmos. Chem. Phys.*, 9, 6521–6529, doi:10.5194/acp-9-6521-2009, 2009.
- Dobson, G. M. B.: Ozone in the Upper Atmosphere and its Relation to Meteorology, *Nature*, 127, 668–672, doi:10.1038/127668a0, 1931.
- Dobson, G. M. B.: Forty years research on atmospheric ozone at Oxford: a history, *Appl. Optics*, 7, 387, doi:10.1364/AO.7.000387, 1968.
- Dupuy, E., Walker, K. A., Kar, J., Boone, C. D., McElroy, C. T., Bernath, P. F., Drummond, J. R., Skelton, R., McLeod, S. D., Hughes, R. C., Nowlan, C. R., Dufour, D. G., Zou, J., Nichitiu, F., Strong, K., Baron, P., Bevilacqua, R. M., Blumenstock, T., Bodeker, G. E., Borsdorff, T., Bourassa, A. E., Bovensmann, H., Boyd, I. S., Bracher, A., Brogniez, C., Burrows, J. P., Catoire, V., Ceccherini, S., Chabrilat, S., Christensen, T., Coffey, M. T., Cortesi, U., Davies, J., De Clercq, C., Degenstein, D. A., De Mazière, M., Demoulin, P., Dodion, J., Firanski, B., Fischer, H., Forbes, G., Froidevaux, L., Fussen, D., Gerard, P., Godin-Beekmann, S., Goutail, F., Granville, J., Griffith, D., Haley, C. S., Hannigan, J. W., Höpfner, M., Jin, J. J., Jones, A., Jones, N. B., Jucks, K., Kagawa, A., Kasai, Y., Kerzenmacher, T. E., Kleinböhl, A., Klekociuk, A. R., Kramer, I., Küllmann, H., Kuttippurath, J., Kyrölä, E., Lambert, J.-C., Livesey, N. J., Llewellyn, E. J., Lloyd, N. D., Mahieu, E., Manney, G. L., Marshall, B. T., McConnell, J. C., McCormick, M. P., McDermid, I. S., McHugh, M., McLinden, C. A., Mellqvist, J., Mizutani, K., Murayama, Y., Murtagh, D. P., Oelhaf, H., Parrish, A., Petelina, S. V., Piccolo, C., Pommereau, J.-P., Randall, C. E., Robert, C., Roth, C., Schneider, M., Senten, C., Steck, T., Strandberg, A., Strawbridge, K. B., Sussmann, R., Swart, D. P. J., Tarasick, D. W., Taylor, J. R., Tétard, C., Thomason, L. W., Thompson, A. M., Tully, M. B., Urban, J., Vanhellemont, F., Vigouroux, C., von Clarmann, T., von der Gathen, P., von Savigny, C., Waters, J. W., Witte, J. C., Wolff, M., and Zawodny, J. M.: Validation of ozone measurements from the Atmospheric Chemistry Experiment (ACE), *Atmos. Chem. Phys.*, 9, 287–343, doi:10.5194/acp-9-287-2009, 2009.
- Eyring, V., Shepherd, T. G., and Waugh, D. W. (Eds.): SPARC Report on the Evaluation of Chemistry-Climate Models, SPARC Report No.5, WCRP-132, WMO/TD-No. 1526, SPARC CCM-Val, 2010.
- Fadnavis, S. and Beig, G.: Quasi-biennial oscillation in ozone and temperature over tropics, *J. Atmos. Sol.-Terr. Phys.*, 71, 257–263, doi:10.1016/j.jastp.2008.11.012, 2009.
- Farman, J. C., Gardiner, B. G., and Shanklin, J. D.: Large losses of total ozone in Antarctica reveal seasonal ClO_x/NO_x interaction, *Nature*, 315, 207–210, doi:10.1038/315207a0, 1985.
- Fischer, H., Birk, M., Blom, C., Carli, B., Carlotti, M., von Clarmann, T., Delbouille, L., Dudhia, A., Ehret, D., Endemann, M., Flaud, J. M., Gessner, R., Kleinert, A., Koopman, R., Langen, J., López-Puertas, M., Mosner, P., Nett, H., Oelhaf, H., Perron, G., Remedios, J., Ridolfi, M., Stiller, G., and Zander, R.: MIPAS: an instrument for atmospheric and climate research, *Atmos. Chem. Phys.*, 8, 2151–2188, doi:10.5194/acp-8-2151-2008, 2008.
- Froidevaux, L., Jiang, Y. B., Lambert, A., Livesey, N. J., Read, W. G., Waters, J. W., Browell, E. V., Hair, J. W., Avery, M. A., McGee, T. J., Twigg, L. W., Summicht, G. K., Jucks, K. W., Margitan, J. J., Sen, B., Stachnik, R. A., Toon, G. C., Bernath, P. F., Boone, C. D., Walker, K. A., Filipiak, M. J., Harwood, R. S., Fuller, R. A., Manney, G. L., Schwartz, M. J., Daffer, W. H., Drouin, B. J., Cofield, R. E., Cuddy, D. T., Jarnot, R. F., Knosp, B. W., Perun, V. S., Snyder, W. V., Stek, P. C., Thurstans, R. P., and Wagner, P. A.: Validation of Aura Microwave Limb Sounder stratospheric ozone measurements, *J. Geophys. Res.-Atmos.*, 113, D15S20, doi:10.1029/2007JD008771, 2008.
- Gebhardt, C., Rozanov, A., Hommel, R., Weber, M., Bovensmann, H., Burrows, J. P., Degenstein, D., Froidevaux, L., and Thompson, A. M.: Stratospheric ozone trends and variability as seen by SCIAMACHY from 2002 to 2012, *Atmos. Chem. Phys.*, 14, 831–846, doi:10.5194/acp-14-831-2014, 2014.
- Götz, F. W. P., Meetham, A. R., and Dobson, G. M. B.: The Vertical Distribution of Ozone in the Atmosphere, *Royal Society of London Proceedings Series A*, 145, 416–446, doi:10.1098/rspa.1934.0109, 1934.
- Huang, F. T., Mayr, H. G., Reber, C. A., Russell III, J. M., Mlynarczyk, M. G., and Mengel, J. G.: Ozone quasi-biennial oscillations (QBO), semiannual oscillations (SAO), and correlations with temperature in the mesosphere, lower thermosphere, and stratosphere, based on measurements from SABER on TIMED and MLS on UARS, *J. Geophys. Res.*, 113, A01316, doi:10.1029/2007JA012634, 2008.
- Hubert, D., Verhoelst, T., Keppens, A., Granville, J., and Lambert, J.-C.: Network-based evaluation of fourteen satellite limb/occultation profilers for the next SPARC and WMO ozone trend assessments, Talk at Quadrennial Ozone Symposium 2012, Toronto, 2012.

2588

E. Eckert et al.: Drifts, trends and periodic variations in MIPAS ozone

- Hubert, D., Lambert, J.-C., Verhoelst, T., Granville, J., and Keppens, A.: Ground-based assessment of the bias and long-term stability of fourteen limb and occultation ozone profile data records, *Atmos. Meas. Tech. Discuss.*, in preparation, 2014.
- Kiefer, M., Aubertin, G., Birk, M., De Laurentis, M., Eckert, E., Kleinert, A., Perron, G., and Wagner, G.: Impact of Improved Corrections for MIPAS Detector Non-Linearity, in: *Atmospheric Composition Validation and Evolution*, Frascati, 13–15 March 2013, Abstract Book, p. 38, ESA, 2013.
- Kirgis, G., Leblanc, T., McDermid, I. S., and Walsh, T. D.: Stratospheric ozone interannual variability (1995–2011) as observed by lidar and satellite at Mauna Loa Observatory, HI and Table Mountain Facility, CA, *Atmos. Chem. Phys.*, 13, 5033–5047, doi:10.5194/acp-13-5033-2013, 2013.
- Kyrölä, E., Laine, M., Sofieva, V., Tamminen, J., Päiväranta, S.-M., Tukiainen, S., Zawodny, J., and Thomason, L.: Combined SAGE II-GOMOS ozone profile data set for 1984–2011 and trend analysis of the vertical distribution of ozone, *Atmos. Chem. Phys.*, 13, 10645–10658, doi:10.5194/acp-13-10645-2013, 2013.
- Laeng, L., Grabowski, U., von Clarmann, T., Stiller, G., Kellmann, S., Kiefer, M., Linden, A., Lossow, S., Bathgate, T., Bernath, P., Boone, C. D., Clerbaux, C., Degenstein, D. and Fritz, S., Froidevaux, L., Hervig, M., Hoppel, K., Lumpe, J., McHugh, M., Sano, T., Sofieva, V., Suzuki, M., Tamminen, J., Urban, J., Walker, K., Weber, M., and Zawodny, J.: Validation of MIPAS IMK/IAA ozone profiles, poster at Quadrennial Ozone Symposium 2012, Toronto, 27–31 August, 2012.
- Llewellyn, E., Lloyd, N. D., Degenstein, D. A., Gattinger, R. L., Petelina, S. V., Bourassa, A. E., Wiensz, J. T., Ivanov, E. V., McDade, I. C., Solheim, B. H., McConnell, J. C., Haley, C. S., von Savigny, C., Sioris, C. E., McLinden, C. A., Griffioen, E., Kaminski, J., Evans, W. F. J., Puckrin, E., Strong, K., Wehrle, V., Hum, R. H., Kendall, D. J. W., Matsushita, J., Murtagh, D. P., Brohede, S., Stegman, J., Witt, G., Barnes, G., Payne, W. F., Piche, L., Smith, K., Warshaw, G., Deslauniers, D. L., Marchand, P., Richardson, E. H., King, R. A., Wevers, I., McCreath, W., Kyrola, E., Oikarinen, L., Leppelmeier, G. W., Auvinen, H., Megie, G., Hauchecorne, A., Lefevre, F., de La Noe, J., Ricaud, P., Frisk, U., Sjöberg, F., von Scheele, F., and Nordh, L.: The OSIRIS instrument on the Odin spacecraft, *Canadian Journal of Physics*, 82, 411–422, doi:10.1139/p04-005, 2004.
- McDermid, I. S., Walsh, T. D., Deslis, A., and White, M. L.: Optical systems design for a stratospheric lidar system, *Appl. Optics*, 34, 6201, doi:10.1364/AO.34.006201, 1995.
- McDermid, S. I., Godin, S. M., and Lindqvist, L. O.: Ground-based laser DIAL system for long-term measurements of stratospheric ozone, *Appl. Optics*, 29, 3603–3612, doi:10.1364/AO.29.003603, 1990.
- Megie, G., Allain, J. Y., Chanin, M. L., and Blamont, J. E.: Vertical profile of stratospheric ozone by lidar sounding from the ground, *Nature*, 270, 329–331, doi:10.1038/270329a0, 1977.
- Molina, M. J. and Rowland, F. S.: Stratospheric sink for chlorofluoromethanes: Chlorine atom-catalysed destruction of ozone, *Nature*, 249, 810–812, 1974.
- Nair, P. J., Godin-Beekmann, S., Froidevaux, L., Flynn, L. E., Zawodny, J. M., Russell III, J. M., Pazmiño, A., Ancellet, G., Steinbrecht, W., Claude, H., Leblanc, T., McDermid, S., van Gijssel, J. A. E., Johnson, B., Thomas, A., Hubert, D., Lambert, J.-C., Nakane, H., and Swart, D. P. J.: Relative drifts and stability of satellite and ground-based stratospheric ozone profiles at NDACC lidar stations, *Atmos. Meas. Tech.*, 5, 1301–1318, doi:10.5194/amt-5-1301-2012, 2012.
- Randel, W. J. and Wu, F.: Isolation of the Ozone QBO in SAGE II Data by Singular-Value Decomposition, *J. Atmos. Sci.*, 53, 2546–2560, doi:10.1175/1520-0469(1996)053<2546:IOTOQJ>2.0.CO;2, 1996.
- Randel, W. J., Wu, F., Swinbank, R., Nash, J., and O'Neill, A.: Global QBO Circulation Derived from UKMO Stratospheric Analyses, *J. Atmos. Sci.*, 56, 457–474, doi:10.1175/1520-0469(1999)056<0457:GQCDFU>2.0.CO;2, 1999.
- Rodgers, C. D.: Inverse Methods for Atmospheric Sounding: Theory and Practice, vol. 2 of *Series on Atmospheric, Oceanic and Planetary Physics*, F. W. Taylor, ed., World Scientific, 2000.
- Schoeberl, M. R., Douglass, A. R., Hilsenrath, E., Bhartia, P. K., Beer, R., Waters, J. W., Gunson, M. R., Froidevaux, L., Gille, J. C., Barnett, J. J., Levelt, P. F., and de Cola, P.: Overview of the EOS Aura Mission, *IEEE T. Geosci. Remote*, 44, 1066–1074, doi:10.1109/TGRS.2005.861950, 2006.
- Steinbrecht, W., Claude, H., Schonenborn, F., McDermid, I. S., Leblanc, T., Godin-Beekmann, S., Keckhut, P., Hauchecorne, A., van Gijssel, J. A. E., Swart, D. P. J., Bodeker, G. E., Parrish, A., Boyd, I. S., Kampfer, N., Hocke, K., Stolarski, R. S., Frith, S. M., Thomason, L. W., Remsberg, E. E., von Savigny, C., Rozanov, A., and Burrows, J. P.: Ozone and temperature trends in the upper stratosphere at five stations of the Network for the Detection of Atmospheric Composition Change, *Int. J. Remote Sens.*, 30, 3875–3886, doi:10.1080/01431160902821841, 2009a.
- Steinbrecht, W., McGee, T. J., Twigg, L. W., Claude, H., Schonenborn, F., Sumnicht, G. K., and Silbert, D.: Intercomparison of stratospheric ozone and temperature profiles during the October 2005 Hohenpeißenberg Ozone Profiling Experiment (HOPE), *Atmos. Meas. Tech.*, 2, 125–145, doi:10.5194/amt-2-125-2009, 2009b.
- Stiller, G., Von Clarmann, T., Eckert, E., Haenel, F., Funke, B., Glatthor, N., Grabowski, U., Kellmann, S., Kiefer, M., Linden, A., Lossow, S., and López-Puertas, M.: Global observation of stratospheric age of air, its temporal variation, and correlation with ozone, poster at Quadrennial Ozone Symposium 2012, Toronto, 27–31 August, 2012.
- Stiller, G. P., Kiefer, M., Eckert, E., von Clarmann, T., Kellmann, S., García-Comas, M., Funke, B., Leblanc, T., Fetzner, E., Froidevaux, L., Gomez, M., Hall, E., Hurst, D., Jordan, A., Kämpfer, N., Lambert, A., McDermid, I. S., McGee, T., Miloshevich, L., Nedoluha, G., Read, W., Schneider, M., Schwartz, M., Straub, C., Toon, G., Twigg, L. W., Walker, K., and Whiteman, D. N.: Validation of MIPAS IMK/IAA temperature, water vapor, and ozone profiles with MOHAVE-2009 campaign measurements, *Atmos. Meas. Tech.*, 5, 289–320, doi:10.5194/amt-5-289-2012, 2012.
- Stiller, G. P., von Clarmann, T., Haenel, F., Funke, B., Glatthor, N., Grabowski, U., Kellmann, S., Kiefer, M., Linden, A., Lossow, S., and López-Puertas, M.: Observed temporal evolution of global mean age of stratospheric air for the 2002 to 2010 period, *Atmos. Chem. Phys.*, 12, 3311–3331, doi:10.5194/acp-12-3311-2012, 2012.
- Tegtmeier, S., Hegglin, M. I., Anderson, J., Bourassa, A. and Brohede, S., Degenstein, D., Froidevaux, L., Fuller, L., Funke, B., Gille, J., Jones, A., Kasai, Y., Kyrola, E., Lingenfeller, G., Lumpe, J., Nardi, B., Neu, J., Pendlebury, D., Remsberg, E.,

E. Eckert et al.: Drifts, trends and periodic variations in MIPAS ozone**2589**

- Roazanov, A., Smith, L., Toohey, M., Urban, J., von Clarmann, T., Walker, K., and Wang, R.: The SPARC Data Initiative: A comparison of ozone climatologies from international limb satellite sounders, *J. Geophys. Res.*, 118, 12229–12247, 2013.
- von Clarmann, T., Höpfner, M., Kellmann, S., Linden, A., Chauhan, S., Funke, B., Grabowski, U., Glatthor, N., Kiefer, M., Schieferdecker, T., Stiller, G. P., and Versick, S.: Retrieval of temperature, H₂O, O₃, HNO₃, CH₄, N₂O, ClONO₂ and ClO from MIPAS reduced resolution nominal mode limb emission measurements, *Atmos. Meas. Tech.*, 2, 159–175, doi:10.5194/amt-2-159-2009, 2009.
- von Clarmann, T., Stiller, G., Grabowski, U., Eckert, E., and Orphal, J.: Technical Note: Trend estimation from irregularly sampled, correlated data, *Atmos. Chem. Phys.*, 10, 6737–6747, doi:10.5194/acp-10-6737-2010, 2010.
- Waters, J. W., Froidevaux, L., Harwood, R. S., Jarnot, R. F., Pickett, H. M., Read, W. G., Siegel, P. H., Cofield, R. E., Filipiak, M. J., Flower, D. A., Holden, J. R., Lau, G. K., Livesey, N. J., Manney, G. L., Pumphrey, H. C., Santee, M. L., Wu, D. L., Cuddy, D. T., Lay, R. R., Loo, M. S., Perun, V. S., Schwartz, M. J., Stek, P. C., Thurstans, R. P., Boyles, M. A., Chandra, K. M., Chavez, M. C., Chen, G.-S., Chudasama, B. V., Dodge, R., Fuller, R. A., Girard, M. A., Jiang, J. H., Jiang, Y., Knosp, B. W., Labelle, R. C., Lam, J. C., Lee, A. K., Miller, D., Oswald, J. E., Patel, N. C., Pukala, D. M., Quintero, O., Scaff, D. M., Vansnyder, W., Tope, M. C., Wagner, P. A., and Walch, M. J.: The Earth Observing System Microwave Limb Sounder (EOS MLS) on the Aura Satellite, *IEEE T. Geosci. Remote*, 44, 1075–1092, doi:10.1109/TGRS.2006.873771, 2006.
- WMO: Scientific Assessment of Ozone Depletion: 2010, Global Ozone Research and Monitoring Project 52, 516 pp., World Meteorological Organisation, Geneva, Switzerland, 2011.
- Zawodny, J. M. and McCormick, M. P.: Stratospheric Aerosol and Gas Experiment II measurements of the quasi-biennial oscillations in ozone and nitrogen dioxide, *J. Geophys. Res.*, 96, 9371–9377, doi:10.1029/91JD00517, 1991.

A.2 MIPAS IMK/IAA CFC-11 (CCl_3F) and CFC-12 (CCl_2F_2) measurements: accuracy, precision and long-term stability

Atmos. Meas. Tech., 9, 3355–3389, 2016
 www.atmos-meas-tech.net/9/3355/2016/
 doi:10.5194/amt-9-3355-2016
 © Author(s) 2016. CC Attribution 3.0 License.



Atmospheric
 Measurement
 Techniques

Open Access

MIPAS IMK/IAA CFC-11 (CCl₃F) and CFC-12 (CCl₂F₂) measurements: accuracy, precision and long-term stability

E. Eckert¹, A. Laeng¹, S. Lossow¹, S. Kellmann¹, G. Stiller¹, T. von Clarmann¹, N. Glatthor¹, M. Höpfner¹, M. Kiefer¹, H. Oelhaf¹, J. Orphal¹, B. Funke², U. Grabowski¹, F. Haenel¹, A. Linden¹, G. Wetzel¹, W. Woiwode¹, P. F. Bernath³, C. Boone⁴, G. S. Dutton^{5,6}, J. W. Elkins⁵, A. Engel⁷, J. C. Gille^{8,9}, F. Kolonjari¹⁰, T. Sugita¹¹, G. C. Toon¹², and K. A. Walker^{4,10}

¹Karlsruhe Institute of Technology, Institute of Meteorology and Climate Research, Karlsruhe, Germany

²Instituto de Astrofísica de Andalucía, CSIC, Granada, Spain

³Department of Chemistry and Biochemistry, Old Dominion University, Norfolk, VA 23529-0126, USA

⁴Department of Chemistry, University of Waterloo, Waterloo, Ontario, Canada

⁵NOAA Earth System Research Laboratory, Boulder, CO 80305, USA

⁶Cooperative Institute for Research in Environmental Sciences, University of Colorado, Boulder, CO 80309, USA

⁷Institut für Atmosphäre und Umwelt, J. W. Goethe Universität, Frankfurt, Germany

⁸National Center for Atmospheric Research, Boulder, Colorado, USA

⁹Center for Limb Atmospheric Sounding, University of Colorado, Boulder, Colorado, USA

¹⁰Department of Physics, University of Toronto, Toronto, Ontario, Canada

¹¹National Institute for Environmental Studies, Tsukuba, Japan

¹²Jet Propulsion Laboratory, California Institute of Technology, Pasadena, CA 91109, USA

Correspondence to: E. Eckert (ellen.eckert@kit.edu)

Received: 21 June 2015 – Published in Atmos. Meas. Tech. Discuss.: 23 July 2015

Revised: 10 June 2016 – Accepted: 15 June 2016 – Published: 28 July 2016

Abstract. Profiles of CFC-11 (CCl₃F) and CFC-12 (CCl₂F₂) of the Michelson Interferometer for Passive Atmospheric Sounding (MIPAS) aboard the European satellite Envisat have been retrieved from versions MIPAS/4.61 to MIPAS/4.62 and MIPAS/5.02 to MIPAS/5.06 level-1b data using the scientific level-2 processor run by Karlsruhe Institute of Technology (KIT), Institute of Meteorology and Climate Research (IMK) and Consejo Superior de Investigaciones Científicas (CSIC), Instituto de Astrofísica de Andalucía (IAA). These profiles have been compared to measurements taken by the balloon-borne cryosampler, Mark IV (MkIV) and MIPAS-Balloon (MIPAS-B), the airborne MIPAS-STRatospheric aircraft (MIPAS-STR), the satellite-borne Atmospheric Chemistry Experiment Fourier transform spectrometer (ACE-FTS) and the High Resolution Dynamic Limb Sounder (HIRDLS), as well as the ground-based Halocarbon and other Atmospheric Trace Species (HATS) network for the reduced spectral resolution period (RR: January 2005–April 2012) of MIPAS. ACE-FTS, MkIV

and HATS also provide measurements during the high spectral resolution period (full resolution, FR: July 2002–March 2004) and were used to validate MIPAS CFC-11 and CFC-12 products during that time, as well as profiles from the Improved Limb Atmospheric Spectrometer, ILAS-II. In general, we find that MIPAS shows slightly higher values for CFC-11 at the lower end of the profiles (below ~15 km) and in a comparison of HATS ground-based data and MIPAS measurements at 3 km below the tropopause. Differences range from approximately 10 to 50 pptv (~5–20 %) during the RR period. In general, differences are slightly smaller for the FR period. An indication of a slight high bias at the lower end of the profile exists for CFC-12 as well, but this bias is far less pronounced than for CFC-11 and is not as obvious in the relative differences between MIPAS and any of the comparison instruments. Differences at the lower end of the profile (below ~15 km) and in the comparison of HATS and MIPAS measurements taken at 3 km below the tropopause mainly stay within 10–50 pptv (corresponding to ~2–10 % for CFC-

Published by Copernicus Publications on behalf of the European Geosciences Union.

3356

E. Eckert et al.: MIPAS IMK/IAA CFC-11 and CFC-12: accuracy, precision and long-term stability

12) for the RR and the FR period. Between ~ 15 and 30 km, most comparisons agree within 10–20 pptv (10–20%), apart from ILAS-II, which shows large differences above ~ 17 km. Overall, relative differences are usually smaller for CFC-12 than for CFC-11. For both species – CFC-11 and CFC-12 – we find that differences at the lower end of the profile tend to be larger at higher latitudes than in tropical and subtropical regions. In addition, MIPAS profiles have a maximum in their mixing ratio around the tropopause, which is most obvious in tropical mean profiles. Comparisons of the standard deviation in a quiescent atmosphere (polar summer) show that only the CFC-12 FR error budget can fully explain the observed variability, while for the other products (CFC-11 FR and RR and CFC-12 RR) only two-thirds to three-quarters can be explained. Investigations regarding the temporal stability show very small negative drifts in MIPAS CFC-11 measurements. These instrument drifts vary between ~ 1 and 3% decade $^{-1}$. For CFC-12, the drifts are also negative and close to zero up to ~ 30 km. Above that altitude, larger drifts of up to $\sim 50\%$ decade $^{-1}$ appear which are negative up to ~ 35 km and positive, but of a similar magnitude, above.

1 Introduction

Chlorofluorocarbons (CFCs) have been monitored for some decades because of their potential to release catalytically active species that destroy stratospheric ozone, which was first discovered by Molina and Rowland (1974). Even though there are also natural sources of halogens, observations focus on man-made CFCs, such as CFC-11 and CFC-12, because increased release of active chlorine species due to elevated amounts of these substances can significantly alter the equilibrium of stratospheric ozone formation and destruction. Under certain conditions (sufficiently cold temperatures for chlorine activation; polar stratospheric clouds, PSCs), this can lead to severe ozone depletion. Since CFCs have very long lifetimes in the atmosphere (52 years with an error range of 43–67 years for CFC-11; 102 years with an error range of 88–122 years for CFC-12, SPARC, 2013) and are insoluble in water, they can easily reach the stratosphere because they are neither destroyed nor washed out before they arrive at these altitude regions. In the stratosphere, halogen source gases, such as CFC-11 or CFC-12, are photolyzed or otherwise broken up and finally converted to so-called reservoir gases, particularly hydrogen chloride (HCl) or chlorine nitrate (ClONO $_2$), by chemical reactions and under the influence of solar ultraviolet radiation. Stratospheric abundances of hydrogen chloride and chlorine nitrate increased significantly during the later decades of the past century (World Meteorological Organization, 2011), as a consequence of intensified anthropogenic emissions of CFCs and other ozone-depleting substances (ODSs), which were used for refrigeration, foam blowing and several other purposes. While di-

rect reactions of ozone with the reservoir species HCl and ClONO $_2$ are not relevant for ozone depletion, these reservoir species are transformed into active chlorine species (ClO $_x$; mainly ClO, Cl and Cl $_2$ O $_2$) under sufficiently cold temperatures. The active chlorine species catalytically destroy ozone via the so-called ClO-dimer cycle (Molina and Molina, 1987) and the synergistic interaction of ClO and BrO (McElroy et al., 1986). Here, heterogeneous reactions on the surface of cold aerosols of PSCs occur and, in combination with sunlight, result in the reactivation of chlorine which can then destroy ozone catalytically and ultimately leads to ozone depletion and the formation of the ozone hole.

Once it was observed (Farman et al., 1985) that these processes could lead to severe ozone depletion in reality, the Montreal Protocol was adopted in 1987 to control the emission of CFCs and other ozone-depleting substances. Afterwards, the emission of CFCs decreased and ceased completely in 2010 (World Meteorological Organization, 2011), which led to decreasing amounts of these species in the atmosphere. However, since several CFCs have lifetimes of up to 100 years and more – which makes them excellent tracers for the Brewer–Dobson circulation (Schoeberl et al., 2005; SPARC, 2013) – significant amounts of these species are still present in the atmosphere. Hence, their monitoring and the closer examination of their evolution in the atmosphere are important tasks, as Kellmann et al. (2012) have shown by illustrating that there are trends in CFC-11 and CFC-12 which can so far only be explained by changes in circulation. In addition to their ozone-depleting potential, CFC-11 and CFC-12 have a pronounced global warming potential (World Meteorological Organization, WMO, e.g., Fig. 1-6-4), which is another reason for monitoring these species. In the following, we describe the data products and the different characteristics of the instruments used in the comparisons (Sect. 2), followed by an explanation of the validation method (Sect. 3). Since the Michelson Interferometer for Passive Atmospheric Sounding (MIPAS) malfunctioned in 2004 and the retrieval setup had to be changed afterwards to address the altered situation, two sets of the data exist for either species, one (FR, full spectral resolution) referring to the period of July 2002 to March 2004 and one (RR, reduced spectral resolution¹) referring to the period of January 2005 to April 2012. The spectral resolution degraded from the FR to the RR period, but more scans in the vertical are performed per profile during the RR period, which leads to better altitude resolution (Kellmann et al., 2012, Table 1). Thus, in Sect. 4 we show the extensive results of the validation of version V5R_220 and V5R_221 (corresponding to the RR period) of MIPAS CFC-11 and CFC-12 products and also a few comparisons for version V5H_20 (corresponding to the FR period) of the same species. The paper concludes with a summary.

¹The respective ESA product is referred to as “optimized resolution”.

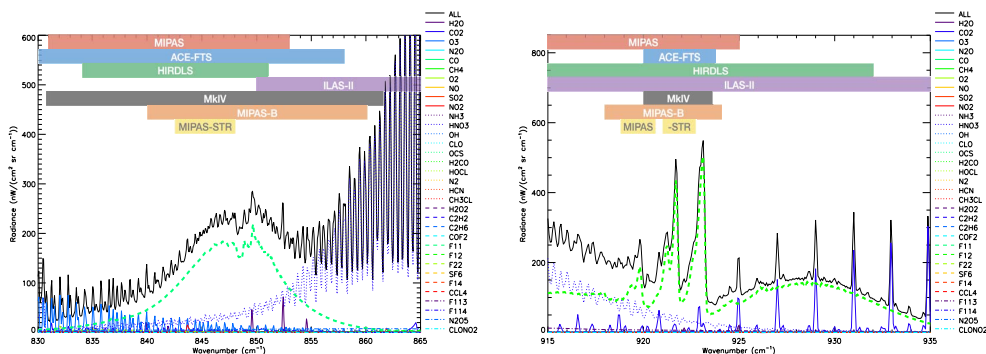


Figure 1. Simulated midlatitude emission spectra of the main regions of CFC-11 (left) and CFC-12 (right) at 20 km in July. The spectral regions used for each instrument are shown. Only ILAS-2 uses a far wider range to retrieve CFC-11 and CFC-12.

2 Instruments

All the instruments used in this study and their main characteristics are summarized in this section. Information on vertical coverage, vertical resolution and utilized spectral region is collected in Table 1. The table also gives an overview of the observation period and spectroscopic data used for the retrievals. The spectral regions used for each remote sensor under consideration are illustrated in Fig. 1, along with the contributions of all interfering species. Besides the Institute of Meteorology and Climate Research/Instituto de Astrofísica de Andalucía (IMK/IAA) data product, MIPAS CFC data by ESA (Raspollini et al., 2013, validated by Engel et al., 2016), Oxford University (The University of Oxford Physics Department, 2008), Forschungszentrum Jülich (Hoffmann et al., 2008) and MIPAS Bologna Facility (Dinelli et al., 2010) also exist. Since these retrievals rely on the same measurements as our data, they are not independent and thus have not been used for comparison.

2.1 MIPAS data and retrieval

The Michelson Interferometer for Passive Atmospheric Sounding (MIPAS) was one of 10 instruments aboard Envisat (Environmental Satellite). The satellite was launched into a polar, sun-synchronous orbit on 1 March 2002. The last contact with the satellite was made on 8 April 2012. This adds up to an observation period of 10 years. Envisat orbited the Earth 14 times a day at an altitude of approx. 800 km. The equator crossing times were 10:00 and 22:00 local time for the descending and ascending node, respectively.

The MIPAS instrument was a high-resolution Fourier transform spectrometer. It measured thermal emissions from the atmospheric limb in the mid-infrared range between 685 and 2410 cm^{-1} (14.6 and 4.1 μm) (Fischer et al., 2008). The MIPAS measurement period is split into two parts based on

the spectral resolution of the measurements. Until March 2004, the measurements were performed with a spectral resolution of 0.025 cm^{-1} (unapodized), which was the nominal setting. Due to an instrumental failure, later measurements, commencing in January 2005, could only be performed with a reduced spectral resolution and a spectral sampling of 0.0625 cm^{-1} . In correspondence, we denote the two periods as full (FR) and reduced (RR) spectral resolution periods, respectively. In the present validation study we focus on measurements that were performed in the “nominal observation mode”. In this mode, spectra at 17 tangent heights between 6 and 68 km were obtained in the FR period. The horizontal sampling was about 1 scan per 510 km and overall, more than 1000 scans were performed per day. During the RR period the sampling improved in the horizontal domain to one scan per 410 km and in the vertical domain to 27 spectra between 7 and 72 km. More than 1300 scans were obtained on a single day, covering the entire latitude range.

The CFC-11 and CFC-12 data sets that are used in this study have been retrieved with the IMK/IAA processor that has been set up together by the Institute of Meteorology and Climate Research (IMK) in Karlsruhe (Germany) and the Instituto de Astrofísica de Andalucía (IAA) in Granada (Spain). The retrieval employs a nonlinear least-squares approach with a first-order Tikhonov-type regularization (von Clarmann et al., 2003, 2009). The simulation of the radiative transfer through the atmosphere is performed by the KOPRA (Karlsruhe Optimized and Precise Radiative transfer Algorithm) model (Stiller, 2000). In the comparisons, we consider data that were retrieved with the retrieval versions V5H_CFC-11_20 and V5H_CFC-12_20 for the FR period as well as V5R_CFC-11_220/221 and V5R_CFC-12_220/221 for the RR period (Kellmann et al., 2012). Version 220 covers the time period from January 2005 to April 2011 and version 221 is attributed to the time afterwards.

Table 1. Overview of important characteristics of the instruments used for the validation of the MIPAS CFC-11 and CFC-12 products. ILAS-II is only used for the validation of the MIPAS high spectral resolution (FR) period. ACE-FTS and MKIV are used to validate the MIPAS data from both periods, while the rest of the instruments only cover the reduced spectral resolution period.

	Emv sat/MIPAS (FR period) RR period	SCISAT/ACE-FTS	Aura/HRDLS	ADEOS-II/ILAS-II	MKV	Cryosampler	MIPAS-B	HATS	MIPAS-STR
Platform/ flight altitude	satellite/ ~800 km	satellite/ 650 km	satellite/ 705 km	satellite/ 803 km	balloon/ ~35–40 km	balloon/ ~34 km	balloon/ ~30–40 km	ground (in Arctic winter)	airplane/17–19 km
Measurement type	limb emission	solar occultation	limb emission	solar occultation	solar occultation	air sampling	limb emission	air sampling	limb emission
Observation period	(2002–2004) 2005–2012	since 2004	2005–2008	Dec. 2002– Oct. 2003	since 1989 ~22 flights	since 1982 ~50 flights	since 1989 24 flights	since 1977 monthly	since 1999 ~50 flights to hourly
Spectroscopic data	HITRAN 2000 ¹	HITRAN 2004 ²	HITRAN 2008 ²	Toon (pseudo- lines) 1995	Toon pseudo- line list	N/A	HITRAN 2000 ¹	N/A	HITRAN 2000 ¹
Spectral resolution	(0.025 cm ⁻¹) 0.0625 cm ⁻¹	0.02 cm ⁻¹	Radiometer	0.129 μm ⁻² ; 0.0032 μm ⁻⁴ ; 0.15 nm ⁻⁵	0.006 cm ⁻¹	N/A	0.0345 cm ⁻¹	N/A	0.036 cm ⁻¹
Vertical coverage	(~6–30 km) ~7–30 km	~6–27 km (316–17.8 hPa)	~8–28 km (316–17.8 hPa)	10–30 km	~5–38 km	~10–35 km	~10–30 km	surface	~5–20 km
CFC-11 Vertical resolution	(~3–7 km) ~2–6 km	~3–4 km	~1–1.2 km	1.5–2.5 km	~2–4 km	~1–2 km	~2–5 km	–	~1–2 km
Utilized microwindows	831–853 cm ⁻¹	830–858 cm ⁻¹ ⁶	834 cm ⁻¹	1610–850 cm ⁻¹ 846 cm ⁻¹	centered near	N/A	840–860 cm ⁻¹	N/A	842.5–848.0 cm ⁻¹
CFC-12 Vertical resolution	(~3–4 up to 8 km) slightly better	~3–4 km	~1–1.2 km	1.5–2.5 km	~2–4 km	~1–2 km	~2–5 km	–	~1–2 km
Utilized microwindows	915–925 cm ⁻¹	922 cm ⁻¹	915–932 cm ⁻¹	1610–850 cm ⁻¹	922–1161 cm ⁻¹	N/A	918–924 cm ⁻¹	N/A	918.9–920.6 cm ⁻¹ & 921.0–922.8 cm ⁻¹

¹ Rothman et al. (2003), ² Rothman et al. (2005) and updates thereof, ³ Spectrometers 1 & 2, ⁴ Spectrometer 3, ⁵ Spectrometer 4, ⁶ further microwindows are used to better constrain interferers.

The only change between these two versions is the source of the temperature a priori data. Initially, the a priori data were based on NILU's (Norwegian Institute of Air Research) post-processing of ECMWF (European Centre for Medium-Range Weather Forecasts) data. Later, they were taken from ECMWF directly as NILU's processing had ceased. Overall, the CFC data sets comprise more than 480 000 individual profiles for the FR period and more than 1.8 million profiles for the RR period. For reasons of legibility, MIPAS Envisat is referred to as MIPAS throughout this document, although other versions of the MIPAS instruments are also considered in this paper.

2.2 Comparison instruments

2.2.1 Cryosampler data

The cryosampler instrument is a balloon-borne cryogenic whole air sampler originally developed at Forschungszentrum Jülich (Germany) in the early 1980s (Schmidt et al., 1987). The cryosampler used in this comparison is the BONBON instrument. The first observations date back to 1982. The instrument consists of a Dewar with 15 stainless steel sampling containers which is filled with liquid neon to cool the sampling containers down to 27 K. This allows the sampling of a sufficient mass of air even at low pressures, which will freeze out immediately. The sampler inlets face downward; hence the BONBON measurements are optimized for the descending leg of the flight in order to avoid contamination from balloon outgassing. After the flight, the collected samples are analyzed on the abundance of a long list of trace gases by means of gas chromatography. In this comparison we consider five balloon flights that were performed by the University of Frankfurt (Germany) (e.g., Laube et al., 2008).

2.2.2 MkIV data

The Mark IV interferometer is a balloon-borne high-resolution Fourier transform spectrometer which has been developed at the Jet Propulsion Laboratory in Pasadena (USA) in the 1980s. The instrument employs the solar occultation technique measuring absorption spectra over a wide wavelength range from 650 to 5650 cm^{-1} (15.39–1.77 μm) with a very high spectral resolution of up to 0.006 cm^{-1} . Since 1989, more than 20 flights were conducted (Toon, 1991; Velazco et al., 2011). The flight duration varies between a few hours and up to 30 h, allowing one or two occultations to be taken during one flight. The occultations cover the altitude range between the tropospheric cloud tops and the floating altitude, which is typically within the 35–40 km range. The vertical sampling is about 2 to 4 km. The profile retrieval is based on an iterative nonlinear least-squares fitting algorithm with a derivative constraint. MkIV CFC-11 retrievals were performed using an empirical pseudo-linelist derived from the laboratory measurements of Li and Varanasi

(1994). MkIV CFC-12 retrievals used a pseudo-linelist derived from the laboratory measurements of Varanasi and Nemtchinov (1994). These linalists, and a description of their derivation, can be found at <http://mark4sun.jpl.nasa.gov/pseudo.html>. The vertical resolution of the retrieved data is close to the vertical sampling.

2.2.3 MIPAS-B data

MIPAS-B denotes a balloon-borne version of the MIPAS type of instruments and can be regarded as a precursor of the satellite instrument that flew on Envisat as described in Sect. 2.1. The instrument was developed in the late 1980s and early 1990s at the Institut für Meteorologie und Klimaforschung in Karlsruhe (Germany) and two models were built (Fischer and Oelhaf, 1996; Friedl-Vallon et al., 2004). MIPAS-B interferometers have been operated since 1989 (von Clarmann et al., 1993) and more than 20 flights have been carried out to date. MIPAS-B covers the wavenumber region from 750 to 2500 cm^{-1} (13.3 to 4 μm). Balloon-borne observations require excellent pointing accuracy which is realized by a sophisticated line of sight stabilization system. Also, multiple spectra taken at the same elevation angle are averaged to reduce the noise of the measurement data for the comparison with MIPAS. Typically, the MIPAS-B floating altitude lies between 30 and 40 km, and limb scans are performed with a vertical sampling of about 1.5 km up to this altitude. The retrieval algorithm for MIPAS-B observations is based on the same retrieval strategy and forward model as that employed by the MIPAS IMK/IAA processor; however the microwindows from which the CFC information is derived are slightly different. In total, eight balloon flights were performed during the lifetime of MIPAS. Five of these flights were conducted during the RR period from 2005 to 2012 which is the key period of the present comparisons.

2.2.4 MIPAS-STR data

The cryogenic Fourier transform infrared limb sounder Michelson Interferometer for Passive Atmospheric Sounding – STRatospheric aircraft (MIPAS-STR; Piesch et al., 1996) aboard the high-altitude research aircraft M55 Geophysica is the airborne sister instrument of MIPAS. Here, we use MIPAS-STR observations during the Arctic RECONCILE campaign (Reconciliation of essential process parameters for an enhanced predictability of Arctic stratospheric ozone loss and its climate interactions; von Hobe et al., 2013) for the validation of MIPAS observations. The characterization, calibration, retrieval and validation of the MIPAS-STR observations during the considered flight on 2 March 2010 are discussed by Woiwode et al. (2012). Characteristics of MIPAS-STR, the data processing and uncertainties of the retrieval results are briefly summarized in the following. Further information on MIPAS-STR is found in Keim et al. (2008), Woiwode et al. (2015) and references therein. MIPAS-STR em-

employs four liquid He-cooled detectors/channels in the spectral range between 725 and 2100 cm^{-1} (13.8 and 4.8 μm). The spectral sampling is 0.036 cm^{-1} . An effective spectral resolution of 0.069 cm^{-1} (full width at half maximum) is obtained after applying the Norton–Beer strong apodization (Norton and Beer, 1976). Depending on the sampling program, the dense MIPAS-STR limb observations cover the vertical range between ~ 5 km and flight altitude (in Arctic winter typically at 17 to 19 km geometrical altitude) and are complemented by upward-viewing observations. A complete limb scan including calibration measurements is recorded typically within 2.4 to 3.8 min. This corresponds to an along-track sampling of about 25–45 km.

Similar to the MIPAS data processing, the forward model KOPRA (Karlsruhe Optimized and Precise Radiative Transfer Algorithm; Stiller, 2000) and the inversion module KOPRAFIT (Höpfner et al., 2001), involving a first-order Tikhonov-type regularization, were used. The retrieval was performed sequentially, i.e., species with low spectral interference with other gases were retrieved first. Then, their mixing ratios were kept constant in the subsequent retrievals of the following species. Additional retrieval parameters were spectral shift and wavenumber-independent background continuum for each microwindow. Typical vertical resolutions of 1–2 km were obtained between the lowest tangent altitude and flight altitude.

2.2.5 Aura/HIRDLS data

The High Resolution Dynamics Limb Sounder (HIRDLS) was an instrument that performed observations aboard NASA's (National Aeronautics and Space Administration) Aura satellite (Gille et al., 2008). The satellite was launched into a sun-synchronous orbit at an altitude of 705 km. During launch, large parts ($\sim 85\%$) of the instrument's aperture got blocked by a plastic film that was dislocated. This impacted both the performance of the radiometer as well as the geographical coverage of the observations. Useful vertical scans could only be performed at a single azimuth angle of 47° backward to the orbital plane on the far side of the sun. Hence, the latitudinal coverage was limited to $65^\circ S$ to $82^\circ N$ and in the longitudinal domain, the coverage degraded to the orbital separation. On 17 March 2008 the instrument's chopper failed, ending the measurement period that started in January 2005.

Like MIPAS, HIRDLS measured the thermal emission at the atmospheric limb in the altitude range between 8 and 80 km. The instrument had 21 channels in the wavelength range between 566.9 and 1632.9 cm^{-1} (17.64 and 6.12 μm). Profile data are retrieved with a maximum a posteriori retrieval based on the optimal estimation theory (Rodgers, 2000). In the present comparison, data from the retrieval version 7 are used (Gille et al., 2014). The single profile precision for both species minimizes between 200 and 100 hPa, with values in the range between 10 and 20%. Below, the

precision is within the order of 50%, while above it degrades with increasing altitude to values of more than 100%. The mean HIRDLS errors shown in the comparisons are derived from the variability of the retrieved species (Gille et al., 2014, Sects. 5 and 5.4.), using the average of 10 sets of 12 consecutive profiles of regions with little variability. In total the HIRDLS data set comprises more than 6.3 million individual profiles that can be used for comparison with the MIPAS reduced resolution observations. A one-time normalization of the HIRDLS radiances relative to the Whole Atmosphere Community Climate Model (WACCM) was completed, and applied to all the HIRDLS CFC radiances. This affects the absolute CFC values but the morphologies and relative values are unchanged.

2.2.6 SCISAT/ACE-FTS data

The Atmospheric Chemistry Experiment Fourier Transform Spectrometer (ACE-FTS) is an instrument aboard the Canadian SCISAT satellite (Bernath et al., 2005). SCISAT was launched into a high inclination (74°) orbit at 650 km altitude on 12 August 2003. The ACE-FTS instrument utilizes the solar occultation technique measuring the attenuation of sunlight by the atmosphere during 15 sunsets and 15 sunrises a day in two latitude bands. The viewing geometry and the satellite orbit allow a latitudinal coverage between $85^\circ S$ and $85^\circ N$ over a year with a clear focus on midlatitudes and high latitudes. The instrument scans the atmosphere between the middle troposphere and 150 km, obtaining spectra in the wavelength range between 750 and 4400 cm^{-1} (13.3 and 2.3 μm) with a spectral resolution of 0.02 cm^{-1} . The vertical sampling varies as function of altitude and is also dependent on the beta angle, which is the angle between the orbit track and the direction the instrument has to look to see the sun. In the middle troposphere the sampling is around 1 km, between 10 and 20 km altitude it is typically between 2 and 3.5 km and in the upper stratosphere and mesosphere the sampling declines to 5 to 6 km. The instrument has a field of view of 1.25 mrad which corresponds to 3–4 km depending on the exact observation geometry.

In the comparisons, ACE-FTS data from the retrieval version 3.5 are employed, which currently cover the time period from early 2004 into 2013. The ACE-FTS retrieval uses a weighted nonlinear least-squares fit method in which pressure and temperature profiles are derived in a first step, followed by the volume mixing ratios of a vast number of species (Boone et al., 2005). The retrieval of CFC-11 data utilizes spectral information from four microwindows. The main window is located between 830 and 858 cm^{-1} (12.05 and 11.65 μm), similar to the MIPAS IMK/IAA retrieval. The other microwindows are much smaller and are centered at 2976.5 cm^{-1} (3.35 μm), 1977.6 cm^{-1} (5.06 μm) and 1970.1 cm^{-1} (5.08 μm). However, the latter microwindows do not contain information on CFC-11 but are included to improve the retrieval for interfering species (Boone et al.,

2013). Individual profiles exhibit precisions within 5 % up to almost 20 km, increasing to 40–50 % at the highest altitudes covered. The ACE-FTS CFC-12 profiles are usually cut off at higher altitudes than the CFC-11 profiles, but exhibit similar precision estimates. The cut-off criteria for CFC-11 and CFC-12 are empirical functions as follows:

- for CFC-11:

$$z_{\text{top,CFC-11}} = 28 - 5 \cdot \sin^2(\varphi); \quad (1)$$

- for CFC-12:

$$z_{\text{top,CFC-12}} = 36 - 8 \cdot \sqrt{\sin(\varphi)}, \quad (2)$$

where $z_{\text{top,CFC-11}}$ and $z_{\text{top,CFC-12}}$ are the altitudes (in kilometers) at which the profile is cut off for CFC-11 and CFC-12, respectively, and φ is the latitude. Overall, there are about 27 000 CFC-11 and CFC-12 profiles available for comparison, of which 375 cover the MIPAS FR period.

2.2.7 ADEOS-II/ILAS-II

The second version of the Improved Limb Atmospheric Spectrometer (ILAS-II) was a Japanese solar occultation instrument aboard the Advanced Earth Observing Satellite-II (ADEOS-II), also known as Midori-II Nakajima et al. (2006). After more than 10 months, on 24 October 2003, the satellite failed due to a malfunction of the solar panels. ADEOS-II used a sun-synchronous orbit at 800 km altitude and an inclination of 98.7°, performing typically 14 orbits per day. The corresponding 28 occultations covered exclusively higher latitudes, i.e., polewards of 64° in the Southern Hemisphere and between 54 and 71° in the northern counterpart. The instrument consisted of four grating spectrometers, obtaining spectral information in the infrared (spectrometer 1: 6.21–11.76 $\mu\text{m}/850\text{--}1610 \text{ cm}^{-1}$; spectrometer 2: 3.00–5.70 $\mu\text{m}/1754\text{--}3333 \text{ cm}^{-1}$; spectrometer 3: 12.78–12.85 $\mu\text{m}/778\text{--}782 \text{ cm}^{-1}$) and very close to the visible wavelength range (spectrometer 4: 753–784 nm/12 755–13 280 cm^{-1}).

The instantaneous field of view was 1 km in the vertical domain and between 2 and 21.7 km in the horizontal domain, depending on the spectrometer.

In the comparisons we employ results from the latest retrieval version 3. The retrieval is based on an onion peeling method Yokota et al. (2002). Multiple parameters for gases and aerosols are derived simultaneously on a 1 km altitude grid using a least-squares fit (Oshchepkov et al., 2006). The CFC results are based on the spectrum obtained by spectrometer 1 that is fitted in its entirety. For the comparisons with MIPAS more than 5600 individual profiles are available, covering the time period from April to October 2003 Nakajima

et al. (2006), and thus provide comparison measurements for the MIPAS FR period. For sunrise measurements, only measurements below 34 km were considered as suggested by the data provider.

2.2.8 HATS data

HATS denotes the Halocarbons and other Atmospheric Trace Species group at NOAA's (National Oceanic and Atmospheric Administration) Earth System Research Laboratory in Boulder (USA). Since 1977 this group has conducted observations of surface levels of N_2O and several CFCs, providing a long-term reference (e.g., Elkins et al., 1993; Montzka et al., 1996). These measurements are analyzed by gas chromatography, either with electron capture detection or with detection by mass spectrometry. The observations started at six locations; currently 15 locations are covered on all continents except Asia. Data from different measurement techniques and instruments are combined to provide the longest possible monthly mean time series for the individual locations. In the comparison we check whether the tropospheric MIPAS observations exceed the upper volume mixing ratio limit that is given by the HATS observations and whether their temporal development is consistent. HATS data are available for more than a dozen stations during the MIPAS measurement period. Their measurements were weighted with the cosine of latitude, and an average was calculated for each month.

3 Validation methods

In order to reduce the influence of natural variability and sampling artifacts, the majority of the comparisons were performed using collocated pairs of measurements. During this study, the coincidence criteria applied in most of the cases were a maximum distance of 1000 km and maximum time difference of 24 h. In the case of HIRDLS the criteria were cut down to a distance of 250 km and a time difference of 6 h, due to the large number of measurements of the instrument. No measurement is taken into account twice, meaning that only the best coincidence is taken in cases where two measurements of one instrument collocate with the same measurement of the other instrument. For MIPAS-B comparisons, diabatic 2-day forward and backward trajectories were calculated by the Free University of Berlin (J. Abalichin, private communication, 2014). The trajectories are based on ECMWF $1.25^\circ \times 1.25^\circ$ analyses and start at different altitudes at the geolocation of the balloon observation to search for a coincidence with the satellite measurement along the trajectory path within a matching radius of 1 h and 500 km. Data of the satellite match have been interpolated onto the trajectory match altitude, such that these values can be directly compared to the MIPAS-B data at the trajectory start point. The MIPAS averaging kernels were not applied in any

of the comparisons, due to two reasons. First of all, most of the instruments used for comparison have a vertical resolution similar to that of MIPAS. In addition, the vertical profiles of CFC-11 and CFC-12 are very smooth. They do not contain any obvious extrema – as, for example, ozone does – and thus smoothing with the MIPAS averaging kernel was shown to have only minor effects on the profiles.

The data of remote sensing instruments used for the comparison were interpolated onto the MIPAS retrieval grid, which is a fixed altitude grid with 1 km spacing in the altitude range relevant for comparison of CFC-11 and CFC-12. When provided on an altitude grid, the instruments' measurements were interpolated linearly onto the MIPAS grid, while in the case of a pressure grid, the MIPAS pressure–altitude relation was used after logarithmic interpolation.

For the comparison of MIPAS-STR, HIRDLS, ACE-FTS and ILAS-II, we use the following statistics: the mean difference:

$$MD = \frac{1}{n} \sum_{i=1}^n (x_{i,MIPAS} - x_{i,comp}); \quad (3)$$

the standard deviation (SD) of the differences:

$$\sigma_{\Delta x} = \sqrt{\frac{1}{n-1} \sum_{i=1}^n ((x_{i,MIPAS} - x_{i,comp}) - MD)^2}; \quad (4)$$

the standard error of the mean differences:

$$\sigma_{\overline{\Delta x}} = \frac{\sigma_{\Delta x}}{\sqrt{n}}; \quad (5)$$

and the combined error of the measurements:

$$\sigma_{combined} = \sqrt{\sigma_{mean,MIPAS}^2 + \sigma_{mean,comp}^2}, \quad (6)$$

where σ_{mean} are the averaged random errors of the respective instruments. $\sigma_{\overline{\Delta x}}$ is the adequate quantity for the assessment of the mean difference.

Correspondingly, if the combined error is smaller than the standard deviation of the differences, this hints at error estimates being too small, e.g., if not all sources of errors are considered or the retrieval error is underestimated. Since the measurements are not taken exactly at the same location and time, natural variability also contributes to differences between the combined error and the standard deviation (von Clarmann, 2006).

For comparisons to the HATS network, MIPAS measurements at 3 km below the tropopause are used. The altitude where the tropopause is located was calculated from each MIPAS temperature profile as follows.

- Between 25° S and 25° N the altitude at 380 K potential temperature was used.
- At higher latitudes the WMO criterion was used, e.g., the altitude where the vertical temperature gradient drops below 2 K km^{-1} and remains that small within a layer of 2 km.

The MIPAS CFC mixing ratio at 3 km below the tropopause altitude is chosen for each MIPAS profile. Cases for which the estimation of the tropopause height went obviously wrong were rejected. All available MIPAS measurements are used. To increase comparability of the data sets, monthly zonal means were calculated from MIPAS measurements in 10° bins. In addition, these zonal means (and their standard deviation) were weighted with the cosine of the latitude to simulate the approach performed for the HATS data. Since some of the MIPAS detectors were shown to have time-dependent nonlinearity correction functions due to detector aging (Eckert et al., 2014), we estimated drifts caused by this feature from a small subset of data. The comparison with HATS exhibits differences in the trends of MIPAS and the HATS time series. We compared the differences in these trends with the drift estimated due to detector aging. For the latter we calculated the mean drift by interpolating the drifts to 3 km below the tropopause and weighting them with the cosine of the latitude.

4 Validation results

The comparisons between MIPAS and the independent measurements were performed by applying the validation schemes described in Sect. 3. The results of these comparisons are discussed in the following, first for CFC-11 and, subsequently, for CFC-12. The mean distance and time for comparisons based on collocated measurements (e.g., with MIPAS-STR, HIRDLS, ACE-FTS and ILAS-II) are shown in Table 2.

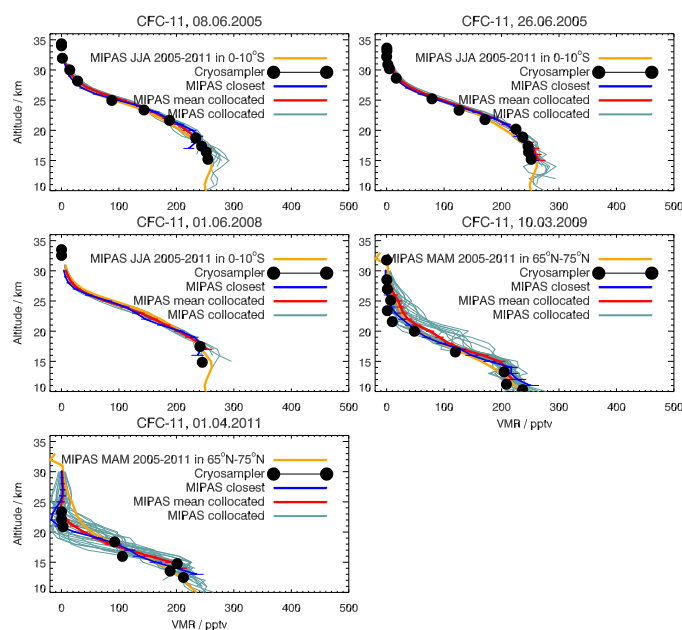
4.1 CFC-11: reduced spectral resolution period (RR)

4.1.1 Results CFC-11: cryosampler

Multiple MIPAS profiles are compared to those of the cryosampler (Fig. 2). For each cryosampler profile (black dots), several MIPAS profiles meet the coincidence criteria (blue-grayish lines). The latter cover a considerable range of variability. The closest MIPAS profile (blue solid line) matches the cryosampler profile remarkably well in all five cases, with maximum differences of 30 pptv ($\sim 13\%$), except for the 10–15 km region on 3 October 2009 (right column, bottom panel). In addition, the mean of all coincident MIPAS profiles (red line) agrees reasonably well with the cryosampler profile, suggesting that the air within the entire region meeting the coincidence criteria is well represented by the cryosampler. Contrary to that, the respective seasonal zonal mean of MIPAS measurements (light orange line) occasionally deviates considerably from the actual measurements, particularly on 1 April 2011. On the other hand, the same seasonal mean (March/April/May 2005–2011) can agree well with the collocated mean and the closest MIPAS profile as well as the cryosampler measurement as for the comparison on 10 March 2009 (lower right panel). This confirms that

Table 2. Mean matching distance and time for comparisons based on collocated measurements.

Envisat/MIPAS data set	MIPAS-STR	Aura/HIRDLS	SCISAT/ACE-FTS	ILAS-II
CFC-11 FR-period	–	–	356 km–6.24 h	365 km–3.25 h
CFC-12 FR-period	–	–	328 km–5.59 h	365 km–3.25 h
CFC-11 RR-period	172 km–1.76 h	199 km–2.89 h	376 km–5.84 h	–
CFC-12 RR-period	172 km–1.76 h	199 km–89 h	379 km–5.99 h	–

**Figure 2.** Comparison of a climatological mean of MIPAS CFC-11 measurements (light orange line), collocated measurements (blue-grayish lines) and their mean profile (red line) and the closest MIPAS profile (blue line) with different flights of the cryosampler (black dots).

both the cryosampler and MIPAS can reliably detect atmospheric conditions deviating largely from the climatological state. Similar patterns were found for the 1 April 2011 comparison of MIPAS and cryosampler for other trace gases for this specific cryosampler flight (Chirkov et al., 2016). In this particular case, strong stratospheric subsidence has led to extraordinarily low mixing ratios of CFCs. This uncommon atmospheric situation went along with substantial ozone destruction (Manney et al., 2011; Sinnhuber et al., 2011).

4.1.2 Results CFC-11: Mark IV

Only one measurement of the balloon-borne MkIV instrument (black line in Fig. 3) coincides with MIPAS measurements during the RR period. Three collocated profiles of

MIPAS (blue-grayish lines) were found, of which also the mean profile (red line) and the closest profile (blue line) are shown. Up to approximately 25 km, the MkIV profile reports higher mixing ratios than all of the MIPAS profiles, especially compared with the closest MIPAS profile. However, the gradient of the MkIV profile and all MIPAS profiles is very much alike between ~ 17 and 24 km. Contradictory to the comparison with the cryosampler, the closest coincident MIPAS profile deviates most from the MkIV profile throughout the whole altitude range. While the three collocated measurements lie within the MkIV error bars from the lower end of the profiles up to ~ 17 km, this is generally not the case from that altitude upwards, but only around the crossing point of the MkIV profile with the MIPAS profiles at about 25–26 km. Up to that altitude, the MkIV profile ex-

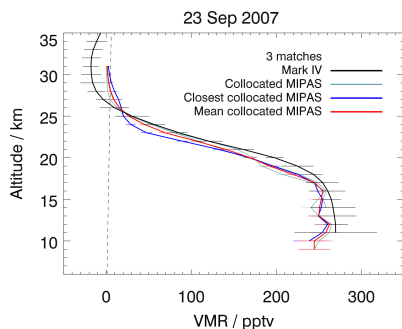


Figure 3. Comparison of one MkIV CFC-11 profile (black line) with three coincident profiles of MIPAS (blue-grayish lines). The closest (blue line) and the mean (red line) of these profiles are shown in addition. The MkIV error estimates are inferred from the fit residuals.

hibits higher mixing ratios of CFC-11 than MIPAS, while above, MkIV shows lower, mostly negative values. However, the differences with the MIPAS mean profile rarely exceed 20 pptv, except for around 20 km where we find deviations of up to 30 pptv. This corresponds to less than 10% at the lower end of the profile and up to 15% around 20 km. Velazco et al. (2011) found similar differences in their comparisons of ACE-FTS and MkIV, which are based on noncoincident validation using a potential vorticity/potential temperature (PV/Theta) coordinate system (Manney et al., 2007). They also find largest deviations of the profiles around or slightly below 20 km, with maximum differences of up to ~18% and minimum differences of the order of ~5% around 17 km. Above 20 km, the mean profile of MIPAS and the MkIV profile agree well. Differences mainly stay within 10%, except for above 26 km where MkIV mixing ratios become negative. Considering the small number of coincident MIPAS profiles (3), the instruments agree reasonably well below 20 km and well between 20 and 26 km.

4.1.3 Results CFC-11: MIPAS-B

For the comparison with two independent measurements of MIPAS-B, trajectory-corrected profiles of the instrument were used (Fig. 4, Sect. 3). In the comparison for the MIPAS-B flight of 24 January 2010, the agreement with MIPAS is remarkably good above ~18 km as it stays well within 10 pptv. Below this altitude the mean profile of all collocated MIPAS measurements (Fig. 4: upper left panel; solid red line) shows higher values than the MIPAS-B profile (solid black line). However, the values of all collocated MIPAS profiles (red squares) cover a wider range, such that the MIPAS-B profile lies within their spread at all altitudes. The profiles deviate by approximately 30 pptv (~30%) at

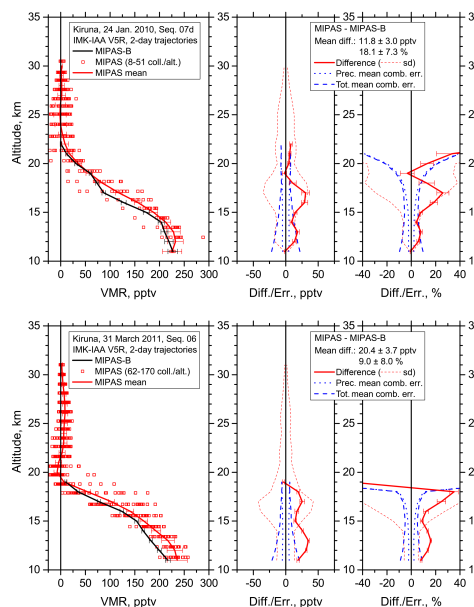


Figure 4. Comparison of a mean profile of MIPAS CFC-11 collocated measurements (left panels: red line) with a profile of MIPAS-B (black line) obtained on 24 January 2010 (upper panels) and 31 March 2011 (lower panels) at Kiruna. The error bars (1σ ; left panel) show the total error without the spectroscopy error for MIPAS and MIPAS-B. The difference is shown in absolute (middle panels) and relative (right panels) terms. The dotted red line is the standard deviation and the dashed blue line is the combined error which consists of the root of the squared error of MIPAS-B and the MIPAS mean.

the largest around 16–17 km (middle and right panel) and stay within 20 pptv (corresponding to ~10% at the lower end of the profile) for the rest of the covered altitude range. Throughout the whole vertical extent, MIPAS shows higher mixing ratios of CFC-11. However, the bias does rarely exceed the standard deviation of the differences. Large percentage errors above 19 km occur due to division by very small absolute amounts of CFC-11 at these altitudes. The combined error shows the total error estimate for both instruments. However, the error component of the spectroscopy was left out, since both instruments use the same spectroscopic data, meaning this effect should cancel out and thus cannot explain possible differences between the combined error and the standard deviation. Below 15 km, the combined error of the two instruments and the standard deviation of the differences are similar, except for the lowermost point of the profile. Above this altitude the combined error is considerably smaller than the standard deviation, hinting at either

an underestimation of the error by one or both of the instruments. Natural variability cannot be excluded as a source of the deviation either. The MIPAS profile is smoother, presumably due to several measurements being averaged to a mean profile. The flight on 31 March 2011 (Fig. 4, lower panels) supports the conclusions drawn from the first comparison. Maximum differences are slightly larger (close to 35 pptv at the largest). The largest deviations between the MIPAS mean profile and the measurements of MIPAS-B appear at altitudes around 13 km, and, here, exceed the standard deviation of the differences. Around 17 km a second peak occurs in the differences, which is at similar altitudes as for the first comparison. Similar as for the first comparison, the combined error and the standard deviation of the differences are very close, while the standard deviation of the differences is significantly larger than the combined error above this altitude. This rather hints at an underestimation of the error by one or both instruments above ~ 15 km than the feature being attributed to natural variability. In general, both comparisons support the impression of MIPAS showing slightly higher values of CFC-11 below ~ 18 km, even though the MIPAS-B profile is still included within the spread of all MIPAS collocated profiles (left panel: red squares). The shape of the profiles, in terms of slope and reversal points, agrees well for both comparisons. Differences might be due to horizontal viewing direction and/or horizontal smoothing by the MIPAS-B measurement, since the observations are combined using trajectories which are associated with the localized coordinates. This is most important in the presence of pronounced atmospheric structures and strong gradients, e.g., the mixing barrier associated with the polar vortex.

4.1.4 Results CFC-11: MIPAS-STR

Seven profile pairs of collocated measurements were found for comparisons of MIPAS with MIPAS-STR (Fig. 5). The comparison is performed using mean profiles, rather than comparing each set of collocated pairs. Since MIPAS-STR profiles were originally retrieved on a finer altitude grid (left panel; blue line) than MIPAS profiles (red line), these profiles were interpolated onto the MIPAS grid (black line). The agreement of the profiles is good and the vertical structure is similar, showing minimum differences around 16–17 km for both instruments. Differences are largest at the bottom end of the profiles at 8 km (middle panel). However, they do not exceed 30 pptv (corresponding to up to $\sim 15\%$ below 12 km and up to $\sim 20\%$ around 14 km at the largest) throughout the rest of the profile and are not significant for the majority of the altitude levels. Above 14 km, the differences mainly stay within 10 pptv corresponding to ~ 3 to 15%. The mean difference oscillates around zero, which is most pronounced at altitudes below ~ 15 km. As for the comparison with MIPAS-B, the total error is shown for both instruments but the spectroscopy error is left out because MIPAS and MIPAS-STR use the same spectroscopic data. The

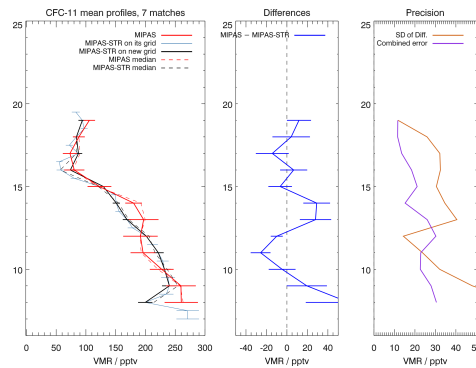


Figure 5. Comparison of mean profiles of MIPAS CFC-11 (left panel, continuous red line) and MIPAS-STR (left panel, continuous black line) for seven collocated measurements taken during a flight on 2 March 2010. The error bars consist of the total error without the spectroscopy error for both MIPAS and MIPAS-STR. The dashed lines show the median of each data set. The middle panel shows the mean difference (blue) of these profiles and the standard error of the mean. The right panel shows the combined error (purple) of the instruments and the standard deviation of the differences (brown).

standard deviation of the differences (right panel; brown line) exceeds the estimated combined error (purple line) for most of the covered altitude range. It is rather likely that this difference is due to natural variability than an underestimation of the error budget of either instrument, since there is also a region (around 12 km) where this is the opposite, even though the mean distance and time difference are only about 170 km and 1 h 45 min, respectively (see Table 2).

4.1.5 Results CFC-11: HIRDLS

The results of the comparison of MIPAS CFC-11 with that of HIRDLS are displayed in Figs. 6–8. Figure 6 shows that the HIRDLS profiles scatter the most at the ends of the profiles, e.g., at rather high altitudes (around ~ 30 km; blue-greenish points) and the lowermost altitudes (around ~ 10 km; red-yellowish points). It is also apparent that the measurements of HIRDLS CFC-11 cover a large range of values at all altitudes, which is evident in the large scatter throughout the whole vertical extent, with the largest spread at the lower end of the profiles, i.e., at high CFC-11 mixing ratios. Negative CFC-11 values do not exist in the HIRDLS results because the retrieval for the volume mixing ratio is logarithmic. The histograms shown in Fig. 7 give a more detailed picture of the frequency distributions of the CFC-11 mixing ratios of MIPAS (top panels) and HIRDLS (bottom panels) measurements at 16 km (left panels) and 23 km (right panels). The mean and the median are close in all four cases. Both

3366

E. Eckert et al.: MIPAS IMK/IAA CFC-11 and CFC-12: accuracy, precision and long-term stability

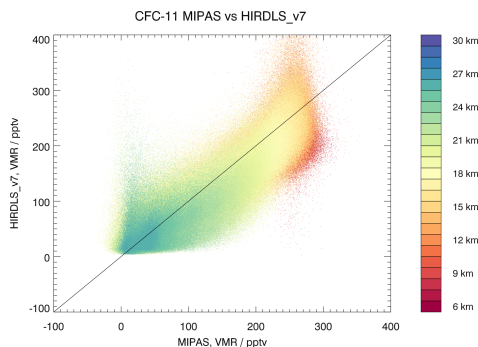


Figure 6. Correlation of collocated MIPAS CFC-11 measurements with HIRDLS measurements during the time period of 2005 to 2008.

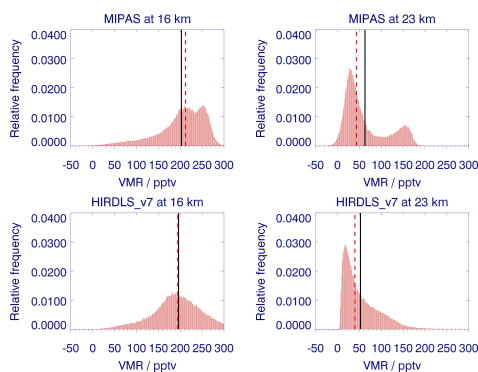


Figure 7. Histogram of collocated MIPAS CFC-11 measurements (top panels) and HIRDLS measurements (bottom panels) for the years of 2005–2008 at 16 km (left panels) and 23 km (right panels). The black line indicates the location of the mean of the sample, while the red dashed line marks the median.

at 16 and at 23 km, MIPAS seems to see a bimodal distribution (which is much more pronounced at 23 km), while HIRDLS only exhibits one obvious peak at 16 km and a slight shoulder, which seems to be a smeared-out second mode, at 23 km. In both cases HIRDLS does not see the distinct second mode at higher values visible in MIPAS measurements around 250 pptv at 16 km and around 150 pptv at 23 km. The peak at lower mixing ratios appears around similar values for both instruments, slightly below 200 pptv at 16 km and between 0 and 50 pptv at 23 km. The maximum is shifted slightly towards lower mixing ratios in the case of HIRDLS.

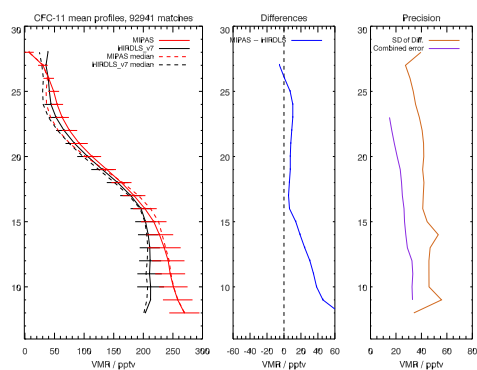


Figure 8. Comparison of mean profiles of MIPAS CFC-11 (left panel, continuous red line) and HIRDLS (left panel, continuous black line) for the years of 2005–2008. The error bars include the total error in the case of MIPAS and the estimated error – which is derived from the average of 10 sets of 12 consecutive profiles of regions with little variability (Gille et al., 2014) – in the case of HIRDLS. The dashed lines show the median of each data set. The middle panel shows the mean difference (blue) of these profiles and the standard error of the mean. The right panel shows the combined error (purple) of the instruments and the standard deviation of the differences (brown).

The comparison of the mean profiles (Fig. 8, left panel), which are calculated from more than 90 000 collocated profiles of HIRDLS (black) and MIPAS (red) over all latitudes, shows good agreement of the two instruments down to ~ 16 km. Deviations stay within 10–15 pptv above this altitude. Below, MIPAS continuously shows higher mixing ratios of CFC-11 than HIRDLS (middle panel), with differences reaching as high as 60 pptv at the bottom end of the profile. This presumably reflects the more pronounced second mode in the MIPAS frequency distribution (Fig. 7). However, MIPAS CFC-11 mixing ratios are no more than 40 pptv ($\sim 20\%$) larger than those of HIRDLS at altitude ranges between 9 and 16 km. At the bottom end of the profiles, the largest deviations of the mean profiles of MIPAS and HIRDLS can be found. The error bars (left panel) shown for MIPAS depict the total error, while HIRDLS error bars represent an estimated error, derived from 10 sets of 12 consecutive profiles at regions of little variability (Gille et al., 2014). In the right panel, the combined error is compared to the standard deviation of the differences. The covered vertical range of the combined error is smaller, since HIRDLS error estimates were only given for these altitude levels. Presumably, a combination of an underestimation of either or both error budgets and natural variability result in the differences between the combined error and the standard deviation of the differences. Due to the fact that the coincidence crite-

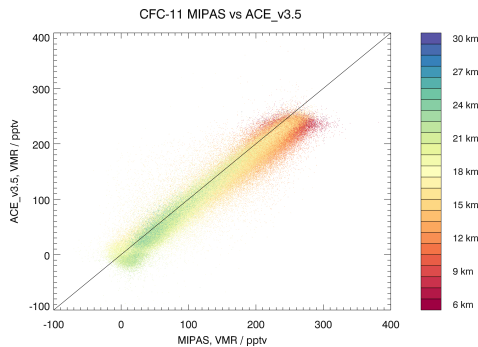


Figure 9. Correlation of collocated MIPAS CFC-11 measurements with ACE-FTS measurements during the time period of 2005 to 2012.

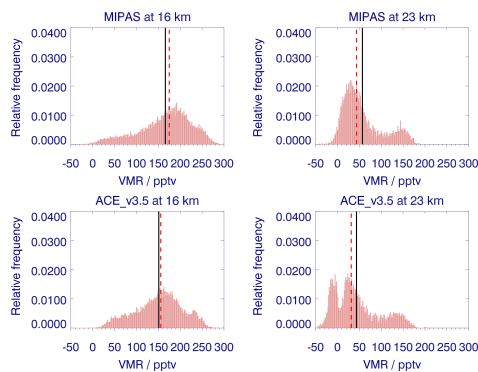


Figure 10. Histogram of MIPAS CFC-11 measurements (top panels) and ACE-FTS measurements (bottom panels) for the years 2005–2012 at 16 km (left panels) and 23 km (right panels). The black line indicates the location of the mean of the sample, while the red dashed line marks the median.

ria allow for certain differences in time and geolocation, the mean distance between the collocated measurements is approximately 200 km and the time difference is nearly 3 h (Table 2). However, this effect is presumably less important than for the comparison with, e.g., ACE-FTS for which the mean distance and time difference are about twice as large as for the comparison with HIRDLS. Overall, the agreement of MIPAS and HIRDLS CFC-11 measurements is excellent down to approximately 15 km as differences rarely exceed 10 pptv. Below that altitude, MIPAS exhibits a slight high bias. However, it is important to remember that HIRDLS CFC radiances have been normalized using WACCM, so slight biases might also occur because of this.

4.1.6 Results CFC-11: ACE-FTS

The correlation between MIPAS and ACE-FTS CFC-11 measurements (Fig. 9) is very close to linear, even though MIPAS measures slightly higher CFC-11 values in general. This is most obvious at higher CFC-11 mixing ratios, e.g., at lower altitudes (red-yellowish points) where the correlation is slightly off the 1:1 relation. The values do not scatter as much as for HIRDLS, presumably due to the fact that in the case of ACE-FTS the signal to noise ratio is better, since it measures in occultation. The distribution of the mixing ratios at 16 km (Fig. 10: left panels) and 23 km (right panels) agree reasonably well for the two instruments. The skewness is very similar for both instruments, but the multimodal scheme is more pronounced for ACE-FTS at 16 km. A frequency maximum of mixing ratios appears slightly below 200 pptv in the case of MIPAS and between 150 and 200 pptv in the case of ACE-FTS. There is a second peak around 250 pptv in the ACE-FTS measurements which is less pronounced in the MIPAS values. At 23 km, both instruments show a bimodal distribution of the mixing ratios, with values peaking between 0 and 50 pptv and close to 150 pptv. The ACE-FTS frequency distribution exhibits an additional peak at negative values, which are unphysical. The upper limit of the ACE-FTS CFC-11 retrieval for the polar region is 23 km. For these occultations, the spectrum presumably contains little CFC-11 signal near 23 km and the retrieval is possibly compensating for some effect (e.g., bad residual from one of the interferers, mild channeling in the interferometer, a contribution to the spectral region from the aerosol layer) by giving negative CFC-11 mixing ratios. Similar to HIRDLS, the main mode at 23 km is shifted to slightly lower values in the case of ACE-FTS compared to MIPAS.

The figure of the mean profile comparison (Fig. 11) supports the conclusion from Fig. 9 that MIPAS sees higher volume mixing ratios of CFC-11. This is most pronounced at lower altitudes, approximately below ~ 17 –18 km (left and middle panel), where MIPAS CFC-11 mixing ratios (red line) are about 20 pptv (less than 10%) higher than those of ACE-FTS, both compared to ACE-FTS on its original grid (blue line) and interpolated onto the MIPAS grid (black line). Again, MIPAS error bars represent the total error. The ACE-FTS errors are the random errors from the least-squares fitting process, the square root of the diagonal elements of the covariance matrix. Additionally, the error budget of the version 3.5 ACE-FTS data contains an additional term in the reported error. This term is derived from the difference between a retrieved CO_2 volume mixing ratio (VMR) profile and the assumed CO_2 VMR profile employed in the pressure/temperature retrieval and is a measure of the ability of the retrieval system to reproduce the fixed input profile for the given occultation (Boone et al., 2013). The right-hand panel shows that the combined error (purple line) is often larger than the standard deviation of the differences (brown line) for almost the complete altitude range. This suggests

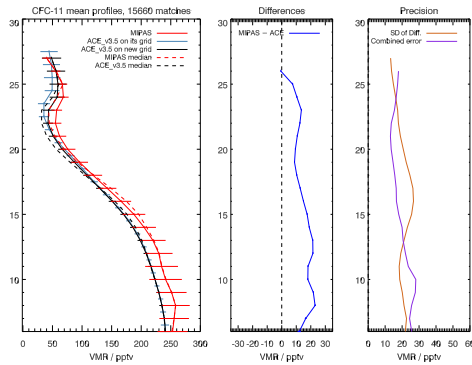


Figure 11. Comparison of mean profiles of MIPAS CFC-11 (left panel, continuous red line) and ACE-FTS (left panel: blue line denotes ACE-FTS on native grid; continuous black line denotes ACE-FTS interpolated onto the MIPAS grid) for the years of 2005–2012. The error bars include the total error for MIPAS and the random errors from the least-squares fitting process for ACE-FTS. The dashed lines show the median of each data set. The middle panel shows the mean difference (blue) of these profiles and the standard error of the mean. The right panel shows the combined error (purple) of the instruments and the standard deviation of the differences (brown).

that for one or both of the instruments, the error budget is overestimated, but rather large natural variability compensates the effect where the standard deviation of the differences exceeds the combined error. The latter plays a more important role than for e.g., HIRDLS, since the coincidence criteria for ACE-FTS with MIPAS are considerably less strict compared to those of the HIRDLS comparison and the mean distance and mean time difference are about 350 km and more than 6 h, respectively (Table 2) and thus are about twice as large as those of the HIRDLS comparison.

Around 25 km (left panel) one can see a feature not known from any previous CFC-11 profiles, represented as a bump of suddenly increasing values. This increase in CFC-11 around 25 km does not originate from an actual atmospheric state, but is simply a sampling issue. ACE-FTS profiles are cut off at the upper end, when the mixing ratios become too small to be retrieved satisfactorily. Since CFC-11 values are largest in the tropics, the profiles are cut off at higher altitudes than in polar regions; i.e., above 23 km only tropical – higher – values are shown. However, Fig. 11 shows the global mean of all collocated ACE-FTS and MIPAS profiles. Hence, around 25 km the mean is suddenly strongly dominated by tropical profiles, dragging it to higher values. Furthermore, it is admittedly not intuitive that regridding systematically adds a bias to the ACE-FTS profiles (interpolation from blue to black line). This shift towards mixing ratios valid at approximately 0.5 km below does not appear in the interpolated sin-

gle profiles but only in the mean of the interpolated profiles. This is a pure sampling effect caused by the same mechanism as the artificial bump explained above: due to the resampling on the MIPAS grid, the ACE-FTS cut-off altitude – and thus the bump – are shifted 500 m downwards.

Overall the MIPAS and ACE-FTS CFC-11 measurements agree reasonably well as the differences stay within 20 pptv over almost the entire altitude range. This comparison contradicts the conclusion from other comparisons that MIPAS has a slight high bias at the lower end of the profile, even though the effect is far less pronounced. If the comparison is broken down into latitude bands (Fig. A2) the bump disappears. In addition, this breakdown into several latitude bands indicates that the tendency of MIPAS to detect higher amounts of CFC-11 at the lower end of the profile is more pronounced at higher latitudes. Similar results have been found by Tegtmeyer et al. (2016), who also find a slight high bias in their comparison of MIPAS and a multi-instrument mean (MIM) CFC-11 that seems to be more pronounced at higher latitudes. This feature is also visible in the latitudinal breakdown of the comparison with HIRDLS (Fig. A1).

The behavior of the tropical profiles in these figures is also interesting. Compared to ACE-FTS, the MIPAS profile shows slightly increasing CFC-11 mixing ratios up to ~15 km. An increase, from the bottom of the profile upwards, is also visible in ACE-FTS, but it is far less pronounced. The latitudinal breakdown for HIRDLS and MIPAS shows that this increase is most pronounced in HIRDLS. This behavior of the mean profile is suspicious, since CFC-11 mixing ratios are expected to be constant throughout the troposphere, since CFC-11 is well mixed, which might hint at problems concerning the retrieval and/or spectroscopic data in this region.

4.1.7 Results CFC-11: HATS

The high bias of MIPAS CFC-11 below approximately 15–17 km detected so far is further quantified by comparison to ground-based measurements of the HATS network (Fig. 12). Similar mixing ratios of stable source gases are to be expected at the surface and in the upper troposphere. Instead, the mean of the MIPAS measurements (continuous red line with large red circles) is about 10 to 15 pptv (~5%) higher than the mean of the data collected by the HATS network (continuous black line). Since the troposphere is well mixed, these values should agree well, which indicates a slight high bias of the MIPAS measurements. Both MIPAS and the HATS data exhibit a descending slope during the RR period (2005–2012 in Fig. 12) in their time series, but the decrease in MIPAS measurements seems to be slightly steeper. This effect is slightly more pronounced than the estimated drift at this altitude (Sect.7, Fig. 34, left panel). Absolute drifts due to detector aging at 3 km below the tropopause were estimated to be -3.58 pptv decade $^{-1}$. The drift estimated from the difference in the trend in Fig. 12 is -6.66 pptv decade $^{-1}$

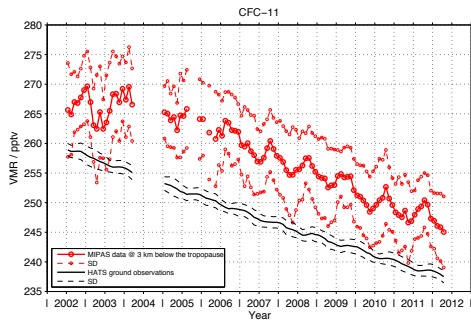


Figure 12. Comparison of MIPAS CFC-11 values at 3 km below the tropopause (red) and ground-based measurements of the HATS network (black). Dashed lines denote the standard deviation.

(see Sect. 3 for details on the method). Therefore, only part of the difference in the trends can be explained by the drift resulting from detector aging. However, the drift estimate due to detector aging is only based on drifts between 35° S and 35° N. Trends in the comparison with HATS result from measurements with almost pole to pole coverage. Thus, the comparison between the drift due to detector aging and the difference in the trends can only serve as an approximation. The amplitude of periodic variations is slightly more pronounced in MIPAS measurements, but qualitatively, both instruments agree well. The standard deviation of the MIPAS data (dashed red line with small red circles) shows that the spread is rather large which is not surprising, considering that the mean includes all MIPAS measurements within this time period, which have a wider spread than the locally confined HATS measurements. Even though some HATS data lie within the standard deviation of the MIPAS measurements, the difference is obviously systematic, supporting the finding that MIPAS CFC-11 is too high in the upper tropopause.

4.2 CFC-11: high spectral resolution time period (FR)

Due to data availability we only compare MIPAS CFC measurements during the FR period with those of MkIV, ACE-FTS, ILAS-II and HATS.

4.2.1 Results CFC-11 V5H: MkIV

During the high spectral resolution (FR) period, two MkIV measurements are coincident with several MIPAS measurements (Fig. 13). While 16 MIPAS profiles were found to coincide with the MkIV profile taken on 16 December 2002, we find even 25 matches for the MkIV measurement taken on 1 April 2003. The color coding is the same as in Fig. 3, showing collocated MIPAS measurements (blue-grayish lines), the mean of these profiles (red line) and the closest MI-

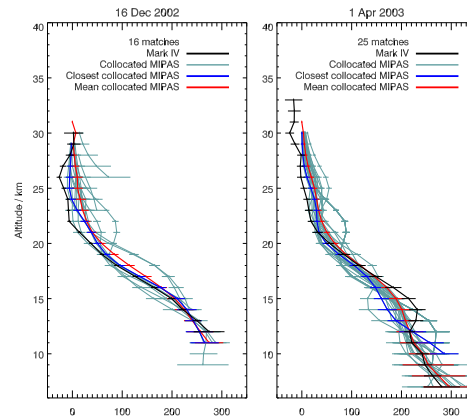


Figure 13. Two MkIV CFC-11 profiles are compared with collocated MIPAS profiles of the FR period. For the measurement on 16 December 2002, 16 collocated MIPAS measurements were found, while 25 MIPAS profiles coincided with the 1 April 2003 MkIV measurement. The setup is similar to Fig. 3.

PAS profile (blue line) compared to the corresponding MkIV measurement (black line). The agreement is excellent up to 15–16 km with differences of less than 20 pptv (up to 10%), while above that altitude MIPAS shows considerably higher values than MkIV for the 16 December 2002 measurement of MkIV. Above 21 km, MkIV even shows negative values at some altitude levels. The second comparison shows larger differences approximately around 15 km, but the agreement with the mean profile of the coincident MIPAS measurements is excellent below that altitude and up to about 20 km. Deviations of MkIV with the MIPAS mean profile range up to ~ 30 pptv in both cases, while larger differences show up for comparisons to the closest MIPAS profile on 1 April 2003. These differences exceed 50 pptv around 15 km. However, the agreement between MIPAS and MkIV measurements of CFC-11 is similarly good for the FR and the RR period.

4.2.2 Results CFC-11 V5H: ACE-FTS

For the comparison of MIPAS CFC-11 with ACE-FTS, 171 profile pairs matching the coincidence criteria were found during the FR period (Fig. 14). As in the case of the MIPAS RR period, the ACE-FTS data were interpolated from their original grid (left panel: blue line) onto the MIPAS grid (black line) and were, after averaging, compared to MIPAS data (red line). Between 10 and 20 km the agreement between the two mean profiles is excellent, while below and above, MIPAS shows higher mixing ratios of CFC-11. From 10 up to 20 km, deviations of the mean profiles mostly stay

3370

E. Eckert et al.: MIPAS IMK/IAA CFC-11 and CFC-12: accuracy, precision and long-term stability

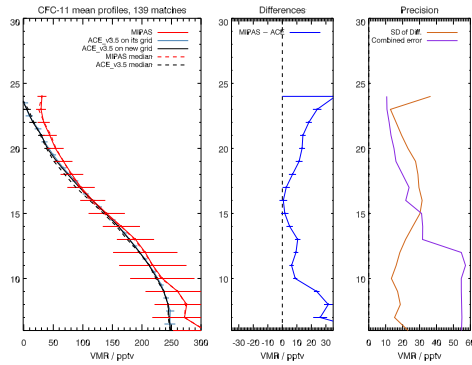


Figure 14. Comparison of mean profiles of MIPAS CFC-11 (left panel, continuous red line) and ACE-FTS (left panel: blue line denotes ACE-FTS on native grid; continuous black line denotes ACE-FTS interpolated onto the MIPAS grid) for February and March 2004, corresponding to the FR period and the MIPAS V5H_CFC-11_20 data set. The dashed lines show the median of each data set. The error bars include the total error for MIPAS and the random errors from the least-squares fitting process for ACE-FTS. The middle panel shows the mean difference (blue) of these profiles and the standard error of the mean. The right panel shows the combined error (purple) of the instruments and the standard deviation of the differences (brown).

within 10–20 pptv (middle panel), corresponding to ~5% around 10 km and ~30% around 20 km. Above and below, the differences are larger and sometimes exceed 30 pptv. Even though the standard error of the mean differences is considerably larger than for the RR period (due to far fewer pairs of collocated profiles), it does not include zero for most of the covered altitude range, indicating that the deviation of the profiles is still significant. The error budget of one of the instruments or both is overestimated below 15 km. This is more pronounced than for the comparison of MIPAS with ACE-FTS during the RR period.

Even though certain similarities with the MIPAS RR period, like the known high bias at the lower end of the profile, occur in the comparison of the MIPAS FR data set with ACE-FTS, the agreement between the two instruments is better than for the RR version in the region between 10 and 20 km. This might be ascribed to the better spectral resolution of MIPAS during the FR period. However, the collocated measurements for the FR period only consist of profiles taken at higher northern latitudes. Thus the result may generally expose differences compared to the RR period, independently from differences due to the altered MIPAS retrieval setup because the mean for the RR period consists of measurements over all latitudes and several years compared to only high latitude profiles taken during February and March 2004 for the FR period.

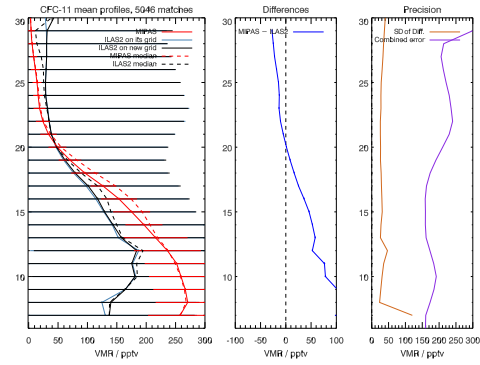


Figure 15. Comparison of mean profiles of MIPAS CFC-11 (left panel, continuous red line) and ILAS-II (left panel: blue line denotes ILAS-II on native grid; continuous black line denotes ILAS-II) for the FR period, corresponding to the MIPAS V5H_CFC-11_20 data set. The dashed lines show the median of each data set. The error bars include the total error for both instruments. The middle panel shows the mean difference (blue) of these profiles and the standard error of the mean. The right panel shows the combined error (purple) of the instruments and the standard deviation of the differences (brown).

4.2.3 Results CFC-11 V5H: ILAS-II

About 5000 matches were found for the comparison of MIPAS CFC-11 measurements with ILAS-II (Fig. 15) during the FR period. However, apart from the approximate altitudes where the vertical gradient changes most rapidly, the MIPAS (red line) and the ILAS-II mean profile (blue line: on its original grid; black line: on the MIPAS altitude grid) do not agree very well. Below 20 km, MIPAS shows higher mixing ratios of CFC-11 than ILAS-II and lower mixing ratios above that altitude. This is the first comparison with the newest version of the ILAS-II CFC-11 and CFC-12 data (version 3). However, a similar feature has already been seen in comparisons of ILAS-II CFC-11 version 1.4 and version 2 measurements with MIPAS-B (Wetzel et al., 2008). The differences of MIPAS and ILAS-II exceed those of other comparisons by far. At the lower end of the profile, deviations go beyond 100 pptv (middle panel), which corresponds to relative differences of ~50%. Another conspicuous feature of this comparison is the very large error bars estimated from the ILAS-II retrieval (left panel: horizontal black and blue lines). However, Wetzel et al. (2008) show similarly large error bars in their comparison of the former version of ILAS-II with MIPAS-B data. Since the right panel of Fig. 15 demonstrates that the combined error of the two instruments (purple line) is far larger than the standard deviation of the differences (brown line), we suspect that the ILAS-II errors are largely overestimated. Above 20 km, Wetzel et al. (2008) also

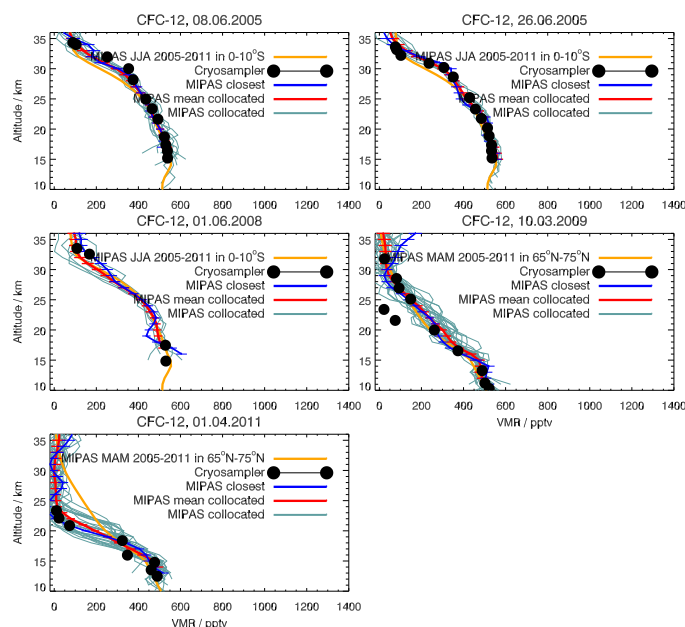


Figure 16. Comparison of an ensemble of MIPAS CFC-12 measurements (light orange lines), collocated measurements (blue-grayish lines) and their mean profile (red line) and the closest MIPAS profile (blue line) with different flights of the cryosampler (black dots).

found higher mixing ratios. All in all, the agreement of MIPAS CFC-11 measurements taken during the FR period with those of ILAS-II is not good as it shows far larger differences at the bottom end of the profile than comparisons with, e.g., ACE-FTS or HATS, that are as big as 50 % and also large deviations at the upper end of the profiles that exceed 100 % above 25 km. Thus, the results for the comparison with ILAS-II should be treated with care, since large differences with MIPAS-B and the former versions of ILAS-II have been found previously.

4.2.4 Results CFC-11 V5H: HATS

The comparison of MIPAS CFC-11 with HATS during the FR period covers less than 2 years (Fig. 12, July 2002–April 2004). This short time period, along with annual variations, is an obstacle to the interpretation of the results. While the MIPAS time series for this period (continuous red line with large red circles) oscillates around a relatively constant value, the HATS time series (black line) shows declining mixing ratios. Even though some values of the HATS measurements lie within the standard deviation of the MIPAS measurements, a systematic deviation is evident. The mixing ratios differ from values of less than 10 pptv (less than 4 %) at the begin-

ning of the compared time series and to slightly higher values of about 12 pptv ($\sim 4.5\%$) at the end. While we consider the differences to be real, since the deviations are systematic and are consistent with the RR time period, we suggest being careful not to overinterpret possible short-term linear variations.

4.3 CFC-12

This section is dedicated to the results of the comparisons of MIPAS CFC-12 measurements with those of the cryosampler, MkIV, MIPAS-B, MIPAS-STR, HIRDLS, ACE-FTS and the HATS network (Figs. 16–26).

4.3.1 Results CFC-12: cryosampler

For CFC-12, as well as for CFC-11, cryosampler measurements (Fig. 16: black dots) were compared to MIPAS measurements. MIPAS measurements fulfilling the coincidence criteria (blue-grayish lines) exhibit a widely spread set of profiles enclosing the cryosampler measurements. In most of the cases, deviations of the cryosampler and the mean collocated MIPAS profile stay within 50 pptv (corresponding to $\sim 10\%$ at the lower end of the profile and increasing above due to smaller volume mixing ratios of CFC-12). The clos-

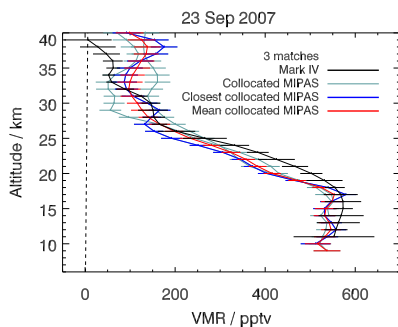


Figure 17. Comparison of one MkIV CFC-12 profile (black line) with three coincident profiles of MIPAS (blue-grayish lines). The closest (blue line) and the mean (red line) of these profiles are shown in addition. The MkIV error estimates are inferred from the fit residuals.

est of these collocated MIPAS profiles (blue line) agrees very well with the cryosampler measurements. Only the cryosampler measurement taken on 3 October 2009 exhibits some outliers, deviating considerably (by ~ 150 pptv) from all coincident MIPAS profiles at about 20–25 km, while the rest of this profile still agrees well (within ~ 50 pptv) with all collocated MIPAS measurements. It is possible that cryosampler captured variations due to laminae of small vertical extent here, which cannot be detected by MIPAS as the spatial resolution is too coarse. While the mean of the collocated MIPAS profiles (red line) comes very close to the cryosampler measurements as well as the closest MIPAS profile, except for the outliers just mentioned, the seasonal latitudinal mean of MIPAS (light orange line) can differ considerably from the cryosampler and the closest MIPAS profile (particularly on 1 April 2011). This provides proof of large natural variability in this case. As already stated for CFC-11, this is presumably due to subsidence in the remarkably cold and stable Arctic polar vortex being present during that winter. Similar as for CFC-11, in the 10 March 2009 comparison cryosampler, the closest MIPAS profile as well as the mean MIPAS profile agree well with the seasonal mean. Therefore, for CFC-12 as well, we can conclude that both instruments are capable of capturing deviations from the mean state of the atmosphere. Even though there are a few cryosampler outliers not matching the MIPAS data, the CFC-12 cryosampler measurements agree very well with those of the mean and the closest MIPAS profile as deviations usually stay within 50 pptv in general.

4.3.2 Results CFC-12: Mark IV

Comparison of MIPAS CFC-12 with MkIV measurements exhibits a similar behavior as for CFC-11 (Fig. 17) up to slightly below 30 km. MkIV (black line) shows higher mixing ratios of CFC-12 than both the mean MIPAS profile (red line) and, even more pronounced, the closest MIPAS profile (blue line). The gradient of the profiles between ~ 20 and 27 km is similar for all profiles. Above approximately 27 km, however, the MIPAS profiles oscillate considerably, which is most apparent in the closest profile. The MkIV profile exhibits small wiggles above that altitude as well, but not as pronounced as any of the MIPAS profiles. Differences of the profiles stay within ~ 50 pptv throughout most of the altitude range between the lower end of the profile up to approximately 27 km, except for levels around 20 km where differences sometimes come close to 100 pptv. These values correspond to 10–15 % for most of the profile below 27 km and slightly over 20 % around 20 km. Velazco et al. (2011) also find higher values of MkIV compared to ACE-FTS throughout their whole altitude comparison range, with an indication of the largest differences occurring around 20 km. However, they only find differences of up to 15 %. Above 35 km, deviations between the MkIV profiles and the MIPAS profiles are noticeably larger. Up to that altitude, however, the comparison of MIPAS with MkIV CFC-12 measurements shows reasonably good agreement, considering only three coincident MIPAS profiles were found.

4.3.3 Results CFC-12: MIPAS-B

Multiple MIPAS profiles coinciding with backward and forward trajectories of two MIPAS-B measurements taken over Kiruna (Sweden) in January 2010 and March 2011 (Fig. 18, upper and lower panels, respectively), were taken into account for the CFC-12 validation with MIPAS-B. For the January 2010 MIPAS-B profile (Fig. 18 upper panels: black line), the agreement with the mean MIPAS profile (red line) is very good. The MIPAS-B profile is embedded in the spread of MIPAS collocated profiles (red squares) throughout the whole vertical range. At altitudes above 17 km, the agreement between MIPAS-B and MIPAS is remarkably good, showing differences smaller than 25 pptv and closing in to zero above 21 km (middle panel). Below 18 km, MIPAS shows slightly larger values of CFC-12, with differences of up to ~ 40 pptv (corresponding to ~ 10 %) at the largest. Below ~ 17 km, these differences are similar to the standard deviation of the instruments (middle and right panel) and considerably smaller above.

Large percentage errors above ~ 22 km occur due to small absolute values of CFC-12 from this altitude upwards. Except for the region below 14 km, the standard deviation of the differences exceeds the total mean combined error of the instruments, suggesting that the error budget for one or both instruments is underestimated. In the comparison with the

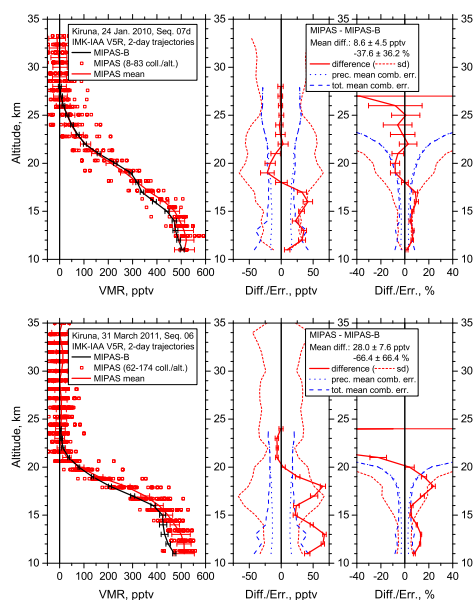


Figure 18. Comparison of a mean profile of MIPAS CFC-12 collocated measurements (left panels: red line) with a profile of MIPAS-B (black line) obtained on 24 January 2010 (upper panels) and 31 March 2011 (lower panels) at Kiruna. The error bars (1σ ; left panel) show the total error without the spectroscopy error for MIPAS and MIPAS-B. The difference is shown in absolute (middle panels) and relative (right panels) terms. The dotted red line is the standard deviation and the dashed blue line is the combined error which consists of the root of the squared error of MIPAS-B and the MIPAS mean.

MIPAS-B measurement taken in March 2011. MIPAS shows considerably higher mixing ratios of CFC-12 below 15 km and around 18 km (Fig. 18, lower panels). From 15 km upwards, the MIPAS-B profile and the MIPAS mean profile show good agreement in gradient and turning points of the profiles and above 19 km they also agree very well quantitatively as the differences are smaller than 7 pptv, closing in to zero at some points. Deviations between MIPAS and MIPAS-B range up to ~ 75 pptv around 12–13 and 18 km (middle panel) in absolute values, corresponding to relative differences of approximately 15 and 30 %, respectively (right panel). However, except for these regions, the two instruments show differences smaller than the standard deviation of the differences. While the shape of the two profiles is far more similar in the first comparison (MIPAS-B flight in January 2010), correction of the less than perfect coincidence, by using trajectories to collect collocated MIPAS measurements, might not have worked that well in this particular

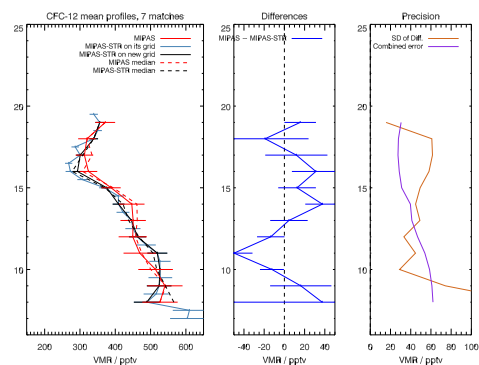


Figure 19. Comparison of mean profiles of MIPAS CFC-12 (left panel, continuous red line) and MIPAS-STR (left panel, continuous black line) for seven collocated measurements taken during a flight on 2 March 2010. The error bars consist of the total error without the spectroscopy error for both MIPAS and MIPAS-STR. The dashed lines show the median of each data set. The middle panel shows the mean difference (blue) of these profiles and the standard error of the mean. The right panel shows the combined error (purple) of the instruments and the standard deviation of the differences (brown).

case. This particular atmospheric situation (winter and spring of 2011) was characterized by extraordinarily low temperatures and a very stable vortex. Due to possibly sharp horizontal gradients, MIPAS-B might have captured an air parcel having different characteristics than the mean of all collocated MIPAS profiles, even though trajectory-corrected collocated profiles were used. Thus deviations due to natural variability might still occur.

4.3.4 Results CFC-12: MIPAS-STR

The comparison of MIPAS-STR and MIPAS mean profiles consists of seven pairs of collocated measurements (Fig. 19). The mean profiles of MIPAS-STR (blue line: on original grid; black: interpolated onto the MIPAS grid) and MIPAS (red line) agree very well. The minimum occurs around the same altitudes (approximately 17 km) and both profiles show a similar behavior of decreasing CFC-12 volume mixing ratios from the bottom of the profile up to the minimum, even though the MIPAS profile oscillates slightly at altitudes below ~ 15 km. The difference oscillates around zero and is very similar in shape with the difference profile of CFC-11 (Fig. 5: middle panel). This is because the same observations were used as in the case of CFC-11. The overall vertical distribution of CFC-11 and CFC-12 indicated by the MIPAS-STR observations fits well with the distribution of these species derived from the MIPAS measurements. This is plausible, since the distribution of the CFCs in the lower stratosphere is predominantly altered by dynamic processes

3374 E. Eckert et al.: MIPAS IMK/IAA CFC-11 and CFC-12: accuracy, precision and long-term stability

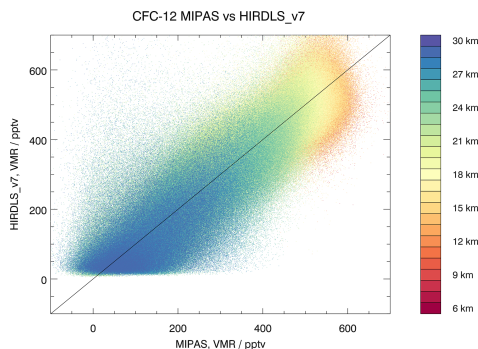


Figure 20. Correlation of collocated MIPAS CFC-12 measurements with HIRDLS measurements during the time period of 2005 to 2008.

and the considered observations of both instruments cover horizontally extended regions (i.e., several degrees in latitude). Differences are largest around 11 km and exhibit deviations of more than 40 pptv, corresponding to approximately 10% (middle panel). Except for this altitude, the differences are mostly insignificant and stay within 30–40 pptv at the largest and are often considerably smaller. This corresponds to less than 10% at the lower end of the profile and less than 5% at the upper end. Again, the total error of both instruments without the spectroscopy error is shown for both instruments. The combined error of the instruments exceeds the standard deviation of the differences from 10 to 12 km. As previously mentioned, this suggests that either one or both of the instruments overestimate their error budget there. As mentioned in Sect. 4.1.4, natural variability might also play a role, even though the mean distance and time difference are rather small as for CFC-11 (Table 2). This probably results in the standard deviation of the differences being larger than the combined error of the instruments outside the region from 10 to 12 km. Overall, the agreement of MIPAS-STR and MIPAS is excellent, since differences rarely exceed 30 pptv and are mostly insignificant.

4.3.5 Results CFC-12: HIRDLS

Comparisons of MIPAS and HIRDLS measurements of CFC-12 are summarized in Figs. 20–22. Figure 20 shows the correlation between MIPAS and HIRDLS measurements. HIRDLS measurements have several outliers in CFC-12, which tend to occur more frequently at smaller mixing ratios/higher altitudes. However, it is still visible that the measured mixing ratios of MIPAS and HIRDLS are correlated linearly in general. Obvious differences appear in Fig. 21, where the frequency of the measured amounts of CFC-12 at 16 km (left panels) and 23 km (right panels) is shown. While

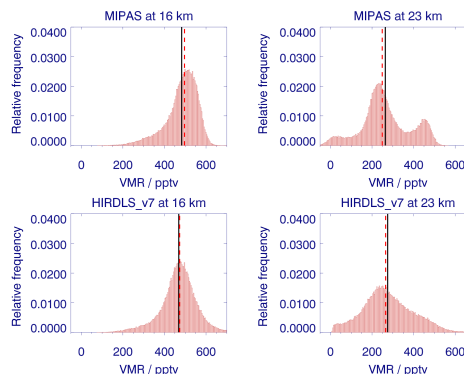


Figure 21. Histogram of collocated MIPAS CFC-12 measurements (top panels) and HIRDLS measurements (bottom panels) for the years of 2005–2008 at 16 km (left panels) and 23 km (right panels). The black line indicates the location of the mean of the sample, while the red dashed line marks the median.

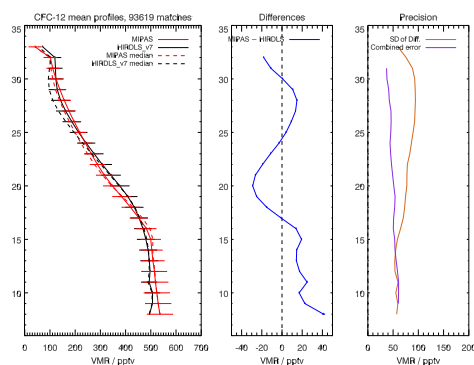


Figure 22. Comparison of mean profiles of MIPAS CFC-12 (left panel, continuous red line) and HIRDLS (left panel, continuous black line) for the years of 2005–2008. The error bars include the total error in the case of MIPAS and the estimated error – which is derived from the average of 10 sets of 12 consecutive profiles of regions with little variability (Gille et al., 2014) – in the case of HIRDLS. The dashed lines show the median of each data set. The middle panel shows the mean difference (blue) of these profiles and the standard error of the mean. The right panel shows the combined error (purple) of the instruments and the standard deviation of the differences (brown).

the distributions look very similar at 16 km, clear differences are visible at 23 km. At 16 km, both measurements' frequencies only show one peak, which is approximately centered between 450 and 500 pptv in the case of HIRDLS and is slightly shifted to higher values in the case of MIPAS, where

the peak is rather centered around 500 pptv and exhibits a steeper histogram at higher mixing ratios. At 23 km one can clearly make out three peaks in the MIPAS distribution, while for HIRDLS this feature is barely visible as it is smeared out quite severely, and thus the rightmost peak is hardly discernible in the HIRDLS distribution. This also leads to a flatter frequency distribution for HIRDLS. The middle maximum peaks at similar amounts of CFC-12 for both instruments and lies between 200 and 250 pptv.

The comparison of the mean profiles of MIPAS (Fig. 22: red line) and HIRDLS collocated measurements (black line) shows very good agreement between the two instruments. The shape of the mean profiles, as well as their maxima and turning points are very similar, even though the MIPAS profile branches off at slightly lower altitudes and exhibits a sharper turn around 16 km. The higher volume mixing ratios of CFC-12, which MIPAS shows below 17 km, stay mostly within ~ 20 pptv ($\sim 4\%$) difference, except from the lowest value (middle panel) which is slightly larger than 40 pptv (close to 10%). Between 18 and 25 km, MIPAS measures smaller amounts of CFC-12 than HIRDLS, with differences of up to nearly 40 pptv (corresponding to $\sim 10\%$). From 25 to 30 km, MIPAS CFC-12 volume mixing ratios agree excellently with those of HIRDLS and differences are generally smaller than 20 pptv, corresponding to $\sim 2.5\%$ around 25 km, about 10% at 28 km and increasing above 30 km.

The combined error of the instruments is similar to the standard deviation of the differences up to ~ 15 km. Above that, the standard deviation of the difference is always larger than the combined error and the difference increases with altitude. This suggests that the error estimate of the two instruments is appropriate in cases where natural variability is negligible. Since the mean spatial and temporal distance between the measurements are almost 200 km and close to 3 h, and thus natural variability might be responsible for the differences between the combined error and the standard deviation of the differences above ~ 15 km, the error estimate of either or both of the instruments might be slightly too conservative.

The latitudinally broken down comparisons (Fig. A3) exhibit similar features as for CFC-11. At higher latitudes, deviations of the profiles at the bottom end seem larger than in tropical or subtropical regions. Overall the agreement between the mean MIPAS and HIRDLS CFC-12 profiles is excellent, since the differences mainly stay within 20 pptv, while the scatter plot shows that this mean is derived from a sample with a rather wide spread. Since HIRDLS CFC radiances have been normalized using WACCM, slight biases might occur due to that normalization.

4.3.6 Results CFC-12: ACE-FTS

The comparison of ACE-FTS and MIPAS CFC-12 profiles is shown in Figs. 23–25. Figure 23 exhibits a correlation of the measurements that is very close to being linear. The agree-

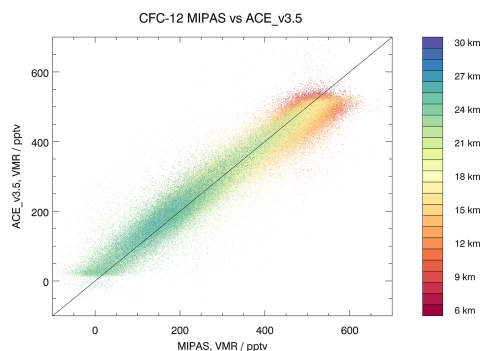


Figure 23. Correlation of collocated MIPAS CFC-12 measurements with ACE-FTS measurements during the time period of 2005 to 2012.

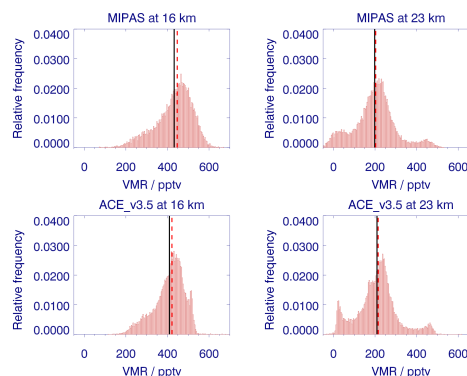


Figure 24. Histogram of MIPAS CFC-12 measurements (top panels) and ACE-FTS measurements (bottom panels) for the years of 2005–2012 at 16 km (left panels) and 23 km (right panels). The black line indicates the location of the mean of the sample, while the red dashed line marks the median.

ment of the two instruments appears to be good, with very few outliers even though MIPAS measures slightly higher volume mixing ratios at large values, e.g., at the lower end of the profile. This impression is supported by Fig. 24, which shows the frequency of MIPAS (top panels) and ACE-FTS (bottom panels) at 16 km (left panels) and 23 km (right panels). It exhibits considerable numbers of MIPAS CFC-12 measurements reporting volume mixing ratios of 500–600 pptv at 16 km, while ACE-FTS does not report appreciable numbers of CFC-12 values above 550 pptv. This leads to a far steeper histogram at higher mixing ratios in the ACE-FTS frequency distribution at 16 km, while the histogram at lower mixing ratios is more similar to that of MIPAS, even though it is still

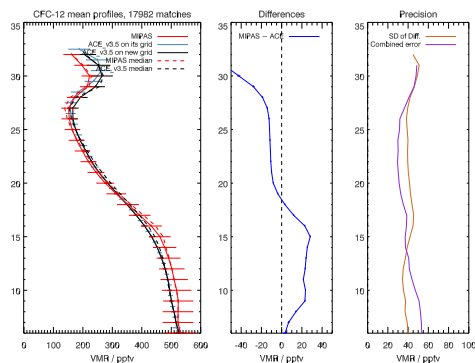


Figure 25. Comparison of mean profiles of MIPAS CFC-12 (left panel, continuous red line) and ACE-FTS (left panel: blue line denotes ACE-FTS on native grid; continuous black line denotes ACE-FTS interpolated onto the MIPAS grid) for the years of 2005–2012. The error bars include the total error for MIPAS and the random errors from the least-squares fitting process for ACE-FTS. The dashed lines show the median of each data set. The middle panel shows the mean difference (blue) of these profiles and the standard error of the mean. The right panel shows the combined error (purple) of the instruments and the standard deviation of the differences (brown).

a bit steeper. The only obvious peak at this altitude occurs at similar volume mixing ratios for both instruments (around 450 pptv in the case of ACE-FTS and between 450 and 500 pptv in the case of MIPAS). At 23 km both instruments clearly show a trimodal distribution, peaking close to zero, around ~ 250 pptv and around ~ 450 pptv. While the left-most peak appears to be more pronounced in the ACE-FTS distribution, the middle and right peaks are very similar. The impression of MIPAS seeing higher values of CFC-12 at the lower end of the profile is confirmed in Fig. 25 as well. While the MIPAS (red line) and the ACE-FTS profiles (blue line: on original grid; black line: interpolated onto the MIPAS grid) are very close together at the bottom end (around ~ 6 km), the MIPAS profile exhibits a steeper ascent than the ACE-FTS profiles, leading to deviating profiles of the instruments up to 18 km. Here, the MIPAS mean profile exhibits volume mixing ratios of CFC-12 that are up to 25–30 pptv (6–7%) higher than those of ACE-FTS (middle panel). From 18 km up to ~ 27 –28 km, MIPAS and ACE-FTS agree remarkably well with deviations of approximately 10 pptv, corresponding to $\sim 3\%$ around 18 km and less than 10% around 27 km. Above these altitudes, ACE-FTS reports higher volume mixing ratios of CFC-12 than MIPAS. Around 30 km, the comparison exhibits the largest deviations, appearing in differences of up to 50 pptv and more (which corresponds to $\sim 25\%$ and more at these altitudes).

The comparison of the estimated precision and the standard deviation of the differences (right panel of Fig. 25) shows that they come close above 13 km, while below this altitude the combined error even exceeds the standard deviation of the differences. This suggests that one or both of the instruments error budgets are overestimated, while this effect if canceled out or even reversed above 13 km by natural variability. Natural variability might play a more important role than for the comparison with HIRDLS, since the HIRDLS coincidence criteria were chosen far more strictly than for the comparison of MIPAS with ACE-FTS. This results in a mean distance and time difference that are similar to CFC-11 with about 375 km and 6 h, respectively (Table 2) and thus almost twice as large as for the comparison with HIRDLS. Both profiles show a bump, which is even more pronounced than for CFC-11. The explanation for this feature is the same as for CFC-11 and illustrates the sampling issue created by the combination of the cut-off of the ACE-FTS profiles at low CFC-12 values and the distribution of the gas, e.g., higher volume mixing ratios at lower latitudes. Different to CFC-11, the bump is not removed completely in the latitudinal breakdown (Fig. A4). An indication of the bump at the upper end of the mean profiles is still visible at midlatitudes, which is presumably attributed to high variability of CFC-12 within these bins. This originates from a similar sampling effect as for the whole set of measurements, just in smaller magnitude. At higher altitudes, the mean profile is again dominated by low-latitude profile contributions, since profiles from higher latitudes are cut off at a lower altitude. As for the comparison with HIRDLS, we observe that differences at the lower end of the profile are largest at higher latitudes for CFC-12.

Again, Tegtmeier et al. (2016) found a similar behavior with a slight high bias in MIPAS CFC-12 that seems to be more pronounced at higher latitudes, even though the relative differences between MIPAS and the MIM are smaller than for CFC-11. Their findings agree well with the results of this study. Despite some differences, the mean MIPAS and ACE-FTS CFC-12 profiles are in good agreement as they stay within 15 pptv between 17 and 28 km and within 30 pptv below, which is slightly larger than in the comparison with HIRDLS for most of the covered altitude range. The scatter plot shows a narrower point cloud than the one for HIRDLS.

4.3.7 Results CFC-12: HATS

Similarly as for CFC-11, a comparison of HATS data with MIPAS measurements at an altitude of 3 km below the estimated tropopause was performed for CFC-12 as well (Fig. 26). This comparison suggests that MIPAS (continuous red line with large circles) detects slightly higher values than the HATS stations (continuous black line) at tropospheric levels. However, this effect is less pronounced than for CFC-11. Deviations mainly stay within 10 pptv, which corresponds to $\sim 2\%$, since CFC-12 amounts are larger than for CFC-11. MIPAS's CFC-12 volume mixing ratios cover a

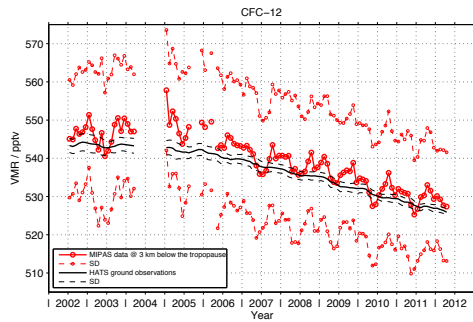


Figure 26. Comparison of MIPAS CFC-12 value estimates at 3 km below the tropopause (red) and ground-based measurements collected by the HATS network (black).

wide range of values, which is reflected in the large standard deviation (dashed red line with small circles) of approximately ± 30 pptv. The values of HATS time series are very close to the MIPAS measurements throughout the whole comparison period. Even though periodic variations in the MIPAS time series have larger amplitudes, the oscillations in both measurements agree with respect to their period and phase. Similar to CFC-11, there is an indication that the MIPAS CFC-12 time series for the RR period (2005–2012) declines faster than that of HATS. The difference in the trends between MIPAS and HATS is -6.85 pptv decade $^{-1}$ (Sect. 3 for details on the method). A similarly large drift (-6.89 pptv decade $^{-1}$) is found for results due to detector aging at 3 km below the tropopause. Hence, for CFC-12 the drift due to detector aging can explain the differences in the trends between MIPAS and HATS to a large extent, even though only drifts between 35° S and 35° N have been analyzed. All in all, differences between the data sets are very small.

4.4 CFC-12: high spectral resolution time period (FR)

4.4.1 Results CFC-12 V5H: MkIV

For the comparison of CFC-12 during the FR period (Fig. 27), 15 collocated MIPAS profiles were found for the MkIV measurement taken on 16 December 2002, and 25 MIPAS profiles coincide with the MkIV measurement taken on 1 April 2003. The mean MIPAS profile (red line) and the MkIV profile (black line) are close in both cases, showing deviations no larger than 50 pptv (corresponding to 10–20% for most of the vertical range) and even considerably smaller at some altitude levels. Deviations with the closest MIPAS profile (blue line) are larger than for the mean profile, similar to the other comparisons for CFC-11, ranging up to ~ 100 pptv. There is a slight indication of the MkIV

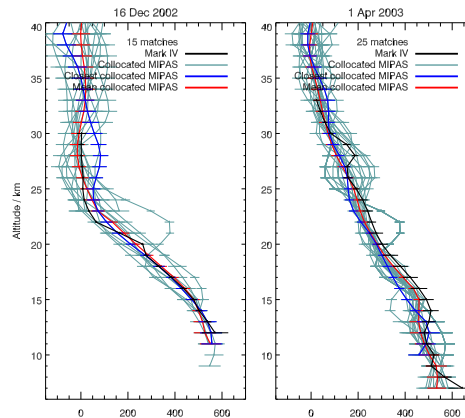


Figure 27. Two MkIV CFC-12 profiles are compared with collocated MIPAS of the FR period. For the measurement on 16 December 2002, 16 collocated MIPAS measurements were found, while 25 MIPAS profiles coincided with the 1 April 2003 MkIV measurement. The setup is similar to Fig. 3.

profile showing larger mixing ratios below 25 km in the 1 April 2003 comparison, while this is not visible in the 16 December 2002 comparison. However, the compared profiles show good agreement in general, with differences up to about twice as large as for the comparison with HIRDLS.

4.4.2 Results CFC-12 V5H: ACE-FTS

The comparison of MIPAS FR CFC-12 and ACE-FTS (Fig. 28) data is very similar to that of the reduced resolution period (RR: Fig. 25), but the agreement is even better around ~ 10 to 15 km. Since the comparison does not reach up beyond 28 km, the bump seen in the mean profiles for the RR period does not appear in either of the mean profiles for the FR period (left panel). This is mainly because collocated measurements only exist at high latitudes for the short overlap of the ACE-FTS period and the MIPAS FR period (February and March 2004). For most of the vertical range the differences stay within ~ 10 pptv (middle panel), corresponding to $\sim 1\%$ at the lower end of the profile and $\sim 20\%$ around 28 km. These values are only exceeded around ~ 10 and 17–18 km, as well as at the lowest altitudes, where differences can reach up to 20–30 pptv ($\sim 6\%$ below 13 km and less than 10% around 17–18 km). MIPAS shows slightly higher mixing ratios than ACE-FTS up to ~ 14 km and lower ones above this altitude. The comparison of the combined error and the standard deviation of the differences (right panel) looks similar to the one for the RR period, just slightly more pronounced, where the combined error exceeds standard deviation of the differences up to ~ 16 km. Above, the stan-

3378

E. Eckert et al.: MIPAS IMK/IAA CFC-11 and CFC-12: accuracy, precision and long-term stability

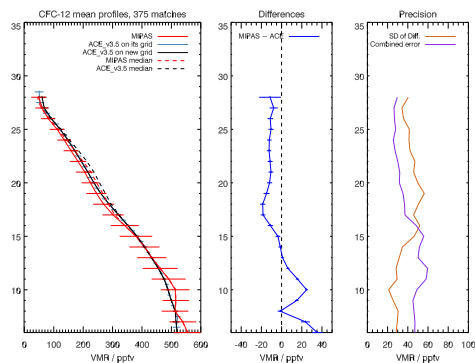


Figure 28. Comparison of mean profiles of MIPAS CFC-12 (left panel, continuous red line) and ACE-FTS (left panel: blue line denotes ACE-FTS on native grid; continuous black line denotes ACE-FTS interpolated onto the MIPAS grid) for February and March 2004, corresponding to the FR period and the MIPAS V5H_CFC-12_20 data set. The dashed lines show the median of each data set. The error bars include the total error for MIPAS and the random errors from the least-squares fitting process for ACE-FTS. The middle panel shows the mean difference (blue) of these profiles and the standard error of the mean. The right panel shows the combined error (purple) of the instruments and the standard deviation of the differences (brown).

standard deviations are not explained by the combined errors. Explanations as for the RR period (Sect. 4.3.6) apply here as well. Overall, the agreement of MIPAS and ACE-FTS CFC-12 measurements is remarkably good for the MIPAS FR period as the differences stay within 15 ppbv for most of the covered altitude range and are thus smaller than in all comparisons for the RR period.

4.4.3 Results CFC-12 V5H: ILAS-II

The comparison of MIPAS CFC-12 measurements from the FR period with ILAS-II measurements (Fig. 29) consists of about 5000 collocated profiles. Throughout the whole altitude range, with very few exceptions, ILAS-II (blue line: on its original grid; black line: on the MIPAS altitude grid) shows higher mixing ratios of CFC-12 than MIPAS (left panel: red line). However, while the mean profiles of MIPAS and ILAS-II agree rather well up to about 17 km, ILAS-II shows considerably larger mixing ratios of CFC-12 above that altitude, which is most pronounced around 25 km. Apart from the lowermost two altitudes, the differences of the mean profiles do not exceed 50 ppbv up to ~17 km (middle panel), which corresponds to relative differences of approximately 10% at the largest. From 17 km upwards however, deviations can be as large as close to 150 ppbv around 25 km, resulting in relative differences of over 100%. Wetzel et al. (2008)

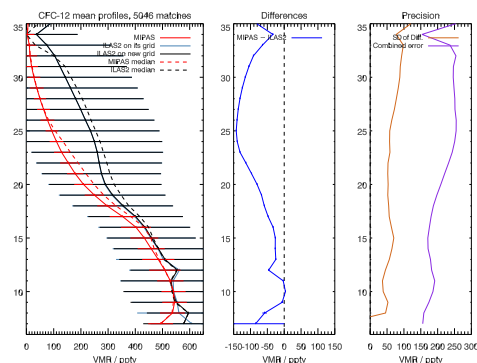


Figure 29. Comparison of mean profiles of MIPAS CFC-12 (left panel, continuous red line) and ILAS-II (left panel: blue line denotes ILAS-II on native grid; continuous black line denotes ILAS-II) for the FR period, corresponding to the MIPAS V5H_CFC-12_20 data set. The dashed lines show the median of each data set. The error bars include the total error for both instruments. The middle panel shows the mean difference (blue) of these profiles and the standard error of the mean. The right panel shows the combined error (purple) of the instruments and the standard deviation of the differences (brown).

find a very similar behavior of ILAS-II version 2 measurements compared to MIPAS-B. The large error bars shown in the left panel presumably result from an overestimated error budget for ILAS-II. Again, we suggest treating conclusions drawn from the comparison with ILAS-II with care, since ACE-FTS shows very good agreement with MIPAS CFC-12 measurements during the FR period, which is supported by the comparison with HATS.

4.4.4 Results CFC-12 V5H: HATS

The short time series of the MIPAS FR period (Fig. 26: July 2002 to April 2004) is compared to the measurements collected by the HATS network during the same time period for CFC-12. Similar as for CFC-11, MIPAS (continuous red line with large red circles) exhibits larger annual and interannual variations than the HATS data (continuous black line) from mid-2002 to early 2004. While MIPAS oscillates around a constant mixing ratio of approximately 550 ppbv at 3 km below the tropopause, the HATS ground-based measurements show mixing ratios well within the range of 540 to 545 ppbv. Thus, the difference between MIPAS and HATS is very small, of an order of ~10 ppbv at the largest, which corresponds to relative differences of less than 2%. Other than for CFC-11, the mixing ratios of both time series stay rather constant during this period. According to the small differences of only ~10 ppbv, we consider the agreement of MIPAS with HATS CFC-12 measurements to be remarkably

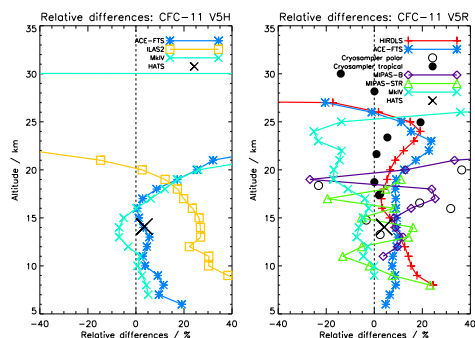


Figure 30. Relative differences between MIPAS CFC-11 for the FR (left) and RR (right) period and each comparison instrument, calculated as $\frac{\text{MIPAS}-\text{Other}}{\text{MIPAS}} \times 100\%$.

good during the FR period, which strongly supports the high accuracy of the MIPAS CFC-12 measurements during the FR period.

5 Overview of the relative differences

Figures 30 and 31 show an overview of the relative differences between MIPAS and the comparison instruments for CFC-11 and CFC-12, respectively. The differences show MIPAS minus the comparison instrument and use MIPAS as a reference.

5.1 Overview: CFC-11

A slight high bias in MIPAS CFC-11 is clearly visible in the comparison with ACE-FTS for the FR period (left) below ~ 10 km and also indicated at the lower end of the differences profile in the comparison with MkIV. For the RR period (right panel), the comparison with HIRDLS shows a high bias in MIPAS CFC-11 below ~ 15 km, where the difference is larger than 20% at the lowest altitude. This high bias at the lower end of the profile does not appear in the RR period comparison with ACE-FTS and MIPAS-B and is far less pronounced in the comparison with MIPAS-STR, where only the value at the lowest altitude level exceeds 20% while oscillating around zero above. While the relative differences between MIPAS and ACE-FTS are around or below 5% between 10 and 18 km for the FR period, they are around 10% between the lowest altitude level and almost 20 km for the RR period. Both ACE-FTS and HIRDLS show relative differences of about 20% close to 25 km. However, one should keep in mind that the volume mixing ratios of CFC-11 are small at this altitude, so that this bias is not that obvious in the absolute comparisons (Figs. 8 and 11). There, the difference is only around 10–15 pptv in both comparisons.

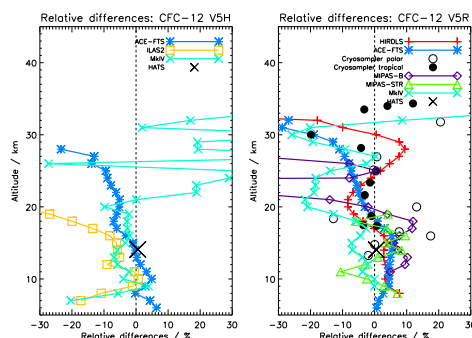


Figure 31. Relative differences between MIPAS CFC-12 for the FR (left) and RR (right) period and each comparison instrument, calculated as $\frac{\text{MIPAS}-\text{Other}}{\text{MIPAS}} \times 100\%$.

Even though the relative differences between MIPAS and MIPAS-STR and MIPAS and MIPAS-B oscillate strongly, the overall impression is that MIPAS shows slightly too high values for CFC-11 during the RR period. This impression is also supported by the comparisons with the cryosampler and HATS, even though HATS only shows a high bias of close to 5% at 3 km below the tropopause. MkIV is the only instrument showing higher volume mixing ratios than MIPAS up to 25 km. The other instruments show a high bias mainly around 10%, that is only exceeded at the lowest altitude levels and above 20 km. For the FR period this bias seems to be slightly smaller in general, while the difference compared to HATS is similar to the RR period. However, both measurement periods are consistent and agree qualitatively and quantitatively to a large extent.

5.2 Overview: CFC-12

Both for the FR period (left) and the RR period (right), relative differences between MIPAS and the comparison instruments stay within 10% below 20 km. While ACE-FTS shows a similar profile for both MIPAS periods, with slightly higher MIPAS values up to 15–17 km and slightly lower MIPAS values above, MkIV measurements agree better with MIPAS during the FR period and show lower MIPAS mixing ratios from ~ 18 to 30 km during the RR period. Relative differences with ILAS-II show that the instrument measures values that are about 20% higher than those acquired by MIPAS at the bottom end of the profile. Above 25 km, all comparisons for both periods indicate a low bias in MIPAS CFC-12, except the one vs. HIRDLS. Overall, relative differences between MIPAS and the comparison instruments are small below 25 km, only occasionally exceeding 10% for most of the comparisons, while above that altitude, there seems to be an indication of MIPAS CFC-12 values being slightly lower.

3380 E. Eckert et al.: MIPAS IMK/IAA CFC-11 and CFC-12: accuracy, precision and long-term stability

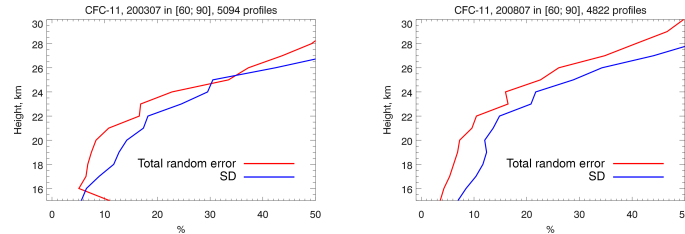


Figure 32. Analysis of MIPAS CFC-11 measurement error in quiescent atmospheric conditions (polar summer). Left panel: FR period; right panel: RR period.

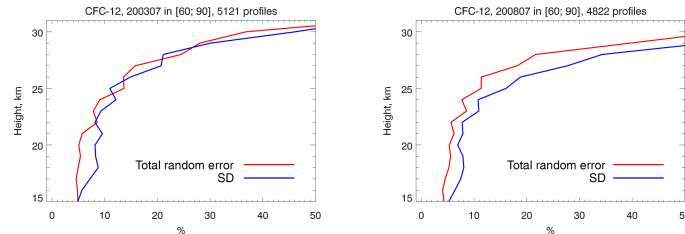


Figure 33. Analysis of MIPAS CFC-12 measurement error in quiescent atmospheric conditions (polar summer). Left panel: FR period; right panel: RR period.

Comparisons with HATS do not indicate a bias in MIPAS CFC-12 measurements, as the difference is only 0.5 % for both the FR and the RR period. The results of the comparisons for both MIPAS measurement periods indicate that the CFC-12 products are very consistent, as they show similar features and differences of similar magnitudes for both data products.

6 MIPAS random error

The assessment of whether MIPAS random error estimates are realistic suffers from possible natural variability and the fact that even though most of the comparison instruments provide the full random error budget, it is not clear whether the random error estimates of the comparison instruments are realistic. Thus, our random error assessment is complemented by the following study; we know that the total observed variability σ_{total} is composed of the natural variability σ_{nat} and the random measurement error estimate σ_{ran} :

$$\sigma_{\text{total}} = \sqrt{\sigma_{\text{nat}}^2 + \sigma_{\text{ran}}^2}. \quad (7)$$

Thus the observed variability can be considered an upper bound of the random measurement error. For calm atmospheric conditions where low natural variability is expected (polar summer), the observed variability should be dominated by the measurement error. The difference between the

observed variability and the measurement error should be small and explainable by the natural variability. If the random measurement error estimate exceeds the observed variability, then the error estimates are too conservative. The results of this analysis for both species and measurement periods are shown in Figs. 32 and 33. For the CFC-12 FR period, the observed variability is fully explained by the estimated random errors. For the other products (CFC-11 FR and RR and CFC-12 RR) about two-thirds to three-quarters of the observed variability are explained, except for CFC-11 RR below 20 km.

7 Long-term stability

7.1 CFC-11

In order to verify the temporal stability of MIPAS CFC-11 measurements, drifts resulting from changing assumptions regarding the nonlinearity correction (Fig. 34) were calculated. As shown by Eckert et al. (2014) and Kiefer et al. (2013), the assumption of the nonlinearity correction for the MIPAS detectors being time-independent cannot be held any more. Time-dependent coefficients for the nonlinearity correction were found to be able to explain drifts between MIPAS and other instruments, e.g., Aura MLS for ozone. Thus, the same method was used to calculate drifts in MIPAS CFC-11

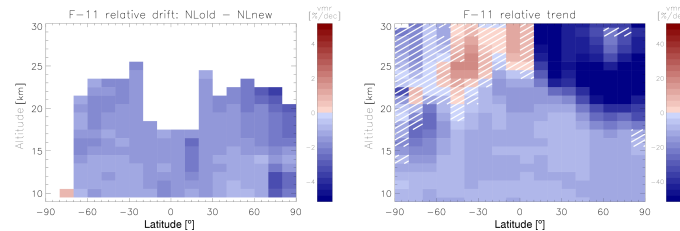


Figure 34. Left panel: altitude–latitude cross section of the instrument drift in MIPAS CFC-11. This drift is calculated by comparing the temporal evolution of CFC-11 from two different setups. One setup uses nonlinearity correction coefficients used for the bulk MIPAS retrieval to date. The other uses newly suggested time-dependent nonlinearity correction coefficients (Eckert et al., 2014, Sect. 3.3). The drift is shown in relative terms, referring to the mean CFC-11 mixing ratio in the middle of the time series. Blueish tiles indicate that the new coefficients result in higher CFC-11 mixing ratios, while reddish tiles indicate the opposite. White areas indicate that there were too few or no data points available to estimate a drift properly. Right panel: altitude–latitude cross section of relative MIPAS CFC-11 trends without drift correction, calculated from data covering January 2005 to April 2012. The trend is weighted with the CFC-11 mixing ratio of the middle of the time series for each tile. Blueish tiles indicate declining CFC-11 mixing ratios, while increasing mixing ratios are represented by reddish tiles. Hatching indicates that the trends are either not significant at 2-sigma level or that χ^2 is more than 10% different from one. Note different color bars.

measurements. MIPAS results produced using the retrieval setup for bulk processing are compared to results derived using newly suggested time-dependent nonlinearity coefficients (see Eckert et al., 2014, Sect. 3.3). The difference between these results is calculated for a subset of measurements taken between June 2005 and October 2011. Subsequently, the temporal development of these differences is assessed by fitting a linear variation to them. The left panel in Fig. 34 shows an Altitude–latitude cross section of the estimated drifts, where bluish tiles indicate that MIPAS is seeing more negative/less positive trends using the old, not time-dependent, nonlinearity coefficients. Red tiles indicate that MIPAS is seeing more positive/less negative trends for using the old setup. The drifts are very small compared to absolute mixing ratios of CFC-11, and only occasionally exceed $2\% \text{ decade}^{-1}$. Larger drifts appear exclusively at high latitudes in the Northern Hemisphere, which is a region with large natural variability, and thus larger differences between the fit and the measurements lead to less reliable results. In order to prove that former results by Kellmann et al. (2012) are still valid, we compared the drift results with the trends for the whole MIPAS time series (Fig. 34, left panel). Reddish tiles indicate positive trends (only in the Southern Hemisphere between 25 and 30 km), while blueish tiles mean that the CFC-11 mixing ratios have decreased during the MIPAS measurement period. Hatching indicates non-significant trends at 2-sigma level. While the trends are very small below ~ 20 km (even ~ 25 km in the tropics), negative trends of down to about -50% were found above this altitude in the Northern Hemisphere. Positive trends range up to $\sim 20\%$. These trends are by far larger than the estimated drifts, and thus the conclusions drawn from these trends by Kellmann

et al. (2012) still hold, i.e., that decadal change in stratospheric circulation is needed to explain the results.

7.2 CFC-12

The temporal stability over the whole MIPAS measurement period was examined for CFC-12, as for CFC-11. The results of the drift estimation (Fig. 35) (left panel) exhibit small, even close to zero, negative drifts in CFC-12 below ~ 30 km. Above that altitude, up to ~ 35 km, larger negative drifts appear, which are largest at midlatitudes and high latitudes and range down to about -50% . From 35 km upwards, large positive drifts were found which exceed 50% at some points, with largest drifts shown at higher altitudes and latitudes. Compared to the trends (Fig. 35, right panel), the drifts are approximately of the same order of magnitude up to ~ 20 km (~ 25 km in the tropics). Between that altitude and ~ 30 km the trends are considerably larger and also show positive values in the Southern Hemisphere. From ~ 30 to 35 km negative trends are almost entirely canceled out by the drifts. This also applies to the positive trends above ~ 35 km. Keeping this in mind, the most pronounced trends are those between ~ 20 and 30 km, which have already been found and interpreted by Kellmann et al. (2012). Since drifts in this altitude range are very small, the conclusions drawn in their paper still hold, and decadal changes in stratospheric circulation are evident. Above ~ 35 km, the apparent trend actually is a drift due to the time-dependent nonlinearity of the detector which has not been accounted for in the bulk processing of the MIPAS data to date. After fixing this for the next data version, by using the new nonlinearity correction coefficients, we assume the MIPAS CFC-12 data will be temporally stable throughout the whole vertical range.

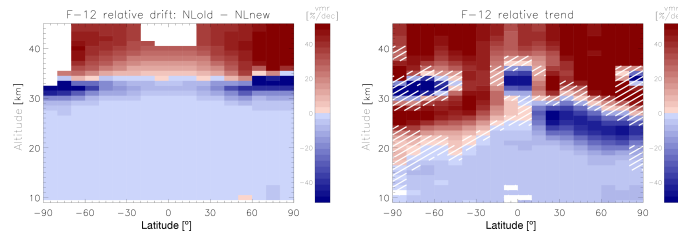


Figure 35. Left panel: altitude–latitude cross section of the instrument drift in MIPAS CFC-12. Blueish tiles indicate that the new coefficients result in higher CFC-12 mixing ratios, while reddish tiles indicate the opposite. White areas indicate that there were too few or no data points available to estimate a drift properly. Right panel: altitude–latitude cross section of relative MIPAS CFC-12 trends, calculated from data covering January 2005 to April 2012. Blueish tiles indicate declining CFC-11 mixing ratios, while increasing mixing ratios are represented by reddish tiles. Hatching indicates that the trends are either not significant at 2-sigma level or that χ^2 is more than 10 % different from one.

8 Conclusions

The MIPAS CFC-11 product shows good overall agreement with the presented collocated observations. A slight high bias is found at low altitudes, below ~ 10 km for the full spectral resolution (FR) period and ~ 15 km for the reduced spectral resolution (RR) period. These differences stay mainly within 50 pptv, corresponding to 25 % at the largest. Larger differences appear in the comparison with ILAS-II, but we suggest treating these results with care since Wetzel et al. (2008) found similarly large differences when comparing MIPAS-B results to a former version of ILAS-II measurements. Differences in CFC-11 tend to be smaller than 30 pptv above 15 km in most cases for the RR period, which corresponds to approximately 20 % at the largest. For the FR period, ACE-FTS and MkIV agree with MIPAS within 20 pptv up to 20 km, but show increasing differences above which exceed 30 pptv at the uppermost level in the case of ACE-FTS and even more in the case of MkIV. Even though the comparisons of the standard deviation in a quiescent atmosphere and the MIPAS error budget suggest that the latter is slightly underestimated, this conclusion cannot be drawn from the comparisons with the other instruments. However, it cannot be falsified either, since it is unclear how reliable the error estimates of the other instruments are and how large the contribution of natural variability is. Except for a few outliers in the comparison with the cryosampler measurement taken on 3 October 2009 and MkIV above ~ 19 km, the CFC-12 product exhibits excellent agreement with all compared instruments. During the FR period both ACE-FTS and MkIV agree very well with MIPAS up to 20 km, with differences staying within 5 %. For the RR period, similarly good agreement is found with all instruments. Maximum differences are of the same order of magnitude as for CFC-11 in the absolute value of about 50 pptv, but since CFC-12 volume mixing ratios are larger than those of CFC-11 in general, the relative deviations of MIPAS from comparison instruments are far smaller and rarely larger than 10 %. This value of relative differences

is not even reached in most of the comparisons as typical values stay within 5 % below 18 km. The comparisons of the standard deviation in a quiescent atmosphere and the MIPAS error budget show that both quantities are very similar for the FR period. This suggests that the error budget was estimated accurately. For the RR period, the results of the comparison of the standard deviation in a quiescent atmosphere and the MIPAS random error are similar to those of CFC-11, and thus suggest a slight underestimation of the error budget for this time period. However, as for CFC-11, this is difficult to deduce or falsify from the comparisons with other instruments. MkIV is the only instrument rather suggesting a low bias in MIPAS CFC-11 and CFC-12 RR measurements. Estimated drifts are small for both species below ~ 25 to 30 km. Above that altitude, CFC-11 is difficult to detect and the test data set for drift estimates from different nonlinearity correction coefficients was sparse, so that no results exist from ~ 25 km upwards. CFC-12 drifts reach up to magnitudes of about 50 % above ~ 30 km, showing large negative values up to ~ 35 km and positive values above. This is reflected in the trend, which is mostly artificial above this altitude. At 3 km below the tropopause, the drift can partly explain the differences in the trends between MIPAS and ground-based HATS CFC-11 data. For CFC-12, the drift is very similar to the differences found in the trends of MIPAS at 3 km below the tropopause and the HATS measurements, and is thus a good candidate for explaining these differences. For future data versions, these results will be taken into account to produce a temporally stable CFC-12 data set, which will then also be suitable for trend analysis above 35 km.

E. Eckert et al.: MIPAS IMK/IAA CFC-11 and CFC-12: accuracy, precision and long-term stability

3383

9 Data availability

All data sets used in this paper can be accessed as follows:

- MIPAS data can be accessed at the following website:
<https://www.imk-asf.kit.edu/english/308.php>.
- The cryosampler data can be obtained by contacting Andreas Engel via email (an.engel@iau.unifrankfurt.de).
- The MkIV data can be found at <http://mark4sun.jpl.nasa.gov/m4data.html>.
- For MIPAS-STR, data from the reconcile campaign have been used, which can be accessed at the following website: <https://www.fp7-reconcile.eu/reconciledata>.
- HIRDLS data can be obtained by using the “Online Archive” at http://disc.sci.gsfc.nasa.gov/uui/datasets/HIRDLS2_V007/summary#citation.
- For SCISAT/ACE-FTS, the most recent data version is available from the ACE team, University of Waterloo, Canada. Publicly available validated data sets can be found at <http://www.ace.uwaterloo.ca/data.html>.
- For ADEOS-II/ILAS-II, as stated on their website (<http://db.cger.nies.go.jp/ilas2/en/>), ILAS-II data inquiries should be made by sending an email to ilas-data@nies.go.jp.
- HATS data can be accessed through the following download links: ftp://ftp.cmdl.noaa.gov/hats/cfcs/cfc11/combined/HATS_global_F11.txt and ftp://ftp.cmdl.noaa.gov/hats/cfcs/cfc12/combined/HATS_global_F12.txt.

3384 E. Eckert et al.: MIPAS IMK/IAA CFC-11 and CFC-12: accuracy, precision and long-term stability

Appendix A

In order to have a closer look at the latitudinal dependence of the differences, we broke the comparison vs. HIRDLS and ACE-FTS down into five latitude bands. We did not do this for the comparisons with other instruments because most of them lack global coverage.

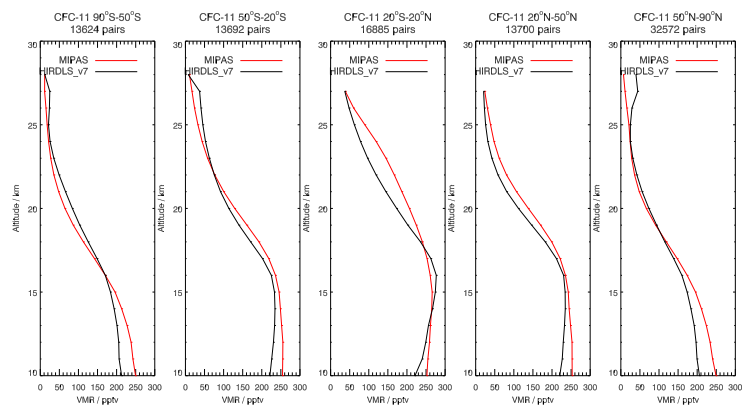


Figure A1. Comparison of mean profiles of MIPAS CFC-11 (red line) and HIRDLS (black line) for different latitude bins for the years of 2005–2008.

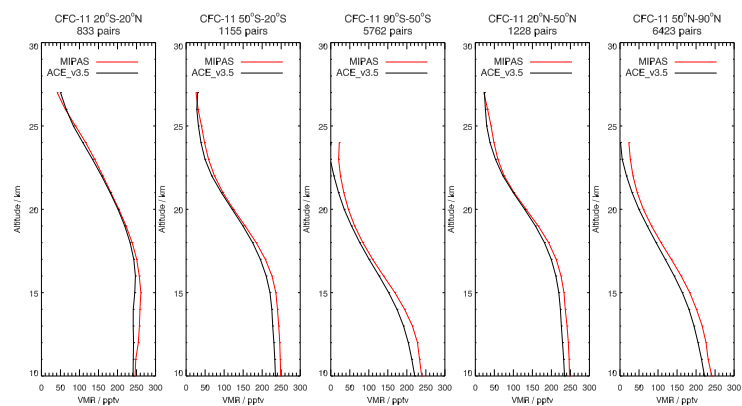


Figure A2. Comparison of mean profiles of MIPAS CFC-11 (red line) and ACE-FTS (black line) for different latitude bins for the years of 2005–2012.

E. Eckert et al.: MIPAS IMK/IAA CFC-11 and CFC-12: accuracy, precision and long-term stability

3385

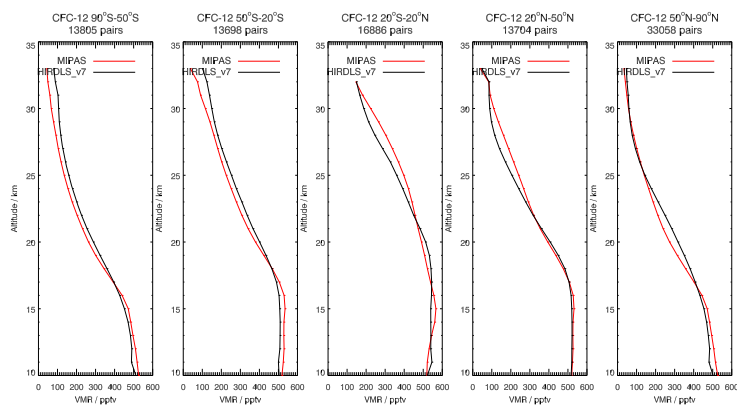


Figure A3. Comparison of mean profiles of MIPAS CFC-12 (red line) and HIRDLS (black line) for different latitude bins for the years of 2005–2008.

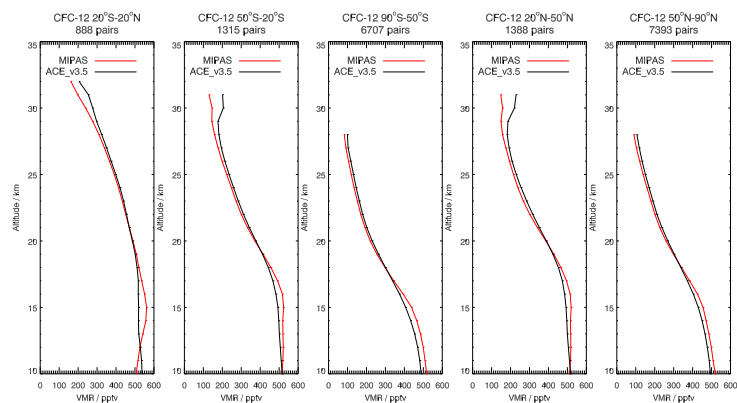


Figure A4. Comparison of mean profiles of MIPAS CFC-12 (red line) and ACE-FTS (black line) for different latitude bins for the years of 2005–2012.

3386 E. Eckert et al.: MIPAS IMK/IAA CFC-11 and CFC-12: accuracy, precision and long-term stability

Acknowledgements. The retrievals of IMK/IAA were partly performed on the HP XC4000 of the Scientific Supercomputing Center (SSC), Karlsruhe, under project grant MIPAS. IMK data analysis was supported by DLR under contract number 50EE0901. MIPAS level 1B data were provided by ESA. We acknowledge support by Deutsche Forschungsgemeinschaft and Open Access Publishing Fund of Karlsruhe Institute of Technology. The Atmospheric Chemistry Experiment (ACE), also known as SCISAT, is a Canadian-led mission mainly supported by the Canadian Space Agency and the Natural Sciences and Engineering Research Council of Canada. Work at the Jet Propulsion Laboratory, California Institute of Technology, was carried out under contract with the National Aeronautics and Space Administration. Data collection and analysis of MIPAS-STR data used here were supported by the EU-project RECONCILE (grant no. 15 226365-FP7-ENV-2008-1) and the BMBF-project ENVIVAL-Life (DLR grant no. 50EE0841). Balloon flights and data analysis of MIPAS-B data used here were supported by the European Space Agency (ESA), the German Aerospace Center (DLR), CNRS (Centre National de la Recherche Scientifique) and CNES (Centre National d'Etudes Spatiales). The ILAS-II project was funded by Ministry of the Environment of Japan.

The article processing charges for this open-access publication were covered by a Research Centre of the Helmholtz Association.

Edited by: L. Hoffmann

References

Bernath, P. F., McElroy, C. T., Abrams, M. C., Boone, C. D., Butler, M., Camy-Peyret, C., Carleer, M., Clerbaux, C., Coheur, P.-F., Colin, R., DeCola, P., De Mazière, M., Drummond, J. R., Dufour, D., Evans, W. F. J., Fast, H., Fussen, D., Gilbert, K., Jennings, D. E., Llewellyn, E. J., Lowe, R. P., Mahieu, E., McConnell, J. C., McHugh, M., McLeod, S. D., Michaud, R., Midwinter, C., Nassar, R., Nichitui, F., Nowlan, C., Rinsland, C. P., Rochon, Y. J., Rowlands, N., Semeniuk, K., Simon, P., Skelton, R., Sloan, J. J., Soucy, M.-A., Strong, K., Tremblay, P., Turnbull, D., Walker, K. A., Walkty, I., Wardle, D. A., Wehrle, V., Zander, R., and Zou, J.: Atmospheric Chemistry Experiment (ACE): Mission overview, *Geophys. Res. Lett.*, 32, L15S01, doi:10.1029/2005GL022386, 2005.

Boone, C. D., Nassar, R., Walker, K. A., Rochon, Y., McLeod, S. D., Rinsland, C. P., and Bernath, P. F.: Retrievals for the atmospheric chemistry experiment Fourier-transform spectrometer, *Appl. Opt.*, 44, 7218–7231, 2005.

Boone, C. D., Walker, K. A., and Bernath, P. F.: Retrievals for the Atmospheric Chemistry Experiment Fourier Transform Spectrometer (ACE-FTS), Version 3, in: *The Atmospheric Chemistry Experiment ACE at 10: A Solar Occultation Anthology*, edited by: Bernath, P. F., A. Deepak Publishing, Hampton, Virginia, USA, 103–127, 2013.

Chirkov, M., Stiller, G. P., Laeng, A., Kellmann, S., von Clarmann, T., Boone, C. D., Elkins, J. W., Engel, A., Glatthor, N., Grabowski, U., Harth, C. M., Kiefer, M., Kolonjari, F., Krummel, P. B., Linden, A., Lunder, C. R., Miller, B. R.,

Montzka, S. A., Mühle, J., O'Doherty, S., Orphal, J., Prinn, R. G., Toon, G., Vollmer, M. K., Walker, K. A., Weiss, R. F., Wiegeler, A., and Young, D.: Global HCFC-22 measurements with MIPAS: retrieval, validation, global distribution and its evolution over 2005–2012, *Atmos. Chem. Phys.*, 16, 3345–3368, doi:10.5194/acp-16-3345-2016, 2016.

Dinelli, B. M., Arnone, E., Brizzi, G., Carlotti, M., Castelli, E., Magnani, L., Papandrea, E., Prevedelli, M., and Ridolfi, M.: The MIPAS2D database of MIPAS/ENVISAT measurements retrieved with a multi-target 2-dimensional tomographic approach, *Atmos. Meas. Tech.*, 3, 355–374, doi:10.5194/amt-3-355-2010, 2010.

Eckert, E., von Clarmann, T., Kiefer, M., Stiller, G. P., Lossow, S., Glatthor, N., Degenstein, D. A., Froidevaux, L., Godin-Beekmann, S., Leblanc, T., McDermid, S., Pastel, M., Steinbrecht, W., Swart, D. P. J., Walker, K. A., and Bernath, P. F.: Drift-corrected trends and periodic variations in MIPAS IMK/IAA ozone measurements, *Atmos. Chem. Phys.*, 14, 2571–2589, doi:10.5194/acp-14-2571-2014, 2014.

Elkins, J. W., Thompson, T. M., Swanson, T. H., Butler, J. H., Hall, B. D., Cummings, S. O., Fisher, D. A., and Raffo, A. G.: Decrease in the growth rates of atmospheric chlorofluorocarbons 11 and 12, *Nature*, 364, 780–783, 1993.

Engel, A., Bönisch, H., Schwarzenberger, T., Haase, H.-P., Grunow, K., Abalichin, J., and Sala, S.: Long-term validation of ESA operational retrieval (version 6.0) of MIPAS Envisat vertical profiles of methane, nitrous oxide, CFC11, and CFC12 using balloon-borne observations and trajectory matching, *Atmos. Meas. Tech.*, 9, 1051–1062, doi:10.5194/amt-9-1051-2016, 2016.

Farman, J. C., Gardiner, B. G., and Shanklin, J. D.: Large losses of total ozone in Antarctica reveal seasonal ClO_x/NO_x interaction, *Nature*, 315, 207–210, 1985.

Fischer, H. and Oelhaf, H.: Remote sensing of vertical profiles of atmospheric trace constituents with MIPAS limb-emission spectrometers, *Appl. Opt.*, 35, 2787–2796, 1996.

Fischer, H., Birk, M., Blom, C., Carli, B., Carlotti, M., von Clarmann, T., Delbouille, L., Dudhia, A., Ehhalt, D., Endemann, M., Flaud, J. M., Gessner, R., Kleinert, A., Koopman, R., Langen, J., López-Puertas, M., Mosner, P., Nett, H., Oelhaf, H., Perron, G., Remedios, J., Ridolfi, M., Stiller, G., and Zander, R.: MIPAS: an instrument for atmospheric and climate research, *Atmos. Chem. Phys.*, 8, 2151–2188, doi:10.5194/acp-8-2151-2008, 2008.

Friedl-Vallon, F., Maucher, G., Kleinert, A., Lengel, A., Keim, C., Oelhaf, H., Fischer, H., Seefeldner, M., and Trieschmann, O.: Design and characterisation of the balloon-borne Michelson Interferometer for Passive Atmospheric Sounding (MIPAS-B2), *Appl. Opt.*, 43, 3335–3355, 2004.

Gille, J., Barnett, J., Arter, P., Barker, M., Bernath, P., Boone, C., Cavanaugh, C., Chow, J., Coffey, M., Craft, J., Craig, C., Di-als, M., Dean, V., Eden, T., Edwards, D. P., Francis, G., Halvorson, C., Harvey, L., Hepplewhite, C., Khosravi, R., Kinnison, D., Krinsky, C., Lambert, A., Lee, H., Lyjak, L., Loh, J., Mankin, W., Massie, S., McInerney, J., Moorhouse, J., Nardi, B., Packman, D., Randall, C., Reburn, J., Rudolf, W., Schwartz, M., Serafin, J., Stone, K., Torpy, B., Walker, K., Waterfall, A., Watkins, R., Whitney, J., Woodard, D., and Young, G.: High Resolution Dynamics Limb Sounder: Experiment overview, recovery, and

- validation of initial temperature data, *J. Geophys. Res.-Atmos.*, 113, D16S43, doi:10.1029/2007JD008824, 2008.
- Gille, J., Gray, L., Cavanaugh, C., Coffey, M., Dean, V., Halvorson, C., Karol, S., Khosravi, R., Kinnison, D., Massie, S., Nardi, B., Rivas, M. B., Smith, L., Torpy, B., Waterfall, A., and Wright, C.: High Resolution Dynamics Limb Sounder Earth Observing System (EOS) Data Description and Quality Version 7 (V7) (HIRDLS Version 7.00.00), http://disc.sci.gsfc.nasa.gov/repository/Mission/HIRDLS/3.3_Product_Documentation/3.3.5_Product_Quality/HIRDLS-DQD_V7.pdf, last access: 10 September, 2014.
- Hoffmann, L., Kaufmann, M., Spang, R., Müller, R., Remedios, J. J., Moore, D. P., Volk, C. M., von Clarmann, T., and Riese, M.: Envisat MIPAS measurements of CFC-11: retrieval, validation, and climatology, *Atmos. Chem. Phys.*, 8, 3671–3688, doi:10.5194/acp-8-3671-2008, 2008.
- Höpfner, M., Blom, C. E., Eche, G., Glatthor, N., Hase, F., and Stiller, G. P.: Retrieval simulations for MIPAS-STR measurements, in: *IRS 2000: Current Problems in Atmospheric Radiation*, edited by: Smith, W. L. and Timofeyev, Y. M., A. Deepak Publishing, Hampton, VA, USA, 1121–1124, 2001.
- Keim, C., Liu, G. Y., Blom, C. E., Fischer, H., Gulde, T., Höpfner, M., Piesch, C., Ravagnani, F., Roiger, A., Schlager, H., and Sitenkov, N.: Vertical profile of peroxyacetyl nitrate (PAN) from MIPAS-STR measurements over Brazil in February 2005 and its contribution to tropical UT NOy partitioning, *Atmos. Chem. Phys.*, 8, 4891–4902, doi:10.5194/acp-8-4891-2008, 2008.
- Kellmann, S., von Clarmann, T., Stiller, G. P., Eckert, E., Glatthor, N., Höpfner, M., Kiefer, M., Orphal, J., Funke, B., Grabowski, U., Linden, A., Dutton, G. S., and Elkins, J. W.: Global CFC-11 (CCl₃F) and CFC-12 (CCl₂F₂) measurements with the Michelson Interferometer for Passive Atmospheric Sounding (MIPAS): retrieval, climatologies and trends, *Atmos. Chem. Phys.*, 12, 11857–11875, doi:10.5194/acp-12-11857-2012, 2012.
- Kiefer, M., Aubertin, G., Birk, M., De Laurentis, M., Eckert, E., Kleinert, A., Perron, G., and Wagner, G.: Impact of Improved Corrections for MIPAS Detector Non-Linearity, in: *Atmospheric Composition Validation and Evolution*, Frascati, Italy, 13–15 March 2013, Abstract Book, p. 38, ESA, 2013.
- Laube, J. C., Engel, A., Bönisch, H., Möbius, T., Worton, D. R., Sturges, W. T., Grunow, K., and Schmidt, U.: Contribution of very short-lived organic substances to stratospheric chlorine and bromine in the tropics – a case study, *Atmos. Chem. Phys.*, 8, 7325–7334, doi:10.5194/acp-8-7325-2008, 2008.
- Li, Z. and Varanasi, P.: Measurement of the absorption cross-sections of CFC-11 at conditions representing various model atmospheres, *J. Quant. Spectrosc. Ra.*, 52, 137–144, doi:10.1016/0022-4073(94)90002-7, 1994.
- Manney, G. L., Daffer, W. H., Zawodny, J. M., Bernath, P. F., Hoppel, K. W., Walker, K. A., Knosp, B. W., Boone, C., Remsberg, E. E., Santee, M. L., Harvey, V. L., Pawson, S., Jackson, D. R., Deaver, L., McElroy, C. T., McLinden, C. A., Drummond, J. R., Pumphrey, H. C., Lambert, A., Schwartz, M. J., Froidevaux, L., McLeod, S., Takacs, L. L., Suarez, M. J., Trepte, C. R., Cuddy, D. C., Livesey, N. J., Harwood, R. S., and Waters, J. W.: Solar occultation satellite data and derived meteorological products: Sampling issues and comparisons with Aura Microwave Limb Sounder, *J. Geophys. Res.-Atmos.*, 112, D24S50, doi:10.1029/2007JD008709, 2007.
- Manney, G. L., Santee, M. L., Rex, M., Livesey, N. J., Pitts, M. C., Veefkind, P., Nash, E. R., Wohltmann, I., Lehmann, R., Froidevaux, L., Poole, L. R., Schoeberl, M. R., Haffner, D. P., Davies, J., Dorokhov, V., Johnson, H. G. B., Kivi, R., Kyrö, E., Larsen, N., Levelt, P. F., Makshtas, A., McElroy, C. T., Nakajima, H., Parrondo, M. C., Tarasick, D. W., von der Gathen, P., Walker, K. A., and Zinoviev, N. S.: Unprecedented Arctic ozone loss in 2011, *Nature*, 478, 469–475, doi:10.1038/nature10556, 2011.
- McElroy, M. B., Salawitch, R. J., Wofsy, S. C., and Logan, J. A.: Reductions of Antarctic ozone due to synergistic interactions of chlorine and bromine, *Nature*, 321, 759–762, doi:10.1038/321759a0, 1986.
- Molina, L. T. and Molina, M. J.: Production of Cl₂O₂ from the Self-Reaction of the ClO Radical, *J. Phys. Chem. A*, 91, 433–436, 1987.
- Molina, M. J. and Rowland, F. S.: Stratospheric sink for chlorofluoromethanes: Chlorine atom-catalysed destruction of ozone, *Nature*, 249, 810–812, 1974.
- Montzka, S. A., Butler, J. H., Myers, R. C., Thompson, T. M., Swanson, T. H., Clarke, A. D., Lock, L. T., and Elkins, J. W.: Decline in the Tropospheric Abundance of Halogen from Halocarbons: Implications for Stratospheric Ozone Depletion, *Science*, 272, 1318–1322, doi:10.1126/science.272.5266.1318, 1996.
- Nakajima, H., Sugita, T., Yokota, T., Kobayashi, H., Sasano, Y., Ishigaki, T., Mogi, Y., Araki, N., Waragai, K., Kimura, N., Iwazawa, T., Kuze, A., Tani, J., Kawasaki, H., Horikawa, M., Togami, T., and Uemura, N.: Characteristics and performance of the Improved Limb Atmospheric Spectrometer-II (ILAS-II) on board the ADEOS-II satellite, *J. Geophys. Res.*, 111, D11S01, doi:10.1029/2005JD006334, 2006.
- Norton, R. H. and Beer, R.: New apodizing functions for Fourier spectrometry, *J. Opt. Soc. Am.*, 66, 259–264, 1976.
- Oshchepkov, S., Sasano, Y., Yokota, T., Nakajima, H., Uemura, N., Saitoh, N., Sugita, T., and Matsuda, H.: ILAS data processing for stratospheric gas and aerosol retrievals with aerosol physical modeling: Methodology and validation of gas retrievals, *J. Geophys. Res.*, 111, D02307, doi:10.1029/2005JD006543, 2006.
- Piesch, C., Gulde, T., Sartorius, C., Friedl-Vallon, F., Seefeldner, M., Wölfel, M., Blom, C. E., and Fischer, H.: Design of a MIPAS instrument for high-altitude aircraft, in: *Proc. 2nd International Airborne Remote Sensing Conference and Exhibition*, ERIM, Ann Arbor, MI, 24–27 June 1996, vol. II, 199–208, 1996.
- Raspollini, P., Carli, B., Carlotti, M., Ceccherini, S., Dehn, A., Dinelli, B. M., Dudhia, A., Flaud, J.-M., López-Puertas, M., Niro, F., Remedios, J. J., Ridolfi, M., Sembhi, H., Sgheri, L., and von Clarmann, T.: Ten years of MIPAS measurements with ESA Level 2 processor V6 – Part 1: Retrieval algorithm and diagnostics of the products, *Atmos. Meas. Tech.*, 6, 2419–2439, doi:10.5194/amt-6-2419-2013, 2013.
- Rodgers, C. D.: *Inverse Methods for Atmospheric Sounding: Theory and Practice*, vol. 2, Series on Atmospheric, Oceanic and Planetary Physics, edited by: Taylor, F. W., World Scientific, Singapore, New Jersey, London, Hong Kong, 2000.
- Rothman, L. S., Barbe, A., Benner, D. C., Brown, L. R., Camy-Peyret, C., Carleer, M. R., Chance, K., Clerbaux, C., Dana, V., Devi, V. M., Fayt, A., Flaud, J.-M., Gamache, R. R., Goldman, A., Jacquemart, D., Jucks, K. W., Lafferty, W. J., Mandin, J.-Y., Massie, S. T., Nemtchinov, V., Newnham, D. A., Perrin, A., Rinsland, C. P., Schroeder, J., Smith, K. M., Smith, M. A. H., Tang,

3388 E. Eckert et al.: MIPAS IMK/IAA CFC-11 and CFC-12: accuracy, precision and long-term stability

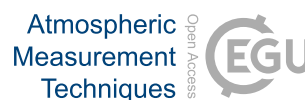
- K., Toth, R. A., Vander Auwera, J., Varanasi, P., and Yoshino, K.: The HITRAN molecular spectroscopic database: edition of 2000 including updates through 2001, *J. Quant. Spectrosc. Ra.*, 82, 5–44, doi:10.1016/S0022-4073(03)00146-8, 2003.
- Rothman, L. S., Jacquemart, D., Barbe, A., Benner, D. C., Birk, M., Brown, L. R., Carleer, M. R., Chackerian Jr., C., Chance, K., Coudert, L. H., Dana, V., Devi, V. M., Flaud, J.-M., Gamache, R. R., Goldman, A., Hartmann, J.-M., Jucks, K. W., Maki, A. G., Mandin, J.-Y., Massie, S. T., Orphal, J., Perrin, A., Rinsland, C. P., Smith, M. A. H., Tennyson, J., Tolchenov, R. N., Toth, R. A., Vander Auwera, J., Varanasi, P., and Wagner, G.: The *HITRAN* 2004 molecular spectroscopic database, *J. Quant. Spectrosc. Ra.*, 96, 139–204, doi:10.1016/j.jqsrt.2004.10.008, 2005.
- Schmidt, U., Kullessa, G., Klein, E., Roeth, E.-P., and Fabian, P.: Intercomparison of balloon-borne cryogenic whole air samplers during the MAP/GLOBUS 1983 campaign, *Planet. Space Sci.*, 35, 647–656, doi:10.1016/0032-0633(87)90131-0, 1987.
- Schoeberl, M. R., Douglass, A. R., Polansky, B., Boone, C., Walker, K. A., and Bernath, P.: Estimation of stratospheric age spectrum from chemical tracers, *J. Geophys. Res.*, 110, D21303, doi:10.1029/2005JD006125, 2005.
- Simnhuber, B.-M., Stiller, G., Ruhnke, R., von Clarmann, T., Kellmann, S., and Aschmann, J.: Arctic winter 2010/2011 at the brink of an ozone hole, *Geophys. Res. Lett.*, 38, L24814, doi:10.1029/2011GL049784, 2011.
- SPARC: SPARC Report on the Lifetimes of Stratospheric Ozone-Depleting Substances, Their Replacements, and Related Species, edited by: Ko, M., Newman, P., Reimann, S., and Strahan, S., 2013.
- Stiller, G. P. (Ed.): The Karlsruhe Optimized and Precise Radiative Transfer Algorithm (KOPRA), vol. FZKA 6487, Wissenschaftliche Berichte, Forschungszentrum Karlsruhe, Karlsruhe, 2000.
- Tegtmeier, S., Hegglin, M. I., Anderson, J., Funke, B., Gille, J., Jones, A., Smith, L., von Clarmann, T., and Walker, K. A.: The SPARC Data Initiative: comparisons of CFC-11, CFC-12, HF and SF6 climatologies from international satellite limb sounders, *Earth Syst. Sci. Data*, 8, 61–78, doi:10.5194/essd-8-61-2016, 2016.
- The University of Oxford Physics Department: Michelson Interferometer for Passive Atmospheric Sounding (MIPAS), <http://www.atm.ox.ac.uk/group/mipas/> (last access: 6 April 2016), 2008.
- Toon, G. C.: The JPL MkIV Interferometer, *Opt. Photonics News*, 2, 19–21, 1991.
- Varanasi, P. and Nemtchinov, V.: Thermal infrared absorption coefficients of CFC-12 at atmospheric conditions, *J. Quant. Spectrosc. Ra.*, 51, 679–687, doi:10.1016/0022-4073(94)90124-4, 1994.
- Velazco, V. A., Toon, G. C., Blavier, J.-F. L., Kleinböhl, A., Manney, G. L., Daffer, W. H., Bernath, P. F., Walker, K. A., and Boone, C.: Validation of the Atmospheric Chemistry Experiment by noncoincident MkIV balloon profiles, *J. Geophys. Res.*, 116, D06306, doi:10.1029/2010JD014928, 2011.
- von Clarmann, T.: Validation of remotely sensed profiles of atmospheric state variables: strategies and terminology, *Atmos. Chem. Phys.*, 6, 4311–4320, doi:10.5194/acp-6-4311-2006, 2006.
- von Clarmann, T., Oelhaf, H., and Fischer, H.: Retrieval of atmospheric O_3 , HNO_3 , CFC-11, and CFC-12 profiles from MIPAS-B-89 limb emission spectra, *Appl. Opt.*, 32, 6808–6817, 1993.
- von Clarmann, T., Glatthor, N., Grabowski, U., Höpfner, M., Kellmann, S., Kiefer, M., Linden, A., Mengistu Tsidu, G., Milz, M., Steck, T., Stiller, G. P., Wang, D. Y., Fischer, H., Funke, B., Gil-López, S., and López-Puertas, M.: Retrieval of temperature and tangent altitude pointing from limb emission spectra recorded from space by the Michelson Interferometer for Passive Atmospheric Sounding (MIPAS), *J. Geophys. Res.*, 108, 4736, doi:10.1029/2003JD003602, 2003.
- von Clarmann, T., Höpfner, M., Kellmann, S., Linden, A., Chauhan, S., Funke, B., Grabowski, U., Glatthor, N., Kiefer, M., Schieferdecker, T., Stiller, G. P., and Versick, S.: Retrieval of temperature, H_2O , O_3 , HNO_3 , CH_4 , N_2O , $ClONO_2$ and ClO from MIPAS reduced resolution nominal mode limb emission measurements, *Atmos. Meas. Tech.*, 2, 159–175, doi:10.5194/amt-2-159-2009, 2009.
- von Hobe, M., Bekki, S., Borrmann, S., Cairo, F., D’Amato, F., Di Donfrancesco, G., Dörnbrack, A., Ebersoldt, A., Ebert, M., Emde, C., Engel, I., Ern, M., Frey, W., Genco, S., Griessbach, S., Groöb, J.-U., Gulde, T., Günther, G., Hösen, E., Hoffmann, L., Homonnai, V., Hoyle, C. R., Isaksen, I. S. A., Jackson, D. R., Jánosi, I. M., Jones, R. L., Kandler, K., Kalicinsky, C., Keil, A., Khaykin, S. M., Khosrawi, F., Kivi, R., Kuttippurath, J., Laube, J. C., Lefèvre, F., Lehmann, R., Ludmann, S., Luo, B. P., Marchand, M., Meyer, J., Mitev, V., Molleker, S., Müller, R., Oelhaf, H., Olschewski, F., Orsolini, Y., Peter, T., Pfeilsticker, K., Piesch, C., Pitts, M. C., Poole, L. R., Pope, F. D., Ravegnani, F., Rex, M., Riese, M., Röckmann, T., Rognerud, B., Roiger, A., Rolf, C., Santee, M. L., Scheibe, M., Schiller, C., Schlager, H., Siciliani de Cumis, M., Sitnikov, N., Søvde, O. A., Spang, R., Spelten, N., Stordal, F., Suminska-Ebersoldt, O., Ulanovski, A., Ungermann, J., Viciani, S., Volk, C. M., vom Scheidt, M., von der Gathen, P., Walker, K., Wegner, T., Weigel, R., Weinbruch, S., Wetzel, G., Wienhold, F. G., Wohlmann, I., Woiwode, W., Young, I. A. K., Yushkov, V., Zobrist, B., and Stroh, F.: Reconciliation of essential process parameters for an enhanced predictability of Arctic stratospheric ozone loss and its climate interactions (RECONCILE): activities and results, *Atmos. Chem. Phys.*, 13, 9233–9268, doi:10.5194/acp-13-9233-2013, 2013.
- Wetzel, G., Sugita, T., Nakajima, H., Tanaka, T., Yokota, T., Friedl-Vallon, F., Kleinert, A., Maucher, G., and Oelhaf, H.: Technical Note: Intercomparison of ILAS-II version 2 and 1.4 trace species with MIPAS-B measurements, *Atmos. Chem. Phys.*, 8, 1119–1126, doi:10.5194/acp-8-1119-2008, 2008.
- Woiwode, W., Oelhaf, H., Gulde, T., Piesch, C., Maucher, G., Ebersoldt, A., Keim, C., Höpfner, M., Khaykin, S., Ravegnani, F., Ulanovsky, A. E., Volk, C. M., Hösen, E., Dörnbrack, A., Ungermann, J., Kalicinsky, C., and Orphal, J.: MIPAS-STR measurements in the Arctic UTLS in winter/spring 2010: instrument characterization, retrieval and validation, *Atmos. Meas. Tech.*, 5, 1205–1228, doi:10.5194/amt-5-1205-2012, 2012.
- Woiwode, W., Suminska-Ebersoldt, O., Oelhaf, H., Höpfner, M., Belyaev, G. V., Ebersoldt, A., Friedl-Vallon, F., Groöb, J.-U., Gulde, T., Kaufmann, M., Kleinert, A., Krämer, M., Kretschmer, E., Kullessa, T., Maucher, G., Neubert, T., Piesch, C., Preusse, P., Riese, M., Rongen, H., Sartorius, C., Schardt, G., Schönfeld, A., Schuettmeyer, D., Sha, M. K., Stroh, F., Ungermann, J., Volk, C. M., and Orphal, J.: Validation of first chemistry mode retrieval results from the new limb-imaging FTS GLORIA with correlative

E. Eckert et al.: MIPAS IMK/IAA CFC-11 and CFC-12: accuracy, precision and long-term stability**3389**

- MIPAS-STR observations, *Atmos. Meas. Tech.*, 8, 2509–2520, doi:10.5194/amt-8-2509-2015, 2015.
- World Meteorological Organization: Scientific Assessment of Ozone Depletion: 2010, Global Ozone Research and Monitoring Project – Report No. 52, 516 pp., Geneva, Switzerland, 2011.
- World Meteorological Organization (WMO): Scientific Assessment of Ozone Depletion: 2014, Global Ozone Research and Monitoring Project – Report No. 55, 416 pp., Geneva, Switzerland, 2014.
- Yokota, T., Nakajima, H., Sugita, T., Tsubaki, H., Itou, Y., Kaji, M., Suzuki, M., Kanzawa, H., Park, J. H., and Sasano, Y.: Improved Limb Atmospheric Spectrometer (ILAS) data retrieval algorithm for Version 5.20 gas profile products, *J. Geophys. Res.*, 107, 8216, doi:10.1029/2001JD000628, 2002.

A.3 MIPAS IMK/IAA Carbon Tetrachloride (CCl_4) Retrieval and first Comparison with other Instruments

Atmos. Meas. Tech., 10, 2727–2743, 2017
https://doi.org/10.5194/amt-10-2727-2017
© Author(s) 2017. This work is distributed under
the Creative Commons Attribution 3.0 License.



MIPAS IMK/IAA carbon tetrachloride (CCl₄) retrieval and first comparison with other instruments

Ellen Eckert¹, Thomas von Clarmann¹, Alexandra Laeng¹, Gabriele P. Stiller¹, Bernd Funke¹, Norbert Glatthor¹, Udo Grabowski¹, Sylvia Kellmann¹, Michael Kiefer¹, Andrea Linden¹, Arne Babenhauserheide¹, Gerald Wetzel¹, Christopher Boone², Andreas Engel³, Jeremy J. Harrison^{4,5,6}, Patrick E. Sheese⁷, Kaley A. Walker^{2,7}, and Peter F. Bernath^{2,8}

¹Karlsruhe Institute of Technology, Institute of Meteorology and Climate Research, Karlsruhe, Germany

²Department of Chemistry, University of Waterloo, Waterloo, Ontario, Canada

³Institut für Atmosphäre und Umwelt, J. W. Goethe Universität, Frankfurt, Germany

⁴Department of Physics, University of Leicester, University Road, Leicester LE1 7RH, UK

⁵National Centre for Earth Observation, University of Leicester, University Road, Leicester LE1 7RH, UK

⁶Leicester Institute for Space and Earth Observation, University of Leicester, University Road, Leicester LE1 7RH, UK

⁷Department of Physics, University of Toronto, Toronto, Ontario, Canada

⁸Department of Chemistry and Biochemistry, Old Dominion University, Norfolk, VA 23529-0126, USA

Correspondence to: Ellen Eckert (ellen.eckert@kit.edu)

Received: 31 December 2016 – Discussion started: 1 February 2017

Revised: 25 May 2017 – Accepted: 8 June 2017 – Published: 28 July 2017

Abstract. MIPAS thermal limb emission measurements were used to derive vertically resolved profiles of carbon tetrachloride (CCl₄). Level-1b data versions MIPAS/5.02 to MIPAS/5.06 were converted into volume mixing ratio profiles using the level-2 processor developed at Karlsruhe Institute of Technology (KIT) Institute of Meteorology and Climate Research (IMK) and Consejo Superior de Investigaciones Científicas (CSIC), Instituto de Astrofísica de Andalucía (IAA). Consideration of peroxyacetyl nitrate (PAN) as an interfering species, which is jointly retrieved, and CO₂ line mixing is crucial for reliable retrievals. Parts of the CO₂ Q-branch region that overlap with the CCl₄ signature were omitted, since large residuals were still found even though line mixing was considered in the forward model. However, the omitted spectral region could be narrowed noticeably when line mixing was accounted for. A new CCl₄ spectroscopic data set leads to slightly smaller CCl₄ volume mixing ratios. In general, latitude–altitude cross sections show the expected CCl₄ features with highest values of around 90 pptv at altitudes at and below the tropical tropopause and values decreasing with altitude and latitude due to stratospheric decomposition. Other patterns, such as subsidence in the polar vortex during winter and early spring, are also visible in the distributions. The decline in CCl₄ abundance during the MI-

PAS Envisat measurement period (July 2002 to April 2012) is clearly reflected in the altitude–latitude cross section of trends estimated from the entire retrieved data set.

1 Introduction

Carbon tetrachloride (CCl₄) is an anthropogenically produced halogen-yielding trace gas and partly responsible for stratospheric ozone depletion. It is also a potent greenhouse gas with a 100-year global warming potential of 1730 (IPCC, 2013; World Meteorological Organization, 2014). CCl₄ was commonly used in fire extinguishers, as a precursor to refrigerants, and in dry cleaning prior to 1990, when it was restricted within the framework of the London Amendment to the Montreal Protocol. Its abundances in the atmosphere increased steadily from the first part of the 20th century. Emissions declined significantly after 1990, as did the amount of CCl₄ in the atmosphere with a few years delay. 2007–2012 bottom-up emissions of 1–4 kilotonnes year⁻¹ were assessed by combining country-by-country reports to the United Nations Environmental Programme (UNEP) (Liang et al., 2016). This bottom-up estimate differs considerably from the 57 (± 17) kilotonnes year⁻¹ top-down emissions

2728

which were evaluated in 2014 (World Meteorological Organization, 2014) using atmospheric measurements and lifetime estimates. Even when possible CCl_4 precursors and unreported, inadvertent emissions are accounted for, the gap between reported bottom-up and estimated top-down CCl_4 emissions cannot be closed, as bottom-up emissions still only add up to 25 kilotonnes year⁻¹ (SPARC, 2016). Besides a sink in the atmosphere, CCl_4 is decomposed in the ocean and the soil with different lifetimes for each sink. Re-assessment of the different lifetime estimates, which are essential for an adequate top-down assessment of emissions, leads to lower emissions of $\sim 40 (\pm 15)$ kilotonnes year⁻¹. While the gap between bottom-up and top-down emissions is now smaller after reassessments, the discrepancy is still not solved entirely. Previous measurements of stratospheric CCl_4 have also been performed by the Atmospheric Chemistry Experiment Fourier Transform Spectrometer (ACE-FTS), a cryosampler instrument employed at Frankfurt University, and the balloon-borne version of the Michelson Interferometer for Passive Atmospheric Sounding (MIPAS-B2). The first version of the balloon-borne MIPAS instrument (MIPAS-B) and ATMOS (Atmospheric Trace Molecule Spectroscopy) also measured CCl_4 , but not during the MIPAS Envisat measurement period (Zander et al., 1996; von Clarmann et al., 1995). Additional measurements, especially vertically well-resolved ones with global coverage such as satellite measurements from MIPAS, can help to improve the understanding of the atmospheric CCl_4 budget and stratospheric lifetime estimate. Furthermore, as a tracer with relatively long stratospheric lifetimes, CCl_4 measurements can improve the understanding of changes in the Brewer–Dobson circulation by further constraining the lower boundary, e.g. processes around the tropopause. In this study, we present the retrieval of CCl_4 distributions from MIPAS limb emission spectra. First, we characterize the MIPAS instrument (Sect. 2), followed by a detailed description of the retrieval and the specific issues that had to be dealt with to derive CCl_4 concentrations (Sect. 3). We then compare the results of the MIPAS Envisat CCl_4 retrieval with those of ACE-FTS, those of the second balloon-borne MIPAS instrument (MIPAS-B2) and those of cryosampler measurements (Sect. 5) and summarize the results in the conclusions (Sect. 6).

2 MIPAS

The Michelson Interferometer for Passive Atmospheric Sounding was one of the instruments aboard the European Environmental Satellite (Envisat). It was launched into a sun-synchronous orbit at an altitude of approximately 800 km on 1 March 2002. On 8 April 2012, all communication with the satellite was lost, ending an observation period of more than 10 years. Envisat orbited the earth 14.4 times a day, crossing the Equator at 10:00 and 22:00 local time. MIPAS measured infrared emissions between 685 and 2410 cm⁻¹

E. Eckert et al.: MIPAS IMK/IAA CCl_4 retrieval

(14.6 and 4.15 μm) (Fischer et al., 2008), which allows for day and nighttime measurements with global coverage. The initial spectral resolution of the instrument was 0.025 cm⁻¹ (0.0483 cm⁻¹ after a “Norton–Beer strong” apodization; Norton and Beer, 1976). An instrument failure in March 2004 led to an observation gap until January 2005 when the instrument was successfully restarted. The first period (June 2002 to March 2004) is referred to as full spectral resolution (FR) period, while the period from January 2005 to April 2012 is referred to as reduced spectral resolution (RR) period. Due to a problem with one of the interferometer slides, MIPAS could only be operated with a spectral resolution of 0.0625 cm⁻¹ (0.121 cm⁻¹ apodized) from January 2005 on. In this study, only measurements from the instrument’s “nominal operation mode” are used. In this mode, the number of tangent altitudes increased from 17 during the FR period to 27 during the RR period. The vertical coverage ranges from 6 km to around 68 km during the FR period and up to around 70 km during the RR period, respectively. MIPAS initially took around 1000 measurements per day. In 2005, operation was resumed at reduced duty cycle. By the end of 2007, MIPAS was back at full duty cycle, which amounts to approximately 1300 RR measurements per day. The horizontal sampling changed from 510 km during the FR period to 410 km during the RR period.

The temperature and various atmospheric trace gases are retrieved from level-1b data using a retrieval processor developed at the Institute of Meteorology and Climate Research at the Karlsruhe Institute of Technology (KIT) in close cooperation with the Instituto de Astrofísica de Andalucía (CSIC) in Granada, Spain. Results shown in this publication cover both the FR and the RR period.

3 Retrieval

The MIPAS Envisat retrieval is based on a non-linear least-squares approach and employs a first-order Tikhonov-type regularization (von Clarmann et al., 2003, 2009).

The radiative transfer is modelled using the Karlsruhe Optimized and Precise Radiative Transfer Algorithm (KOPRA) model (Stiller, 2000). The spectral regions used for the retrieval of CCl_4 are 772.0–791.0 and 792.0–805.0 cm⁻¹. The gap from 791.0 to 792.0 cm⁻¹ is necessary, since even when accounting for line mixing, strong effects from the CO_2 Q-branch still occur in the residuals. Several results from previous steps in the retrieval chain were used to derive CCl_4 (Table 1) including the spectral shift (z_{tangent}), the temperature (T), the horizontal temperature gradient (T_{grad}) and mixing ratio profiles of HNO_3 , ClO , CFC-11 , C_2H_6 , HCN , ClONO_2 and HNO_4 . In addition, several species were found to improve the retrieval whenever their mixing ratio profiles were fitted alongside CCl_4 . These are peroxyacetyl nitrate (PAN), CH_3CCl_3 , HCFC-22 , O_3 , H_2O , C_2H_2 and COF_2 . Although for most of these species results from preceding retrieval

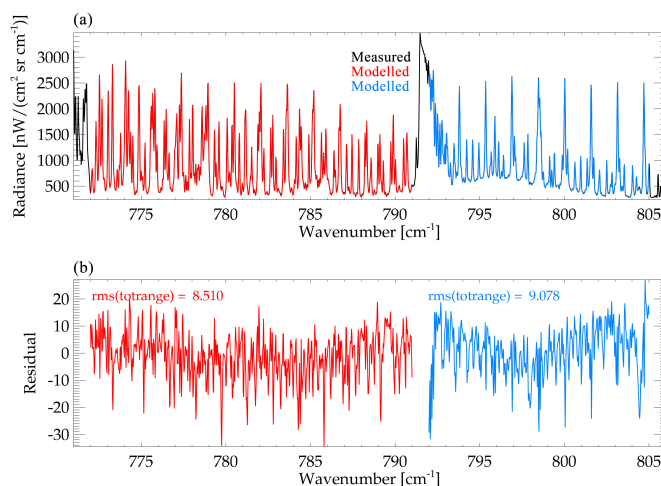


Figure 1. Exemplary spectra of MIPAS CCl₄ at 12 km during the FR period (September 2003): (a) spectra; (b) residuals.

Table 1. Retrieval details on the spectroscopic region, species imported from preceding retrieval steps and variables fitted jointly during the retrieval process. Brackets denote mixing ratios.

Spectral regions	Imported from preceding retrieval steps	Jointly fitted variables
772.0–791.0 cm ⁻¹	Shift(z_{tangent})	[PAN](z)
792.0–805.0 cm ⁻¹	$T(z)$	[CH ₃ CCl ₃](z)
	$T_{\text{grad}}(z)$	[HCFC-22](z)
	[HNO ₃](z)	[O ₃](z)
	[ClO](z)	[H ₂ O](z)
	[CFC-11](z)	[C ₂ H ₂](z)
	[C ₂ H ₆](z)	[COF ₂](z)
	[HCN](z)	Continuum(z)
	[ClONO ₂](z)	offset
	[HNO ₄](z)	

steps are available, fitting their concentrations jointly with that of CCl₄ reduces the fit residuals significantly. This is attributed to spectroscopic inconsistencies of the interferers' spectroscopic data between the spectral region where these were retrieved and the spectral region where CCl₄ is analyzed. Also fitted were a background continuum accounting for spectral contributions from aerosols and a radiance offset which is constant for all tangent altitudes (Table 1). These retrieval settings lead to spectral fits as displayed in Figs. 1 and 2, where an example for the FR period and the RR period is shown, respectively. The measured spectra are plotted in black (not discernible from the best fit modelled in the fitting window), while the red and the blue lines represent the

modelled spectra of the regions from 772.0 to 791.0 and from 792.0 to 805.0 cm⁻¹, respectively. Some periodic residuals are visible in both the FR and the RR period. These result from less than perfectly fitted CO₂ but, as will be shown in Sect. 5, are only of minor relevance for the accuracy of the retrieved CCl₄.

3.1 Information cross-talk with PAN

The signature of PAN is particularly prominent in the spectral region of CCl₄ and can thus be retrieved during the same retrieval step. Actually, jointly fitting PAN is very important for the CCl₄ retrieval. Since PAN was already retrieved from MIPAS spectra before (Glatthor et al., 2007), it is of obvious interest to investigate the PAN results from the CCl₄–PAN joint retrieval in comparison with those from the original PAN retrieval. There, CCl₄ was fitted alongside PAN but the retrieval was not yet optimized for CCl₄.

We find slightly higher volume mixing ratios of PAN throughout most of the altitude–latitude cross section (Fig. 3). As a consequence, areas showing unphysical mixing ratios below zero in the original retrievals (left panel of Fig. 3) are now slightly positive or very close to zero. This suggests that jointly fit PAN from the retrieval optimized for CCl₄ might be more accurate than PAN retrieved using the old CCl₄ distributions.

3.2 Line mixing

Since the spectral region where CCl₄ is retrievable contains a CO₂ Q-branch, the retrieval is set up to account for

2730

E. Eckert et al.: MIPAS IMK/IAA CCl_4 retrieval

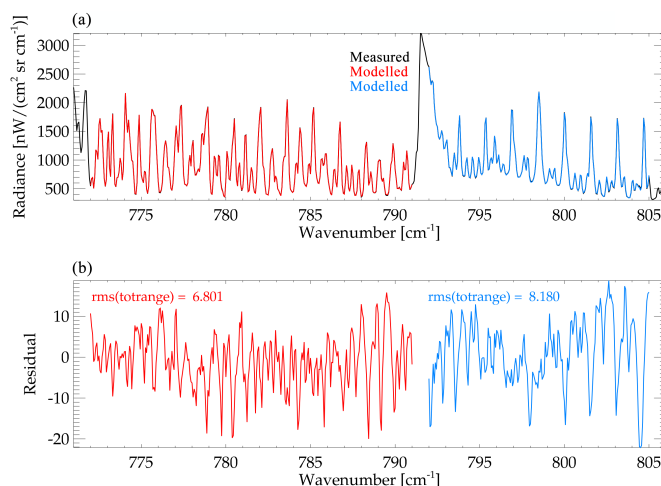


Figure 2. Exemplary spectra of MIPAS CCl_4 at 11.5 km during the RR period (July 2008): (a) spectra; (b) residuals.

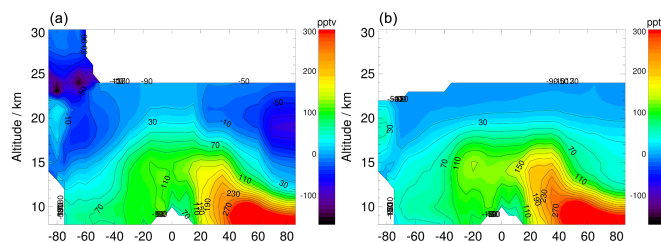


Figure 3. PAN altitude–latitude cross sections (July 2008) from a separate retrieval using the old CCl_4 distributions (a) and resulting from a joint retrieval with CCl_4 (b).

line mixing (Funke et al., 1998). This was done by using the Rosenkranz approximation (Rosenkranz, 1975). Tests were also performed using the computationally more demanding direct diagonalization, but this approach was not found to noticeably change the results of the retrieval. This is possibly the case because the microwindows were carefully selected to omit major spectral signatures of the CO_2 Q-branch and because the effect of line mixing is generally smaller at stratospheric pressure levels. However, it was still necessary to omit parts of the CO_2 Q-branch. Figures 4 and 5 show spectra where the full spectral region was fitted. In Fig. 4, line mixing was not considered and thus a large peak in the residual is visible close to 791.0 cm^{-1} . In Fig. 5, the Rosenkranz approximation was used to account for line mixing. Even though the residual is considerably smaller than without line mixing taken into account – as would be expected – peaks

significantly larger than for the remainder of the window are still visible between 791.0 and 792.0 cm^{-1} . Although inclusion of line mixing significantly reduces the residuals in the CO_2 branch, the residuals are still unacceptably large there. With the Rosenkranz approximation, however, the spectral region excluded from the fit could be narrowed from 791.0 to 792.0 cm^{-1} from 790.5 to 792.5 cm^{-1} .

3.3 New CCl_4 spectroscopic data

During the ongoing development of the MIPAS Envisat CCl_4 retrieval, a new CCl_4 spectroscopic data set was published by Harrison et al. (2017). Figure 6 shows the influence of these spectroscopic data on an altitude–latitude cross section of CCl_4 distributions of July 2008. The upper panel shows what stratospheric CCl_4 distributions retrieved with

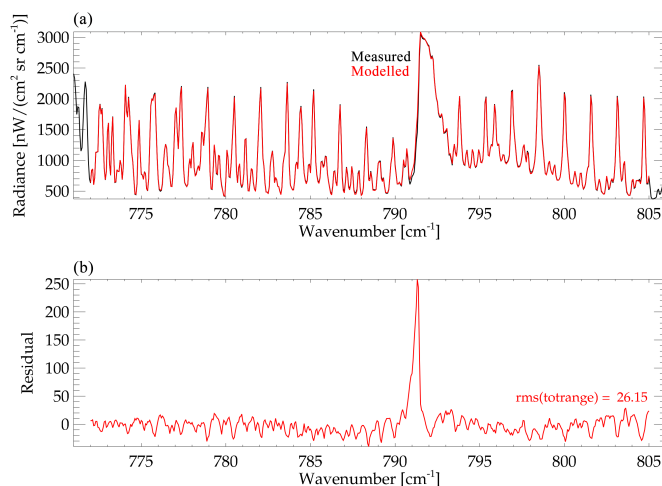


Figure 4. Impact of the CO₂ Q-branch at 11.5 km altitude without considering line mixing: (a) spectra; (b) residuals. Black: measured spectrum, hardly discernible because overplotted by modelled spectra.

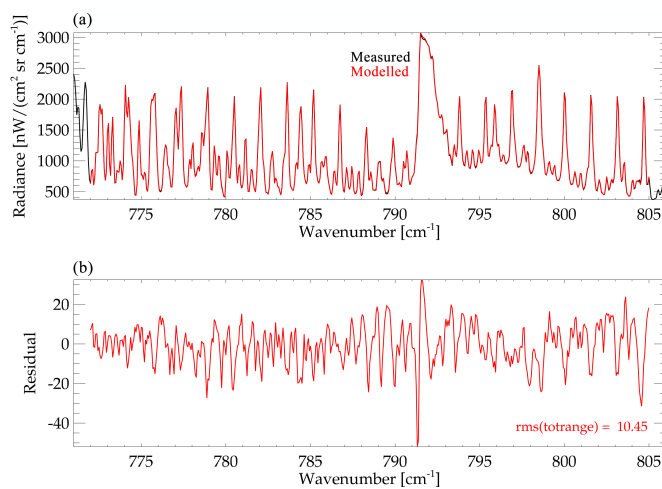


Figure 5. Impact of the CO₂ Q-branch at 11.5 km altitude taking line mixing into account: (a) spectra; (b) residuals. Black: measured spectrum, hardly discernible because overplotted by modelled spectra. Note the different scale of the residual axis compared to Fig. 4.

the original spectroscopic data set as presented in HITRAN 2000 (Nemchinov and Varanasi, 2003) look like. The lower panel shows the same cross section, but using the new spectroscopic data set by Harrison et al. (2017) for an otherwise identical retrieval setup. While the qualitative and morpho-

logical features of the distribution are very similar, lower volume mixing ratios of CCl₄ result when the new spectroscopic data set is used. Comparing these with reported values of ground-based measurements as presented in SPARC (2016) indicates that the updated spectroscopic data lead to results

2732

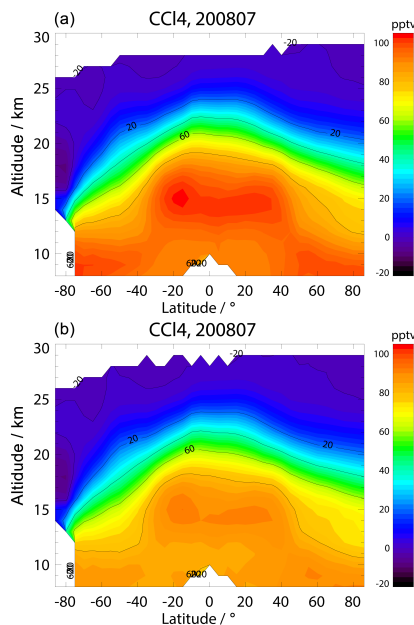


Figure 6. Altitude–latitude cross section of July 2008, using the spectroscopic data set by Nemtchinov and Varanasi (2003) (a) and using the new spectroscopic data by Harrison et al. (2017) (b).

which, in the tropopause region, agree better with tropospheric measurements. Tropospheric volume mixing ratios are reported to be at approximately 95 pptv, which is very close to what MIPAS Envisat presents around the tropical tropopause and at midlatitudes of the Northern Hemisphere when using the new spectroscopic data set. In contrast, using HITRAN 2000 sometimes results in volume mixing ratios above 100 pptv in the same region. Thus, we consider the new spectroscopic data set more adequate for the retrieval of CCl_4 .

4 Results

4.1 Distributions

Figures 7 and 8 and the lower panel of Fig. 6 give an overview of the latitudinal and altitude distribution of CCl_4 of different time periods. All of the altitude–latitude cross sections show the expected patterns of CCl_4 with a rapid decrease with increasing altitude in the stratosphere, as the gas is photolyzed there. In addition, highest volume mixing ratios appear at the Equator where CCl_4 , along with many other

E. Eckert et al.: MIPAS IMK/IAA CCl_4 retrieval

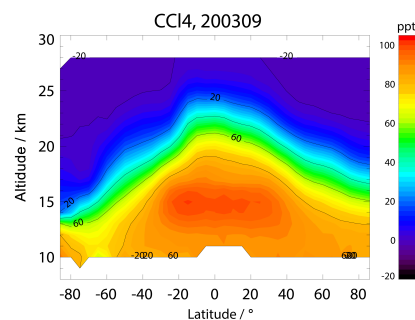


Figure 7. Altitude–latitude cross sections of MIPAS CCl_4 for the FR period (September 2003).

trace gases, enters the stratosphere due to the upward transport associated with the Brewer–Dobson circulation. During January 2010, March 2011 and particularly April 2011, subsidence of higher stratospheric air results in reduced mixing ratios over the North Pole. In Spring 2011, an unusually stable northern polar vortex resulted in severe ozone depletion and particularly strong subsidence (Manney et al., 2011; Sinnhuber et al., 2011), which is reflected in the observations shown here. In general, MIPAS Envisat shows higher volume mixing ratios in the lower stratosphere during the FR period, which fits well with the overall decline in CCl_4 abundance in the atmosphere due to its restriction under the Montreal Protocol. This impression is also supported by the lower panel in Fig. 6, which shows lower overall volume mixing ratios than MIPAS sees during the FR period but which are still slightly higher than during 2010 and 2011. All cross sections show a maximum in the CCl_4 volume mixing ratios around the tropical tropopause connected with values of similar magnitude at lower altitudes of northern extratropical regions. This pattern was also seen in HCFC-22 (Chirkov et al., 2016) and could be linked to the Asian monsoon. Calculations with the Chemical Lagrangian Model of the Stratosphere (CLaMS) by Vogel et al. (2016) show that there indeed exists a mechanism which can produce local maxima in the upper troposphere in 2-D distributions of source gases. So, the monsoon might offer an explanation for the patterns seen in CCl_4 around these atmospheric regions as well.

4.2 Altitude resolution

The vertical resolution of the CCl_4 profiles is very similar for the FR and the RR period. From about 2.5 to 3 km at the lower end of the profiles, it degrades to approximately 5 km at ~ 25 km and ~ 7 km at ~ 30 km, calculated as the full width at half maximum of the row of the averaging kernel matrix (Rodgers, 2000). The degrees of freedom are usually around 3.5 for the FR period and close to 4.0 for the RR

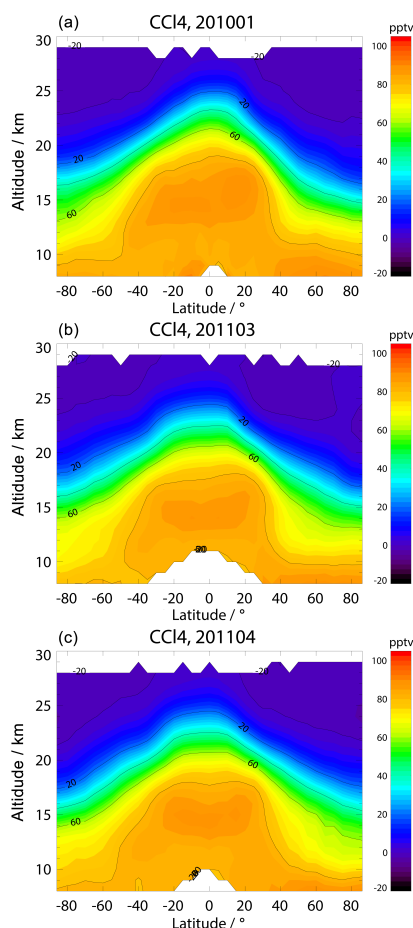


Figure 8. Altitude–latitude cross sections of MIPAS CCl₄ for the RR period. (a–c) January 2010, March 2011 and April 2011.

period (Fig. 9). This is presumably attributed to the finer vertical sampling during the RR period with 27 tangent altitudes compared to 17 tangent altitudes during the FR period. The signal decreases rapidly with altitude, as the volume mixing ratios of CCl₄ do. Above 30 km, hardly any CCl₄ information is available in the MIPAS spectra. Slightly below 20 km, the averaging kernels show negative side wiggles which are more pronounced during the FR period (left panel) than the RR period (right panel).

4.3 Error budget

Tables 2 and 3 list the error budgets for midlatitudes during the FR and RR period between 10 and 40 km. Examples for other latitudes can be found in the Appendix (Tables A1–A6). For legibility reasons, the errors are only given every 5 km, although the retrieval grid is 1 km. Errors due to elevation uncertainties of the line of sight (LOS) and uncertainties of several contributing species are given. All profiles show a strong increase in the relative errors at and above 30 km. During the FR period, the absolute total errors are fairly similar below this altitude, while large differences can occur from 20 km upwards. Absolute errors are close to 3 pptv between 10 and 25 km and around 5 to 6 pptv at 15 km where larger error appear for all atmospheric situations except the polar summer one where the errors stay close to 3 pptv. The largest error component is measurement noise (third column), while at 15 km significant parameter errors have to be considered, in particular the elevation uncertainties of the LOS and instrument line shape (ILS). Beyond this, uncertainties of HNO₄ and ClONO₂ profiles, frequency calibration (shift) and temperature contribute to the total error. The decrease of retrieval noise towards higher altitudes is explained by the coarser altitude resolution at higher altitudes. For the RR period, the patterns look slightly different. There is no peak in the total error around 15 km, but the total error is either rather constant at lower altitudes or decreases with altitude. Contributions to the error budget are, however, similar to the FR period.

Figure 10 compares the estimated total error with the deviation of the profiles in a quiescent atmosphere. This comparison was created in a similar way as in Eckert et al. (2016, Sect. 6). Up to 18 km altitude, the sample standard deviation of MIPAS Envisat results is only slightly larger than the estimated error. Thus, these profiles suggest that the estimated error can explain most of the variability in the CCl₄ profiles up to approximately 18 km. Correspondingly, the error estimate can be considered realistic from the bottom of the profile up to this altitude.

4.4 Trends

Figure 11 shows an altitude–latitude cross section of MIPAS Envisat CCl₄ trends. These trends were estimated by the same method as described by Eckert et al. (2014), which is based on the method by von Clarmann et al. (2010). In addition to the setup used by Eckert et al. (2014), the El-Niño–Southern Oscillation (ENSO) was also taken into account. The data set used for trend calculation covers the entire MIPAS Envisat measurement period from July 2002 to April 2012. The distribution of the trends agrees well with the trends estimated by Valeri et al. (2017), who calculated trends from MIPAS Envisat V7 data they formerly retrieved and displayed them on a pressure–latitude grid. The most likely cause of differences between their and our trend es-

2734

E. Eckert et al.: MIPAS IMK/IAA CCl_4 retrieval

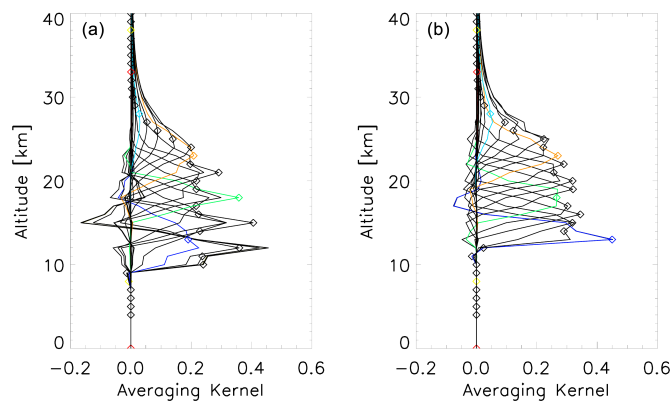


Figure 9. Rows of exemplary averaging kernels of MIPAS CCl_4 . (a) FR period (September 2003). (b) RR period (July 2008).

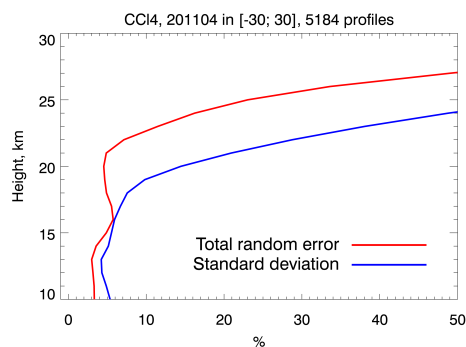


Figure 10. Comparison of the estimated total error with the standard deviation of several MIPAS profiles for a quiescent atmospheric situation (Equator). Red: total error budget; blue: standard deviation.

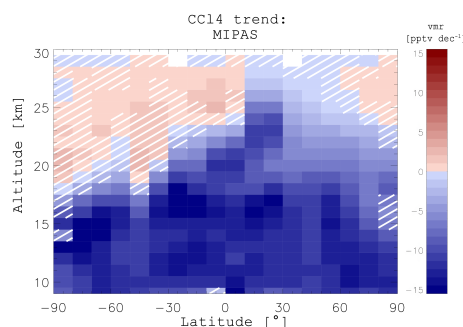


Figure 11. Altitude–latitude cross sections of MIPAS CCl_4 trends covering the entire measurement period from July 2002 to April 2012. Red colours indicate increasing CCl_4 volume mixing ratios. Blue colours indicate declining CCl_4 concentrations. Hatching shows where no statistically significant trends could be calculated at 2σ confidence level.

timates are the underlying MIPAS spectra. We use MIPAS V5 spectra which were found to be subject to an instrument drift due to detector aging (Eckert et al., 2014). Valeri et al. (2017) use version 7 spectra, where an attempt was made to tackle the problem of detector aging during the level-1 processing. However, Hubert et al. (2016) show that there is still a drift problem in the version 7 MIPAS temperatures. Since these temperature drifts are expected to propagate onto the retrieved CCl_4 mixing ratios, it is not clear if version 5 or version 7 is more adequate for trend analysis. In spite of these differences and technical differences

in the level-2 data processing, the trends inferred by Valeri et al. (2017) and ours show important common features. In both data sets a hemispheric asymmetry is found, with

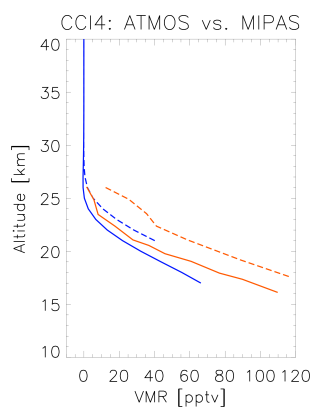
positive trends in the Southern Hemisphere around 25 km (although the region is larger in our data set) and negative trends in the Northern Hemisphere in almost the whole altitude range. Also the average magnitudes of the inferred trends agree reasonably well between both data sets.

Table 2. Error estimates for a midlatitude profile during the FR period. Errors are given in pptv (relative errors in %).

Altitude	Total error	Noise	Total parameter	Gain	LOS	HNO ₄	Shift	ILS	Temperature	ClONO ₂
40	0.0 (69.4)	0.0 (57.2)	0.0 (38.8)	0.0 (24.5)	0.0 (22.5)	0.0 (18.2)	0.0 (1.7)	0.0 (9.2)	0.0 (6.3)	0.0 (5.5)
35	0.0 (68.4)	0.0 (56.7)	0.0 (39.1)	0.0 (23.5)	0.0 (21.5)	0.0 (18.4)	0.0 (1.7)	0.0 (9.0)	0.0 (6.3)	0.0 (5.7)
30	0.2 (71.0)	0.2 (64.3)	0.1 (33.8)	0.1 (20.3)	0.1 (17.9)	0.1 (20.3)	0.0 (1.8)	0.0 (3.0)	0.0 (5.1)	0.0 (5.1)
25	2.3 (480.8)	2.2 (459.9)	0.7 (144.2)	0.4 (79.4)	0.0 (3.8)	0.6 (115.0)	0.0 (10.0)	0.0 (0.7)	0.1 (23.0)	0.1 (17.3)
20	2.9 (5.3)	2.4 (4.4)	1.6 (2.9)	0.0 (0.1)	1.5 (2.8)	0.1 (0.3)	0.0 (0.0)	0.7 (1.2)	0.1 (0.2)	0.1 (0.2)
15	5.0 (4.9)	2.1 (2.1)	4.5 (4.5)	0.7 (0.7)	4.0 (4.0)	0.1 (0.1)	0.1 (0.1)	2.0 (2.0)	0.1 (0.1)	0.1 (0.1)
10	2.7 (3.1)	2.5 (2.8)	0.9 (1.0)	0.2 (0.2)	0.2 (0.3)	0.3 (0.3)	0.1 (0.1)	0.4 (0.4)	0.5 (0.6)	0.1 (0.1)

Table 3. Error estimates for a midlatitude profile during the RR period. Errors are given in pptv (relative errors in %).

Altitude	Total error	Noise	Total parameter	Gain	LOS	HNO ₄	Shift	ILS	Temperature	ClONO ₂
40	0.0 (214.1)	0.0 (127.1)	0.0 (173.9)	0.0 (73.6)	0.0 (147.2)	0.0 (24.8)	0.0 (2.5)	0.0 (24.8)	0.0 (24.1)	0.0 (13.4)
35	0.0 (211.3)	0.0 (128.1)	0.0 (172.9)	0.0 (70.4)	0.0 (147.3)	0.0 (25.0)	0.0 (2.6)	0.0 (24.3)	0.0 (23.7)	0.0 (13.4)
30	0.2 (141.2)	0.1 (123.6)	0.1 (61.8)	0.0 (15.9)	0.1 (47.7)	0.0 (24.7)	0.0 (2.8)	0.0 (22.1)	0.0 (2.8)	0.0 (11.5)
25	2.4 (187.3)	2.2 (171.7)	0.9 (67.1)	0.2 (14.0)	0.4 (30.4)	0.4 (33.6)	0.1 (4.8)	0.6 (44.5)	0.0 (0.0)	0.2 (16.4)
20	3.5 (15.0)	2.6 (11.1)	2.4 (10.3)	0.1 (0.4)	2.3 (9.9)	0.1 (0.4)	0.1 (0.3)	0.1 (0.5)	0.1 (0.2)	0.0 (0.1)
15	3.3 (6.1)	2.0 (3.7)	2.6 (4.8)	0.5 (1.0)	2.5 (4.6)	0.1 (0.3)	0.0 (0.1)	0.1 (0.2)	0.1 (0.1)	0.0 (0.0)
10	5.7 (6.1)	4.3 (4.6)	3.7 (4.0)	1.1 (1.2)	3.5 (3.8)	0.2 (0.2)	0.0 (0.0)	0.4 (0.4)	0.4 (0.4)	0.1 (0.1)

**Figure 12.** Qualitative comparison of profiles from ATMOS (orange) taken during the ATLAS-3 mission (as shown in Zander et al., 1996, Fig. 1) and climatological means of MIPAS (blue) during 3–12 November of each year. Solid lines refer to midlatitude measurements (35–49° N). Dashed lines indicate subtropical measurements (20–35° N).

5 Comparisons

5.1 Historical comparisons

5.1.1 ATMOS

The ATMOS instrument measured in solar occultation covering the spectral region from 600 to 4700 cm⁻¹ with a spectral resolution of 0.01 cm⁻¹. ATMOS took measurements in 1985, 1992, 1993 and 1994. The ATMOS profiles shown in Fig. 12 were extracted directly from Zander et al. (1996, Fig. 1). CCl₄ volume mixing ratio profiles in the subtropics (20–35° N; thin dashed lines) and at midlatitudes (35–49° N; thin full lines) are presented there. Measurements were taken from 3 to 12 November in 1994 during the ATLAS-3 shuttle mission. We depicted midlatitude profiles as solid lines and subtropical profiles as dashed lines in Fig. 12 of this paper. To compare the ATMOS profiles with MIPAS Envisat, we used MIPAS Envisat data of all years from 3 to 12 November and calculated an arithmetic mean for both latitude bands (subtropics and midlatitudes). In Fig. 12, MIPAS Envisat profiles are shown in blue, while the ATMOS profiles are shown in orange. The ATMOS profiles show higher volume mixing ratios than those of MIPAS Envisat, because they were measured shortly after CCl₄ emissions were restricted and, thus, volume mixing ratios used to be higher in the atmosphere. However, the general shapes of the ATMOS profiles agree well with those of MIPAS Envisat. Both MIPAS Envisat and ATMOS show CCl₄ mixing ratios which quickly decrease with altitude. The slopes of decline are similar above ~20 km. Largest differences are visible at the lower end of

2736

the midlatitude profiles. ATMOS CCl_4 mixing ratios also agree well with Liang et al. (2016, Fig. 2) where a time series of CCl_4 surface mixing ratios over several decades is shown. Volume mixing ratios at the lower end of the profiles are noticeably higher than 100 pptv, which is in very good agreement with peak values of CCl_4 shown in Liang et al. (2016, Fig. 2) for the time around and shortly after 1990. Taking the temporal development of the surface mixing ratios into account, ATMOS and MIPAS Envisat measurements provide a coherent picture.

5.1.2 MIPAS-B

The first balloon-borne version of the MIPAS instrument was developed prior to the satellite instrument in the late 1980s and early 1990s at the Institute of Meteorology and Climate Research (IMK) in Karlsruhe (Fischer and Oelhaf, 1996). Measurements with this instrument have been taken since 1989 (von Clarmann et al., 1993) and first profiles of CCl_4 were derived from a flight at Kiruna, Sweden, on 14 March 1992 (von Clarmann et al., 1995). Due to the strong decrease of CCl_4 with altitude, a clear signal of the gas could not be identified at tangent altitudes of 14.5 km and above. Thus, only the spectrum at 11.3 km was analyzed and the total amount of CCl_4 was estimated by scaling the vertical profile and using information on the shape as measured in polar winter conditions before. This leads to an estimated concentration of approximately 110 pptv at 11.3 km, which is slightly higher than the peak surface values in the long time series of CCl_4 shown in Liang et al. (2016). Ground-based measurements shown in there support favouring the MIPAS Envisat CCl_4 retrieval with the new spectroscopic data set, since respective results agree better with measurements shown in Liang et al. (2016). MIPAS-B results overestimate the ground-based measurements slightly providing a consistent picture when taking differences in the volume mixing ratios into account which result from the old versus the new spectroscopic data set.

5.2 Comparisons with collocated measurements

All collocated measurements were analyzed using spectroscopic data of Nemtchinov and Varanasi (2003), which are included in the HITRAN 2000 database (Rothman et al., 2003). Thus, in order to allow for a meaningful comparison and not to mask possible other differences, a dedicated MIPAS Envisat comparison data set was generated which is based on these spectroscopic data as well.

5.2.1 ACE-FTS

The Atmospheric Chemistry Experiment Fourier Transform Spectrometer is one of two instruments aboard the Canadian Satellite SCISAT-1. On 12 August 2003, it was launched into a 74° orbit at 650 km to ensure a focus on higher latitudes. It covers the globe from 85° S to 85° N. Since ACE-

E. Eckert et al.: MIPAS IMK/IAA CCl_4 retrieval

FTS is an occultation instrument, it takes measurements during 15 sunrises and 15 sunsets a day within two latitude bands. The vertical scan range covers altitudes from the middle troposphere up to 150 km. Wavelengths between 750 and 4400 cm^{-1} (13.3 and 2.3 μm) can be detected with a spectral resolution of 0.02 cm^{-1} . The vertical sampling depends on the altitude as well as the beta angle. The latter is the angle between the orbit track and the path from the instrument to the sun. The sampling ranges from ~ 1 km between 10 and 20 km to ~ 2 –3.5 km around 35 km and declines to 5–6 km at the upper end of the vertical range. The field of view covers 3–4 km, which is approximately similar to the vertical resolution of the instrument. Comparisons in this study were made using version 3.5 of the ACE-FTS data. The CCl_4 retrieval is performed between 787.5 and 805.5 cm^{-1} at altitudes from 7 to 25 km (Allen et al., 2009).

For the comparison with ACE-FTS (Fig. 13), coincident profiles within 2 h time difference and no further than 5° latitude and 10° longitude away were used. Profiles at latitudes higher than 60° S were omitted. Between the lower end and ~ 16 km the agreement is always close to 10 %, with slightly larger differences below 10 km than between 10 and 15 km. Above 15 km, the mean profiles deviate more strongly and exceed relative differences of 50 % above 19 km (Fig. 13d). However, differences above 19 km are not as apparent in the absolute comparison (Fig. 13a). The volume mixing ratio difference stays within similar values up to near 25 km. Since CCl_4 decreases rapidly with altitude, this difference is far more pronounced in relative terms. MIPAS shows slightly lower volume mixing ratios than ACE-FTS, in general. Part of this might be attributed to PAN not being accounted for in the ACE-FTS v3.5 retrieval (Harrison et al., 2017). With PAN missing from the forward model calculations, the retrieval increases CCl_4 to compensate. Preliminary ACE-FTS version 4 results indicate that retrieved CCl_4 will skew lower when PAN is included. However, Harrison et al. (2017) do not investigate the magnitude of the effect of including PAN versus not including it. Other items changed in the retrieval, e.g. the microwindow set and new cross sections, so it is not clear how much of the decrease in CCl_4 can be attributed to the inclusion of PAN as an interferer in the ACE-FTS retrieval. Nevertheless, the agreement between MIPAS Envisat and ACE is very good, staying within the 10 % range for the differences up to above 15 km.

5.2.2 MIPAS-B2

MIPAS-B2 is the follow-up of MIPAS-B (Friedl-Vallon et al., 2004), which was lost in 1992. MIPAS-B and MIPAS-B2 measurements add up to more than 20 flights to date. MIPAS-B2 covers the spectral range from 750 to 2500 cm^{-1} (13.3 and 4 μm) and vertical ranges up to the floating altitude of typically around 30–40 km. The vertical sampling is approximately 1.5 km. The spectral region used for the MIPAS-B2 retrieval ranges from 786.0 to 806.0 cm^{-1} . MIPAS-B2

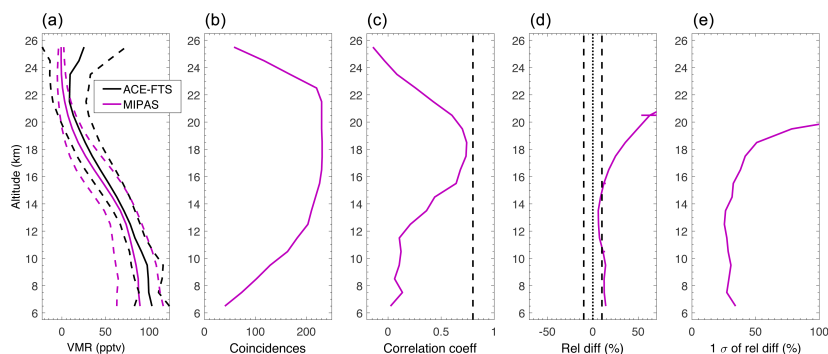


Figure 13. Comparison of MIPAS Envisat and version 3.5 ACE-FTS CCl₄. (a) Mean profiles of all coincident profiles (black: ACE-FTS; magenta: MIPAS). Dashed lines show the standard deviations of the mean profiles. (b) Number of coincident points per altitude. (c) Correlation coefficient of the mean profiles. (d) Relative differences of the mean profiles. (e) One standard deviation of the relative differences of the mean profiles.

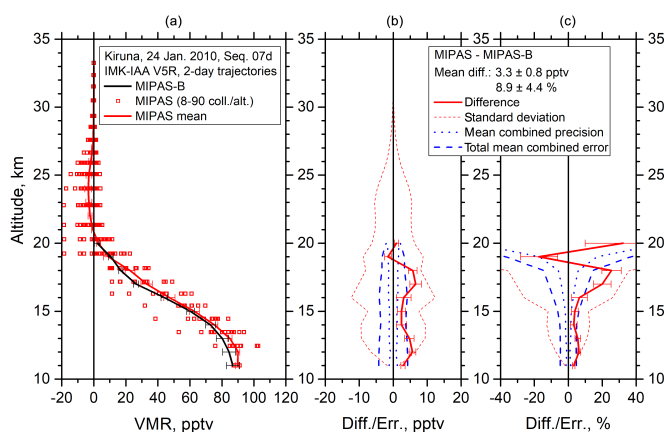


Figure 14. Comparison of MIPAS Envisat and MIPAS-B2 CCl₄ for the MIPAS-B2 flight on 24 January 2010 over Kiruna, Sweden. (a) Mean profile of all coincident profiles (black line: MIPAS-B2; red line: MIPAS mean; red squares: coincident MIPAS measurements). (b) Absolute total error budget without consideration of the spectroscopy error. (c) Relative error budget – red continuous line: difference between the mean profiles; red dotted line: standard deviation; blue dotted line: mean combined precision; blue dashed line: total mean combined error.

and MIPAS Envisat use the same retrieval strategy and forward model to derive vertical profiles.

Figures 14 and 15 show CCl₄ measurements from a single flight of MIPAS-B2 each, compared with collocated measurements of MIPAS Envisat along diabatic 2-day backward and forward trajectories. These trajectories were calculated at Free University of Berlin (Naujokat and Grunow, 2003) and are based on European Centre for Medium-Range Weather Forecasts (ECMWF) $1.25^\circ \times 1.25^\circ$ analyses. The trajectories

start at different altitudes at the respective geolocation of the balloon measurement. Coincidence criteria for this comparison were 1 h and 500 km within the temporal and spacial range of the trajectories. Figure 14 shows a comparison with the MIPAS-B2 flight on 24 January 2010. The comparison with the MIPAS Envisat mean profile (red line), which was calculated from the ensemble of all collocated MIPAS Envisat measurements (red squares), agrees with the MIPAS-B2 measurement (black line) within 5 pptv for most of the

2738

E. Eckert et al.: MIPAS IMK/IAA CCl_4 retrieval

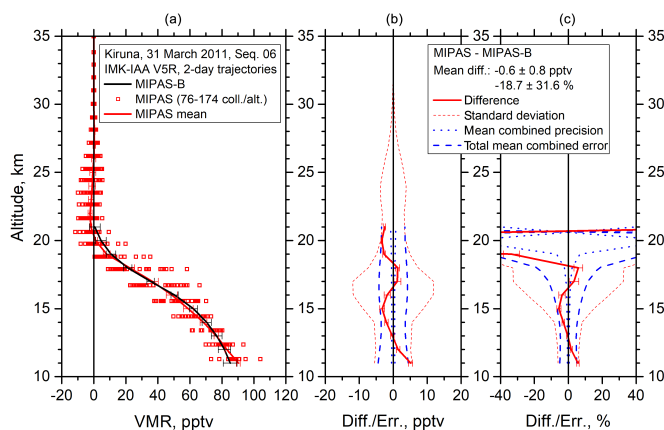


Figure 15. Comparison of MIPAS Envisat and MIPAS-B2 CCl_4 for the MIPAS-B2 flight on 31 March 2011 over Kiruna, Sweden. (a) Mean profile of all coincident profiles (black line: MIPAS-B2; red line: MIPAS mean; red squares: coincident MIPAS measurements). (b) Absolute total error budget without consideration of the spectroscopy error. (c) Relative error budget – red continuous line: difference between the mean profiles; red dotted line: standard deviation; blue dotted line: mean combined precision; blue dashed line: total mean combined error.

altitude range. The MIPAS-B2 measurement lies well within the spread of all collocated MIPAS Envisat profiles. The difference (middle panel) is always close to the total combined error, which includes all error estimates except the spectroscopy error. The latter has not been included because a MIPAS Envisat retrieval setup was used for this comparison which is based on the same spectroscopic data as the MIPAS-B2 retrieval. The right panel shows the relative error, which stays well within 5% up to 17 km. Only between 16 and 18 km, the relative difference noticeably exceeds the combined error of the instruments.

The comparison of the MIPAS-B2 flight on 31 March 2011 (Fig. 15) with MIPAS Envisat presents even better agreement. The difference between the two profiles never exceeds 5 pptv (middle panel) and stays within or close to the combined error of the instruments throughout the whole altitude range. Larger deviations in the relative differences only occur above 18 km, where the combined error of the instruments also increases rapidly, because of small volume mixing ratios of CCl_4 . Overall, the comparisons with MIPAS-B2 show excellent agreement between the two instruments. This suggests that the MIPAS Envisat CCl_4 error estimates are realistic and that the residuals in the CO_2 lines mentioned in Sect. 3.2 have no major impact on the CCl_4 retrieval. This is also supported by Fig. 10, at least up to about 18 km, since the standard deviation of the profiles can be explained by the MIPAS Envisat error estimates to a large extent.

5.2.3 Cryosampler

The cryosampler whose measurements are used here was developed at Forschungszentrum Jülich (Germany) in the early 1980s (Schmidt et al., 1987) and is a balloon-borne instrument. It collects whole air samples which are then frozen during the flight and analyzed using gas chromatography after the flight. In this analysis, a flight performed on 1 April 2011 by the University of Frankfurt (Fig. 16 black circles) is compared to collocated MIPAS Envisat profiles that lie within 1000 km and 24 h of the cryosampler profile. The MIPAS Envisat profiles used for the comparison are those retrieved with the new spectroscopic data set (continuous blue line: closest MIPAS profile; red line: MIPAS mean profile; blue-greyish lines: all collocated MIPAS profiles). In addition, the closest profile produced with the old spectroscopic data set is shown (dashed blue line). The only difference between the blue line and the dashed blue line are the different spectroscopic data sets. It is clearly visible that the closest MIPAS profile produced with the new spectroscopic data comes closer to the cryosampler measurements, even though these still show slightly lower volume mixing ratios of CCl_4 . A similar pattern of two outliers (second and fourth lowest cryosampler measurements) was also seen in a comparison of cryosampler and MIPAS measurements of CFC-11 and CFC-12 (Eckert et al., 2016), even though the second lowest outlier is not as obvious for the CFCs. However, this might be an indication that cryosampler captured fine structures (like laminae) produced by the unique atmospheric situation in spring 2011 (Manney et al., 2011; Sinnhuber

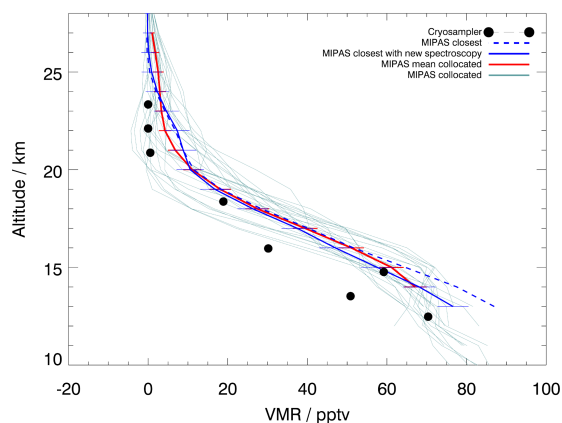


Figure 16. Comparison of MIPAS Envisat and cryosampler CCl₄. The cryosampler measurement was taken on 1 April 2011. The continuous and dashed blue lines are the respective closest MIPAS Envisat profiles calculated using the new and the old spectroscopic data set.

et al., 2011), which MIPAS Envisat cannot resolve due to its coarser vertical resolution. All other cryosampler measurements lie within the spread of the collocated MIPAS Envisat profiles. Taking this into account, the overall agreement of MIPAS and cryosampler is good and Fig. 16 supports the assumption that the retrieval is improved by the usage of the new spectroscopic data set.

6 Conclusions

Vertical profiles of CCl₄ were retrieved from MIPAS Envisat limb emission spectra considering various interfering trace gases and with PAN playing a particularly important role. Using line mixing in the forward model made it possible to narrow the spectral region that had to be omitted due to large residuals and thus to include additional information useful for the retrieval of CCl₄, even though parts of the CO₂ Q-branch still had to be excluded. Introducing a new spectroscopic data set (Harrison et al., 2017) resulted in lower volume mixing ratios of CCl₄, which agree better with other results, e.g. tropospheric values shown in Liang et al. (2016) and cryosampler measurements. The expected atmospheric distribution patterns are clearly visible in altitude–latitude cross sections. These show higher volume mixing ratios of CCl₄ in the tropics and at lower altitudes, which quickly decrease above the tropopause due to photolysis. They also decrease with increasing latitude and thus follow the Brewer–Dobson circulation. A maximum in the tropics connected with higher values of CCl₄ below the northern extratropical tropopause is a feature also seen in HCFC-22 (Chirkov et al., 2016), where it was associated with the uplift in the Asian monsoon, so CCl₄ distributions in this region might have a

similar explanation. Trends of the entire measurement period from July 2002 to April 2012 show good agreement with trends estimated by Valeri et al. (2017). Comparisons with ACE-FTS and MIPAS-B2 show very good agreement and historical measurements of MIPAS-B2 and ATMOS are coherent with MIPAS Envisat CCl₄ results using the new spectroscopic data. MIPAS profiles retrieved using the new spectroscopic data set agree well with cryosampler and deviations between the measurements can be explained reasonably. The latter comparison also suggests that the new spectroscopic data set improves the MIPAS Envisat CCl₄ retrieval. The MIPAS Envisat estimated error can explain most of the variability of a set of profiles measured during quiescent atmospheric conditions up to 18 km, so the error estimate seems to be realistic. This is also supported by the comparison of MIPAS Envisat and MIPAS-B2 where the differences between the measurements stay mostly within the combined error of the instruments. Putting differences resulting from different special resolutions aside, the comparison with the cryosampler profile also suggests favouring the spectroscopic data set introduced by Harrison et al. (2017) over the data set used before.

Data availability. MIPAS data can be accessed at the following website: <https://www.imk-asf.kit.edu/english/308.php>. The cryosampler data can be obtained by contacting Andreas Engel via email (an.engel@iau.unifrankfurt.de). Information on MIPAS-B can be found at the following website: <http://www.imk-asf.kit.edu/english/ffb.php>. For SCISAT/ACE-FTS, the most recent data version is available from the ACE team, University of Waterloo, Canada. Publicly available validated data sets can be found at <http://www.ace.uwaterloo.ca/data.html>.

2740

E. Eckert et al.: MIPAS IMK/IAA CCl₄ retrieval

Appendix A: Error estimates

Table A1. Error estimates for an equatorial profile during the FR period. Errors are given in pptv (relative errors in %).

Altitude	Total error	Noise	Total parameter	Gain	LOS	HNO ₄	Shift	ILS	Temperature	ClONO ₂
40	0.0 (210.6)	0.0 (178.7)	0.0 (114.8)	0.0 (70.2)	0.0 (45.3)	0.0 (55.5)	0.0 (6.0)	0.0 (37.6)	0.0 (30.0)	0.0 (17.2)
35	0.0 (214.1)	0.0 (183.5)	0.0 (116.2)	0.0 (67.3)	0.0 (45.3)	0.0 (55.7)	0.0 (6.0)	0.0 (37.3)	0.0 (30.0)	0.0 (17.1)
30	0.2 (195.8)	0.2 (177.1)	0.1 (85.8)	0.1 (51.3)	0.0 (23.3)	0.1 (54.1)	0.0 (5.2)	0.0 (17.7)	0.0 (23.3)	0.0 (14.0)
25	2.3 (30.4)	2.2 (29.0)	0.9 (11.9)	0.4 (4.8)	0.5 (7.1)	0.5 (7.1)	0.1 (0.8)	0.2 (2.6)	0.2 (2.8)	0.1 (1.3)
20	2.8 (3.8)	2.5 (3.4)	1.3 (1.8)	0.2 (0.2)	0.8 (1.2)	0.1 (0.2)	0.0 (0.0)	0.9 (1.2)	0.3 (0.4)	0.1 (0.2)
15	5.3 (5.5)	2.2 (2.3)	4.9 (5.1)	0.9 (1.0)	4.2 (4.4)	0.2 (0.2)	0.1 (0.1)	2.3 (2.4)	0.4 (0.4)	0.1 (0.1)
10	2.8 (3.2)	2.6 (2.9)	1.0 (1.1)	0.2 (0.2)	0.1 (0.1)	0.2 (0.2)	0.1 (0.1)	0.3 (0.4)	0.8 (0.9)	0.1 (0.1)

Table A2. Error estimates for a polar summer profile during the FR period. Errors are given in pptv (relative errors in %).

Altitude	Total error	Noise	Total parameter	Gain	LOS	HNO ₄	Shift	ILS	Temperature	ClONO ₂
40	0.0 (95.1)	0.0 (64.2)	0.0 (69.4)	0.0 (38.5)	0.0 (46.2)	0.0 (19.8)	0.0 (1.4)	0.0 (19.0)	0.0 (11.3)	0.0 (5.1)
35	0.0 (93.7)	0.0 (64.1)	0.0 (69.0)	0.0 (39.4)	0.0 (46.8)	0.0 (19.7)	0.0 (1.4)	0.0 (19.0)	0.0 (11.3)	0.0 (5.2)
30	0.2 (117.2)	0.2 (87.9)	0.1 (73.2)	0.1 (39.5)	0.1 (53.7)	0.1 (26.4)	0.0 (1.8)	0.0 (11.2)	0.0 (11.2)	0.0 (5.9)
25	2.5 (212.9)	2.2 (187.4)	1.2 (102.2)	0.5 (43.4)	0.9 (73.3)	0.6 (51.1)	0.1 (4.4)	0.1 (8.2)	0.1 (11.1)	0.1 (8.5)
20	2.4 (42.2)	2.1 (36.9)	1.2 (21.1)	0.1 (1.7)	1.2 (21.1)	0.2 (4.0)	0.0 (0.6)	0.0 (0.4)	0.1 (1.5)	0.0 (0.7)
15	2.8 (4.7)	1.7 (2.9)	2.3 (3.9)	0.1 (0.2)	2.2 (3.7)	0.2 (0.4)	0.1 (0.1)	0.5 (0.9)	0.2 (0.3)	0.1 (0.1)
10	3.0 (3.7)	2.3 (2.8)	2.0 (2.4)	0.1 (0.1)	1.4 (1.7)	0.1 (0.1)	0.1 (0.1)	1.2 (1.5)	0.3 (0.3)	0.0 (0.0)

Table A3. Error estimates for a polar winter profile during the FR period. Errors are given in pptv (relative errors in %).

Altitude	Total error	Noise	Total parameter	Gain	LOS	HNO ₄	Shift	ILS	Temperature	ClONO ₂
40	0.0 (45.8)	0.0 (34.7)	0.0 (30.5)	0.0 (16.7)	0.0 (20.8)	0.0 (9.3)	0.0 (0.9)	0.0 (7.4)	0.0 (5.8)	0.0 (4.4)
35	0.0 (46.6)	0.0 (34.6)	0.0 (29.3)	0.0 (16.0)	0.0 (20.0)	0.0 (9.3)	0.0 (0.9)	0.0 (7.3)	0.0 (5.9)	0.0 (4.4)
30	0.2 (47.8)	0.2 (40.7)	0.1 (26.3)	0.0 (11.7)	0.1 (19.4)	0.0 (10.5)	0.0 (0.7)	0.0 (1.8)	0.0 (4.1)	0.0 (4.1)
25	2.4 (58.5)	2.2 (53.6)	1.1 (26.8)	0.4 (8.8)	0.8 (19.7)	0.6 (13.6)	0.0 (0.4)	0.1 (2.4)	0.1 (2.9)	0.2 (5.1)
20	2.8 (22.8)	2.7 (22.0)	0.9 (7.3)	0.0 (0.4)	0.8 (6.8)	0.3 (2.4)	0.1 (0.4)	0.0 (0.1)	0.0 (0.1)	0.1 (1.0)
15	4.4 (7.7)	1.8 (3.1)	4.0 (7.0)	0.0 (0.1)	3.9 (6.8)	0.2 (0.4)	0.0 (0.0)	0.9 (1.6)	0.1 (0.1)	0.0 (0.1)
10	2.7 (3.1)	2.5 (2.9)	0.9 (1.0)	0.2 (0.2)	0.5 (0.6)	0.1 (0.1)	0.1 (0.1)	0.1 (0.1)	0.5 (0.6)	0.1 (0.1)

Table A4. Error estimates for an equatorial profile during the RR period. Errors are given in pptv (relative errors in %).

Altitude	Total error	Noise	Total parameter	Gain	LOS	HNO ₄	Shift	ILS	Temperature	ClONO ₂
40	0.0 (3058.9)	0.0 (2867.7)	0.0 (879.4)	0.0 (172.1)	0.0 (124.3)	0.0 (726.5)	0.0 (47.8)	0.0 (372.8)	0.0 (18.2)	0.0 (210.3)
35	0.0 (18560.0)	0.0 (17998.0)	0.0 (5511.9)	0.0 (899.9)	0.0 (899.9)	0.0 (4443.2)	0.0 (303.7)	0.0 (2531.0)	0.0 (146.2)	0.0 (1293.6)
30	0.2 (73.5)	0.2 (60.7)	0.1 (41.6)	0.0 (13.1)	0.1 (19.5)	0.0 (14.1)	0.0 (2.0)	0.1 (31.3)	0.0 (3.5)	0.0 (3.5)
25	2.6 (19.9)	2.0 (15.3)	1.6 (12.2)	0.4 (3.2)	1.2 (9.2)	0.3 (2.4)	0.1 (0.5)	0.9 (6.9)	0.1 (0.6)	0.1 (0.5)
20	3.3 (5.5)	2.4 (4.0)	2.2 (3.7)	0.6 (1.0)	2.1 (3.5)	0.1 (0.1)	0.1 (0.1)	0.3 (0.5)	0.1 (0.2)	0.0 (0.1)
15	6.2 (7.3)	5.1 (6.0)	3.6 (4.3)	1.0 (1.2)	3.4 (4.0)	0.4 (0.5)	0.0 (0.0)	0.0 (0.0)	0.5 (0.6)	0.0 (0.0)
10	6.2 (7.3)	4.9 (5.8)	3.7 (4.4)	1.1 (1.3)	3.5 (4.1)	0.4 (0.5)	0.0 (0.0)	0.1 (0.1)	0.5 (0.6)	0.0 (0.1)

E. Eckert et al.: MIPAS IMK/IAA CCl₄ retrieval

2741

Table A5. Error estimates for a polar summer profile during the RR period. Errors are given in pptv (relative errors in %).

Altitude	Total error	Noise	Total parameter	Gain	LOS	HNO ₄	Shift	ILS	Temperature	ClONO ₂
40	0.0 (336.8)	0.0 (307.1)	0.0 (158.5)	0.0 (96.1)	0.0 (56.5)	0.0 (73.3)	0.0 (2.2)	0.0 (70.3)	0.0 (2.7)	0.0 (12.9)
35	0.0 (333.4)	0.0 (296.4)	0.0 (148.2)	0.0 (92.6)	0.0 (55.6)	0.0 (72.2)	0.0 (2.0)	0.0 (67.6)	0.0 (2.7)	0.0 (13.0)
30	0.2 (299.3)	0.2 (273.3)	0.1 (123.6)	0.1 (80.7)	0.0 (52.1)	0.1 (69.0)	0.0 (0.4)	0.0 (27.3)	0.0 (3.1)	0.0 (7.5)
25	2.2 (72.1)	2.1 (68.9)	0.6 (19.3)	0.3 (10.2)	0.1 (2.9)	0.5 (15.7)	0.0 (0.6)	0.0 (1.0)	0.0 (0.5)	0.1 (1.9)
20	3.0 (16.2)	2.2 (11.9)	2.0 (10.8)	0.0 (0.1)	2.0 (10.8)	0.1 (0.4)	0.1 (0.5)	0.4 (2.3)	0.0 (0.2)	0.0 (0.1)
15	2.8 (3.9)	2.2 (3.1)	1.8 (2.5)	0.2 (0.3)	1.6 (2.3)	0.1 (0.2)	0.0 (0.0)	0.8 (1.2)	0.0 (0.1)	0.0 (0.0)
10	3.0 (3.6)	1.8 (2.2)	2.5 (3.0)	0.2 (0.3)	2.2 (2.6)	0.0 (0.1)	0.1 (0.2)	1.0 (1.2)	0.1 (0.1)	0.0 (0.0)

Table A6. Error estimates for a polar winter profile during the RR period. Errors are given in pptv (relative errors in %).

Altitude	Total error	Noise	Total parameter	Gain	LOS	HNO ₄	Shift	ILS	Temperature	ClONO ₂
40	0.0 (632.5)	0.0 (367.3)	0.0 (510.1)	0.0 (204.0)	0.0 (448.9)	0.0 (67.3)	0.0 (9.8)	0.0 (24.5)	0.0 (61.2)	0.0 (36.7)
35	0.0 (608.6)	0.0 (342.4)	0.0 (494.5)	0.0 (190.2)	0.0 (437.4)	0.0 (66.6)	0.0 (9.5)	0.0 (22.8)	0.0 (60.9)	0.0 (36.1)
30	0.2 (369.8)	0.1 (228.9)	0.2 (281.8)	0.1 (112.7)	0.1 (264.1)	0.0 (42.3)	0.0 (6.0)	0.0 (2.5)	0.0 (33.5)	0.0 (22.9)
25	2.9 (308.3)	2.2 (233.9)	1.8 (191.3)	0.7 (76.5)	1.6 (170.1)	0.4 (41.5)	0.1 (6.1)	0.2 (26.6)	0.2 (20.2)	0.2 (23.4)
20	2.9 (46.0)	2.7 (42.8)	1.1 (17.4)	0.1 (1.4)	1.0 (15.9)	0.2 (2.5)	0.1 (1.2)	0.3 (4.6)	0.1 (0.9)	0.1 (1.3)
15	3.4 (5.1)	2.3 (3.4)	2.5 (3.7)	0.3 (0.5)	2.4 (3.6)	0.1 (0.2)	0.0 (0.1)	0.5 (0.7)	0.1 (0.1)	0.0 (0.0)
10	2.2 (2.6)	1.5 (1.8)	1.6 (1.9)	0.0 (0.0)	1.4 (1.7)	0.1 (0.1)	0.0 (0.0)	0.7 (0.9)	0.2 (0.2)	0.0 (0.0)

2742

Competing interests. The authors declare that they have no conflict of interest.

Acknowledgements. The retrievals of IMK/IAA were partly performed on the HP XC4000 of the Scientific Supercomputing Center (SSC) Karlsruhe under project grant MIPAS. IMK data analysis was supported by DLR under contract number 50EE0901. MIPAS level 1B data were provided by ESA. We acknowledge support by Deutsche Forschungsgemeinschaft and Open Access Publishing Fund of Karlsruhe Institute of Technology. This work was supported by the DFG project for the “Consideration of lifetimes of tracers for the determination of stratospheric age spectra and the Brewer–Dobson Circulation (COLIBRI)”. The Atmospheric Chemistry Experiment (ACE), also known as SCISAT, is a Canadian-led mission mainly supported by the Canadian Space Agency and the Natural Sciences and Engineering Research Council of Canada. Balloon flights and data analysis of MIPAS-B data used here were supported by the European Space Agency (ESA), the German Aerospace Center (DLR), CNRS (Centre National de la Recherche Scientifique) and CNES (Centre National d’Etudes Spatiales).

The article processing charges for this open-access publication were covered by a Research Centre of the Helmholtz Association.

Edited by: Helen Worden

Reviewed by: Hugh C. Pumphrey and one anonymous referee

References

Allen, N. D. C., Bernath, P. F., Boone, C. D., Chipperfield, M. P., Fu, D., Manney, G. L., Oram, D. E., Toon, G. C., and Weisenstein, D. K.: Global carbon tetrachloride distributions obtained from the Atmospheric Chemistry Experiment (ACE), *Atmos. Chem. Phys.*, 9, 7449–7459, <https://doi.org/10.5194/acp-9-7449-2009>, 2009.

Chirkov, M., Stiller, G. P., Laeng, A., Kellmann, S., von Clarmann, T., Boone, C. D., Elkins, J. W., Engel, A., Glatthor, N., Grabowski, U., Harth, C. M., Kiefer, M., Kolonjari, F., Krummel, P. B., Linden, A., Lunder, C. R., Miller, B. R., Montzka, S. A., Mühle, J., O’Doherty, S., Orphal, J., Prinn, R. G., Toon, G., Vollmer, M. K., Walker, K. A., Weiss, R. F., Wiese, A., and Young, D.: Global HCFC-22 measurements with MIPAS: retrieval, validation, global distribution and its evolution over 2005–2012, *Atmos. Chem. Phys.*, 16, 3345–3368, <https://doi.org/10.5194/acp-16-3345-2016>, 2016.

Eckert, E., von Clarmann, T., Kiefer, M., Stiller, G. P., Lossow, S., Glatthor, N., Degenstein, D. A., Froidevaux, L., Godin-Beekmann, S., Leblanc, T., McDermid, S., Pastel, M., Steinbrecht, W., Swart, D. P. J., Walker, K. A., and Bernath, P. F.: Drift-corrected trends and periodic variations in MIPAS IMK/IAA ozone measurements, *Atmos. Chem. Phys.*, 14, 2571–2589, <https://doi.org/10.5194/acp-14-2571-2014>, 2014.

Eckert, E., Laeng, A., Lossow, S., Kellmann, S., Stiller, G., von Clarmann, T., Glatthor, N., Höpfner, M., Kiefer, M., Oelhaf, H., Orphal, J., Funke, B., Grabowski, U., Haanel, F., Linden, A.,

E. Eckert et al.: MIPAS IMK/IAA CCl₄ retrieval

Wetzel, G., Woiwode, W., Bernath, P. F., Boone, C., Dutton, G. S., Elkins, J. W., Engel, A., Gille, J. C., Kolonjari, F., Sugita, T., Toon, G. C., and Walker, K. A.: MIPAS IMK/IAA CFC-11 (CCl₃F) and CFC-12 (CCl₂F₂) measurements: accuracy, precision and long-term stability, *Atmos. Meas. Tech.*, 9, 3355–3389, <https://doi.org/10.5194/amt-9-3355-2016>, 2016.

Fischer, H. and Oelhaf, H.: Remote sensing of vertical profiles of atmospheric trace constituents with MIPAS limb-emission spectrometers, *Appl. Opt.*, 35, 2787–2796, 1996.

Fischer, H., Birk, M., Blom, C., Carli, B., Carlotti, M., von Clarmann, T., Delbouille, L., Dudhia, A., Ehalt, D., Endemann, M., Flaud, J. M., Gessner, R., Kleinert, A., Koopman, R., Langen, J., López-Puertas, M., Mosner, P., Nett, H., Oelhaf, H., Perron, G., Remedios, J., Ridolfi, M., Stiller, G., and Zander, R.: MIPAS: an instrument for atmospheric and climate research, *Atmos. Chem. Phys.*, 8, 2151–2188, <https://doi.org/10.5194/acp-8-2151-2008>, 2008.

Friedl-Vallon, F., Maucher, G., Kleinert, A., Lengel, A., Keim, C., Oelhaf, H., Fischer, H., Seefeldner, M., and Trieschmann, O.: Design and characterisation of the balloon-borne Michelson Interferometer for Passive Atmospheric Sounding (MIPAS-B2), *Appl. Opt.*, 43, 3335–3355, 2004.

Funke, B., Stiller, G. P., von Clarmann, T., Eehle, G., and Fischer, H.: CO₂ Line Mixing in MIPAS Limb Emission Spectra and its Influence on Retrieval of Atmospheric Parameters, *J. Quant. Spectrosc. Ra.*, 59, 215–230, 1998.

Glatthor, N., von Clarmann, T., Fischer, H., Funke, B., Grabowski, U., Höpfner, M., Kellmann, S., Kiefer, M., Linden, A., Milz, M., Steck, T., and Stiller, G. P.: Global peroxyacetyl nitrate (PAN) retrieval in the upper troposphere from limb emission spectra of the Michelson Interferometer for Passive Atmospheric Sounding (MIPAS), *Atmos. Chem. Phys.*, 7, 2775–2787, <https://doi.org/10.5194/acp-7-2775-2007>, 2007.

Harrison, J. J., Boone, C. D., and Bernath, P. F.: New and improved infra-red absorption cross sections and ACE-FTS retrievals of carbon tetrachloride (CCl₄), *J. Quant. Spectrosc. Ra.*, 186, 139–149, <https://doi.org/10.1016/j.jqsrt.2016.04.025>, 2017.

Hubert, D., Keppens, A., Granville, J., and Lambert, J.-C.: Multi-TASTE Phase F Validation Report/Comparison of MIPAS ML2PP 7.03 products to sonde and lidar, TN-BIRA-IASB-MultiTASTE-Phase-F-MIPAS-ML2PP7-Iss1-RevB, BIRA-IASB, Brussels, Belgium, 2016.

IPCC: Contribution of Working Group I to the Fifth Assessment Report of the Intergovernmental Panel on Climate Change, in: *Climate Change 2013: The Physical Science Basis*, edited by: Stocker, T., Qin, D., Plattner, G.-K., Tignor, M., Allen, S., Boschung, J., Nauels, A., Xia, Y., Bex, V., and Midgley, P., Cambridge University Press, Cambridge, UK, New York, NY, USA, 33–115, 2013.

Liang, Q., Newman, P., and Reimann, S.: SPARC Report on the Mystery of Carbon tetrachloride, SPARC Report No. 7, WCRP-13, SPARC, 2016.

Manney, G. L., Santee, M. L., Rex, M., Livesey, N. J., Pitts, M. C., Veefkind, P., Nash, E. R., Wohltmann, I., Lehmann, R., Froidevaux, L., Poole, L. R., Schoeberl, M. R., Haffner, D. P., Davies, J., Dorokhov, V., Johnson, H. G. B., Kivi, R., Kyrö, E., Larsen, N., Levelt, P. F., Makshtas, A., McElroy, C. T., Nakajima, H., Parrondo, M. C., Tarasick, D. W., von der Gathen, P., Walker, K. A., and Zinoviev, N. S.: Un-

E. Eckert et al.: MIPAS IMK/IAA CCl₄ retrieval

2743

- precedented Arctic ozone loss in 2011, *Nature*, 478, 469–475, <https://doi.org/10.1038/nature10556>, 2011.
- Naujokat, B. and Grunow, K.: The stratospheric arctic winter 2002/03: balloon flight planning by trajectory calculations, in: *European Rocket and Balloon Programmes and Related Research*, edited by: Warmbein, B., ESA Special Publication, Vol. 530, 421–425, 2003.
- Nemtchinov, V. and Varanasi, P.: Thermal infrared absorption cross-sections of {CCl₄} needed for atmospheric remote sensing, *J. Quant. Spectrosc. Ra.*, 82, 473–481, [https://doi.org/10.1016/S0022-4073\(03\)00171-7](https://doi.org/10.1016/S0022-4073(03)00171-7), 2003.
- Norton, H. and Beer, R.: New apodizing functions for Fourier spectrometry, *J. Opt. Soc. Am.*, 66, 259–264, 1976.
- Rodgers, C. D.: *Inverse Methods for Atmospheric Sounding: Theory and Practice*, in: *Series on Atmospheric, Oceanic and Planetary Physics*, edited by: Taylor, F. W., Vol. 2, World Scientific, Singapore, New Jersey, London, Hong Kong, 2000.
- Rosenkranz, P. W.: Shape of the 5 mm Oxygen Band in the Atmosphere, *IEEE T. Antenn. Propag.*, 23, 498–506, 1975.
- Rothman, L. S., Barbe, A., Benner, D. C., Brown, L. R., Camy-Peyret, C., Carleer, M. R., Chance, K., Clerbaux, C., Dana, V., Devi, V. M., Fayt, A., Flaud, J.-M., Gamche, R. R., Goldman, A., Jacquemart, D., Jucks, K. W., Lafferty, W. J., Mandin, J.-Y., Massie, S. T., Nemtchinov, V., Newnham, D. A., Perrin, A., Rinsland, C. P., Schroeder, J., Smith, K. M., Smith, M. A. H., Tang, K., Toth, R. A., Vander Auwera, J., Varanasi, P., and Yoshino, K.: The HITRAN molecular spectroscopic database: edition of 2000 including updates through 2001, *J. Quant. Spectrosc. Ra.*, 82, 5–44, [https://doi.org/10.1016/S0022-4073\(03\)00146-8](https://doi.org/10.1016/S0022-4073(03)00146-8), 2003.
- Schmidt, U., Kullessa, G., Klein, E., Roeth, E.-P., and Fabian, P.: intercomparison of balloon-borne cryogenic whole air samplers during the MAP/GLOBUS 1983 campaign, *Planet. Space Sci.*, 35, 647–656, [https://doi.org/10.1016/0032-0633\(87\)90131-0](https://doi.org/10.1016/0032-0633(87)90131-0), 1987.
- Sinnhuber, B.-M., Stiller, G., Ruhnke, R., von Clarmann, T., Kellmann, S., and Aschmann, J.: Arctic winter 2010/2011 at the brink of an ozone hole, *Geophys. Res. Lett.*, 38, L24814, <https://doi.org/10.1029/2011GL049784>, 2011.
- SPARC: SPARC Report on the Mystery of Carbon tetrachloride, edited by: Liang, Q. and Newman, P. A., 2016.
- Stiller, G. P. (Ed.): *The Karlsruhe Optimized and Precise Radiative Transfer Algorithm (KOPRA)*, *Wissenschaftliche Berichte*, Vol. FZKA 6487, Forschungszentrum Karlsruhe, Karlsruhe, 2000.
- Valeri, M., Barbara, F., Boone, C., Ceccherini, S., Gai, M., Maucher, G., Raspollini, P., Ridolfi, M., Sgheri, L., Wetzel, G., and Zoppetti, N.: CCl₄ distribution derived from MIPAS ESA V7 data: validation, trend and lifetime estimation, *Atmos. Chem. Phys. Discuss.*, <https://doi.org/10.5194/acp-2016-1163>, in review, 2017.
- Vogel, B., Günther, G., Müller, R., Grooß, J.-U., Afchine, A., Bozem, H., Hoor, P., Krämer, M., Müller, S., Riese, M., Rolf, C., Spelten, N., Stiller, G. P., Ungerermann, J., and Zahn, A.: Long-range transport pathways of tropospheric source gases originating in Asia into the northern lower stratosphere during the Asian monsoon season 2012, *Atmos. Chem. Phys.*, 16, 15301–15325, <https://doi.org/10.5194/acp-16-15301-2016>, 2016.
- von Clarmann, T., Oelhaf, H., and Fischer, H.: Retrieval of atmospheric O₃, HNO₃, CFC-11, and CFC-12 profiles from MIPAS-B-89 limb emission spectra, *Appl. Opt.*, 32, 6808–6817, 1993.
- von Clarmann, T., Linden, A., Oelhaf, H., Fischer, H., Friedl-Vallon, F., Piesch, C., Seefeldner, M., Völker, W., Bauer, R., Engel, A., and Schmidt, U.: Determination of the stratospheric organic chlorine budget in the spring arctic vortex during MIPAS B limb emission spectra and air sampling experiments, *J. Geophys. Res.*, 100, 13979–13997, 1995.
- von Clarmann, T., Glatthor, N., Grabowski, U., Höpfner, M., Kellmann, S., Kiefer, M., Linden, A., Mengistu Tsidu, G., Milz, M., Steck, T., Stiller, G. P., Wang, D. Y., Fischer, H., Funke, B., Gil-López, S., and López-Puertas, M.: Retrieval of temperature and tangent altitude pointing from limb emission spectra recorded from space by the Michelson Interferometer for Passive Atmospheric Sounding (MIPAS), *J. Geophys. Res.*, 108, 4736, <https://doi.org/10.1029/2003JD003602>, 2003.
- von Clarmann, T., Höpfner, M., Kellmann, S., Linden, A., Chauhan, S., Funke, B., Grabowski, U., Glatthor, N., Kiefer, M., Schieferdecker, T., Stiller, G. P., and Versick, S.: Retrieval of temperature, H₂O, O₃, HNO₃, CH₄, N₂O, ClONO₂ and ClO from MIPAS reduced resolution nominal mode limb emission measurements, *Atmos. Meas. Tech.*, 2, 159–175, <https://doi.org/10.5194/amt-2-159-2009>, 2009.
- von Clarmann, T., Stiller, G., Grabowski, U., Eckert, E., and Orphal, J.: Technical Note: Trend estimation from irregularly sampled, correlated data, *Atmos. Chem. Phys.*, 10, 6737–6747, <https://doi.org/10.5194/acp-10-6737-2010>, 2010.
- World Meteorological Organization (WMO): *Scientific Assessment of Ozone Depletion: 2014*, *Global Ozone Research and Monitoring Project – Report No. 55*, 416 pp., Geneva, Switzerland, 2014.
- Zander, R., Mahieu, E., Gunson, M. R., Abrams, M. C., Chang, A. Y., Abbas, M. M., Aelig, C., Engel, A., Goldman, A., Irion, F. W., Kämpfer, N., Michelson, H. A., Newchurch, M. J., Rinsland, C. P., Salawitch, R. J., Stiller, G. P., and Toon, G. C.: The 1994 northern midlatitude budget of stratospheric chlorine derived from ATMOS/ATLAS-3 observations, *Geophys. Res. Lett.*, 23, 2357–2360, 1996.

B. Copies of Co-Authored Publications relevant for this Thesis

B.1 Technical Note: Trend estimation from irregularly sampled, correlated data

Atmos. Chem. Phys., 10, 6737–6747, 2010
 www.atmos-chem-phys.net/10/6737/2010/
 doi:10.5194/acp-10-6737-2010
 © Author(s) 2010. CC Attribution 3.0 License.



Technical Note: Trend estimation from irregularly sampled, correlated data

T. von Clarmann, G. Stiller, U. Grabowski, E. Eckert, and J. Orphal

Karlsruhe Institute of Technology, Institute for Meteorology and Climate Research, Karlsruhe, Germany

Received: 16 November 2009 – Published in Atmos. Chem. Phys. Discuss.: 21 December 2009

Revised: 12 July 2010 – Accepted: 12 July 2010 – Published: 22 July 2010

Abstract. Estimation of a trend of an atmospheric state variable is usually performed by fitting a linear regression line to a set of data of this variable sampled at different times. Often these data are irregularly sampled in space and time and clustered in a sense that error correlations among data points cause a similar error of data points sampled at similar times. Since this can affect the estimated trend, we suggest to take the full error covariance matrix of the data into account. Superimposed periodic variations can be jointly fitted in a straightforward manner, even if the shape of the periodic function is not known. Global data sets, particularly satellite data, can form the basis to estimate the error correlations. State-dependent amplitudes of superimposed periodic corrections result in a non-linear optimization problem which is solved iteratively.

1 Introduction

Correct trend estimation is a key question in the discussion of climate change (IPCC, 2007). While fitting a straight line to a sample of data is an almost trivial task, errors in the data set and non-representativeness of the sample add some difficulty to the problem. Assuming normally distributed errors which are uncorrelated over the sample, each data point is simply weighted by the inverse of its variance to obtain a best linear unbiased estimate of the trend (Aitken, 1935). Methods applicable to least squares fitting of data where both the dependent and the independent variables are affected by errors have recently been reviewed by Cantrell (2008).

If the assumption of normal error distribution is questionable, robust linear regression methods help to reduce the sensitivity of the trend to outliers in the sample (Muhlbauer

et al. 2009 and references therein). Another cure against non-normality of distributions of residuals are bootstrap methods, introduced by Efron (1979) as a variant to jackknife methods and applied to atmospheric trend analysis by, e.g. Cox et al. (2002), Gardiner et al. (2008) or Vigouroux et al. (2008).

Besides non-normality of the distribution of residuals, correlations between the sampled data are another class of problems. When using multisite means to infer a trend, the standard errors of the means σ_{mean} which determine the weight of each mean in the regression analysis are not the standard deviation σ of the sample over the sites divided by the square root of the number of sites M but

$$\sigma_{\text{mean}} = \sqrt{\sigma^2 \left(\frac{1 + (M-1)\bar{r}_{\text{inter}}}{M} \right)}, \quad (1)$$

where \bar{r}_{inter} is the average intersite correlation coefficient (Jones et al., 1997). This can easily be verified by multiplication of the averaging operator from the left and right to the intersite covariance matrix $\mathbf{S}_{\text{inter}}$ according to multivariate Gaussian error propagation:

$$\sigma_{\text{mean,inter}}^2 = \left(\frac{1}{M}, \dots, \frac{1}{M} \right) \mathbf{S}_{\text{inter}} \begin{pmatrix} \frac{1}{M} \\ \vdots \\ \frac{1}{M} \end{pmatrix}, \quad (2)$$

where the element at position (i, k) of $\mathbf{S}_{\text{inter}}$ is $r_{\text{inter}, i, k} \sigma^2$. This approach solves the problem of intersite correlations and is applicable, e.g., if measurements of the same set of sites are used over the whole period. σ_{mean} calculated under consideration of \bar{r}_{inter} accounts for the fact that the available sites do not fully represent the population, i.e., the sample mean at a given time is not necessarily identical to the global mean. Since the same set of stations is used over the whole period, the measurements at the given sites are not a random sample.

Weatherhead et al. (1998) discuss how autocorrelations of noise in the data affect the precision of the estimated trend,



Correspondence to: T. von Clarmann
 (thomas.clarmann@kit.edu)

6738

and they provide a practical method to consider these autocorrelations to avoid over-optimistic confidence estimated with respect to inferred linear trends. Further, these authors present a tool to estimate the required length of the time series to significantly detect a trend.

None of these papers, however, tackles the problem of how to derive trends on the basis of inhomogeneous data sets. In this technical note, we investigate the problem that the sampled data are clustered in a sense that the data are groupwise correlated in the time domain. This is the case when data inhomogeneities cause systematic deviations between subsets of the data of time series. Through irregular sampling in time, these systematic deviations map onto the time series as errors correlated in the time domain. A typical example would be the estimation of a trend of one atmospheric state variable from measurements at two different latitudes, where one measurement site dominates the earlier part and the other measurement site the later part of the time series. The neglected latitudinal dependence of the observed quantity maps onto the time domain if the atmosphere is irregularly sampled at the different observation sites. Such data sets, where the target variable depends on further variables (e.g. latitude, calibration standard) except the independent variable of the regression analysis (e.g., time), we call inhomogeneous, and the unconsidered independent variables we call “hidden variables”. Irregular sampling of inhomogeneous data leads to clustering, because certain values of the independent variable may go along with certain values of the hidden variable. This dependence can be formulated as correlations, typically the larger, the more similar the value of the hidden variable is. Other reasons for such kind of groupwise correlations, besides latitude-dependence, are: data based on multiple measurement systems relying on different calibration standards (Engel et al., 2009), combination of data from two measurement systems which cover different episodes like H₂O measurements from HALOE (Randel et al., 2004; Rosenlof and Reid, 2008) and MIPAS (Milz et al., 2005); and data sets where the operation mode has been changed during the time interval under assessment e.g. MIPAS H₂O measurements before (Milz et al., 2009) and after 2004 (von Clarmann et al., 2009), when the instrument was operated at different spectral resolutions.

All these systematic differences between subsets of the data causing data inhomogeneity can be described as error correlations, which, if neglected, will not only render the significance analysis of the trend insignificant, but can actually change the slope of the regression line, i.e. lead to different trends.

In Sect. 2 of this paper we present a closed-form solution to infer a linear regression line from correlated measurements. In Sect. 3 we discuss the issue of seasonal or other periodic corrections and propose formalisms to infer these corrections directly from the measurements. Applicability of each of the schemes proposed will be demonstrated on the basis of selected case studies. While the proposed concept is

T. von Clarmann et al.: Trend estimation from clustered data

quite straightforward rather than novel, we hope that it may be useful to the climate research community where currently error covariances in irregularly sampled data often seem to be ignored, even when inhomogeneous datasets are analyzed.

2 Linear trends of clustered data

Assuming a linear trend, we can approximate the temporal development of an atmospheric state variable y as a straight line. A straight line is defined as

$$\hat{y}(x; a, b) = a + bx, \quad (3)$$

where the $\hat{}$ symbol indicates a modeled or estimated rather than a measured state variable. In our application x is the time of the measurement, but this concept of regression of clustered data is applicable to a wider context.

For normally distributed, but possibly interdependent errors of y_n , $n=1\dots N$, $N \geq 2$, of which the ex ante¹ estimates are represented by the $N \times N$ covariance matrix \mathbf{S}_y , this straight line is the optimal regression line for which the cost function

$$\chi^2 = (\mathbf{y} - (\mathbf{a}e + \mathbf{b}\mathbf{x}))^T \mathbf{S}_y^{-1} (\mathbf{y} - (\mathbf{a}e + \mathbf{b}\mathbf{x})) \quad (4)$$

is minimum, where $\mathbf{e}=(1, \dots, 1)^T$ and $\mathbf{x}=(x_1, \dots, x_N)^T$, $\mathbf{y}=(y_1, \dots, y_N)^T$, and T denotes the transpose of a matrix. Coefficients a and b are inferred in a well established manner by setting the derivatives $\partial\chi^2/\partial a$ and $\partial\chi^2/\partial b$ to zero. This gives

$$\begin{aligned} \frac{\partial\chi^2}{\partial a} &= -2\mathbf{e}^T \mathbf{S}_y^{-1} (\mathbf{y} - \mathbf{a}e - \mathbf{b}\mathbf{x}) = 0; \\ \mathbf{e}^T \mathbf{S}_y^{-1} \mathbf{y} &= \mathbf{e}^T \mathbf{S}_y^{-1} \mathbf{a}e + \mathbf{e}^T \mathbf{S}_y^{-1} \mathbf{b}\mathbf{x}; \\ a &= \frac{\mathbf{e}^T \mathbf{S}_y^{-1} \mathbf{y} - \mathbf{e}^T \mathbf{S}_y^{-1} \mathbf{b}\mathbf{x}}{\mathbf{e}^T \mathbf{S}_y^{-1} \mathbf{e}} \end{aligned} \quad (5)$$

and

$$\begin{aligned} \frac{\partial\chi^2}{\partial b} &= -2\mathbf{x}^T \mathbf{S}_y^{-1} (\mathbf{y} - \mathbf{a}e - \mathbf{b}\mathbf{x}) = 0; \\ \mathbf{x}^T \mathbf{S}_y^{-1} \mathbf{y} - \mathbf{x}^T \mathbf{S}_y^{-1} \mathbf{a}e - \mathbf{x}^T \mathbf{S}_y^{-1} \mathbf{b}\mathbf{x} &= 0 \\ \mathbf{x}^T \mathbf{S}_y^{-1} \mathbf{y} &= \mathbf{x}^T \mathbf{S}_y^{-1} \mathbf{b}\mathbf{x} + \mathbf{x}^T \mathbf{S}_y^{-1} \mathbf{a}e. \end{aligned} \quad (6)$$

Combining Eqs. 5 and 6 gives

$$\begin{aligned} \mathbf{x}^T \mathbf{S}_y^{-1} \mathbf{y} &= \mathbf{x}^T \mathbf{S}_y^{-1} \mathbf{b}\mathbf{x} + \mathbf{x}^T \mathbf{S}_y^{-1} \mathbf{a}e \\ &= \mathbf{x}^T \mathbf{S}_y^{-1} \mathbf{b}\mathbf{x} + \mathbf{x}^T \mathbf{S}_y^{-1} \mathbf{e} \frac{\mathbf{e}^T \mathbf{S}_y^{-1} \mathbf{y} - \mathbf{e}^T \mathbf{S}_y^{-1} \mathbf{b}\mathbf{x}}{\mathbf{e}^T \mathbf{S}_y^{-1} \mathbf{e}}. \end{aligned} \quad (7)$$

¹Ex ante error estimates we call error estimates based on propagation of assumed primary errors through the system, which can be calculated before the measurement actually has been made, as opposed to ex post error estimates which are based on the standard deviation of a sample of measurements (von Clarmann, 2006).

This can be rearranged as

$$\mathbf{x}^T \mathbf{S}_y^{-1} b \mathbf{x} - \frac{\mathbf{x}^T \mathbf{S}_y^{-1} \mathbf{e} \mathbf{e}^T \mathbf{S}_y^{-1} b \mathbf{x}}{\mathbf{e}^T \mathbf{S}_y^{-1} \mathbf{e}} = \quad (8)$$

$$\mathbf{x}^T \mathbf{S}_y^{-1} \mathbf{y} - \frac{\mathbf{x}^T \mathbf{S}_y^{-1} \mathbf{e} \mathbf{e}^T \mathbf{S}_y^{-1} \mathbf{y}}{\mathbf{e}^T \mathbf{S}_y^{-1} \mathbf{e}}$$

and finally solved to give b :

$$b = \frac{\mathbf{x}^T \mathbf{S}_y^{-1} \mathbf{y} - \frac{\mathbf{x}^T \mathbf{S}_y^{-1} \mathbf{e} \mathbf{e}^T \mathbf{S}_y^{-1} \mathbf{y}}{\mathbf{e}^T \mathbf{S}_y^{-1} \mathbf{e}}}{\mathbf{x}^T \mathbf{S}_y^{-1} \mathbf{x} - \frac{\mathbf{x}^T \mathbf{S}_y^{-1} \mathbf{e} \mathbf{e}^T \mathbf{S}_y^{-1} \mathbf{x}}{\mathbf{e}^T \mathbf{S}_y^{-1} \mathbf{e}}} \quad (9)$$

$$= \frac{\mathbf{x}^T \mathbf{S}_y^{-1} \mathbf{y} \mathbf{e}^T \mathbf{S}_y^{-1} \mathbf{e} - \mathbf{x}^T \mathbf{S}_y^{-1} \mathbf{e} \mathbf{e}^T \mathbf{S}_y^{-1} \mathbf{y}}{\mathbf{x}^T \mathbf{S}_y^{-1} \mathbf{x} \mathbf{e}^T \mathbf{S}_y^{-1} \mathbf{e} - \mathbf{x}^T \mathbf{S}_y^{-1} \mathbf{e} \mathbf{e}^T \mathbf{S}_y^{-1} \mathbf{x}}.$$

Inserting this into Eq. 5 allows to calculate a :

$$a = \frac{\mathbf{x}^T \mathbf{S}_y^{-1} \mathbf{y} - \mathbf{e}^T \mathbf{S}_y^{-1} \mathbf{x} b}{\mathbf{e}^T \mathbf{S}_y^{-1} \mathbf{e}} \quad (10)$$

$$= \frac{\mathbf{e}^T \mathbf{S}_y^{-1} \mathbf{y} - \mathbf{e}^T \mathbf{S}_y^{-1} \mathbf{x} \frac{\mathbf{x}^T \mathbf{S}_y^{-1} \mathbf{y} \mathbf{e}^T \mathbf{S}_y^{-1} \mathbf{e} - \mathbf{x}^T \mathbf{S}_y^{-1} \mathbf{e} \mathbf{e}^T \mathbf{S}_y^{-1} \mathbf{y}}{\mathbf{x}^T \mathbf{S}_y^{-1} \mathbf{x} \mathbf{e}^T \mathbf{S}_y^{-1} \mathbf{e} - \mathbf{x}^T \mathbf{S}_y^{-1} \mathbf{e} \mathbf{e}^T \mathbf{S}_y^{-1} \mathbf{x}}}{\mathbf{e}^T \mathbf{S}_y^{-1} \mathbf{e}}$$

$$= \frac{\mathbf{e}^T \mathbf{S}_y^{-1} \mathbf{y} \mathbf{x}^T \mathbf{S}_y^{-1} \mathbf{x} - \mathbf{e}^T \mathbf{S}_y^{-1} \mathbf{x} \mathbf{x}^T \mathbf{S}_y^{-1} \mathbf{y}}{\mathbf{e}^T \mathbf{S}_y^{-1} \mathbf{x} \mathbf{x}^T \mathbf{S}_y^{-1} \mathbf{x} - \mathbf{e}^T \mathbf{S}_y^{-1} \mathbf{x} \mathbf{x}^T \mathbf{S}_y^{-1} \mathbf{x}}.$$

For unity \mathbf{S}_y this reduces to the widely used parameters \tilde{a} and \tilde{b} of a regression line for data points of uncorrelated errors of equal variance:

$$\tilde{a} = \frac{\sum y_n}{N} - \tilde{b} \frac{\sum x_n}{N}, \quad (11)$$

where

$$\tilde{b} = \frac{N \sum x_n y_n - \sum x_n \sum y_n}{N \sum x_n^2 - (\sum x_n)^2} \quad (12)$$

The uncertainty of the slope b is:

$$\sigma_b^2 = \left(\frac{\partial b}{\partial \mathbf{y}} \right) \mathbf{S}_y \left(\frac{\partial b}{\partial \mathbf{y}} \right)^T \quad (13)$$

$$= \left(\frac{\mathbf{e}^T \mathbf{S}_y^{-1} \mathbf{x} \mathbf{x}^T \mathbf{S}_y^{-1} - \mathbf{x}^T \mathbf{S}_y^{-1} \mathbf{e} \mathbf{e}^T \mathbf{S}_y^{-1}}{\mathbf{x}^T \mathbf{S}_y^{-1} \mathbf{x} \mathbf{e}^T \mathbf{S}_y^{-1} \mathbf{e} - \mathbf{x}^T \mathbf{S}_y^{-1} \mathbf{e} \mathbf{e}^T \mathbf{S}_y^{-1} \mathbf{x}} \right).$$

$$\mathbf{S}_y \left(\frac{\mathbf{e}^T \mathbf{S}_y^{-1} \mathbf{x} \mathbf{x}^T \mathbf{S}_y^{-1} - \mathbf{x}^T \mathbf{S}_y^{-1} \mathbf{e} \mathbf{e}^T \mathbf{S}_y^{-1}}{\mathbf{x}^T \mathbf{S}_y^{-1} \mathbf{x} \mathbf{e}^T \mathbf{S}_y^{-1} \mathbf{e} - \mathbf{x}^T \mathbf{S}_y^{-1} \mathbf{e} \mathbf{e}^T \mathbf{S}_y^{-1} \mathbf{x}} \right)^T,$$

where $\left(\frac{\partial b}{\partial \mathbf{y}} \right) = \left(\frac{\partial b}{\partial y_1} \dots \frac{\partial b}{\partial y_N} \right)$. The uncertainty of axis intercept a is estimated accordingly:

$$\sigma_a^2 = \left(\frac{\partial a}{\partial \mathbf{y}} \right) \mathbf{S}_y \left(\frac{\partial a}{\partial \mathbf{y}} \right)^T \quad (14)$$

$$= \left(\frac{\mathbf{x}^T \mathbf{S}_y^{-1} \mathbf{x} \mathbf{e}^T \mathbf{S}_y^{-1} - \mathbf{e}^T \mathbf{S}_y^{-1} \mathbf{x} \mathbf{x}^T \mathbf{S}_y^{-1}}{\mathbf{e}^T \mathbf{S}_y^{-1} \mathbf{x} \mathbf{x}^T \mathbf{S}_y^{-1} \mathbf{x} - \mathbf{e}^T \mathbf{S}_y^{-1} \mathbf{x} \mathbf{x}^T \mathbf{S}_y^{-1} \mathbf{x}} \right).$$

$$\mathbf{S}_y \left(\frac{\mathbf{x}^T \mathbf{S}_y^{-1} \mathbf{x} \mathbf{e}^T \mathbf{S}_y^{-1} - \mathbf{e}^T \mathbf{S}_y^{-1} \mathbf{x} \mathbf{x}^T \mathbf{S}_y^{-1}}{\mathbf{e}^T \mathbf{S}_y^{-1} \mathbf{x} \mathbf{x}^T \mathbf{S}_y^{-1} \mathbf{x} - \mathbf{e}^T \mathbf{S}_y^{-1} \mathbf{x} \mathbf{x}^T \mathbf{S}_y^{-1} \mathbf{x}} \right)^T$$

From comparison of Eqs. (9) and (12) we see that the error correlations do not only change the estimated error of the trend but also affect the trend itself, e.g. rotate the regression line.

Evaluation of Eq. (9) requires knowledge of the covariance matrix \mathbf{S}_y . For some error sources such error assumptions are available and reasonable assumptions on correlations within a class of measurements can be made; if, e.g., different subsets of the data are based on different calibration standards, perfect correlation, i.e., $r=1$, is appropriate for the calibration error component within each such subset. The bias between the subsets has to be estimated, and a fully correlated block of which each element is the square of the estimated bias between the n -th and the first data subset has to be added to that part of the covariance matrix which represents the n -th data subset. The following equation shows the construction of a covariance matrix for a dataset composed of two data subsets biased against each other by an unknown offset whose absolute value is estimated at $\text{bias}_{2,1}$:

$$\mathbf{S}_y = \mathbf{S}_{\text{noise}} + \begin{pmatrix} \left(\begin{array}{ccc} \text{bias}_{2,1}^2 & \dots & \text{bias}_{2,1}^2 \\ \vdots & \ddots & \vdots \\ \text{bias}_{2,1}^2 & \dots & \text{bias}_{2,1}^2 \end{array} \right) & \begin{pmatrix} 0 & \dots & 0 \\ \vdots & \ddots & \vdots \\ 0 & \dots & 0 \end{pmatrix} \\ \begin{pmatrix} 0 & \dots & 0 \\ \vdots & \ddots & \vdots \\ 0 & \dots & 0 \end{pmatrix} & \begin{pmatrix} 0 & \dots & 0 \\ \vdots & \ddots & \vdots \\ 0 & \dots & 0 \end{pmatrix} \end{pmatrix}, \quad (15)$$

where $\mathbf{S}_{\text{noise}}$ is the measurement noise covariance matrix. For evaluation of error covariances representing other error sources, external data may be needed. Typical error correlations in a time series can be caused by the fact that the sample is composed of measurements at various locations. If the mean measurement times at two locations differ, any difference in the expectation value of the state variable with, e.g., latitude, will map onto the trend. If the latitudinal dependence is too complicated for a simple correction, or if there is a non-negligible residual location-related error even after correction, the related error correlation should be included in the covariance matrix \mathbf{S}_y . Covariances between sites i and k can be estimated from N global satellite data sets as

$$r_{i,k} \sigma_i \sigma_k = \sum_{n=1}^N \frac{(x_{i,n} - \bar{x}_i)(x_{k,n} - \bar{x}_k)}{N-1}, \quad (16)$$

where $r_{i,k}$ is the correlation coefficient between sites i and k . Three caveats have to be noted in this context:

- the N global data sets should be measured in a time window short enough to justify neglect of any trend;
- when Eq. (16) is used to derive the variance (i.e. $i=k$) characterizing the representativeness of site i , the variance representing the satellite data measurement error must be subtracted; if the measurement errors of the satellite data are intercorrelated, the respective covariance matrix has to be subtracted from the covariance

6740

Table 1. Case Study 1.

Case	$\Delta T^{(1)}$ (K)	$\sigma_{\Delta T}^{2(2)}$ (K ²)	$r^{(3)}$	a (K)	b (K/yr)
1.1	0.0	0.31	1	217.77±0.80	0.05±0.10
1.2	0.0	0.0	0	217.84±0.57	0.04±0.08
1.3	0.0	0.31	0	217.88±0.66	0.03±0.08
1.4	-2.0	4.0	1	216.72±1.91	0.18±0.27
1.5	-2.0	0.0	0	215.00±0.57	0.41±0.08
1.6	-2.0	4.0	0	216.24±0.87	0.25±0.11

(1) ΔT : artificial bias added to first three measurements;

(2) $\sigma_{\Delta T}^2$: additional variance in the related block of S_y to account for bias;

(3) r : correlation coefficient applied to related block of S_y to account for bias.

matrix derived according to Eq. (16) to obtain the inter-site covariance matrix;

(c) the finite spatial resolution of satellite measurements might be an issue.

In any case, the covariance matrix describing the uncertainty due to the hidden variable is added to the – often diagonal – covariance matrix characterizing the measurement noise of the given sample. In a more general context where various error sources independent of each other are considered, the covariance matrix representing the total uncertainty of the dataset is calculated as the sum of the respective covariance matrices.

Case Study 1:

The trend estimator of Eq. 9 is applied to tropical (30°S to 30°N) annual temperature averages at 25 km altitude inferred from limb infrared measurements recorded with the MIPAS instrument (Fischer et al., 2008). Temperature retrievals for the years 2002 to 2004 are based on measurements when MIPAS was operated at full spectral resolution (von Clarmann et al., 2003), while measurements from 2005 to 2009 are based on reduced spectral resolution measurements (von Clarmann et al., 2009). This different operation mode potentially causes an unknown bias between the subsets of data, which we estimate at ± 0.56 K and account for by adding

$$\begin{pmatrix} 0.56\text{K} \\ 0.56\text{K} \\ 0.56\text{K} \end{pmatrix} (0.56\text{K}; 0.56\text{K}; 0.56\text{K}) = \begin{pmatrix} 0.31\text{K}^2; 0.31\text{K}^2; 0.31\text{K}^2 \\ 0.31\text{K}^2; 0.31\text{K}^2; 0.31\text{K}^2 \\ 0.31\text{K}^2; 0.31\text{K}^2; 0.31\text{K}^2 \end{pmatrix} \quad (17)$$

to the block of S_y which refers to the years 2002 to 2004. The other error component is the estimated standard error of the

T. von Clarmann et al.: Trend estimation from clustered data

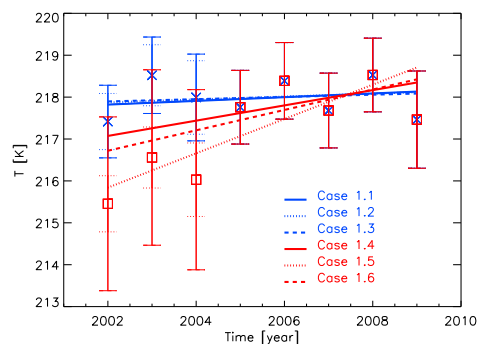


Fig. 1. Linear trends from MIPAS annual mean temperatures at 25 km altitude, 30°S–30°N. Cases 1.1–1.3 are based on measurement data as they are, while an artificial bias of -2 K has been applied to temperatures of the years 2002–2004 in cases 1.4–1.6. In cases 1.1 and 1.4 covariances were treated correctly; in cases 1.2 and 1.5 the bias was neglected and in cases 1.3 and 1.6 only the variances of the bias were considered while its covariances were neglected. After 2004, data used for case studies 1.1–1.3 are identical to those used for case studies 1.4–1.6. Solid error bars are total errors while dotted error bars are random errors only.

annual mean, which is variable due to the different sample size for each year. The x-coordinate of our data set is the time since 2000, i.e. the intercept refers to the year 2000.

We calculate the regression parameters using the full covariance matrix (case 1.1) as described above, for a simplified case where the bias is ignored (case 1.2), and for a test case where only the variances of the bias are considered but not the covariances (case 1.3). Results are shown in Fig. 1 and compiled in Table 1.

Results seem to be quite robust with respect to the change of the MIPAS operation mode, i.e. the actual bias between the data subsets might be smaller than anticipated. Thus the correct statistical treatment of the bias is not critical. In none of the case studies there is a significant trend detected (we call a trend significant if it exceeds twice its uncertainty; for Gaussian errors this corresponds roughly to 5% level of significance). In order to assess the robustness of the trend analysis scheme to data with large, correlated error components, we repeat the case studies mentioned above, but introduce an artificial bias of -2 K to the data subset covering the years 2002 to 2004 and modify the covariance matrix accordingly (case 1.4). Larger data errors propagate to larger estimated errors in the regression parameters, but the scheme is robust in a sense that still no significant trend is produced. In case study 1.5 the same manipulated data are used, but the artificial error is neglected in the covariance matrix. The bias maps onto the regression parameters and causes an artificial, apparently significant trend. In case study 1.6, the

T. von Clarmann et al.: Trend estimation from clustered data

6741

data uncertainty is considered as an uncorrelated error, i.e., the additional variances are considered but covariances are set to zero. The artificial trend still appears to be significant. This proves the importance of correct consideration of covariances. This example has been chosen for demonstration purposes. We neither claim that all possible error correlations in the MIPAS data have been perfectly quantified, nor should the inferred trends be used for extrapolation towards longer term analysis.

3 Consideration of the annual cycle and related problems

A linear trend may be superimposed with a periodic function of known periodic time, e.g. diurnal or seasonal variation, etc. There are several options to tackle this problem.

If the sample is large enough, the linear trend can be evaluated for subsets of data recorded at the same phase of the periodical variation, and the overall trend is calculated as an optimal (i.e. weighted inversely by the variances) mean of the individual trends. This requires binning of data; in the case of a seasonal cycle, the linear trend can be estimated as the mean of the trend over all Januaries, Februaries, etc. Problems occur when the amplitude of the seasonal cycle has a trend in itself and the whole observation time interval is not an integer multiple of the time of one cycle.

Another option is subtraction of the periodic signal prior to trend estimation. The periodic component of the signal can either be imported from an external source (model, independent data) or from the sample itself. The latter approach is not quite trivial, because the inferred mean periodical signal will, in turn, depend on the trend (periodic analysis usually is defined only for stationary time series, i.e. zero trend), such that either an iterative approach or a multivariate optimization (see below) is required. Care has to be taken to consider the reduction of degrees of freedom implied by inferring the correction from the data themselves. In the following, we will discuss how the periodic correction can be estimated simultaneously with the trend.

3.1 Correction by sine and cosine functions

The problem of the non-stationary nature of time series, which is by definition inherent in trend analysis, can be solved by retrieving the trend, the amplitude of the periodic variation, and possibly the phase and the shape of the oscillation in one step. In the case of a known function of unknown amplitude (e.g. sine), the amplitude can be fitted along with the trend. In the case of unknown phase, it is usually more appropriate to fit amplitudes of a sine and a cosine of the same period length rather than the amplitude and the phase, in order to keep the fit linear. A regression model involving

a linear trend superimposed with a single harmonic variation of unknown phase but known period length l is written as

$$\hat{y}(x; a, b, c, d) = a + bx + c \sin \frac{2\pi x}{l} + d \cos \frac{2\pi x}{l}. \quad (18)$$

Setting the partial derivatives of

$$\chi^2 = (\mathbf{y}(\mathbf{x}) - \hat{\mathbf{y}}(\mathbf{x}))^T \mathbf{S}_y^{-1} (\mathbf{y}(\mathbf{x}) - \hat{\mathbf{y}}(\mathbf{x})) \quad (19)$$

with respect to the parameters of the regression model to zero gives

$$\frac{\partial \chi^2}{\partial a} = -2\mathbf{e}^T \mathbf{S}_y^{-1} (\mathbf{y}(\mathbf{x}) - a\mathbf{e} - b\mathbf{x} - c\mathbf{v}_{\sin} - d\mathbf{v}_{\cos}) = 0 \quad (20)$$

$$\frac{\partial \chi^2}{\partial b} = -2\mathbf{x}^T \mathbf{S}_y^{-1} (\mathbf{y}(\mathbf{x}) - a\mathbf{e} - b\mathbf{x} - c\mathbf{v}_{\sin} - d\mathbf{v}_{\cos}) = 0 \quad (21)$$

$$\frac{\partial \chi^2}{\partial c} = -2\mathbf{v}_{\sin}^T \mathbf{S}_y^{-1} (\mathbf{y}(\mathbf{x}) - a\mathbf{e} - b\mathbf{x} - c\mathbf{v}_{\sin} - d\mathbf{v}_{\cos}) = 0 \quad (22)$$

$$\frac{\partial \chi^2}{\partial d} = -2\mathbf{v}_{\cos}^T \mathbf{S}_y^{-1} (\mathbf{y}(\mathbf{x}) - a\mathbf{e} - b\mathbf{x} - c\mathbf{v}_{\sin} - d\mathbf{v}_{\cos}) = 0, \quad (23)$$

where $\mathbf{v}_{\sin} = (\sin \frac{2\pi x_1}{l}, \dots, \sin \frac{2\pi x_N}{l})^T$, and

$\mathbf{v}_{\cos} = (\cos \frac{2\pi x_1}{l}, \dots, \cos \frac{2\pi x_N}{l})^T$. Equations (20–23) form a system of four equations linear in a, b, c and d , of the type

$$\mathbf{T} \begin{pmatrix} a \\ b \\ c \\ d \end{pmatrix} = \mathbf{q} \quad (24)$$

where

$$T_{1,1} = 2\mathbf{e}^T \mathbf{S}_y^{-1} \mathbf{e} \quad (25)$$

$$T_{1,2} = 2\mathbf{e}^T \mathbf{S}_y^{-1} \mathbf{x}$$

\vdots

$$T_{4,4} = 2\mathbf{v}_{\cos}^T \mathbf{S}_y^{-1} \mathbf{v}_{\cos}$$

$$q_1 = 2\mathbf{e}^T \mathbf{S}_y^{-1} \mathbf{y}(\mathbf{x})$$

\vdots

$$q_4 = 2\mathbf{v}_{\cos}^T \mathbf{S}_y^{-1} \mathbf{y}(\mathbf{x}).$$

For $N \geq 4$ and non-singularity of \mathbf{T} , Eq. (24) can be unambiguously solved for the four parameters $a \dots d$. This can be done by any linear equation program package at hand. The advantage of this approach is that it does not require a stationary time series to evaluate the amplitudes of the oscillations. If need be, this type of analysis can also involve multiple periodic functions of different periods, which may be

made subject to lowpass filtering. This generalization of the schemes presented here to applications with more than one pair of periodic functions is straightforward, and the relationship to harmonic analysis is obvious if the period lengths are chosen to be integer fractions of the longest one. Problems with singularity of \mathbf{T} will occur if the number of data points is smaller than the number of period lengths plus 2.

The covariance matrix $\mathbf{S}_{a,b,c,d}$ of the regression parameters is

$$\begin{aligned} \mathbf{S}_{a,b,c,d} &= \begin{pmatrix} \frac{\partial a}{\partial y} \\ \frac{\partial b}{\partial y} \\ \frac{\partial c}{\partial y} \\ \frac{\partial d}{\partial y} \end{pmatrix} \mathbf{S}_y \begin{pmatrix} \frac{\partial a}{\partial y} \\ \frac{\partial b}{\partial y} \\ \frac{\partial c}{\partial y} \\ \frac{\partial d}{\partial y} \end{pmatrix}^T \\ &= \left(\mathbf{T}^{-1} \begin{pmatrix} \partial \mathbf{q} \\ \partial \mathbf{y} \end{pmatrix} \right) \mathbf{S}_y \left(\mathbf{T}^{-1} \begin{pmatrix} \partial \mathbf{q} \\ \partial \mathbf{y} \end{pmatrix} \right)^T \\ &= \left(\mathbf{T}^{-1} \begin{pmatrix} 2\mathbf{e}^T \mathbf{S}_y^{-1} \\ 2\mathbf{x}^T \mathbf{S}_y^{-1} \\ 2\mathbf{v}^T \sin \mathbf{S}_y^{-1} \\ 2\mathbf{v}^T \cos \mathbf{S}_y^{-1} \end{pmatrix} \right) \mathbf{S}_y \\ &\times \left(\mathbf{T}^{-1} \begin{pmatrix} 2\mathbf{e}^T \mathbf{S}_y^{-1} \\ 2\mathbf{x}^T \mathbf{S}_y^{-1} \\ 2\mathbf{v}^T \sin \mathbf{S}_y^{-1} \\ 2\mathbf{v}^T \cos \mathbf{S}_y^{-1} \end{pmatrix} \right)^T. \end{aligned} \quad (26)$$

The off-diagonal elements of \mathbf{S}_y will determine whether the data errors map either predominantly onto the slope or onto the axis intercept of the regression curve. For example, large positive correlations throughout the data lead to large intercept errors while the slope remains quite well determined with sometimes surprisingly small uncertainties. The extreme case would be fully correlated data errors. It is well known that such a constant bias in the data does not affect the trend at all. Consideration of full covariance matrices allows the correct treatment of realistic cases, where the errors are neither purely random nor purely systematic but may include correlations within subsets of the data.

The uncertainties estimated by Eq. (26) include the propagation of data errors onto the regression parameters but not uncertainties caused by the use of an inappropriate model (e.g. neglect of higher order or periodic components).

3.1.1 Case Study 2:

The trend estimator of Eqs. (18–25) is applied to tropical (30°S to 30°N) “pseudomonthly” MIPAS temperature averages at 25 km. A “pseudomonth” we call a time period of 32 days, chosen to be an integer division of the mean period of the semi-annual oscillation (SAO) which was first detected by Reed (1965). The period of the SAO in the MIPAS data set is estimated at 192 days, which is in good agreement with SAO period length of about 194 days at 30 km as reported by Guharay et al. (2009). We extend the method

Table 2. Case Study 2.

Case	$\Delta T^{(1)}$ (K)	$\sigma_{\Delta T}^{2(2)}$ (K ²)	$r^{(3)}$	a (K)	b (K/yr)
2.1	0.0	0.31	1	219.24±0.25	-0.09±0.03
2.2	0.0	0.0	0	219.14±0.10	-0.08±0.02
2.3	0.0	0.31	0	218.75±0.28	-0.04±0.04
2.4	-2.0	4.0	1	219.24±0.26	-0.09±0.03
2.5	-2.0	0.0	0	215.83±0.10	0.35±0.02
2.6	-2.0	4.0	0	215.70±0.91	0.34±0.14

- (1) ΔT : artificial bias added to first three measurements;
 (2) $\sigma_{\Delta T}^2$: additional variance in the related block of \mathbf{S}_y to account for bias;
 (3) r : correlation coefficient applied to related block of \mathbf{S}_y to account for bias.

described in the theory part towards two sine and two cosine terms as to include also the quasi-biennial oscillation (c.f. Baldwin et al. 2001). Its period length is assumed to be 25 months, in agreement with data provided by Freie Universität Berlin (<http://www.geo.fu-berlin.de/met/ag/strat/produkte/qbo/index.html>). The case studies for this application, particularly the treatment of biases, were selected as in case study 1.

Correct treatment of the original MIPAS data and their correlations (case study 2.1) results in a negative trend, neglect of correlations (case study 2.2) and their simplified treatment (case study 2.3) lead to small negative temperature trends (Table 2 and Fig. 2). The trend obtained from case study 2.3 is insignificant. More interesting is the assessment of the data superimposed with an artificial bias: If the bias is considered correctly in the covariance matrix (case study 2.4), it does not change the trend by any substantial amount, while otherwise (case studies 2.5 and 2.6) there is an apparent positive trend, which appears significant. This demonstrates how powerful the concept of bias consideration in the error covariance matrix is to remedy data inhomogeneities.

3.2 Correction by a discrete empirical function

If the shape of the periodic variation is not known a priori, it can be inferred from the data themselves in one step with the trend estimation. For data binned in the time domain (e.g. when monthly means are used to infer a trend with superimposed seasonal variation) corrections for each phase (e.g. monthly corrections) are fitted along with slope and axis intercept. The regression model then is

$$\hat{y} = a + bx + c_{j(x)}, \quad (27)$$

where $c_{j(x)}$ is the (e.g., monthly) correction applicable to the measurement made at time x . The cost function to be minimized for this application is

T. von Clarmann et al.: Trend estimation from clustered data

6743

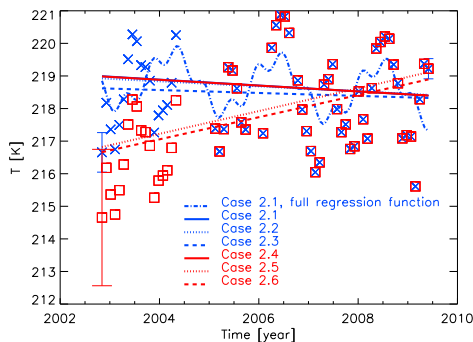


Fig. 2. Linear trends from MIPAS 32-day mean temperatures at 25 km altitude, 30°S–30°N, with consideration of sine and cosine corrections for the quasi-biennial oscillation and the semi-annual oscillation. Test cases represent different treatment of the bias, for details see Fig. 1. The linear term of the regression function is shown for all cases 2.1–2.6, while, for reasons of clarity, the full regression curve is shown for case 2.1 only. Representative error bars include both the random error and – if considered in the respective case – the bias.

$$\chi^2 = (y(x) - (ae + bx + Ue))^T S_y^{-1} (y(x) - (ae + bx + Ue)) \quad (28)$$

where c is a vector of length J , where J is the number of phase bins ($J=12$ in the case of monthly corrections in an annual cycle) representing the applicable corrections for each phase bin, and U is a selection matrix with all elements in the n -th row zero except for column j , where j represents the month when measurement x_n was made, where the matrix element is one. $N \geq J+2$ is required, and for each phase bin at least one measurement must be available. Minimization of χ^2 to get the regression parameters follows the same strategy as described in Sect. 3, i.e. the derivatives of χ^2 with respect to the regression parameters a , b and c are set zero and the resulting system of linear equations is solved. However, the derivative with respect to the axis intercept and that with respect to the additive corrections lead to linearly dependent equations. Thus, the equation

$$\frac{\partial \chi^2}{\partial a} = 0 \quad (29)$$

is dropped for reasons of redundancy, and

$$\sum_{j=1}^J c_j = 0 \quad (30)$$

is included to constrain the solution to zero mean periodic corrections.

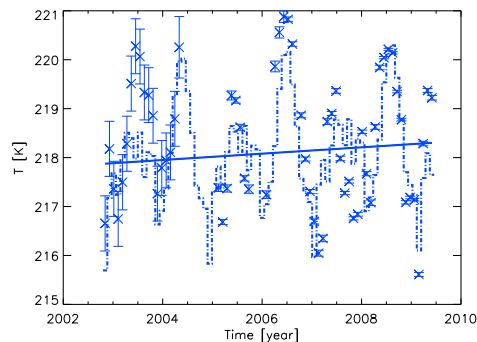


Fig. 3. Linear trends from MIPAS 32-day mean temperatures at 25 km altitude, 30°S–30°N, using the discrete empirical periodical correction, as described in Sect. 3.2. Both the linear part of the regression function and the complete regression function are shown. No artificial bias has been added to the data in this case study.

Case Study 3:

Here we use the same binned MIPAS temperature data as for case studies 2.1–2.3. A periodicity of 25 bins is assumed to match the quasi-biennial oscillation. The trend is estimated at 0.06 ± 0.01 K/yr (Fig. 3). The estimated uncertainty is the propagation of the measurement error on the trend and includes the random error and the bias only; no other error sources are considered; particularly temperatures might not be perfectly described by the regression model chosen, and the time series of limited length might not be representative for a longer term. As a side aspect, differences in the trends compared to those inferred in case study 2 (Fig. 2, c.f. case 2.1) demonstrate the importance of the choice of the regression model.

3.3 Correction by a continuous empirical function

If binning or averaging in the time domain is to be avoided, the discrete application of the correction can be replaced by a continuous time-dependence. This might be advisable if data are available on a time-grid finer than the bin-width, and if the variation of y within a bin is large. The actual correction for a given $y(x)$ can then be estimated by, e.g., linear, interpolation, leading to the regression model

$$\hat{y} = a + bx + c_{j(x)} w_{n,j(x)} + c_{j(x)+1} w_{n,j(x)+1} \quad (31)$$

where c are periodic corrections at predefined phases and w their weights. More specifically, $c_{j(x)}$ and $c_{j(x)+1}$ are the periodic corrections referring to the closest times before/after the measurement time x (e.g. for each 1st of the month when

6744

the measurement was made, and the 1st of the following month, respectively). The weighting factors w are

$$w_{n,j(x)} = \frac{d_j(x) - d(x_n)}{d_j(x)} \quad (32)$$

and

$$w_{n,j(x)+1} = \frac{d(x_n)}{d_j(x)}, \quad (33)$$

where $d_j(x)$ is the difference between the times related to $c_j(x)$ and c_{j+1} (e.g. the number of days of the month) and $d(x)$ is difference between the actual measurement time and the time related to $c_j(x)$ (e.g. the day of the month). Periodicity is assumed in a sense that $c_j(x) = c_{j(x + \sum d_j)}$. The number of parameters to be fitted still is $J+2$, as with the approach involving binning in the time domain. The cost function to be minimized for this application has the same structure as Eq. (28):

$$\chi^2 = \left(\mathbf{y}(x) - (\mathbf{a}e + \mathbf{b}x + \mathbf{W}c) \right)^T \mathbf{S}_y^{-1} \left(\mathbf{y}(x) - (\mathbf{a}e + \mathbf{b}x + \mathbf{W}c) \right) \quad (34)$$

\mathbf{W} is a matrix with all elements in the n -th row zero except for column j and $j+1$ (or 1, if j denotes the last column), where j and $j+1$ represent the month when measurement n was made, and the subsequent month, respectively. The respective matrix elements are the weights of the monthly correction factors c_j and c_{j+1} , as defined by Eqs. (32–33). The minimization of the cost functions of Eqs. (28) and (34) and error estimation follows the same scheme as outlined for the cost function in Eq. (19), except that the zero mean constraint for $c_1 \dots c_j$ has to substitute the equation involving the partial derivative of χ^2 with respect to a , as in Sect. 4.2.

Case Study 4:

In this case study we use MIPAS tropical (30° S to 30° N) daily mean temperatures at 25 km altitude. As in case study 3, 27 independent periodic correction terms are jointly inferred from the data along with axis intercept and linear trend; contrary to case study 3, the actual correction applicable to a data point is determined by linear interpolation between the two correction terms representing the nominal times before and after the actual measurement time. The inferred trend is 0.06 ± 0.01 K/yr (Fig. 4), as in case study 3. As in the preceding case studies, random errors and the bias due to the change in the MIPAS measurement mode are the only errors considered.

3.4 Correction by functions of state-dependent amplitude

Often the amplitude of the periodic variation depends linearly on the actual mean state $a+bx$:

T. von Clarmann et al.: Trend estimation from clustered data

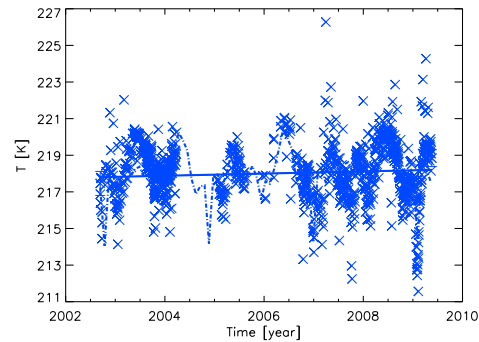


Fig. 4. Linear trends from MIPAS daily mean temperatures at 25 km altitude, 30°S–30°N, using the continuous empirical periodical correction, as described in Sect. 3.3. Both the linear part of the regression function (solid line) and the complete regression function (dash dot) are shown.

$$\begin{aligned} \hat{y}(x; a, b, c, d) &= a + bx \\ &+ (a + bx)c \sin \frac{2\pi x}{l} + \\ &(a + bx)d \cos \frac{2\pi x}{l} \\ &= a + bx \\ &+ ac \sin \frac{2\pi x}{l} + bxc \sin \frac{2\pi x}{l} + \\ &ad \cos \frac{2\pi x}{l} + bxd \cos \frac{2\pi x}{l} \end{aligned} \quad (35)$$

This is typically the case with concentrations of atmospheric constituents: When the average abundance is larger, also the diurnal or annual cycle is expected to have a larger amplitude. Minimization of the related cost function leads to a nonlinear system of equations, because x appears both in the argument of the trigonometric function and in its multiplier. Since for such problems there exists no straight-forward closed-form solution, this system of nonlinear equations is suggested to be linearized and iteratively solved for a_{i+1} , b_{i+1} , c_{i+1} , and d_{i+1} , where i is the iteration index. The dependence of the amplitudes of the periodic components on the actual state are calculated from the results of the preceding iteration step:

$$\begin{aligned} 0 &= -2e^T \mathbf{S}_y^{-1} \left(\mathbf{y}(x) - a_{i+1}e - b_{i+1}x - \right. \\ &c_{i+1} \text{diag} \left((a_i e + b_i x) \mathbf{v}_{\sin}^T \right) - \\ &\left. d_{i+1} \text{diag} \left((a_i e + b_i x) \mathbf{v}_{\cos}^T \right) \right); \end{aligned} \quad (36)$$

T. von Clarmann et al.: Trend estimation from clustered data

6745

$$0 = -2\mathbf{x}^T \mathbf{S}_y^{-1} \left(\mathbf{y}(\mathbf{x}) - a_{i+1}\mathbf{e} - b_{i+1}\mathbf{x} - c_{i+1} \text{diag} \left((a_i\mathbf{e} + b_i\mathbf{x}) \mathbf{v}_{\sin}^T \right) - d_{i+1} \text{diag} \left((a_i\mathbf{e} + b_i\mathbf{x}) \mathbf{v}_{\cos}^T \right) \right); \quad (37)$$

$$0 = -2 \left(\text{diag} \left((a_i\mathbf{e} + b_i\mathbf{x}) \mathbf{v}_{\sin}^T \right) \right)^T \mathbf{S}_y^{-1} \times \left(\mathbf{y}(\mathbf{x}) - a_{i+1}\mathbf{e} - b_{i+1}\mathbf{x} - c_{i+1} \text{diag} \left((a_i\mathbf{e} + b_i\mathbf{x}) \mathbf{v}_{\sin}^T \right) - d_{i+1} \text{diag} \left((a_i\mathbf{e} + b_i\mathbf{x}) \mathbf{v}_{\cos}^T \right) \right); \quad (38)$$

$$0 = -2 \left(\text{diag} \left((a_i\mathbf{e} + b_i\mathbf{x}) \mathbf{v}_{\cos}^T \right) \right)^T \mathbf{S}_y^{-1} \times \left(\mathbf{y}(\mathbf{x}) - a_{i+1}\mathbf{e} - b_{i+1}\mathbf{x} - c_{i+1} \text{diag} \left((a_i\mathbf{e} + b_i\mathbf{x}) \mathbf{v}_{\sin}^T \right) - d_{i+1} \text{diag} \left((a_i\mathbf{e} + b_i\mathbf{x}) \mathbf{v}_{\cos}^T \right) \right); \quad (39)$$

Again the equation involving $\partial\chi^2/\partial a=0$ is replaced by $c_1+\dots+c_J=0$. The iteration can be initialized with

$$a_0 = \sum_{n=1}^N \frac{y_n}{N} \quad (40)$$

and

$$b_0 = 0 \quad (41)$$

and is supposed to converge for cases where the trend is sufficiently small and/or the amplitude of the superimposed periodic function is sufficiently small compared to the y_n values. In both cases, the time-dependence of the amplitude is only a small perturbation of a function dominated by its linear terms. Similar considerations apply to periodic corrections as suggested in Eqs. (27) and (31).

Case Study 5:

The approach involving state-dependent amplitudes of periodic corrections is applicable particularly to trace gas abundances rather than temperature. We use MIPAS southern polar (60°–90° S) monthly CFC-11 mean mixing ratios at 20 km altitude. Its negative trend is a consequence of the

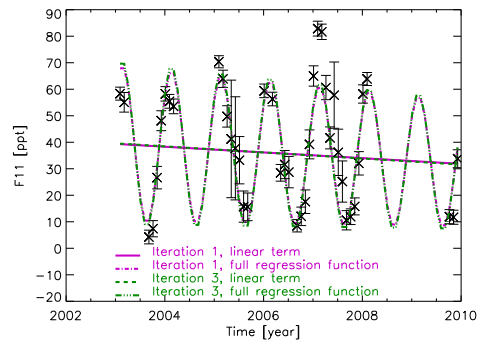


Fig. 5. Linear trends from MIPAS monthly mean CFC-11 at 20 km altitude, 60°S–90° S, using periodical correction of state-dependent amplitude, as described in Sect. 3.4. The fit converges after the third iteration.

Montreal Protocol, and the annual variation is driven by atmospheric circulation and, particularly, subsidence of CFC-depleted air in the polar winter stratosphere. Since the efficiency of loss reactions leading to CFC-depletion is proportional to its abundance, application of a correction function of an abundance-dependent amplitude is appropriate. Also in this case the change in the MIPAS measurement mode in 2004 makes the dataset inhomogeneous. In the related covariance matrix we consider an unknown bias between the data subsets of ± 2 ppt. Due to the moderate trend the iteration converges rapidly. The regression function after the first iteration is

$$[\text{CFC} - 11]/\text{ppt} = 42.62 - 1.08t + (42.62 - 1.08t)(0.575\sin(2\pi t) + 0.491\cos(2\pi t)), \quad (42)$$

where t is the time since 2000 in years. After the third iteration the final regression function is reached (Fig. 5):

$$[\text{CFC} - 11]/\text{ppt} = 43.04 - 1.15t + (43.04 - 1.15t)(0.599\sin(2\pi t) + 0.522\cos(2\pi t)) \quad (43)$$

The uncertainty of the trend is ± 0.38 ppt/yr.

4 Conclusions

In case of irregular temporal and spatial sampling and/or multiple measurement systems, intersite and/or intersystem error correlations have to be considered for trend estimation. To disregard the correlations not only renders the significance analysis meaningless, but leads to wrong estimates of the trend itself. Intersite correlations as well as correlation lengths in the time domain can be estimated from satellite data, where, however, the limited spatial resolution of

remote measurements can add some difficulty. The regression model can easily be adapted for periodic corrections of known period length but unknown phase, shape and amplitude. This scheme solves the problem that usual approaches to infer periodic corrections rely on the time series being stationary, which is inherently not true in the case of trend estimation. State-dependent amplitudes of superimposed periodic corrections can be appropriate when trends of trace gas abundances are evaluated and result in a non-linear optimization problem which is solved iteratively.

Acknowledgements. ESA has provided MIPAS level-1B data.

Edited by: W. Lahoz

References

- Aitken, A. C.: On Least squares and linear combinations of observations, *P. Roy. Soc. Edinb.*, 55, 42–48, 1935.
- Baldwin, M. P., Gray, L. J., Dunkerton, T. J., Hamilton, K., Haynes, P. H., Randel, W. J., Holton, J. R., Alexander, M. J., Hirota, I., Horinouchi, T., Jones, D. B. A., Kinniersley, J. S., Marquardt, C., Sato, K., and Takahashi, M.: The quasi-biennial oscillation, *Rev. Geophys.*, 39, 179–229, 2001.
- Cantrell, C. A.: Technical Note: Review of methods for linear least-squares fitting of data and application to atmospheric chemistry problems, *Atmos. Chem. Phys.*, 8, 5477–5487, doi:10.5194/acp-8-5477-2008, 2008.
- Cox, M., Harris, P., Hilton, M., and Woods, P.: Method for evaluating trends in ozone concentration data and its application to data from the UK Rural Ozone Monitoring Network, NPL Report CMSC 15/02, 2002.
- Efron, B.: The 1977 Rietz lecture: Bootstrap methods: Another look at the jackknife, *Ann. Stat.*, 7, 1–26, 1979.
- Engel, A., Möbius, T., Bönisch, H., Schmidt, U., Heinz, R., Levin, I., Atlas, E., Aoki, S., Nakazawa, T., Sugawara, S., Moore, F., Hurst, D., Elkins, J., Schauffler, S., Andrews, A., and Boering, K.: Age of stratospheric air unchanged within uncertainties over the past 30 years, *Nat. Geosci.*, 2, 28–31, 2009.
- Fischer, H., Birk, M., Blom, C., Carli, B., Carlotti, M., von Clarmann, T., Delbouille, L., Dudhia, A., Ehnhalt, D., Endemann, M., Flaud, J. M., Gessner, R., Kleinert, A., Koopman, R., Langen, J., López-Puertas, M., Mosner, P., Nett, H., Oelhaf, H., Perron, G., Remedios, J., Ridolfi, M., Stiller, G., and Zander, R.: MIPAS: an instrument for atmospheric and climate research, *Atmos. Chem. Phys.*, 8, 2151–2188, doi:10.5194/acp-8-2151-2008, 2008.
- Gardiner, T., Forbes, A., de Mazière, M., Vigouroux, C., Mahieu, E., Demoulin, P., Velasco, V., Notholt, J., Blumenstock, T., Hase, F., Kramer, I., Sussmann, R., Stremme, W., Mellqvist, J., Strandberg, A., Ellingsen, K., and Gauss, M.: Trend analysis of greenhouse gases over Europe measured by a network of ground-based remote FTIR instruments, *Atmos. Chem. Phys.*, 8, 6719–6727, doi:10.5194/acp-8-6719-2008, 2008.
- Guharay, A., Nath, D., Pant, P., Pande, B., Russell III, J. M., and Pandey, K.: Observation of semiannual and annual oscillation in equatorial middle atmospheric long term temperature pattern, *Ann. Geophys.*, 27, 4273–4280, doi:10.5194/angeo-27-4273-2009, 2009.
- T. von Clarmann et al.: Trend estimation from clustered data
- IPCC: Climate Change 2007: The Physical Science Basis, Contribution of Working Group I to the Fourth Assessment Report of the Intergovernmental Panel on Climate Change, edited by: Solomon, S., Qin, D., Manning, M., Chen, Z., Marquis, M., Averyt, K. B., Tignor, M., and Miller, H. L., Cambridge University Press, Cambridge, UK and New York, NY, USA, 996 pp., 2007.
- Jones, P. D., Osborn, T. J., and Briffa, K. R.: Estimating sampling errors in large-scale temperature averages, *J. Climate*, 10, 2548–2568, 1997.
- Milz, M., von Clarmann, T., Fischer, H., Glatthor, N., Grabowski, U., Höpfner, M., Kellmann, S., Kiefer, M., Linden, A., Mengistu Tsidu, G., Steck, T., Stiller, G. P., Funke, B., López-Puertas, M., and Koukouli, M. E.: Water vapor distributions measured with the Michelson Interferometer for Passive Atmospheric Sounding on board Envisat (MIPAS/Envisat), *J. Geophys. Res.*, 110, D24307, doi:10.1029/2005JD005973, 2005.
- Milz, M., Clarmann, T. v., Bernath, P., Boone, C., Buehler, S. A., Chauhan, S., Deuber, B., Feist, D. G., Funke, B., Glatthor, N., Grabowski, U., Griesfeller, A., Haeefe, A., Höpfner, M., Kämpfer, N., Kellmann, S., Linden, A., Müller, S., Nakajima, H., Oelhaf, H., Remsberg, E., Rohs, S., Russell III, J. M., Schiller, C., Stiller, G. P., Sugita, T., Tanaka, T., Vömel, H., Walker, K., Wetzel, G., Yokota, T., Yushkov, V., and Zhang, G.: Validation of water vapour profiles (version 13) retrieved by the IMK/IAA scientific retrieval processor based on full resolution spectra measured by MIPAS on board Envisat, *Atmos. Meas. Tech.*, 2, 379–399, doi:10.5194/amt-2-379-2009, 2009.
- Mühlbauer, A., Spichtinger, P., and Lohmann, U.: Application and comparison of robust linear regression methods for trend estimation, *J. Appl. Meteorol. Climat.*, 48, 1961–1970, doi:10.1175/2009JAMC1851.1, 2009.
- Randel, W. J., Wu, F., Oltmans, S. J., Rosenlof, K., and Nedoluha, G. E.: Interannual changes of stratospheric water vapor and correlations with tropical tropopause temperatures, *J. Atmos. Sci.*, 61, 2133–2148, 2004.
- Reed, R. J.: The quasi-biennial oscillation of the atmosphere between 30 and 50 km over Ascension Island, *J. Atmos. Sci.*, 22, 331–333, 1965.
- Rosenlof, K. H. and Reid, G. C.: Trends in the temperature and water vapor content of the tropical lower stratosphere: Sea surface connection, *J. Geophys. Res.*, 113, D06107, doi:10.1029/2007JD009109, 2008.
- Vigouroux, C., De Mazière, M., Demoulin, P., Servais, C., Hase, F., Blumenstock, T., Kramer, I., Schneider, M., Mellqvist, J., Strandberg, A., Velasco, V., Notholt, J., Sussmann, R., Stremme, W., Rockmann, A., Gardiner, T., Coleman, M., and Woods, P.: Evaluation of tropospheric and stratospheric ozone trends over Western Europe from ground-based FTIR network observations, *Atmos. Chem. Phys.*, 8, 6865–6886, doi:10.5194/acp-8-6865-2008, 2008.
- von Clarmann, T., Glatthor, N., Grabowski, U., Höpfner, M., Kellmann, S., Kiefer, M., Linden, A., Mengistu Tsidu, G., Milz, M., Steck, T., Stiller, G. P., Wang, D. Y., Fischer, H., Funke, B., Gil-López, S., and López-Puertas, M.: Retrieval of temperature and tangent altitude pointing from limb emission spectra recorded from space by the Michelson Interferometer for Passive Atmospheric Sounding (MIPAS), *J. Geophys. Res.*, 108(D23), 4736, doi:10.1029/2003JD003602, 2003.

T. von Clarmann et al.: Trend estimation from clustered data

6747

von Clarmann, T.: Validation of remotely sensed profiles of atmospheric state variables: strategies and terminology, *Atmos. Chem. Phys.*, 6, 4311–4320, doi:10.5194/acp-6-4311-2006, 2006.

von Clarmann, T., Höpfner, M., Kellmann, S., Linden, A., Chauhan, S., Funke, B., Grabowski, U., Glatthor, N., Kiefer, M., Schieferdecker, T., Stiller, G. P., and Versick, S.: Retrieval of temperature, H₂O, O₃, HNO₃, CH₄, N₂O, ClONO₂ and ClO from MIPAS reduced resolution nominal mode limb emission measurements, *Atmos. Meas. Tech.*, 2, 159–175, doi:10.5194/amt-2-159-2009, 2009.

Weatherhead, E. C., Reinsel, G. C., Tiao, G. C., Meng, X.-L., Choi, D., Cheang, W.-K., Keller, T., DeLuisi, J., Wuebbles, D. J., Kerr, J. B., Miller, A. J., Oltmans, S. J., and Frederick, F. E.: Factors affecting the detection of trends: Statistical considerations and applications to environmental data, *J. Geophys. Res.*, 103, 17149–17161, 1998.

B.2 Global CFC-11 (CCl_3F) and CFC-12 (CCl_2F_2) measurements with the Michelson Interferometer for Passive Atmospheric Sounding (MIPAS): retrieval, climatologies and trends

Atmos. Chem. Phys., 12, 11857–11875, 2012
www.atmos-chem-phys.net/12/11857/2012/
doi:10.5194/acp-12-11857-2012
© Author(s) 2012. CC Attribution 3.0 License.



Global CFC-11 (CCl₃F) and CFC-12 (CCl₂F₂) measurements with the Michelson Interferometer for Passive Atmospheric Sounding (MIPAS): retrieval, climatologies and trends

S. Kellmann¹, T. von Clarmann¹, G. P. Stiller¹, E. Eckert¹, N. Glatthor¹, M. Höpfner¹, M. Kiefer¹, J. Orphal¹, B. Funke², U. Grabowski¹, A. Linden¹, G. S. Dutton^{3,4}, and J. W. Elkins³

¹Karlsruhe Institute of Technology (KIT), Institute for Meteorology and Climate Research (IMK), Karlsruhe, Germany

²Instituto de Astrofísica de Andalucía, CSIC, Granada, Spain

³NOAA Earth System Research Laboratory, Boulder, CO 80305, USA

⁴Cooperative Institute for Research in Environmental Sciences, University of Colorado, Boulder, CO 80309, USA

Correspondence to: S. Kellmann (sylvia.kellmann@kit.edu)

Received: 11 June 2012 – Published in Atmos. Chem. Phys. Discuss.: 25 July 2012

Revised: 29 November 2012 – Accepted: 3 December 2012 – Published: 17 December 2012

Abstract. Vertical profiles of CFC-11 (CCl₃F) and CFC-12 (CCl₂F₂) have been measured with the Michelson Interferometer for Passive Atmospheric Sounding (MIPAS) with global coverage under daytime and nighttime conditions. The profile retrieval is based on constrained nonlinear least squares fitting of measured limb spectral radiance to modeled spectra. CFC-11 is measured in its ν_4 -band at 850 cm⁻¹, and CFC-12 is analyzed in its ν_6 -band at 922 cm⁻¹. To stabilize the retrievals, a Tikhonov-type smoothing constraint is applied. Main retrieval error sources are measurement noise and elevation pointing uncertainties. The estimated CFC-11 retrieval errors including noise and parameter errors but excluding spectroscopic data uncertainties are below 10 pptv in the middle stratosphere, depending on altitude, the MIPAS measurement mode and the actual atmospheric situation. For CFC-12 the total retrieval errors are below 28 pptv at an altitude resolution varying from 3 to 5 km. Time series of altitude/latitude bins were fitted by a simple parametric approach including constant and linear terms, a quasi-biennial oscillation (QBO) proxy and sine and cosine terms of several periods. In the time series from 2002 to 2011, quasi-biennial and annual oscillations are clearly visible. A decrease of stratospheric CFC mixing ratios in response to the Montreal Protocol is observed for most altitudes and latitudes. However, the trends differ from the trends measured in the troposphere, they are even positive at some latitudes and altitudes, and can in some cases only be explained by decadal changes in atmospheric age of air spectra or vertical mixing patterns.

1 Introduction

Prior to the reduced emissions in response to the Montreal Protocol signed in 1987, CFC-11 (CCl₃F) and CFC-12 (CCl₂F₂) were the major sources of stratospheric chlorine. The stratospheric chlorine loading reached its maximum in 1996/1997, and a slow decline of stratospheric total chlorine has been observed since then (Rinsland et al., 2003). Beyond being a source for reactive chlorine, which plays a major role in stratospheric ozone depletion (Molina and Rowland, 1974), the long lifetimes of these species (Ko and Sze, 1982) make them ideal tracers for dynamic processes such as subsidence (e.g., Toon et al., 1992), horizontal transport, and mixing (e.g., Waugh et al., 1997).

Recently, evidence has been found that the lifetimes of CFC-11 and CFC-12 might have been underestimated, and their reevaluation is considered a high priority action in atmospheric sciences, because of their role as a source of ozone destructing substances (Ko et al., 2012). A necessary prerequisite for a reassessment of lifetime of these CFCs are stratospheric measurements.

Atmospheric chlorofluorocarbon (CFC) abundances have been measured since the early 1970s (Lovelock, 1971). A variety of in-situ and remote sensing techniques has been developed for this purpose in the following years, see, e.g., the bibliography in Goldman et al. (1976). Stratospheric CFC abundances are typically measured by air sampling techniques and subsequent laboratory analysis (e.g., Lueb et al.,

1975; Heidt et al., 1975; Engel et al., 1998), by in-situ techniques (e.g., Robinson et al., 1977; Bujok et al., 2001; Romashkin et al., 2001), or remotely by infrared spectroscopy from balloon-borne (e.g., Murcray et al., 1975; Williams et al., 1976) or space-borne (e.g., Zander et al., 1987) platforms in solar occultation geometry. More recent solar occultation instruments used for CFC-detection include the Improved Limb Atmospheric Spectrometer (ILAS) (Khosravi et al., 2004) and the Atmospheric Chemistry Experiment (ACE) (Mahieu et al., 2008; Brown et al., 2011).

Independent of a solar background signal, CFCs can also be measured by limb emission spectroscopy, as first documented by Brasunas et al. (1986) and Kunde et al. (1987). Space-borne limb emission measurements of CFCs were reported by Roche et al. (1993) for the Cryogenic Limb Array Etalon Spectrometer (CLAES), by Bingham et al. (1997) for the Cryogenic Infrared Radiance Instrumentation for Shuttle (CIRRIS 1A), by Spang et al. (1997) for the Cryogenic IR spectrometers and Telescopes (CRISTA), and by Khosravi et al. (2009) for the High Resolution Dynamics Limb Sounder (HIRDLS) instrument onboard NASA's Earth Observing System (EOS) Aura satellite. This series of space-borne limb-emission CFC-measurements has been continued with the Michelson Interferometer for Passive Atmospheric Sounding (MIPAS) (Höpfner et al., 2007; Hoffmann et al., 2008). In this paper, we present the retrieval of CFC-11 and CFC-12 volume mixing ratio (VMR) profiles from limb emission MIPAS spectra and report on the climatology and trends of retrieved profiles. These climatologies have been prepared as a contribution to the SPARC (Stratospheric Processes and their Role in Climate) data initiative (Hegglin and Tegtmeier, 2011).

2 MIPAS data

MIPAS is a cryogenic limb emission Fourier transform spectrometer designed for measurement of trace species from space (Endemann and Fischer, 1993; European Space Agency, 2000; Endemann et al., 1996; Fischer and Oelhaf, 1996; Fischer et al., 2008). It is part of the instrumentation of the Environmental Satellite (ENVISAT) which was launched into a sun-synchronous polar orbit on 1 March 2002. MIPAS was operated from July 2002 to March 2004 with full spectral resolution (FR) specification (0.05 cm^{-1} in terms of full width at half maximum, after apodization with the "strong" Norton and Beer (1976) function, corresponding to a maximum optical path difference of 20 cm). After a failure of one of the interferometer slide, MIPAS was operated since January 2005 in the reduced spectral resolution (RR) mode (0.121 cm^{-1}) with an optical path difference of 8.0 cm. We consider MIPAS measurements only in the so-called nominal measurement modes of both the FR and the RR period (see Table 1). Data presented here were recorded from July 2002 to April 2011, which equates to

Table 1. Scan sequences for MIPAS FR and RR measurements (Dudhia, 2012). The RR-Nominal mode heights are latitude dependent.

Measurement mode	FR-Nominal	RR-Nominal
Version acronym	V3O	V5R
Horizontal spacing	510 km	410 km
Optical path difference	20 cm	8 cm
Spectral resolution	full:	reduced:
apodized	0.05 cm^{-1}	0.121 cm^{-1}
Sweeps/scans	17	27
Scan no. 1	68 km	70 km
Scan no. 2	60 km	66 km
Scan no. 3	52 km	62 km
Scan no. 4	47 km	58 km
Scan no. 5	42 km	54 km
Scan no. 6	39 km	50 km
Scan no. 7	36 km	46 km
Scan no. 8	33 km	43 km
Scan no. 9	30 km	40 km
Scan no. 10	27 km	37 km
Scan no. 11	24 km	34 km
Scan no. 12	21 km	31 km
Scan no. 13	18 km	29 km
Scan no. 14	15 km	27 km
Scan no. 15	12 km	25 km
Scan no. 16	9 km	23 km
Scan no. 17	6 km	21 km
Scan no. 18		19.5 km
Scan no. 19		18 km
Scan no. 20		16.5 km
Scan no. 21		15 km
Scan no. 22		13.5 km
Scan no. 23		12 km
Scan no. 24		10.5 km
Scan no. 25		9 km
Scan no. 26		7.5 km
Scan no. 27		6 km
Average number of geolocations per orbit	~ 74	~ 96

about 2 million profiles for CFC-11 and CFC-12. The data analysis reported in this paper relies on the ESA-provided so-called level-1B data product which includes calibrated phase-corrected and geolocated radiance spectra (Nett et al., 1999), ESA data versions MIPAS/4.61 to MIPAS/4.62 for measurements recorded from 2002 to 2004, and MIPAS/5.02 to MIPAS/5.06 for measurements recorded since 2005. All spectra under consideration were obtained according to the standard measurement scenarios with nominal tangent altitudes from the upper troposphere to the mesosphere. Table 1 lists the scan sequences for MIPAS FR (July 2002–March 2004) and RR (since 2005) nominal measurement modes (Dudhia, 2012). Data versions presented in this paper

are V3O.CFC11.10 and V3O.CFC12.10 for FR measurements and V5R.CFC11.220 and V5R.CFC12.220 for RR measurements.

Version 6 of the operational ESA data product, just recently released, also includes CFC-11 and CFC-12. Besides data presented in this study, there exist also MIPAS CFC data retrieved by different data analysis algorithms (Dinelli et al., 2010; Hoffmann et al., 2008; Moore et al., 2006; Dudhia, 2012).

3 CFC retrievals

The retrieval of CFC-11 and CFC-12 profiles presented here was performed with a MIPAS data processor dedicated for scientific applications, which has been developed at the Institute for Meteorology and Climate Research (IMK) and complemented by components specific to treatment of non-local thermodynamic equilibrium (non-LTE) developed at the Instituto de Astrofísica de Andalucía (IAA). Non-LTE effects are not relevant to the retrieval of CFCs. The general strategy of the IMK/IAA data processing has been documented in von Clarmann et al. (2003b). It underwent a pre-flight functionality study and validation by cross-comparison with various other data-processors within the framework of a blind test retrieval study (von Clarmann et al., 2003a).

CFC-11 and CFC-12 are retrieved by constrained multi-parameter non-linear least squares fitting of modeled to measured spectra. Spectral data from all tangent altitudes are analyzed within one inversion process, as suggested by Carlotti (1988). VMR vertical profiles are retrieved on a fixed, i.e. tangent altitude independent height grid which is finer than the tangent altitude spacing (50 retrieval altitudes for CFC-11: 1-km steps from 4 to 45 km, then 5-km grid spacing to 50 km, 10-km steps from 60 to 100 km, and 20-km step to 120 km. 60 retrieval altitudes for CFC-12: 1-km steps from 4 to 44 km, then 2-km grid spacing from 46 to 70 km, 5-km steps from 75 to 80 km, and 10-km steps from 90 to 120 km). The horizontal spacing is 510 km for the FR resolution data nominal mode and 410 km for the RR nominal mode. In order to obtain stable profiles, the profiles have been constrained such that the first order finite difference quotient $\Delta\text{VMR}/\Delta\text{altitude}$ at adjacent altitude gridpoints was minimized, using the formalism as proposed by Tikhonov (1963). For both trace gases we use a zero a priori profile. The strength of the regularization has been chosen altitude-dependent with a scheme proposed by Steck (2002).

Forward modeling of spectra is performed with the Karlsruhe Optimized and Precise Radiative Transfer Algorithm (KOPRA) (Stiller, 2000; Stiller et al., 2002) using a dedicated spectroscopic database for MIPAS compiled by Flaud et al. (2003). CFC-11 and CFC-12 bands were modeled by 2-dimensional interpolation of pressure-, temperature-, and wavenumber-resolved laboratory measurements (Varanasi, 1992; Varanasi and Nemtchinov, 1994) to the actual atmo-

spheric pressures and temperatures. The spectroscopic uncertainty of this data has been estimated in the literature to be 5% (Rothman et al., 1998; Rinsland et al., 2005), however the spectral resolution (0.03 cm^{-1} and 0.01 cm^{-1} at pressures below 40 Torr, which corresponds to 53.3 hPa) of the laboratory data may introduce small systematic errors, together with the interpolation to different temperatures and pressures. Indeed, CFC-11 and CFC-12 show dense and sharp spectral structure at very high spectral resolution, even in the Q-branches (see, e.g., Orphal, 1991; McNaughton et al., 1994, 1995; D'Amico et al., 2002). It is also important to note that comparisons of the absolute band intensities (see, e.g., Varanasi and Nemtchinov, 1994; D'Amico et al., 2002) with other studies show larger differences. For these reasons, the absolute uncertainty of the spectroscopic data is estimated to be 10%, in the absence of further information.

Local spherical homogeneity of the atmosphere is assumed here, i.e., atmospheric state parameters related to one limb sounding sequence are not allowed to vary with latitude or longitude but only with altitude. The only exception is temperature: For data versions V5R.CFC11.220 and V5R.CFC12.220, a horizontal temperature gradient, calculated from ECMWF temperature fields, was taken into consideration in a range of $\pm 400\text{ km}$ around the tangent point to reduce related retrieval artifacts (Kiefer et al., 2010).

Prior to trace gas retrievals, a spectral shift correction is applied first. Then elevation pointing correction and the temperature retrieval are performed (von Clarmann et al., 2003b, 2009b), and these data are used in the subsequent trace gas retrievals. The most recent CFC data versions (V5R.CFC11.220 and V5R.CFC12.220) are based on a temperature and pointing retrieval where ozone and water vapor are jointly retrieved. This reduces the dependence of related a priori information on these species and related error propagation. Older data versions (V4O) where information on O_3 and H_2O was taken from climatologies during the temperature and elevation pointing retrieval led to temperature artifacts at about 30° N/S where the climatology was switched from the tropical to the mid-latitude case. These artifacts propagated onto the species retrievals and led to rabbit-ears-like structures in the altitude/latitude cross-sections of tropospheric source gases, which are no longer found in the V5R.CFC11.220 and V5R.CFC12.220 data. After temperature and line of sight (LOS) retrieval, the next steps are dedicated H_2O and O_3 retrievals for which the results were found superior over the results of the joint retrieval of temperature, elevation pointing, ozone, and water vapor. After that, species abundances are retrieved in the order HNO_3 , CH_4 together with N_2O , ClONO_2 , N_2O_5 , ClO , and finally CFC-11 and CFC-12. Each gas is retrieved in its specific spectral region, where results from preceding species abundance retrievals are used as input for the next species retrieval.

3.1 CFC-11

CFC-11 was analyzed in the $831.0\text{--}853.0\text{ cm}^{-1}$ spectral region, which covers the main part of the ν_4 band. Main interfering species in this region are H_2O , the HNO_3 ν_5 band, and the COCl_2 ν_5 band (Toon et al., 2001). In order to avoid propagation of uncertainties of a priori knowledge on these species to the CFC-11 profiles, their abundances were jointly fit along with CFC-11 in this analysis window. Although H_2O results are available from preceding retrievals, joint-fitting led to reduced residuals in the H_2O lines, most probably due to inconsistencies between spectroscopic data in the H_2O analysis windows and the CFC-11 analysis window. Furthermore, a background-dependent continuum signal and a zero-radiance calibration correction were determined along with the species abundances, as discussed in von Clarmann et al. (2003b). At tangent heights above 40 km CFC-11 is far below the detection limit. Thus, to save computing time, we used the twelve lowermost tangent heights, which correspond to altitudes between 5 km and 38 km for the FR data, and the nineteen lowermost tangent heights, which cover the 5 km and 40 km altitude range for the RR data.

Retrieval error estimates for sample FR and RR CFC-11 retrievals are shown in Table 2 and Table 3, respectively. The high resolution measurement was taken at high southern latitudes on 21 May 2003. The estimated total retrieval error is 6.4 pptv at 25 km and 45.0 pptv at 10 km altitude. The RR measurement was taken in northern mid-latitudes on 19 September 2009. The related estimated total retrieval error is 6.1 pptv at 25 km and 19.0 pptv at 10 km altitude. For both measurement modes, the total retrieval error in the middle stratosphere (above 15–20 km) is dominated by measurement noise, while in the troposphere and lower stratosphere the leading error sources are uncertainties in elevation pointing (line of sight error), uncertainties in the abundances of the peroxyacetyl nitrate (PAN), NH_3 , and OCS abundances, as well as spectral calibration uncertainties (gain error) and temperature uncertainties.

Selected rows of the CFC-11 averaging kernel matrices for both measurement modes are shown in Fig. 1. The altitude resolution in terms of full width at half maximum of a row of the averaging kernel matrix is about 4 km for the FR measurements, and about 2 to 3 km for the RR measurements. The averaging kernels are well-behaved in the sense that they peak at their nominal altitudes between about 6 km and 25 km for high spectral resolution and between about 10 and 25 km for RR measurements. Below and above, the retrievals are particularly sensitive to the real atmosphere below the nominal altitude. This is because the retrieval is strongly regularized to cope with the low sensitivity at these altitudes. The retrieved CFC-11 profiles represent approximately 4 to 7 degrees of freedom for the FR measurements and 5 to 9 degrees of freedom for the RR measurements, respectively. The better vertical resolution in the RR data is caused by finer vertical sampling.

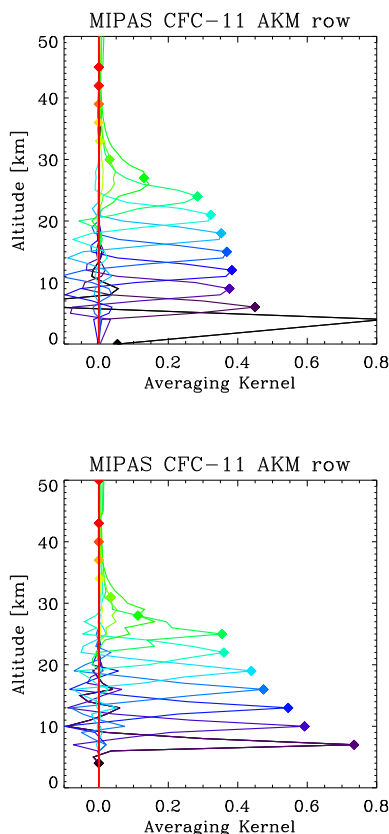


Fig. 1. Rows of averaging kernels of CFC-11 measurements for FR nominal mode (top) and RR nominal mode (bottom). Diamonds represent the nominal altitudes (i.e. the diagonal value of the averaging kernel matrix). Only every third kernel is shown.

The horizontal information smearing (we intentionally avoid the term “horizontal resolution” because the resolution can never be better than the horizontal sampling) was estimated on the basis of 2-D averaging kernels, evaluated on the basis of 2-D Jacobians of 1-D retrievals as described in von Clarmann et al. (2009a). The horizontal information smearing of a MIPAS retrieval in terms of full width at half maximum of the horizontal component of the 2-D averaging kernel is approximately 200–500 km, depending on measurement mode and altitude (Table 4). In many cases, the smearing is smaller than the horizontal sampling, implying that the horizontal resolution is limited by the horizontal sampling grid rather than the horizontal information smearing.

Table 2. Error budget of a V3O.CFC11.10 (FR nominal mode) retrieval from spectra recorded at 63° S, 164° E on 21 May 2003 at 22:51 UTC, for selected altitudes. The errors are given in units of pptv (%). The total error is the sum of measurement noise and parameter error. The parameter error is the sum of uncertainties in interfering species and instrumental properties, which interact as random error sources (PAN, NH₃, ..., OCS).

V3O CFC-11 Height	Total Error	Measurement Noise	Parameter Error	PAN	NH ₃	Line Of Sight	Gain	Temperature	OCS
30 km	1.9 (28.4)	1.8 (26.9)	0.4 (6.7)	0.3 (4.2)	0.1 (1.8)	0.3 (4.6)	<0.1 (<0.1)	<0.1 (0.5)	0.1 (0.9)
25 km	6.4 (17.4)	6.1 (16.6)	1.9 (5.2)	0.6 (1.7)	0.6 (1.6)	1.6 (4.4)	0.2 (0.5)	0.2 (0.6)	0.3 (0.9)
20 km	8.0 (12.7)	5.9 (9.4)	5.5 (8.8)	1.4 (2.2)	0.6 (0.9)	5.2 (8.3)	0.7 (1.1)	0.4 (0.7)	0.5 (0.8)
15 km	9.3 (4.9)	2.8 (1.5)	8.8 (4.7)	5.0 (2.6)	1.8 (1.0)	6.8 (3.6)	1.4 (0.7)	1.0 (0.5)	0.9 (0.5)
10 km	45.0 (15.7)	4.0 (1.4)	44.0 (15.3)	44.0 (15.3)	1.9 (0.7)	4.2 (1.5)	0.1 (<0.1)	0.4 (0.1)	1.3 (0.5)

Table 3. Error budget of a V5R.CFC11.220 (RR nominal mode) retrieval from spectra recorded at 37° N, 29° W on 19 September 2009 at 00:11 UTC for selected altitudes. The errors are given in units of pptv (%). Details as for Table 2.

V5R CFC-11 Height	Total Error	Measurement Noise	Parameter Error	PAN	NH ₃	Line Of Sight	Gain	Temperature	OCS
30 km	1.9 (35.2)	1.7 (31.5)	0.7 (12.6)	0.6 (10.9)	0.1 (1.4)	0.3 (5.9)	0.1 (1.6)	<0.1 (0.3)	<0.1 (0.4)
25 km	6.1 (14.8)	5.5 (13.3)	2.6 (6.3)	1.1 (2.7)	<0.1 (0.1)	2.3 (5.6)	0.1 (0.2)	0.1 (0.2)	0.1 (0.3)
20 km	9.8 (6.7)	5.5 (3.7)	8.2 (5.6)	1.1 (0.7)	0.2 (0.2)	8.0 (5.4)	1.4 (1.0)	0.3 (0.2)	0.2 (0.1)
15 km	11.0 (4.4)	4.8 (1.9)	9.3 (3.7)	0.9 (0.4)	0.6 (0.3)	8.7 (3.5)	3.1 (1.2)	0.5 (0.2)	0.3 (0.1)
10 km	19.0 (7.7)	4.5 (1.8)	18.0 (7.3)	8.6 (3.5)	2.3 (0.9)	15.0 (6.1)	5.8 (2.4)	1.0 (0.4)	0.8 (0.3)

Table 4. Horizontal information smearing (full width at half maximum of the horizontal component of the 2-D averaging kernel) for CFC-11.

Mode	Nominal full	Nominal reduced
25 km	440 km	468 km
20 km	335 km	497 km
15 km	293 km	159 km
10 km	199 km	295 km

The information displacement is the horizontal distance between the point where most information comes from and the nominal geolocation of the limb scan, which is defined as the geolocation of the tangent point of the middle line of sight in a MIPAS limb scan. Compared to the nominal geolocation, the tangent points are displaced towards the satellite for the lowermost tangent altitude and in the opposite direction for the uppermost tangent altitude. This displacement is caused by the satellite movement and the position of the tangent point as a function of the elevation angle. Beyond this, also atmospheric opacity and regularization of the retrievals contribute to the information displacement. In Table 5 the CFC-11 weighted displacements are listed for altitudes of interest. Negative distances are displacements away from the satellite, beyond the tangent point. Positive distances are dis-

placements towards the satellite. Except for higher altitudes the displacements are small compared to the horizontal sampling distance.

Figure 2 shows examples of a measured versus best fit modeled CFC-11 spectra, along with related residual spectra. For the FR measurement, a spectrum recorded at about 14 km tangent altitude is shown, which was measured on 21 May 2003. The broad spectral signature of CFC-11 is well reproduced. The root mean square (rms) of the residual is 16.91 nW (cm² sr cm⁻¹)⁻¹ which is about equal to the nominal noise equivalent spectral radiance (NESR) in the wavenumber region 830–850 cm⁻¹, which is 15 nW (cm² sr cm⁻¹)⁻¹ for apodized spectra. The RR spectrum was recorded at about 14 km tangent altitude on 19 September 2009. Also this spectrum is well reproduced and the rms of the residual is 12.78 nW (cm² sr cm⁻¹)⁻¹, which also is about equal to the nominal apodized noise equivalent spectral radiance of 12 nW (cm² sr cm⁻¹)⁻¹.

3.2 CFC-12

CFC-12 was analyzed in the 915.0–925.0 cm⁻¹ spectral region, which covers the central part of the ν₆ band. Main interfering signals are caused by the CO₂ 10001 ← 00011 so-called laser band, the HNO₃ 2ν₉ band, H₂O and a weak PAN band. All these interfering species were jointly fit along with continuum and offset-correction. In contrast to CFC-11, we used all available tangent heights for the CFC-12 retrieval,

Table 5. Information displacement for CFC-11 retrievals. Negative distances are displacements away from the satellite, beyond the tangent point. Positive distances are displacements towards the satellite.

Mode Spectr. Resol.	Nominal full	Nominal reduced
25 km	561 km	249 km
20 km	112 km	82 km
15 km	-74 km	105 km
10 km	-146 km	4 km

because the measurable signal of CFC-12 extends to higher altitudes than that of CFC-11.

Error estimates for CFC-12 FR and RR measurements are shown in Table 6 and Table 7, respectively. The estimated total retrieval error of CFC-12 retrieved from high spectral resolution measurements is 20.0 pptv for 25 km and 18.0 pptv for 10 km altitude. At 20 km and above measurement noise is the leading error source, while below parameter errors are dominating. The main parameter error components are the line of sight elevation pointing error, gain calibration error, the error of the horizontal (along track) temperature gradient, the temperature error itself, and the uncertainty in the NH_3 profile. For RR CFC-12 retrievals, the relative importance of the various error sources is similar, except that the horizontal temperature inhomogeneities do not appear as error source since horizontal temperature gradients were accounted for in the retrieval. In the stratosphere, total retrieval errors are only slightly larger than for high spectral resolution measurements (22.0 pptv at 25 km) but at 10 km the error is much larger (64.0 pptv) because of propagated parameter uncertainties, for the example chosen.

The altitude resolution in terms of full width at half maximum of a row of the averaging kernel matrix is about 3 to 5 km for the FR measurements and about 3 to 4 km for the RR measurements. This corresponds to 6–9 degrees of freedom for FR measurements and 9–13 for RR measurements. CFC-12 averaging kernels are shown in Fig. 3. They are well-behaved between about 8 and 40 km for high spectral retrievals and between 10 and 50 km for RR measurements. As for CFC-11, the better altitude resolution of the RR measurements is due to the better vertical sampling.

Figure 4 shows examples of measured (black) versus fitted (red) CFC-12 spectra. The high spectral resolution measurement was recorded on 21 May 2003 at the border of the southern polar cap and the tangent altitude is 11 km. The measured spectrum is well reproduced and the rms of the residual is $19.15 \text{ nW}(\text{cm}^2 \text{sr cm}^{-1})^{-1}$ which is slightly higher than the nominal noise equivalent spectral radiance. The RR was recorded on 19 September 2009 at a tangent altitude of 11 km. Here the rms of the fit residual ($13.84 \text{ nW}(\text{cm}^2 \text{sr cm}^{-1})^{-1}$) is even slightly less than the nominal noise equivalent spectral radiance.

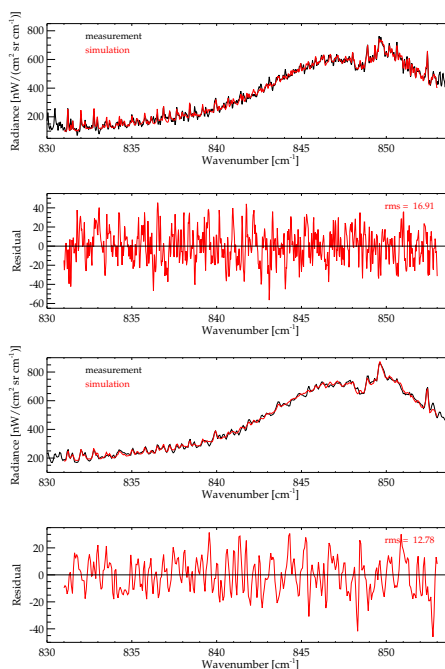


Fig. 2. Typical measured (black) and calculated (red) spectra of CFC-11 and the fit residual in 14 km in the 831 and 853 cm^{-1} spectral region for the FR (top) and the RR (bottom) nominal measurement modes.

The horizontal information smearing of CFC-12 retrievals is approximately 300 km at altitudes below 24 km and more than 400 km above for the FR retrievals (Table 8). For the RR retrievals assessed here, it is between about 300 km and more than 500 km. As for CFC-11, the information displacement is clearly smaller than the horizontal measurement grid (Table 9).

4 The SPARC climatologies

MIPAS CFC climatologies have been developed from the retrieved data presented here and prepared in compliance with the methodical and data format requirements of the SPARC (Stratospheric Processes and their Role in Climate) data initiative (Hegglin and Tegtmeier, 2011). The climatology consists of zonal monthly mean fields of CFC volume mixing ratios on 28 pressure levels of 300, 250, 200, 170, 150, 130, 115, 100, 90, 80, 70, 50, 30, 20, 15, 10, 7, 5, 3, 2, 1.5, 1.0, 0.7, 0.5, 0.3, 0.2, 0.15, 0.1 hPa. Along with these monthly means,

Table 6. Error budget of a V3O.CFC12.10 (FR nominal mode) retrieval from spectra recorded at 63° S, 164° E on 21 May 2003 at 22:51 UTC for selected altitudes. The errors are given in units of pptv (%). Details as for Table 2.

V3O CFC-12 Height	Total Error	Measurement Noise	Parameter Error	Line Of Sight	Gain	Temp. Inhomog.	Temp.	NH ₃
35 km	21.0 (87.6)	21.0 (87.6)	1.6 (6.7)	0.7 (2.9)	1.2 (5.0)	0.5 (1.9)	0.6 (2.7)	<0.1 (0.1)
30 km	20.0 (58.6)	20.0 (58.6)	3.1 (9.1)	3.0 (8.8)	0.3 (0.9)	0.2 (0.6)	0.1 (0.4)	0.1 (0.2)
25 km	20.0 (13.2)	18.0 (11.9)	8.6 (5.7)	8.4 (5.5)	1.0 (0.6)	<0.1 (<0.1)	1.1 (0.7)	<0.1 (<0.1)
20 km	20.0 (7.4)	15.0 (5.5)	13.0 (4.8)	13.0 (4.8)	3.4 (1.3)	0.6 (0.2)	2.1 (0.8)	0.2 (0.1)
15 km	18.0 (3.8)	9.4 (2.0)	15.0 (3.1)	15.0 (3.1)	3.5 (0.7)	0.4 (0.1)	2.7 (0.6)	0.8 (0.2)
10 km	18.0 (2.5)	12.0 (1.7)	13.0 (1.8)	8.0 (1.1)	4.5 (0.6)	2.6 (0.4)	1.5 (0.2)	8.8 (1.2)

Table 7. Error budget of a V5R.CFC12.220 (RR nominal mode) retrieval from spectra recorded at 37° N, 29° W on 19 September 2009 at 00:11 UTC, for selected altitudes. The errors are given in units of pptv (%). Details as for Table 2.

V5R CFC-12 Height	Total Error	Measurement Noise	Parameter Error	Line Of Sight	Gain	Temp.	Shift	NH ₃
35 km	28.0 (32.1)	27.0 (31.0)	6.7 (7.7)	6.3 (7.2)	2.1 (2.4)	0.5 (0.6)	0.4 (0.4)	0.1 (0.1)
30 km	24.0 (22.9)	22.0 (21.0)	8.8 (8.4)	8.4 (8.0)	2.5 (2.4)	0.6 (0.6)	0.3 (0.3)	0.1 (0.1)
25 km	22.0 (9.0)	21.0 (8.6)	5.1 (2.1)	4.2 (1.7)	2.9 (1.2)	0.7 (0.3)	0.2 (0.1)	<0.1 (<0.1)
20 km	22.0 (5.3)	16.0 (3.9)	15.0 (3.6)	14.0 (3.4)	5.1 (1.2)	1.2 (0.3)	0.1 (<0.1)	<0.1 (<0.1)
15 km	22.0 (4.1)	15.0 (2.8)	16.0 (3.0)	13.0 (2.4)	9.3 (1.7)	1.7 (0.3)	0.1 (<0.1)	0.2 (<0.1)
10 km	64.0 (12.0)	13.0 (2.4)	63.0 (11.9)	57.0 (10.7)	27.0 (5.1)	6.3 (1.2)	0.1 (<0.1)	1.3 (0.2)

Table 8. Horizontal information smearing (full width at half maximum of the horizontal component of the 2-D averaging kernel) for CFC-12.

Mode Spectr. Resol.	Nominal full	Nominal reduced
35 km	503 km	510 km
30 km	430 km	444 km
25 km	406 km	557 km
20 km	304 km	394 km
15 km	250 km	578 km
10 km	262 km	292 km

Table 9. Information displacement for CFC-12 retrievals.

Mode Spectr. Resol.	Nominal full	Nominal reduced
35 km	187 km	-19 km
30 km	153 km	13 km
25 km	-61 km	40 km
20 km	-87 km	83 km
15 km	-177 km	147 km
10 km	-373 km	-61 km

standard deviations and sample sizes are provided. Technical details of the generation of these climatologies follow the approach published by von Clarmann et al. (2012).

4.1 CFC-11 observations

Figure 5 shows monthly zonal means of CFC-11 between 200 hPa and 10 hPa for September 2002, December 2003, March 2008, and June 2010. Largest mixing ratios are seen in the tropics in the upwelling branch of the Brewer-Dobson circulation. With increasing altitude and latitude mixing ratios become smaller, reflecting photochemical and OH-driven CFC-depletion in aged air. The decrease of CFC-11 from the years 2002 to 2010 is noticeable particularly in the tropical

tropopause, where the air is youngest. Here the effect of reduced CFC emissions in response to the Montreal Protocol is best visible.

Figures 6 and 7 illustrate the temporal evolution of CFC-11 for all latitudes between July 2002 and April 2011 at selected altitude levels from 200 hPa to 15 hPa. Between April and December 2004 no MIPAS data are available because of the instrument failure mentioned in Sect. 2. Particularly at 200 hPa there is an obvious bias between the FR and the RR data, mainly caused by the improved vertical resolution of the latter. Nevertheless, the decadal decrease of CFC-11 is well observable in these time series at all altitudes over the entire measuring period. Furthermore, the annual cycle is clearly visible, and it is in opposite phase in the Southern versus the Northern Hemisphere, following the local season. In

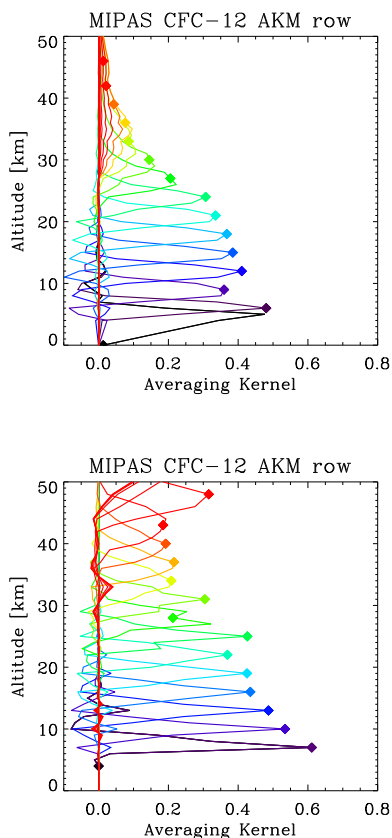


Fig. 3. Rows of averaging kernels of CFC-12 measurements for FR nominal mode (top) and RR (bottom) nominal measurement modes. Diamonds represent the nominal altitudes (i.e. the diagonal value of the averaging kernel matrix). Only every third kernel is shown.

the stratosphere, minimum mixing ratios are found in the polar winter, due to the subsidence of old air depleted of CFCs. In the troposphere, there is a polar summer minimum, consistent with the seasonal cycle seen in in-situ and flask data published by Butler et al. (1998). All time series show, as expected, the maxima of the CFC-11 volume mixing ratios in the tropical and subtropical zone between 30°S to 30°N . The region of large CFC-11 amounts, however, is not symmetrical around the equator but shifted by a couple of degrees to northern latitudes. The stratospheric mixing barrier, discernable by the region of the largest CFC-11 zonal gradient at 15 hPa, 20 hPa, 50 hPa, and 70 hPa varies with season

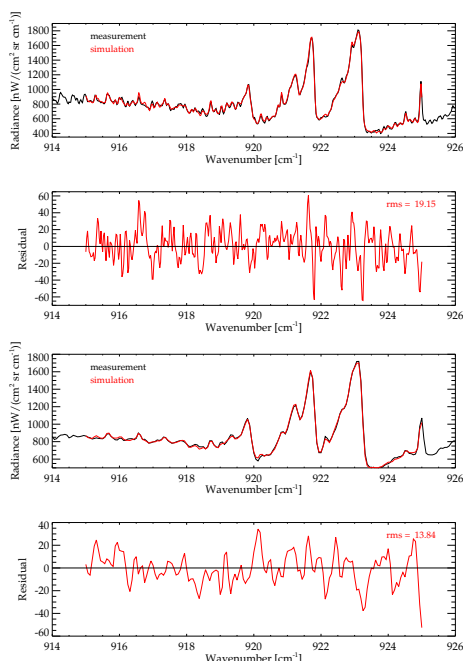


Fig. 4. Typical measured (black) and calculated (in red) spectra of CFC-12 and the fit residual in 11 km in the $915.0\text{--}925.0\text{ cm}^{-1}$ spectral region for the FR (top) and the RR (bottom) spectral resolution nominal modes.

between 20° , 25° , 30° and 40° , respectively, in the Northern Hemisphere, compared to 12° , 15° , 20° and 30° in the Southern Hemisphere. A difference between hemispheres was also found by Palazzi et al. (2011). At 15 hPa, 20 hPa and 50 hPa a clear signal of the quasi-biennial oscillation (QBO) is visible.

4.2 CFC-12 observations

Figure 8 shows monthly zonal mean CFC-12 mixing ratio distributions between 200 hPa and 1 hPa of CFC-12 in September 2002, December 2003, March 2008, and June 2010. The structures are similar to those of CFC-11 but the CFC-12 survives the transport into higher altitudes in the ascending branch of the Brewer-Dobson circulation, because it is more stable under sunlit conditions. Also for CFC-12 a decrease with time is observable, but it is much less pronounced than that of CFC-11. This is because the decomposition of CFC-12 in the atmosphere is slower than that of CFC-11. The lifetime of CFC-12 in the stratosphere of about

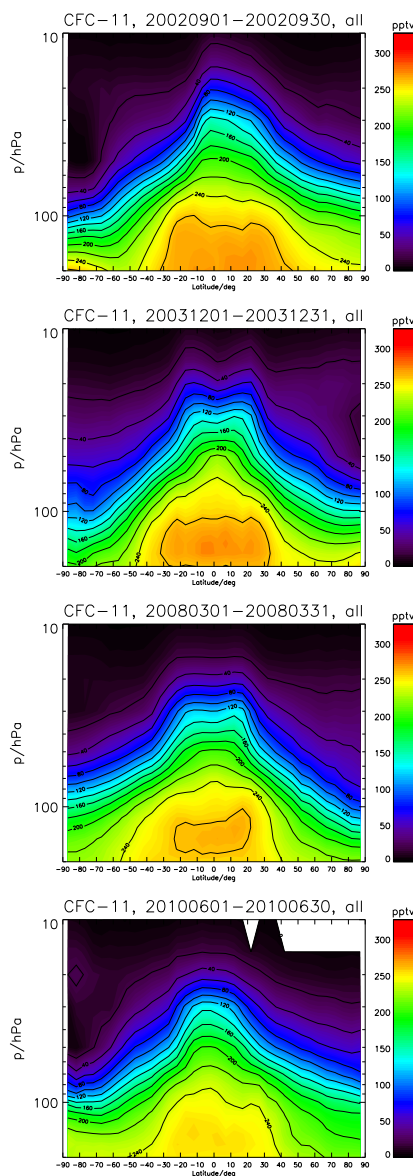


Fig. 5. CFC-11 monthly zonal mean distribution between 200 hPa and 10 hPa in September 2002, December 2003, March 2008, and June 2010.

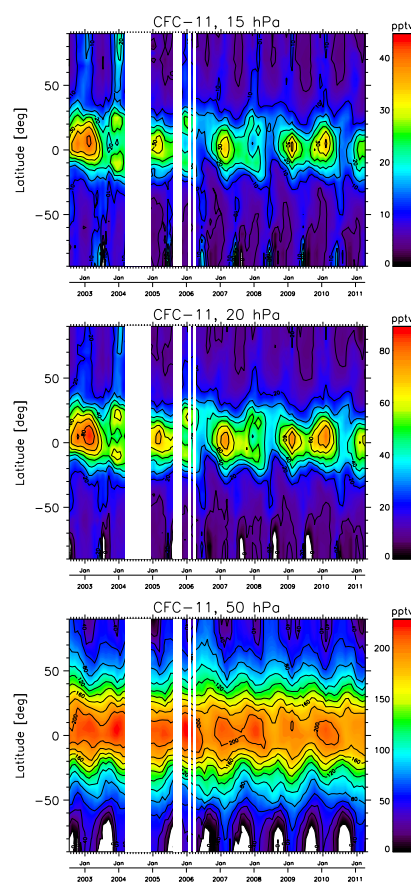


Fig. 6. Time series of CFC-11 as a function of latitude between July 2002 and April 2011 in 15 hPa, 20 hPa and 50 hPa. Note there is no MIPAS data available between April and December 2004. The white spots in the southern polar region indicate data gaps due to the existence of not detected polar stratospheric clouds, because no retrievals are possible below cloud top altitude.

100 yr is larger than that of CFC-11 which is about 45 yr (Cunnold et al., 1997; Volk et al., 1997). Time series (Fig. 9 and Fig. 10) show basically the same features already discussed for CFC-11 (negative trend, annual cycle, QBO, and asymmetry around the equator). Also for CFC-12 there is a bias between FR and RR measurements, most pronounced at lower altitudes.

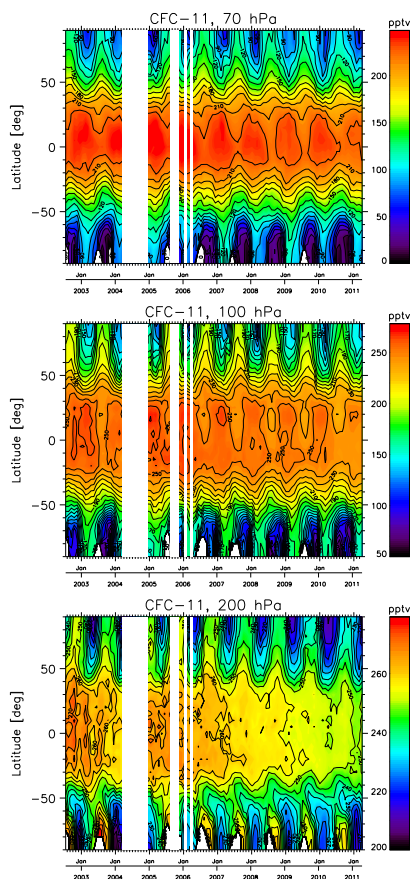


Fig. 7. Time series of CFC-11 as a function of latitude between July 2002 and April 2011 in 70 hPa, 100 hPa and 200 hPa. The increased CFC values in the southern polar regions at 200 hPa are not reliable and indicate not detected clouds.

5 Trends

5.1 Method

Time series of monthly mean CFC-11 and CFC-12 mixing ratios at selected altitudes and for 10° latitude bins have been analyzed by fitting the following regression function to the data (Stiller et al., 2012)

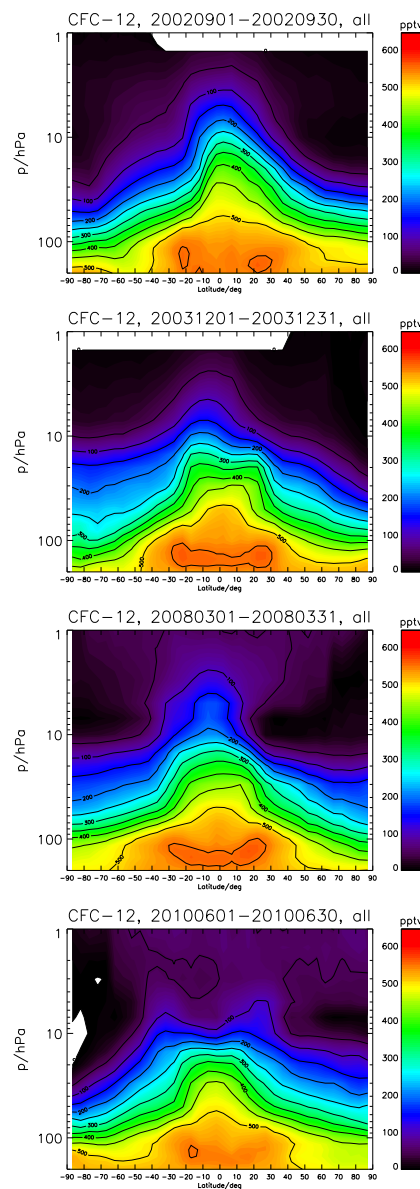


Fig. 8. CFC-12 monthly zonal mean distribution between 200 hPa and 1 hPa in September 2002, December 2003, March 2008, and June 2010.

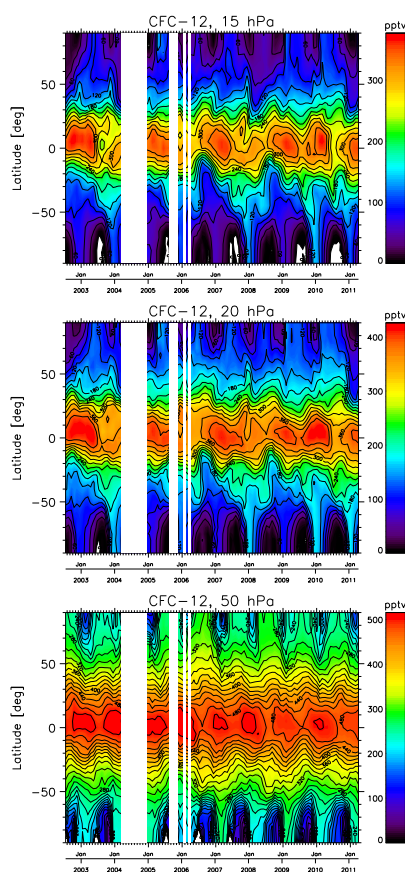


Fig. 9. Time series of CFC-12 as a function of latitude between July 2002 and April 2011 at 15 hPa, 20 hPa and 50 hPa. Details as for Fig. 6.

$$\text{VMR}(t) = a + bt + c_1\text{qbo}_1(t) + d_1\text{qbo}_2(t) + \sum_{n=2}^9 \left(c_n \sin \frac{2\pi t}{l_n} + d_n \cos \frac{2\pi t}{l_n} \right) \quad (1)$$

where t is time, qbo_1 and qbo_2 are quasi-biennial oscillation (QBO) indices. The terms under the sum are 8 sine and cosine functions of the period length l_n , which represent the seasonal and the semi-annual cycle and their “overtones” with period lengths of 3, 4, 8, 9, 18, and 24 months. Sine and cosine of the same period length are

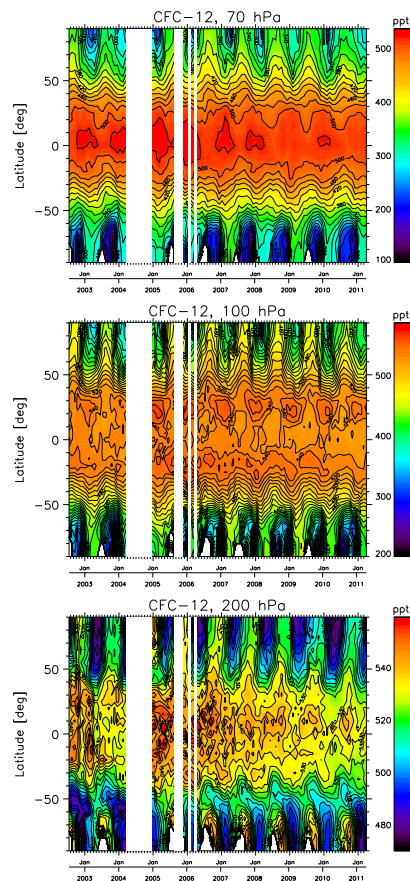


Fig. 10. Time series of CFC-12 as a function of latitude between July 2002 and April 2011 at 70 hPa, 100 hPa and 200 hPa. Details as for Fig. 7.

both fitted to account for any phase shift of the variation. The terms qbo_1 and qbo_2 are the normalized Singapore winds at 30 hPa and 50 hPa. These are provided by the Free University of Berlin via <http://www.geo.fu-berlin.de/met/ag/strat/produkte/qbo/index.html>. As suggested by Kyrölä et al. (2010), we exploit the approximate orthogonality of qbo_1 and qbo_2 to emulate any QBO phase shift by their combination with different weights. Coefficients a , b , c_1 , ..., c_9 , d_1 , ..., d_9 are fitted to the data using the method of von Clarmann et al. (2010), where the full error covariance matrix of mixing ratios is considered, with the squared standard errors of the monthly means as the diagonal terms. In a first step of

the analysis, covariances are only important to consider any bias between the FR and the RR CFC measurements due to the change of the MIPAS measurement modes. Since these biases are thought to be primarily caused by different altitude resolutions, they can depend on altitude and latitude. For each time series at a certain altitude and latitude band, the bias can simply be treated as a fully correlated error component of one data subset. This method is very robust with respect to the estimate of the residual bias used to create the covariance matrix. Consideration of the bias in the covariance matrix has been shown to be equivalent to the inference of the bias from the data themselves with an optimal estimation scheme where the a priori variance of the residual bias equals the residual bias component in our covariance matrix (cf. von Clarmann et al., 2001). From the fit residuals, additional autocorrelated error terms are estimated and added to the initial covariances, as described by Stiller et al. (2012). A second trend fit is performed with the enhanced covariance matrix, which is then used for the scientific analysis.

5.2 Results for CFC-11

Trends of CFC-11 based on monthly zonal mean mixing ratios in 10° latitude bins have been calculated for selected altitudes. Data coverage was good from July 2002 to March 2004 with measurements available for about 16 to 31 days per month. From 2005 to 2007 data coverage was quite inhomogeneous when the number of days for which nominal mode measurements were available varied from 2 to 30 days per month, while since then MIPAS has again been operated at full duty cycle and nearly continuous coverage. Figure 11 shows examples of measured and best fitting time series. A negative trend is obvious in all these examples, as well as the annual variation, and the bias between the data subsets V30_CFC11_10 and V5R_CFC11_220. The minima of mid-latitude measurements occur in local winter (left panels). The amplitude of the annual cycle is largest at polar latitudes. In the tropical time series a clear QBO signal is visible (upper right panel), while the amplitude of the annual cycle is largely reduced compared to higher latitudes.

Liang et al. (2008) report northern and southern hemispheric averaged monthly mean surface CFC-11 and CFC-12 mixing ratios between January 1977 and December 2004 based on measurements of different long-term observations (Prinn et al., 2000; Montzka et al., 1999; Thompson et al., 2004). Their CFC-11 monthly mean values in the year 2002 are about 260 pptv which coincides well with the starting point of our regression line with mixing ratios between 260 to 265 pptv at ~ 10 km altitude. CFC-11 measurements are also provided by the Halocarbons and other Atmospheric Trace Species (HATS) group at NOAA/ESRL (Elkins et al., 2012a). They provide a combined data set from various NOAA/ESRL measurement programs; the method for combining the various NOAA/ESRL measurement programs into one data set is described by Hall et al. (2011). These CFC-

11 measurements for April 2011 are about 240 pptv which agrees very well with our values between 229 and 242 pptv at 10 km altitude (Fig. 11, right middle panel, left and right lower panel).

The inferred trends from 2002–2011 for all latitude/altitude bins are summarized in Fig. 12, along with estimated 1-sigma uncertainties and significance of the trends in terms of multiples of sigma. The estimated uncertainties include the additional autocorrelated error term discussed in Sect. 5.1 and are consistent with the fit residuals in a sense that the reduced χ^2 values are close to unity. In wide parts of the atmosphere highly significant negative trends between -10 and -40 pptv per decade are found. These trends agree well with the tropospheric trends of about -25 pptv per decade in the same period measured by the HATS group (Elkins et al., 2012a) and the data reported by Butler et al. (1998) (-23 pptv per decade), of which the extension to current dates can be found on <http://www.esrl.noaa.gov/gmd/hats/graphs/graphs.html>.

Differences between the MIPAS percentage trends and the age-corrected tropospheric trends are shown in Fig. 13. Age of air has been taken from Stiller et al. (2012). We would like to stress that we do not necessarily expect the stratospheric trends to reproduce the tropospheric ones with a time lag depending on the age of stratospheric air, because stratospheric circulation could change, affecting the time lag and possibly the level of depletion of the air observed. For an atmosphere without changes in stratospheric dynamics and delta-shaped age spectra, the differences shown in Fig. 13 are expected to be zero throughout. However we find positive and negative trend differences of several ten percent. The positive trend values between 10 – 90° S in the stratosphere between about 22 km and 30 km altitude can be explained by air with broad age spectra, containing particularly old air which has entered the stratosphere prior to about 1993 when tropospheric CFC-11 concentrations reached their maximum. The mean age alone, which is about 5 yr in this altitude/latitude-range (Stiller et al., 2012) cannot explain the positive trend. In the upper northern hemispheric stratosphere, trends are more negative than expected from the tropospheric trends corrected for the age of air. This is the region where Stiller et al. (2012) have found a pronounced increase in the age of stratospheric air, which, however, cannot alone explain the larger negative trends. Instead, changing circulation and/or mixing patterns which heavily affect the shape of the age spectra may be able to explain both, the increase of age of air and the stronger negative CFC-11 trends. However, a fully consistent explanation is not yet available.

5.3 Results for CFC-12

The findings on periodic and quasi-periodic variations of CFC-11 also apply to CFC-12 (Fig. 14). The annual variation and the QBO are well represented by the regression model. In comparison to the CFC-12 mixing ratios of ~ 543 pptv as

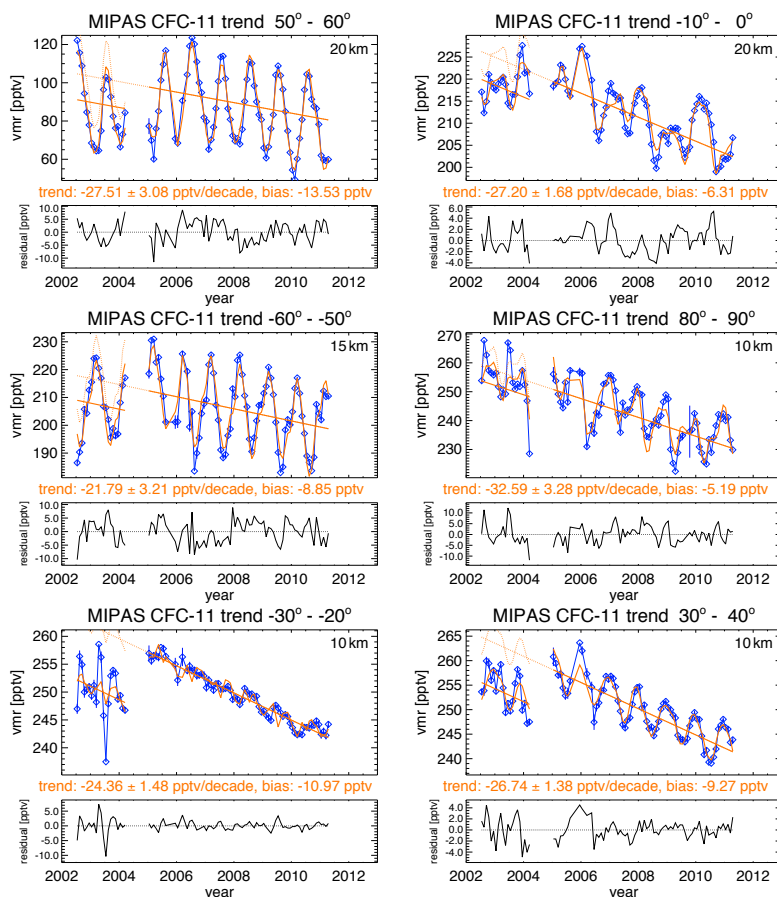


Fig. 11. Temporal evolution of CFC-11 for northern mid-latitudes (50° N to 60° N) at 20 km (top left panel), inner tropics (0° S to 10° N) at 20 km (top right panel), southern mid-latitudes (50° S to 60° S) at 15 km altitude (middle left panel), northern polar latitudes (80° N to 90° N) at 10 km altitude (middle right panel), southern subtropics (20° S to 30° S) at 10 km altitude (lower right panel), and northern mid-latitudes (30° N to 40° N) at 10 km (lower right panel). The blue diamonds are the MIPAS data points; the bold solid orange curve is the fit through the data. The linear part of the regression represented by the straight orange line. The dotted orange curve and straight line are the respective bias-corrected fit and its linear component, respectively. In the lower part of each panel, the residuals between MIPAS CFC-11 monthly zonal means and the trend-corrected regression function are shown. The trend of CFC-11 in pptv per decade, its uncertainty, and the bias between the data subsets FR and RR are printed in orange font.

reported by Liang et al. (2008) for the year 2002 our values at the starting point of the regression line in 2002 are slightly lower with mixing ratios between 524 and 537 pptv. The HATS group reports mixing ratios for a CFC-12 data set combined from various NOAA/ESRL measurement programs of about 528 pptv for April 2011 (Elkins et al., 2012b),

which is slightly higher than the MIPAS data at the end of the regression line where mixing ratios vary with latitude between 506 and 508 pptv (Fig. 14, right middle panel, left and right lower panel).

A survey of the inferred trends is given in Fig. 15. The patterns of positive and negative trends of CFC-12 are similar

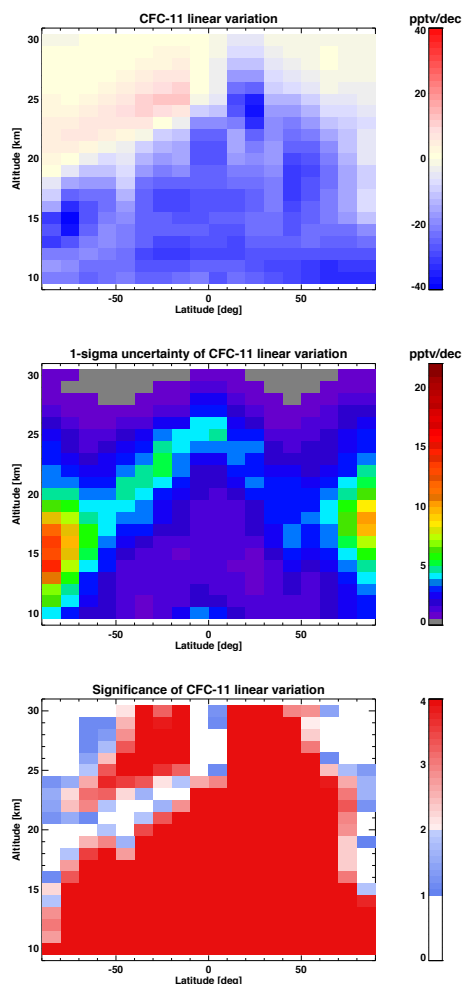


Fig. 12. CFC-11 trends over the years 2002 to 2011 as a function of altitude and latitude in pptv per decade (top); 1-sigma trend uncertainties (middle); and significance of the trend in terms of multiples of sigma (bottom). Numerical values are found in the Supplement.

to those of CFC-11 but are better visible. In the troposphere and in the lower stratosphere where relatively young air is observed consistently (Waugh and Hall, 2002; Stiller et al., 2012), the trends are negative throughout, with typical values around -20 pptv per decade, which again is in agreement with tropospheric trend measurements by Elkins et al.

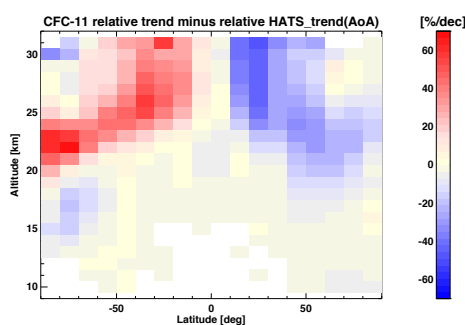


Fig. 13. Differences of relative trends between MIPAS and HATS data under consideration of the age of air over the years 2002 to 2011 as a function of altitude and latitude in % per decade for CFC-11. The data gaps are due to missing age of air data. Numerical values are found in the Supplement.

(2012a) and the extension of the record by Butler et al. (1998). Particularly large negative trends are observed in the middle northern hemispheric stratosphere, with largest negative values at $20\text{--}30^\circ\text{N}$, 25 km altitude. Similar to CFC-11, these negative trends are larger than the age corrected tropospheric trends (Fig. 16), and occur again in the region where Stiller et al. (2012) found the increase in mean age of air. Similar to CFC-11, we suggest that changing circulation and/or mixing patterns affect the shape of age spectra and may lead to steepening of the trends relative to the tropospheric ones. Above this region (above 20–30 km altitude at latitudes from $90\text{--}20^\circ\text{N}$, respectively), slightly positive trends have been found. With an age of approximately 6 yr, the starting point of the time series (2002) refers to tropospheric air in 1996, when CFC-12 was still increasing. For the positive trends in the middle southern hemispheric stratosphere the same explanation as for CFC-11 applies. The effect is, however, more pronounced for CFC-12, because its tropospheric maximum was reached later. Of course there are also other possible explanations for differences between stratospheric and tropospheric CFC-trends, e.g. decadal variations of subsidence or mixing of CFC-depleted air from higher altitudes. All plausible explanations, however, imply decadal changes in stratospheric dynamics.

6 Conclusions

Global altitude-resolved zonal mean distributions of stratospheric CFC-11 and CFC-12 were inferred from MIPAS measurements. Altitude- and latitude resolved time series show the expected annual cycle (strongest at high latitudes) and QBO signal (strongest in the tropics). As expected as response to the Montreal Protocol, at most altitudes and

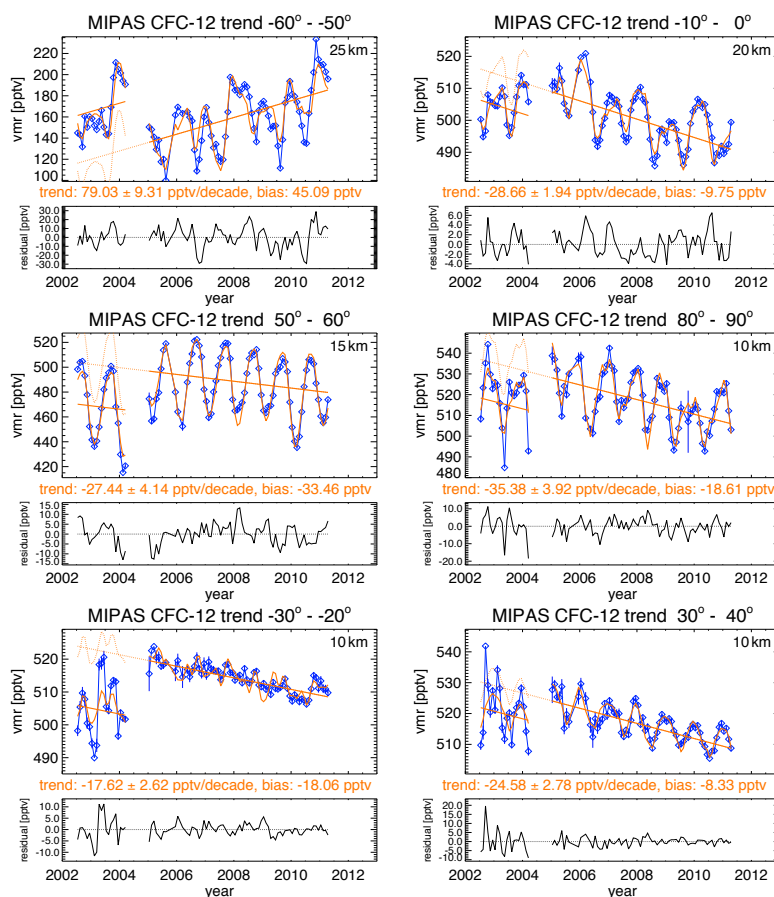


Fig. 14. Temporal evolution of CFC-12 for southern mid-latitudes (50° S to 60° S) at 25 km (top left panel), inner tropics (0° S to 10° S) at 20 km (top right panel), northern mid-latitudes (50° N to 60° N) at 15 km altitude (middle left panel), and northern polar latitudes (80° N to 90° N) at 10 km altitude (middle right panel) southern subtropics (20° S to 30° S) at 10 km altitude (lower right panel), and northern mid-latitudes (30° N to 40° N) at 10 km (lower right panel). Details as for Fig. 11.

latitudes negative trends are observed, which are on average consistent to the trends of tropospheric CFC-11 and CFC-12 mixing ratios. However, the CFC trends in the stratosphere vary with altitude and latitude, and in some regions even positive trends are observed. Generally speaking, trends are mostly negative where age trends as reported by Stiller et al. (2012) are positive and vice versa, but this picture is not fully consistent. All plausible explanations for the observed CFC-trends involve some kind of decadal change in stratospheric dynamics. Either substantial changes in the shape of the age

spectra or changes in vertical mixing patterns are needed to solve the apparent contradiction. The use of these MIPAS CFC-measurements for a quantitative analysis of stratospheric age-of-air spectra under consideration of their altitude and latitude dependent lifetimes will be a major focus for our research in the next years.

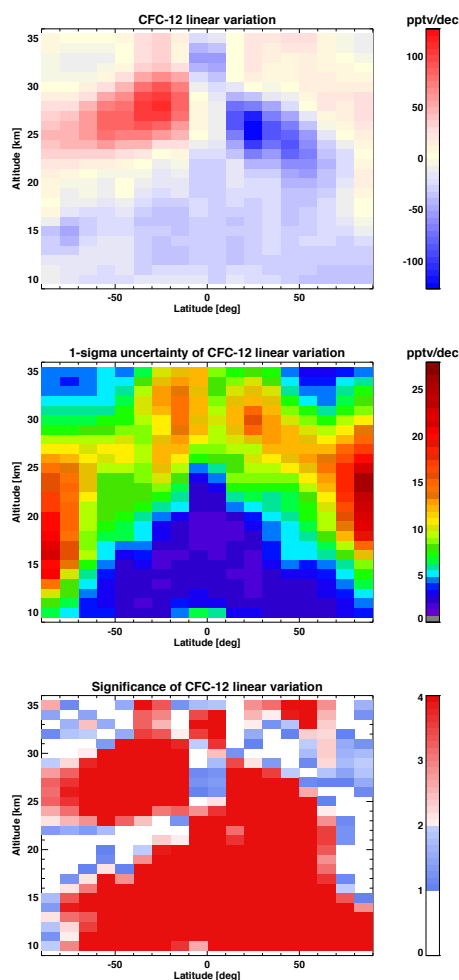


Fig. 15. CFC-12 trends over the years 2002 to 2011 as a function of altitude and latitude in pptv per decade (top); 1-sigma trend uncertainties (middle); and significance of the trend in terms of multiples of sigma (bottom). Numerical values are found in the Supplement.

IMK/IAA generated MIPAS/Envisat data can be obtained by registered users from the data server: <http://www.imk-asf.kit.edu/english/308.php>.

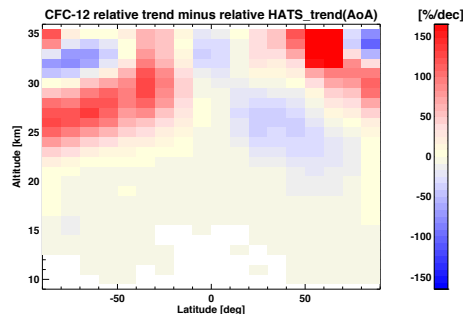


Fig. 16. As for Fig. 13 but for CFC-12. Numerical values are found in the Supplement.

Supplementary material related to this article is available online at: <http://www.atmos-chem-phys.net/12/11857/2012/acp-12-11857-2012-supplement.zip>.

Acknowledgements. ESA has provided MIPAS Level-1B data. Meteorological analysis data have been provided by ECMWF. Development of CFC-11 and CFC-12 data retrieval was partly funded by the German Federal Ministry of Education and Research (BMBF) under contract no. 50EE0901. We acknowledge support by Deutsche Forschungsgemeinschaft and Open Access Publishing Fund of Karlsruhe Institute of Technology. Partial support for NOAA/ESRL ground based measurements is from the Atmospheric Composition and Climate Program of NOAA's Climate Program Office.

The service charges for this open access publication have been covered by a Research Centre of the Helmholtz Association.

Edited by: J. B. Burkholder

References

- Bingham, G. E., Zhou, D. K., Bartschi, B. Y., Anderson, G. P., Smith, D. R., Chetwynd, J. H., and Nadile, R. M.: Cryogenic Infrared Radiance Instrumentation for Shuttle (CIRRIS 1A) Earth limb spectral measurements, calibration, and atmospheric O_3 , HNO_3 , CFC-12, and CFC-11 profile retrieval, *J. Geophys. Res.*, 102, 3547–3558, 1997.
- Brasunas, J. C., Kunde, V. G., Hanel, R. A., Walser, D., Herath, L. W., Buijs, H. L., Bérubé, J. N., and McKinnon, J.: Balloon-borne cryogenic spectrometer for measurement of lower stratospheric trace constituents, in: *Proc. SPIE*, vol. 619, 80–88, SPIE, Bellingham, WA, USA, 1986.
- Brown, A. T., Chipperfield, M. P., Boone, C., Wilson, C., Walker, K. A., and Bernath, P. F.: Trends in atmospheric halogen contain-

S. Kellmann et al.: Global CFC-11 and CFC-12 measurements with MIPAS

11873

- ing gases since 2004, *J. Quant. Spectrosc. Radiat. Transfer*, 112, 2552–2566, doi:10.1016/j.jqsrt.2011.07.005, 2011.
- Bujok, O., Tan, V., Klein, E., Nopper, R., Bauer, R., Engel, A., Gerhards, M.-T., Afchine, A., McKenna, D. S., Schmidt, U., Wienhold, F. G., and Fischer, H.: GHOST – A Novel Airborne Gas Chromatograph for In Situ Measurements of Long-Lived Tracers in the Lower Stratosphere: Method and Applications, *J. Atmos. Chem.*, 39, 37–64, 2001.
- Butler, J. H., Montzka, S. A., Clarke, A. D., Lobert, J. M., and Elkins, J. W.: Growth and distribution of halons in the atmosphere, *J. Geophys. Res.*, 103, 1503–1511, 1998.
- Carlotti, M.: Global-fit approach to the analysis of limb-scanning atmospheric measurements, *Appl. Opt.*, 27, 3250–3254, 1988.
- Cunnold, D. M., Weiss, R. F., Prinn, R. G., Hartley, D., Simmonds, P. G., Fraser, P. J., Miller, B., Alyea, F. N., and Porter, L.: GAGE/AGAGE measurements indicating reductions in global emissions of CCl_3F and CCl_2F_2 in 1992–1994, *J. Geophys. Res.*, 102, 1259–1269, 1997.
- D’Amico, G., Snels, M., Hollenstein, H., and Quack, M.: Analysis of the $\nu_3 + \nu_7$ combination band of CF_2Cl_2 from spectra obtained by high resolution diode laser and FTIR supersonic jet techniques, *Phys. Chem. Chem. Phys.*, 4, 1531–1536, doi:10.1039/B110919G, 2002.
- Dinelli, B. M., Arnone, E., Brizzi, G., Carlotti, M., Castelli, E., Magnani, L., Papandrea, E., Prevedelli, M., and Ridolfi, M.: The MIPAS2D database of MIPAS/ENVISAT measurements retrieved with a multi-target 2-dimensional tomographic approach, *Atmos. Meas. Tech.*, 3, 355–374, doi:10.5194/amt-3-355-2010, 2010.
- Dudhia, A.: <http://www.atm.ox.ac.uk/group/mipas/rmodes.html>, last access: 16 July 2012.
- Elkins, J. W., Montzka, S. A., Hall, B., and Dutton, G.: Combined Chlorofluorocarbon-11 data from the NOAA/ESRL global monitoring division, <http://www.esrl.noaa.gov/gmd/hats/combined/CFC11.html>, National Oceanic & Atmospheric Administration, Earth System Research Laboratory, Global Monitoring Division, Dept. of Commer., Boulder, CO, USA, 2012a.
- Elkins, J. W., Montzka, S. A., Hall, B., and Dutton, G.: Combined Chlorofluorocarbon-12 data from the NOAA/ESRL global monitoring division, <http://www.esrl.noaa.gov/gmd/hats/combined/CFC12.html>, National Oceanic & Atmospheric Administration, Earth System Research Laboratory, Global Monitoring Division, Dept. of Commer., Boulder, CO, USA, 2012b.
- Endemann, M. and Fischer, H.: Envisat’s High-Resolution Limb Sounder: MIPAS, *ESA bulletin*, 76, 47–52, 1993.
- Endemann, M., Gare, P., Smith, D., Hoerning, K., Fladt, B., and Gessner, R.: MIPAS Design Overview and Current Development Status, in: Proceedings EUROPTO series, Optics in Atmospheric Propagation, adaptive systems, and Lidar techniques for Remote Sensing, Taormina, Italy, 24–26 September 1996, vol. 2956, 124–135, 1996.
- Engel, A., Schmidt, U., and McKenna, D.: Stratospheric trends of CFC-12 over the past two decades: Recent observational evidence of declining growth rates, *Geophys. Res. Lett.*, 25, 3319–3322, 1998.
- European Space Agency: Envisat, MIPAS An instrument for atmospheric chemistry and climate research, ESA Publications Division, ESTEC, P.O. Box 299, 2200 AG Noordwijk, The Netherlands, SP-1229, 2000.
- Fischer, H. and Oelhaf, H.: Remote sensing of vertical profiles of atmospheric trace constituents with MIPAS limb-emission spectrometers, *Appl. Opt.*, 35, 2787–2796, 1996.
- Fischer, H., Birk, M., Blom, C., Carli, B., Carlotti, M., von Clarmann, T., Delbouille, L., Dudhia, A., Ehhalt, D., Endemann, M., Flaud, J. M., Gessner, R., Kleinert, A., Koopman, R., Langen, J., López-Puertas, M., Mosner, P., Nett, H., Oelhaf, H., Perron, G., Remedios, J., Ridolfi, M., Stiller, G., and Zander, R.: MIPAS: an instrument for atmospheric and climate research, *Atmos. Chem. Phys.*, 8, 2151–2188, doi:10.5194/acp-8-2151-2008, 2008.
- Flaud, J.-M., Piccolo, C., Carli, B., Perrin, A., Coudert, L. H., Teffo, J.-L., and Brown, L. R.: Molecular line parameters for the MIPAS (Michelson Interferometer for Passive Atmospheric Sounding) experiment, *Atmos. Oceanic Opt.*, 16, 172–182, 2003.
- Goldman, A., Bonomo, F. S., and Murcray, D. G.: Statistical-band-model analysis and integrated intensity of the $10.8 \mu\text{m}$ band of CF_2Cl_2 , *Geophys. Res. Lett.*, 3, 309–312, 1976.
- Hall, B. D., Dutton, G. S., Mondeel, D. J., Nance, J. D., Rigby, M., Butler, J. H., Moore, F. L., Hurst, D. F., and Elkins, J. W.: Improving measurements of SF₆ for the study of atmospheric transport and emissions, *Atmos. Meas. Tech.*, 4, 2441–2451, doi:10.5194/amt-4-2441-2011, 2011.
- Hegglin, M. and Tegtmeier, S.: The SPARC Data Initiative, *SPARC Newsletter*, 36, 22–23, 2011.
- Heidt, L. E., Lueb, R., Pollock, W., and Ehhalt, D. H.: Stratospheric Profiles of CCl_3F and CCl_2F_2 , *Geophys. Res. Lett.*, 2, 445–447, doi:10.1029/GL002i010p00445, 1975.
- Hoffmann, L., Kaufmann, M., Spang, R., Müller, R., Remedios, J. J., Moore, D. P., Volk, C. M., von Clarmann, T., and Riese, M.: Envisat MIPAS measurements of CFC-11: retrieval, validation, and climatology, *Atmos. Chem. Phys.*, 8, 3671–3688, doi:10.5194/acp-8-3671-2008, 2008.
- Höpfner, M., von Clarmann, T., Engelhardt, M., Fischer, H., Funke, B., Glatthor, N., Grabowski, U., Kellmann, S., Kiefer, M., Linden, A., López-Puertas, M., Milz, M., Steck, T., Stiller, G. P., Wang, D. Y., Ruhnke, R., Kouker, W., Reddmann, T., Bernath, P., Boone, C., and Walker, K. A.: Comparison between ACE-FTS and MIPAS IMK/IAA profiles of O_3 , H_2O , N_2O , CH_4 , CFC-11, CFC-12, HNO_3 , ClONO_2 , NO_2 , N_2O_5 , CO , and SF₆ in February/March 2004, in: Proc. Third Workshop on the Atmospheric Chemistry Validation of Envisat, (ACVE-3), 4–7 December, 2006, ESRIN, Frascati, Italy, vol. ESA SP-642, CD-ROM, ESA Publications Division, ESTEC, Postbus 299, 2200 AG Noordwijk, The Netherlands, 2007.
- Khosravi, R., Lambert, A., Lee, H., Gille, J., Barnett, J., Francis, G., Edwards, D., Halvorson, C., Massie, S., Craig, C., Krinsky, C., McInerney, J., Stone, K., Eden, T., Nardi, B., Hepplewhite, C., Mankin, W., and Coffey, M.: Overview and characterization of retrievals of temperature, pressure, and atmospheric constituents from the High Resolution Dynamics Limb Sounder (HIRDLS) measurements, *J. Geophys. Res.*, 114, D20304, doi:10.1029/2009JD011937, 2009.
- Khosravi, F., Müller, R., Irie, H., Engel, A., Toon, G. C., Sen, B., Aoki, S., Nakazawa, T., Traub, W. A., Jucks, K. W., Johnson, D. G., Oelhaf, H., Wetzel, G., Sugita, T., Kanzawa, H., Yokota, T., Nakajima, H., and Sasano, Y.: Validation of CFC-12 measurements from the Improved Limb Atmospheric Spectrometer (ILAS) with the version 6.0 retrieval algorithm, *J. Geophys. Res.*, 109, D06311, doi:10.1029/2003JD004325, 2004.

- Kiefer, M., Arnone, E., Dudhia, A., Carlotti, M., Castelli, E., von Clarmann, T., Dinelli, B. M., Kleinert, A., Linden, A., Milz, M., Papandrea, E., and Stiller, G.: Impact of temperature field inhomogeneities on the retrieval of atmospheric species from MIPAS IR limb emission spectra, *Atmos. Meas. Tech.*, 3, 1487–1507, doi:10.5194/amt-3-1487-2010, 2010.
- Ko, M., Newman, P., Reinmann, S., and Strahan, S. E.: Lifetime of halogen source gases, available at: <http://sparclima.vs89.snowflakehosting.ch/activities/lifetime-halogen-gases/>, last access: 16 July 2012.
- Ko, M. K. W. and Sze, N. D.: A 2-D model calculation of atmospheric lifetimes for N₂O, CFC-11 and CFC-12, *Nature*, 297, 317–319, 1982.
- Kunde, V. G., Brasunas, J. C., Conrath, B. J., Hanel, R. A., Herman, J. R., Jennings, D. E., Maguire, W. C., Walser, D. W., Annen, J. N., Silverstein, M. J., Abbas, M. M., Herath, L. W., Buijs, H. L., Berube, H. L., and McKinnon, J.: Infrared spectroscopy of the lower stratosphere with a balloon-borne cryogenic Fourier spectrometer, *Appl. Opt.*, 26, 545–553, 1987.
- Kyrölä, E., Tamminen, J., Sofieva, V., Bertaux, J. L., Hauchecorne, A., Dalaudier, F., Fussen, D., Vanhellefont, F., Fanton d'Andon, O., Barrot, G., Guirlet, M., Fehr, T., and Saavedra de Miguel, L.: GOMOS O₃, NO₂, and NO₃ observations in 2002–2008, *Atmos. Chem. Phys.*, 10, 7723–7738, doi:10.5194/acp-10-7723-2010, 2010.
- Liang, Q., Stolarski, R. S., Douglass, A. R., Newman, P. A., and Nielsen, J. E.: Evaluation of emissions and transport of CFCs using surface observations and their seasonal cycles and the GEOS CCM simulation with emissions-based forcing, *J. Geophys. Res.*, 113, D14302, doi:10.1029/2007JD009617, 2008.
- Lovelock, J. E.: Atmospheric fluorine compounds as indicators of air movements, *Nature*, 230, 379, doi:10.1038/230379a0, 1971.
- Lueb, R. A., Ehhalt, D. H., and Heidt, L. E.: Balloon-borne low temperature air sampler, *Rev. Sci. Instr.*, 46, 702–705, 1975.
- Mahieu, E., Duchatelet, P., Demoulin, P., Walker, K. A., Dupuy, E., Froidevaux, L., Randall, C., Catoire, V., Strong, K., Boone, C. D., Bernath, P. F., Blavier, J.-F., Blumenstock, T., Coffey, M., De Mazière, M., Griffith, D., Hannigan, J., Hase, F., Jones, N., Jucks, K. W., Kagawa, A., Kasai, Y., Mebarki, Y., Mikuteit, S., Nassar, R., Notholt, J., Rinsland, C. P., Robert, C., Schrems, O., Senten, C., Smale, D., Taylor, J., Tétard, C., Toon, G. C., Warneke, T., Wood, S. W., Zander, R., and Servais, C.: Validation of ACE-FTS v2.2 measurements of HCl, HF, CCl₃F and CCl₂F₂ using space-, balloon- and ground-based instrument observations, *Atmos. Chem. Phys.*, 8, 6199–6221, doi:10.5194/acp-8-6199-2008, 2008.
- McNaughton, D., McGilvery, D., and Robertson, E. G.: High-resolution FTIR-jet spectroscopy of CCl₂F₂, *J. Chem. Soc., Faraday Trans.*, 90, 1055–1060, doi:10.1039/FT9949001055, 1994.
- McNaughton, D., McGilvery, D., and Robertson, E. G.: High resolution FTIR spectroscopy of CFC's in a supersonic jet expansion, *J. Mol. Struct.*, 348, 1–4, 1995.
- Molina, M. J. and Rowland, F. S.: Stratospheric sink for chlorofluoromethanes: Chlorine atom-catalysed destruction of ozone, *Nature*, 249, 810–812, 1974.
- Montzka, S. A., Butler, J. H., Elkins, J. W., Thompson, T. M., Clarke, A. D., and Lock, L. T.: Present and future trends in the atmospheric burden of ozone-depletion halogens, *Nature*, 398, 690–694, 1999.
- Moore, D. P., Waterfall, A. M., and Remedios, J. J.: The potential for radiometric retrievals of halocarbon concentrations from the MIPAS-E instrument, *Adv. Space Res.*, 37, 2238–2246, doi:10.1026/j.asr.2005.06.058, 2006.
- Murcray, D. G., Bonomo, F. S., Brooks, J. N., Goldman, A., Murcray, F. H., and Williams, W. J.: Detection of fluorocarbons in the stratosphere, *Geophys. Res. Lett.*, 2, 109–112, 1975.
- Nett, H., Carli, B., Carlotti, M., Dudhia, A., Fischer, H., Flaud, J.-M., Perron, G., Raspollini, P., and Ridolfi, M.: MIPAS Ground Processor and Data Products, in: Proc. IEEE 1999 International Geoscience and Remote Sensing Symposium, 28 June–2 July 1999, Hamburg, Germany, 1692–1696, 1999.
- Norton, H. and Beer, R.: New apodizing functions for Fourier spectrometry, *J. Opt. Soc. Am.*, 66, 259–264, (Errata *J. Opt. Soc. Am.*, 67, 419, 1977), 1976.
- Orphal, J.: Bestimmung von Linienparametern in der ν₈-Bande von CF₂Cl₂ (CFC-12) mittels hochauflösender Diodenlaserspektroskopie, Master's thesis, Humboldt-Universität zu Berlin, 1991.
- Palazzi, E., Fierli, F., Stiller, G. P., and Urban, J.: Probability density functions of long-lived tracer observations from satellite in the subtropical barrier region: data intercomparison, *Atmos. Chem. Phys.*, 11, 10579–10598, doi:10.5194/acp-11-10579-2011, 2011.
- Prinn, R. G., Weiss, R. F., Fraser, P. J., Simmonds, P. G., Cunnold, D. M., Alyea, F. N., O'Doherty, S., Salameh, P., Miller, B. R., Huang, J., Wang, R. H. J., Hartley, D. E., Harth, C., Steele, L. P., Sturrock, G., Midgley, P. M., and McCulloch, A.: A history of chemically and radiatively important gases in air deduced from ALE/GAGE/AGAGE, *J. Geophys. Res.*, 105, 17751–17792, doi:10.1029/2000JD900141, 2000.
- Rinsland, C. P., Mahieu, E., Zander, R., Jones, N. B., Chipperfield, M. P., Goldman, A., Anderson, J., Russell III, J. M., Demoulin, P., Notholt, J., Toon, G. C., Blavier, J.-F., Sen, B., Sussmann, R., Wood, S. W., Meier, A., Griffith, D. W. T., Chiou, L. S., Murcray, F. J., Stephen, T. M., Hase, F., Mikuteit, S., Schulz, A., and Blumenstock, T.: Long-term trends of inorganic chlorine from ground-based infrared solar spectra: Past increases and evidence for stabilization, *J. Geophys. Res.*, 108, 4252, doi:10.1029/2002JD003001, 2003.
- Rinsland, C. P., Goldman, A., Mahieu, E., Zander, R., Chiou, L. S., Hannigan, J. W., Wood, S. W., and Elkins, J. W.: Long-Term Evolution in the Tropospheric Concentration of CCl₂F₂ (chlorofluorocarbon 12) Derived from High Spectral Resolution Infrared Solar Absorption Spectra: Retrieval and Comparison with in situ Surface Measurements, *J. Quant. Spectrosc. Radiat. Transfer*, 92, 201–209, doi:10.1016/j.jqsrt.2004.07.022, 2005.
- Robinson, E., Rasmussen, R. A., Krasnec, J., Pierotti, D., and Jakubovic, M.: Halocarbon measurements in the Alaskan troposphere and lower stratosphere, *Atmos. Environ.*, 11, 215–223, 1977.
- Roche, A. E., Kumer, J. B., Mergenthaler, J. L., Ely, G. A., Uplinger, W. G., Potter, J. F., James, T. C., and Sterritt, L. W.: The Cryogenic Limb Array Etalon Spectrometer CLAES on UARS: Experiment Description and Performance, *J. Geophys. Res.*, 98, 10763–10775, 1993.
- Romashkin, P. A., Hurst, D. F., Elkins, J. W., Dutton, G. S., Fahey, D. W., Dunn, R. E., Moore, F. L., Myers, R. C., and Hall, B. D.: In Situ Measurements of Long-Lived Trace Gases in the Lower

S. Kellmann et al.: Global CFC-11 and CFC-12 measurements with MIPAS

11875

- Stratosphere by Gas Chromatography, *J. Atmos. Oceanic Technol.*, 18, 1195–1204, 2001.
- Rothman, L. S., Rinsland, C. P., Goldman, A., Massie, T., Edwards, D. P., Flaud, J.-M., Perrin, A., Camy-Peyret, C., Dana, V., Mandin, J.-Y., Schroeder, J., McCann, A., Gamache, R. R., Wattson, R. B., Yoshino, K., Chance, K. V., Jucks, K. W., Brown, L. R., Nemtchinov, V., and Varanasi, P.: The HITRAN molecular spectroscopic database and HAWKS (HITRAN Atmospheric Workstation): 1996 Edition, *J. Quant. Spectrosc. Radiat. Transfer*, 60, 665–710, 1998.
- Spang, R., Riese, M., and Offermann, D.: CFC11 Measurements by CRISTA, *Adv. Space Res.*, 19, 575–578, 1997.
- Steck, T.: Methods for determining regularization for atmospheric retrieval problems, *Appl. Opt.*, 41, 1788–1797, 2002.
- Stiller, G. P., ed.: The Karlsruhe Optimized and Precise Radiative Transfer Algorithm (KOPRA), vol. FZKA 6487 of *Wissenschaftliche Berichte*, Forschungszentrum Karlsruhe, 2000.
- Stiller, G. P., von Clarmann, T., Funke, B., Glatthor, N., Hase, F., Höpfner, M., and Linden, A.: Sensitivity of trace gas abundances retrievals from infrared limb emission spectra to simplifying approximations in radiative transfer modelling, *J. Quant. Spectrosc. Radiat. Transfer*, 72, 249–280, 2002.
- Stiller, G. P., von Clarmann, T., Haenel, F., Funke, B., Glatthor, N., Grabowski, U., Kellmann, S., Kiefer, M., Linden, A., Losow, S., and López-Puertas, M.: Observed temporal evolution of global mean age of stratospheric air for the 2002 to 2010 period, *Atmos. Chem. Phys.*, 12, 3311–3331, doi:10.5194/acp-12-3311-2012, 2012.
- Thompson, T. M., Butler, J. H., Daube, B. C., Dutton, G. S., Elkins, J. W., Hall, B. D., Hurst, D. F., King, D. B., Kline, E. S., Lafleur, B. G., Lind, J., Lovitz, S., Mondeel, D. J., Montzka, S. A., Moore, F. L., Nance, J. D., Neu, J. L., Romashkin, P. A., Scheffer, A., and Snible, W. J.: Halocarbons and other atmospheric trace species, in: Summary Rep. 27 2002–2003, edited by: Schnell, R. C., 115–135, *Clim. Monit. Diagn. Lab.*, Dept. of Commer., Boulder, CO, USA, 2004.
- Tikhonov, A.: On the solution of incorrectly stated problems and method of regularization, *Dokl. Akad. Nauk. SSSR*, 151, 501–504, 1963.
- Toon, G. C., Farmer, C. B., Shaper, P. W., Lowes, L. L., Norton, R. H., Schoeberl, M. R., Lait, L. R., and Newman, P. A.: Evidence for Subsidence in the 1989 Arctic Winter Stratosphere from Airborne Infrared Composition Measurements, *J. Geophys. Res.*, 97, 7963–7970, 1992.
- Toon, G. C., Blavier, J.-F., Sen, B., and Drouin, B. J.: Atmospheric CO₂ measured by solar occultation spectrometry, *Geophys. Res. Lett.*, 28, 2835–2838, 2001.
- Varanasi, P.: Absorption Coefficients of CFC-11 and CFC-12 needed for Atmospheric Remote Sensing and Global Warming Studies, *J. Quant. Spectrosc. Radiat. Transfer*, 48, 205–219, 1992.
- Varanasi, P. and Nemtchinov, V.: Thermal Infrared Absorption Coefficients of CFC-12 at Atmospheric Conditions, *J. Quant. Spectrosc. Radiat. Transfer*, 51, 679–687, 1994.
- Volk, C. M., Elkins, J. W., Fahey, D. W., Dutton, G. S., Gilligan, J. M., Loewenstein, M., Podolske, J. R., Chan, K. R., and Gunson, M. R.: Evaluation of source gas lifetimes from stratospheric observations, *J. Geophys. Res.*, 102, 25543–25564, doi:10.1029/97JD02215, 1997.
- von Clarmann, T., Grabowski, U., and Kiefer, M.: On the role of non-random errors in inverse problems in radiative transfer and other applications, *J. Quant. Spectrosc. Radiat. Transfer*, 71, 39–46, 2001.
- von Clarmann, T., Ceccherini, S., Doicu, A., Dudhia, A., Funke, B., Grabowski, U., Hilgers, S., Jay, V., Linden, A., López-Puertas, M., Martín-Torres, F.-J., Payne, V., Reburn, J., Ridolfi, M., Schreier, F., Schwarz, G., Siddans, R., and Steck, T.: A blind test retrieval experiment for infrared limb emission spectrometry, *J. Geophys. Res.*, 108, 4746, doi:10.1029/2003JD003835, 2003a.
- von Clarmann, T., Glatthor, N., Grabowski, U., Höpfner, M., Kellmann, S., Kiefer, M., Linden, A., Mengistu Tsidu, G., Milz, M., Steck, T., Stiller, G. P., Wang, D. Y., Fischer, H., Funke, B., Gil-López, S., and López-Puertas, M.: Retrieval of temperature and tangent altitude pointing from limb emission spectra recorded from space by the Michelson Interferometer for Passive Atmospheric Sounding (MIPAS), *J. Geophys. Res.*, 108, 4736, doi:10.1029/2003JD003602, 2003b.
- von Clarmann, T., De Clercq, C., Ridolfi, M., Höpfner, M., and Lambert, J.-C.: The horizontal resolution of MIPAS, *Atmos. Meas. Tech.*, 2, 47–54, doi:10.5194/amt-2-47-2009, 2009a.
- von Clarmann, T., Höpfner, M., Kellmann, S., Linden, A., Chauhan, S., Funke, B., Grabowski, U., Glatthor, N., Kiefer, M., Schieferdecker, T., Stiller, G. P., and Versick, S.: Retrieval of temperature, H₂O, O₃, HNO₃, CH₄, N₂O, ClONO₂ and ClO from MIPAS reduced resolution nominal mode limb emission measurements, *Atmos. Meas. Tech.*, 2, 159–175, doi:10.5194/amt-2-159-2009, 2009b.
- von Clarmann, T., Stiller, G., Grabowski, U., Eckert, E., and Orphal, J.: Technical Note: Trend estimation from irregularly sampled, correlated data, *Atmos. Chem. Phys.*, 10, 6737–6747, doi:10.5194/acp-10-6737-2010, 2010.
- von Clarmann, T., Funke, B., Glatthor, N., Kellmann, S., Kiefer, M., Kirner, O., Sinnhuber, B.-M., and Stiller, G. P.: The MIPAS HOCl climatology, *Atmos. Chem. Phys.*, 12, 1965–1977, doi:10.5194/acp-12-1965-2012, 2012.
- Waugh, D. W. and Hall, T. M.: Age of stratospheric air: theory, observations, and models, *Rev. Geophys.*, 40, 1010, doi:10.1029/2000RG000101, 2002.
- Waugh, D. W., Plumb, R. A., Elkins, J. W., Fahey, D. W., Boering, K. A., Dutton, G. S., Volk, C. M., Keim, E., Gao, R.-S., Daube, B. C., Wofsy, S. C., Loewenstein, M., Podolske, J. R., Chan, K. R., Proffitt, M. H., Kelly, K. K., Newman, P. A., and Lait, L. R.: Mixing of polar vortex air into middle latitudes as revealed by tracer-tracer scatterplots, *J. Geophys. Res.*, 102, 13119–13134, 1997.
- Williams, W. J., Kosters, J. J., Goldman, A., and Murcray, D. G.: Measurements of stratospheric halocarbon distributions using infrared techniques, *Geophys. Res. Lett.*, 3, 379–382, 1976.
- Zander, R., Rinsland, C. P., Farmer, C. B., and Norton, R. H.: Infrared spectroscopic measurements of halogenated source gases in the stratosphere with the ATMOS instrument, *J. Geophys. Res.*, 92, 9836–9850, 1987.

B.3 Reassessment of MIPAS age of air trends and variability

Atmos. Chem. Phys., 15, 13161–13176, 2015
www.atmos-chem-phys.net/15/13161/2015/
doi:10.5194/acp-15-13161-2015
© Author(s) 2015. CC Attribution 3.0 License.



Atmospheric
Chemistry
and Physics
Open Access
EGU

Reassessment of MIPAS age of air trends and variability

F. J. Haenel¹, G. P. Stiller¹, T. von Clarmann¹, B. Funke², E. Eckert¹, N. Glatthor¹, U. Grabowski¹, S. Kellmann¹, M. Kiefer¹, A. Linden¹, and T. Reddmann¹

¹Karlsruhe Institute of Technology, Institute for Meteorology and Climate Research, Karlsruhe, Germany

²Instituto de Astrofísica de Andalucía (CSIC), 18008 Granada, Spain

Correspondence to: F. J. Haenel (florian.haenel@kit.edu)

Received: 1 April 2015 – Published in Atmos. Chem. Phys. Discuss.: 26 May 2015

Revised: 27 October 2015 – Accepted: 9 November 2015 – Published: 27 November 2015

Abstract. A new and improved setup of the SF₆ retrieval together with a newly calibrated version of MIPAS-ENVISAT level 1b spectra (version 5, ESA data version 5.02/5.06) was used to obtain a new global SF₆ data set, covering the total observational period of MIPAS from July 2002 to April 2012 for the first time. Monthly and zonally averaged SF₆ profiles were converted into mean age of air using a tropospheric SF₆-reference curve. The obtained data set of age of air was compared to airborne age of air measurements. The temporal evolution of the mean age of air was then investigated in 10° latitude and 1–2 km altitude bins. A regression model consisting of a constant and a linear trend term, two proxies for the quasi-biennial oscillation variation, sinusoidal terms for the seasonal and semiannual variation and overtones was fitted to the age of air time series. The annual cycle for particular regions in the stratosphere was investigated and compared to other studies. The age of air trend over the total MIPAS period consisting of the linear term was assessed and compared to previous findings of Stiller et al. (2012). While the linear increase of mean age is confirmed to be positive for the northern midlatitudes and southern polar middle stratosphere, differences are found in the northern polar upper stratosphere, where the mean age is now found to increase as well. The magnitude of trends in the northern midlatitude middle stratosphere is slightly lower compared to the previous version and the trends fit remarkably well to the trend derived by Engel et al. (2009). Negative age of air trends found by Stiller et al. (2012) are confirmed for the lowermost tropical stratosphere and lowermost southern midlatitudinal stratosphere. Differences to the previous data versions occur in the middle tropical stratosphere around 25 km, where the trends are now negative. Overall, the new latitude–altitude distribution of trends appears to be less patchy and more co-

herent than the previous one. The new data provide evidence of an accelerating shallow branch of the Brewer–Dobson circulation, at least in the Southern Hemisphere. Finally the age of air decadal trends are compared to trends calculated with simulated SF₆ values by the Karlsruhe Simulation Model of the Middle Atmosphere (KASIMA) and good agreement is found. The hemispheric asymmetry in the trends found in the MIPAS data is also indicated in the trends calculated with simulated SF₆ values by the KASIMA model.

1 Introduction

While it is widely accepted that climate change with enhanced greenhouse-gas abundances leads to a warming of the troposphere and a cooling of the stratosphere, the secondary effects, in particular on the global circulation in the stratosphere, the Brewer–Dobson circulation (BDC), are still an issue of current research (Butchart, 2014). A changing BDC will have large impact on the overall composition of the stratosphere, on the ozone budget and distribution (Shepherd, 2008; Li et al., 2009) and on the lifetimes of ozone-depleting substances such as CFCs (Butchart and Scaife, 2001; Douglass et al., 2008) and greenhouse gases. The mean age of air (AoA), which is the average transit time of an air parcel from the entry point of the stratosphere, the tropical tropopause, has become a measure for the strength of the BDC in particular for observational analysis (Hall and Plumb, 1994; Waugh and Hall, 2002). The mean age of air comprises both information on the speed of the advection and the amount of mixing and stirring exerted on the air parcel. Modern general circulation models and chemistry–climate models consistently simulate an acceleration of the BDC in a greenhouse-gas-

13162

F. J. Haenel et al.: Reassessment of MIPAS age of air trends and variability

induced changing climate (Rind et al., 1990; Butchart and Scaife, 2001; Butchart et al., 2006; Austin and Li, 2006; Garcia and Randel, 2008; Li et al., 2008; Calvo and Garcia, 2009; McLandress and Shepherd, 2009; Butchart et al., 2010; Okamoto et al., 2011; Bunzel and Schmidt, 2013; Oberländer et al., 2013). So far, however, this expected speeding up of the BDC has not been confirmed by observations. Engel et al. (2009) provided a 30-year record of mean age of air derived from CO₂ and SF₆ balloon-borne measurements which showed a slight but insignificant increase of mean age over the years 1975–2005 for northern midlatitudes, which would indicate a decelerated BDC. Bönisch et al. (2011) reported an acceleration of the shallow branch of the BDC for the time period 1979–2009, while they found an unchanged deep branch. Diallo et al. (2012) investigated the age of stratospheric air in the ERA-Interim reanalysis over the period 1989–2010 and stated that the shallow and the deep branch of the BDC may evolve differently. They found a negative and significant age of air trend in the lower stratosphere and a positive but insignificant trend in the middle stratosphere. Stiller et al. (2008, 2012) provided the first global data set on age of air derived from satellite SF₆ measurements. In their paper MIPAS-ENVISAT level 1b spectra of versions 3 and 4 were used to retrieve vertical profiles of SF₆ distributed over the whole globe for the time period September 2002 to January 2010. Monthly zonal means were converted into mean age of air, from which decadal trends were inferred for latitude and altitude bins.

The derived age of air trends were found to be spatially inhomogeneous with regions of increasing mean age of air and regions of decreasing age of air. The non-homogeneity of trends was also reported by Monge-Sanz et al. (2013), who also found a significant increasing trend in the mean age of air over northern midlatitudes in an multiannual CTM simulation driven by ERA-Interim winds over the period 1990–2009 and confirmed the measurements by Stiller et al. (2012) and Engel et al. (2009). In their model study they already noticed a hemispheric asymmetry, which was also later found by Mahieu et al. (2014) with SLIMCAT model calculations. Ploeger et al. (2015) confirmed this hemispheric asymmetry with calculations of the CLaMS model, also driven by ERA-Interim data, and found positive trends in the Northern Hemisphere and negative trends in the Southern Hemisphere for the time period 2002–2012.

The work presented here is a continuation of the work of Stiller et al. (2012). An extended and improved SF₆ data set is provided on the basis of a newly calibrated version of MIPAS-ENVISAT level 1b spectra (version 5, ESA data version 5.02/5.06). This new global SF₆ data set for the first time covers the total MIPAS period from July 2002 to April 2012.

The characteristics of the MIPAS instrument are presented in Sect. 2. The improvements on the retrieval setup are discussed in Sect. 3. The characteristics and morphology of the new global SF₆ data set and the resulting age of air data set are assessed in Sect. 4. Then the temporal develop-

ment is investigated and compared with the previous findings (Sect. 5). In Sect. 6, MIPAS-derived AoA trends are compared with trends calculated with simulated SF₆ values from the Karlsruhe Simulation Model of the Middle Atmosphere (KASIMA). Finally, in Sect. 7, we summarize the lessons learned about possible changes of the BDC.

2 MIPAS

MIPAS (Michelson Interferometer for Passive Atmospheric Sounding) is a Fourier transform infrared spectrometer aboard ENVISAT (Environmental Satellite; Fischer et al., 2000) and was designed for the detection of mid-infrared limb emission spectra in the middle and upper atmosphere. The atmospheric spectra were inverted into vertical profiles of atmospheric pressure, temperature and volume mixing ratios (vmrs) of at least 30 trace constituents. Details of the MIPAS instrument can be found in Fischer et al. (2008).

In 2004 the operation of the MIPAS instrument was interrupted due to a problem with the interferometer slide. The optical path difference was then reduced, implying a deterioration of the spectral resolution from 0.025 to 0.0625 cm⁻¹. The first phase of the mission (2002–2004) is usually referred to as the MIPAS full-resolution (FR) period, while the second phase (2005–2012) is called the reduced-resolution (RR) period.

Because of the long optical path through the atmospheric layers, MIPAS could also detect trace gases with very low mixing ratios. Vertical information was gained by scanning the atmosphere at different elevation angles with different tangent altitudes. MIPAS could observe atmospheric parameters in the altitude range from 5 to 160 km with minimum and maximum steps of 1 and 8 km respectively (Fischer et al., 2008).

3 Improvement of the retrieval of SF₆ mixing ratios

Data processing relies on constrained least squares fitting using the Tikhonov (Tikhonov, 1963) regularization approach. Further details of the MIPAS data processor used are described in von Clarmann et al. (2003, 2009). Information on temperature and line of sight, as well as the spectral shift, was taken from preceding MIPAS retrievals performed prior to SF₆ in the sequential retrieval chain.

While the retrieval of SF₆ by Stiller et al. (2012) relied on ESA version 4.61/4.62 and 4.67 calibrated radiance spectra, we have used version 5.02/5.06 spectra provided by ESA in the course of reprocessing of the data. These data are considered superior with respect to 4.61/4.62/4.67, in particular because the spectra of the FR period no longer suffered from a calibration insufficiency which was reported as “baseline oscillations” in Stiller et al. (2008) and the whole data set is better calibrated now. Further technical details on the MIPAS level 1b data can be found at <https://earth.esa.int/>

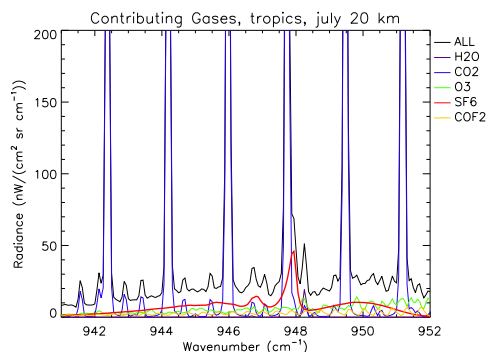


Figure 1. Contributing trace gases to a typical spectrum measured at midlatitudes in July at 20 km (low resolution) with the SF₆ signature in red.

web/sppa/mission-performance/esa-missions/envisat/mipas/products-and-algorithms/products-information.

Beyond this, the SF₆ retrieval setup has been improved over that used by Stiller et al. (2012). Improvements are related to the consideration of non-local thermodynamic equilibrium emission of interfering CO₂ lines, the treatment of interfering species in general and the details of the joint retrieval of the background continuum. The implementation of the altitude dependence of the regularization strength has been slightly changed. The definition of the analysis window (941–952 cm⁻¹, see Fig. 1), the regularization strength of the inverse problem and the spectroscopic database chosen remained unchanged since no improvements over the approach by Stiller et al. (2012) could be achieved with respect to these. Spectroscopic data were used from a dedicated MIPAS database for gases like H₂O, CO₂, O₃ and COF₂ (Flaud et al., 2003). For N₂O, NH₃, CFC-12 and SF₆ the spectroscopic database HITRAN2000 (Rothman et al., 2003) was used. Tests with varying regularization parameters did not lead to any retrieval improvements, i.e. the regularization strength chosen by Stiller et al. (2012) has been confirmed to be adequate. The new SF₆ data described and used here are version V5h_SF6_20 for the FR data product and V5r_SF6_222 and V5r_SF6_223 for the RR period. The latter two data versions have no discernible differences; their different version numbers just reflect different sources of ECMWF meteorological analysis data used in the retrieval. In the FR V5h_SF6_20 data version the artefact of the previous version caused by radiance baseline oscillations in the level 1 data described in Stiller et al. (2008) is no longer an issue and has been totally overcome.

3.1 Non-local thermodynamic equilibrium

The Q branch of the ν_3 band of SF₆ at 947.9 cm⁻¹ analysed here is strongly superimposed by the CO₂ laser band (00011 → 10001) at 947.74 cm⁻¹ and lies just above the first hot band (01111 → 11101) line at 947.94 cm⁻¹ (see Fig. 1). These CO₂ emission bands deviate from local thermodynamic equilibrium (LTE) in the middle atmosphere, particularly during daytime. Stiller et al. (2012) approximated the non-LTE effect by treating the CO₂ laser band and hot band emissions as emissions from different (non-CO₂) species and by fitting their “virtual abundances” along with the SF₆ retrieval. While these virtual abundances have no physical meaning, they helped to model fairly well the CO₂ laser band emission and to avoid related spectral residuals and error propagation. Contrary to that, our refined analysis relies on explicit modelling of the non-LTE emissions of the CO₂ laser and hot bands. In the course of a preceding CO retrieval (Funke et al., 2007), the vibrational temperatures of the CO₂ laser band and the hot band were calculated for the actual atmospheric conditions. Since the radiative transfer code used in our retrieval, the Karlsruhe Optimized and Precise Radiative Transfer Algorithm (KOPRA, Stiller, 2000; Stiller et al., 2002; Funke and Höpfner, 2000), supports calculation of non-LTE emissions, these could directly be used for the calculation of the laser band signal and hot band emissions. This improves considerably the description of the CO₂ emissions and reduces the residuals between the observed and modelled spectra, leading eventually to improved SF₆ results (compare residuals at the position of CO₂ lines in Fig. 2).

3.2 Interfering gases

Figure 1 shows the spectral window used for the SF₆ retrieval and the expected spectral contributions of contributing species for MIPAS reduced resolution at 20 km in midlatitudes for July. The signature of the target species SF₆ (red solid line) is quite weak compared to some of the interfering species. Thus a careful treatment of the interfering species is essential to minimize related error propagation. Since for some of the interfering species no reliable a priori information on their abundances is available, these gases are jointly fitted along with SF₆. For other interferents, abundance information is available from preceding MIPAS retrievals; however, inconsistent spectroscopic data or calibration inconsistencies in the SF₆ analysis window and the interferents’ dedicated analysis windows can cause artefacts when the known abundances are used to model the contribution of these gases in the SF₆ analysis window. Thus, it is occasionally adequate to jointly fit these gases along with SF₆, too. Stiller et al. (2012) have used abundance information from climatologies or preceding MIPAS retrievals for all interfering species except for CO₂ and H₂O, which were fitted jointly along with SF₆. In the new retrieval scheme the

13164

F. J. Haenel et al.: Reassessment of MIPAS age of air trends and variability

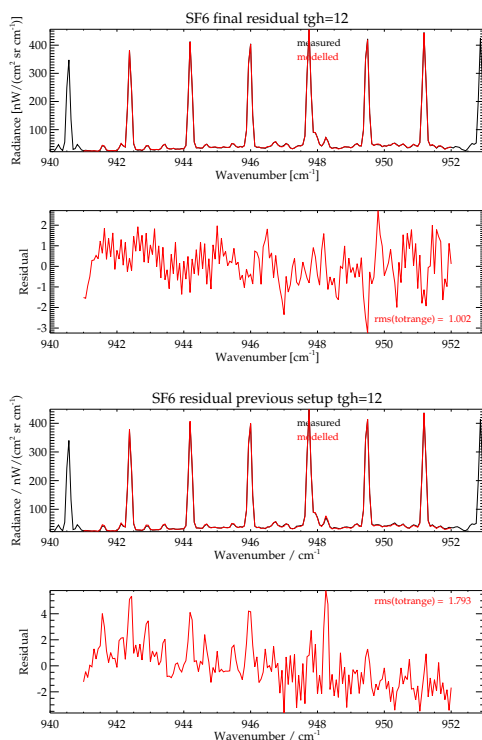


Figure 2. Coadded spectra (measured and modelled) and residuals for tangent height 12 (approx. 24 km) over 1 day for the final retrieval setup (upper panels) and for the previous retrieval setup (lower panels).

trace gases CO_2 and ozone were additionally joint fitted. This helped to minimize the residual of the fit and also removed a slight tilt of the residual in spectral space. For all gases a first order Tikhonov-type regularisation was chosen, which means that the slope of the profile was forced to some constraint, rather than forcing the profile towards an a priori profile as done in the optimal estimation approach. Usually the constant zero profile served as a priori profile and in this way oscillations in the profile are damped and the profile becomes smoother. In the following we present a gas-by-gas discussion of our treatment of all interfering species.

3.2.1 CO_2

CO_2 is the main contributing gas of all emitters in the SF_6 analysis window (microwindow) used (blue solid lines in Fig. 1). As mentioned above the maximum of the SF_6 spectral signature is just underneath of the wing of a CO_2 laser

line. In order to get an accurate value of the SF_6 mixing ratio from radiances emitted in the SF_6 microwindow, a very precise modelling of the CO_2 is crucial. We have used a non-LTE model to account for the CO_2 emissions in the middle atmosphere and fitted it jointly with SF_6 . The first guess profile in the iterative procedure was taken from climatologies (Remedios et al., 2007).

3.2.2 H_2O

A water vapour signature is located near the SF_6 Q branch at 948.26 cm^{-1} , so a considerable information crosstalk is expected between the H_2O and the SF_6 signals. The water vapour profile resulting from the preceding retrieval in dedicated microwindows (prefit) was used as a priori and first guess profile for every geolocation. The regularization strength associated with H_2O was adjusted such that the correction with respect to the initial H_2O profile had about 1 to 1.5 degrees of freedom. Basically the profiles have the shape of the prefit profile and only a shift of the prefit profile is allowed. The residual near the water vapour line was not reduced when the regularization for water vapour was relaxed. Variations of the regularization for water vapour or the choice of related a priori (constant zero or water prefit) did not have any discernible effect on the SF_6 retrieval.

3.2.3 COF_2

There is not much vertically resolved information contained on COF_2 in the microwindow, but fitting this trace gas jointly with the target species helped to minimize the residuals. A climatological profile served as a priori and first guess profile since there was no prefit of COF_2 available. The regularization was chosen relatively strong such that the resulting COF_2 profiles have about 1.5 to 3.5 degrees of freedom.

3.2.4 O_3

Like COF_2 , ozone does not contribute much to the signal in the microwindow, but prefits from the ozone retrieval existed. Thus, the ozone prefits served as a priori and first guess profiles. Together with the joint fit of COF_2 , the joint fit of ozone helped to remove a tilt in the residual. The regularization applied allowed the ozone profiles to have about 1.5 to 3.5 degrees of freedom.

3.2.5 Further species

Profiles of N_2O , NH_3 and CFC-12 were imported from a database (Remedios et al., 2007). Since the signals of these gases are small, related uncertainties are tolerable.

3.3 Background continuum and radiance offset

In the previous SF_6 retrieval by Stiller et al. (2012) background continuum radiation was considered up to an altitude

of 33 km. In the atmosphere continuum radiation, i.e. radiation which is only varying very slightly in spectral space (in contrast to spectral lines), is emitted by clouds, dust or other aerosol particles. Also the sum of very far wings of spectral lines, no more accounted for by the line by line calculation, can contribute to the continuum radiation. In general it was assumed that a consideration of continuum radiation above 33 km was not necessary, particularly because there are no aerosol contributions expected above the Junge layer. However, it turned out that fitting continuum radiation up to higher altitudes (50 km) could eliminate an artefact in the retrieved SF₆ profile: while in the retrieval of Stiller et al. (2012) an unexplained local maximum in SF₆ occurred around 36 km in the tropics, this supposedly unphysical feature vanishes completely with the new continuum treatment. This provides evidence that there is additional continuum radiation in the atmosphere which if not accounted for leads to elevated SF₆ mixing ratios, since the SF₆ signature is also of broad band nature. The approach of a joint fit of the continuum radiation up to higher altitudes also helped to improve retrievals of other species. In addition, a recent paper pointed out that there is evidence of aerosol particles even above the Junge layer due to meteoric dust (Neely III et al., 2011). In our retrievals we also fit a constant radiance offset jointly in order to account for a possible residual shift in radiance due to imperfect radiance calibration. This offset had to be strongly regularized in order to cope with the pronounced linear interdependence of the continuum and offset Jacobians.

3.4 Miscellaneous

The consideration of continuum up to higher altitudes allowed the usage of more upper tangent heights. While the previous retrieval setup only used the first 19 out of 27 tangent heights in MIPAS reduced-resolution mode, the new setup incorporated information from measurements of 22 tangent heights. This allowed more information from higher altitudes to be gained, i.e. the averaging kernel diagonals increased slightly at higher altitudes. In addition, the root mean square (RMS) of the residuals in upper tangent heights decreased. Hence, with the new retrieval setup for the first time it made sense to include 22 tangents height instead of 19. The new mean SF₆ profiles contain more information in the altitude range 40–50 km, show more structure and depend less on the prior information there.

3.5 Discussion of the retrieval refinement

In Fig. 2 an example for the residual between measured and simulated spectrum at tangent height 12 (approx. 24 km) of the final retrieval setup (upper panels) and the previous setup (lower panels) is shown. To reduce the noise, measured and modelled spectra have been coadded over the period of 1 day. One can see that the residuals improved substantially. Especially the CO₂ lines and the water vapour line (compare with

Table 1. Previous and final RMS of the residual for tangent altitude 12, 14 and 16 with coadded spectra over 1 day.

Latitude band	RMS previous	RMS final	Rel. improvement
Tangent altitude 12 ≈ 24 km			
0–30	1.861	1.108	40 %
30–60	1.704	1.188	30 %
60–90	1.092	1.001	8.3 %
–30–0	2.034	1.157	43 %
–60––30	2.361	1.390	41 %
–90––60	2.808	1.871	33 %
Tangent altitude 14 ≈ 28 km			
0–30	1.567	1.003	36 %
30–60	1.365	0.909	33 %
60–90	1.021	1.001	2 %
–30–0	1.786	1.035	42 %
–60––30	1.987	1.229	38 %
–90––60	2.432	1.684	31 %
Tangent altitude 16 ≈ 31 km			
0–30	1.921	1.040	46 %
30–60	1.294	1.025	21 %
60–90	1.012	0.946	7 %
–30–0	1.971	1.034	48 %
–60––30	1.969	1.117	43 %
–90––60	2.037	1.547	24 %

Fig. 1) are fit much better and overall the RMS of the residual has been reduced from about 1.8 to 1.0 nW (cm² sr cm^{–1})^{–1} in this example.

Also a slight tilt of the residual in spectral space was removed. The improvements achieved in the residuals are dependent on altitude and latitude. In Table 1 we present previous and final RMS of the residuals between measured and modelled spectra resolved in latitude bands of 30° for our example day for three selected tangent altitudes. The relative improvements are largest in the tropics, amounting to about 40 %, and are smallest in the northern polar stratosphere, where infrared radiances are small, because our example data were a day in boreal winter.

With the new retrieval setup the unexplained “nose”, a local maximum in the tropical SF₆ profiles at 36 km, no longer appeared after considering the continuum above the standard altitude of 33 km up to an altitude of 50 km.

The vertical resolution of the new SF₆ data is slightly degraded compared to the previous version and varies now from 4 to 6 km at 20 km, from 7 to 10 km at 30 km and from 12 to 18 km at 40 km altitude due to the inclusion of more gases in the fit, which was done to achieve a higher accuracy and less systematic errors.

13166

F. J. Haenel et al.: Reassessment of MIPAS age of air trends and variability

4 The new SF₆ data set and age of air distributions

With the new retrieval setup, the complete set of nominal mode MIPAS data was processed and approx. 2.3 million SF₆ profiles have been retrieved. The profiles belong to geolocations that cover the whole globe and the full MIPAS period from July 2002 to April 2012 but with several data gaps in between. The single profiles scatter a lot and the noise error is too large (in the order of 20 %) to provide useful age of air information from single profiles. However, averaged profiles lead to meaningful SF₆ profiles.

The new SF₆ data set exhibits similar features as the previous one described in Stiller et al. (2012), e.g. the SF₆ vmrs are increasing with time at all latitudes. Seasonal influences can be identified, such as very low mixing ratios at the end of austral winter in the southern polar latitudes. A figure showing the time series of SF₆ over latitude is included in the Supplement.

4.1 Conversion of SF₆ into age of air

For the calculation of AoA from SF₆ abundances a SF₆ reference curve is necessary. The theoretical concept of age of air as derived by Hall and Plumb (1994) requires the knowledge of SF₆ mixing ratios at the entry point into the stratosphere, i.e. the tropical tropopause region, over a long period of time. As pointed out by Stiller et al. (2012) such a long-term observational data set is not available. Only ground-based observations can provide the necessary reference data. However, transport times from the surface to the tropical tropopause are somewhat uncertain and can amount to days or even hours (to the top of convection) to weeks or months (to the top of the tropical tropopause layer). Using surface data as a reference can imply a high bias in this order of magnitude on the AoA data.

This has to be kept in mind when comparing MIPAS AoA distributions to model data, for which time 0 is set by tropopause crossing of the air parcel.

We have constructed the SF₆ reference curve as described in Stiller et al. (2012) using NOAA/ESRL SF₆ data. For the period 1995 to November 2013 smoothed ground-based global-mean combined flask and in situ data (Hall et al., 2011) are used, while for times before 1995 a linear approximation from Hall et al. (2011) ($y = 0.125 + 0.215 \times (t - 1985)$) is applied. The reference curve is extended with a linear extrapolation until June 2014 to deal with MIPAS SF₆ values slightly higher than the reference values at that certain time that can occur sporadically due to their random errors.

The AoA is then calculated by simply mapping the measured SF₆ value on the reference curve and reading of the reference time. The time difference, the so-called lag time, approximates the AoA. According to Hall and Plumb (1994) this lag time is only equivalent to the mean age of air when the used tracer is growing strictly linear, i.e. the reference curve has to be linear. Because our constructed reference

curve appears to be slightly non-linear, a correction is applied. Within an iterative procedure the reference curve is convoluted with a typical age spectrum. More details of this non-linearity correction are discussed in Stiller et al. (2012).

SF₆ is a stable tracer in the stratosphere. However, it has a mesospheric sink. Every winter SF₆-depleted air from the mesosphere subsides into the polar vortex leading to “apparent ages” which are considerably larger than the true ages. This “overaging” is most pronounced in the polar vortices, where AoA derived from SF₆ can be greater by 2 or more years (Vaugh and Hall, 2002). However, due to in-mixing of some of the vortex air into midlatitudes, the entire stratosphere is affected to a certain degree. This should be kept in mind when comparing AoA calculated from SF₆ abundances with AoA calculated from other tracers or model studies. Stiller et al. (2012) estimated the global effect of overaging to about 0.08 years per year of age for the Southern Hemisphere and to about 0.04 years per year of age for the Northern Hemisphere.

4.2 Global distribution of AoA

The derived monthly zonal means of AoA have a precision in terms of the standard error of the means of 0.06–0.4 years for the reduced-resolution period and of 0.08–0.5 years for the full-resolution period. Most of the monthly means are composed of 500–800 single values when fully occupied.

The global distribution of the newly derived AoA data set can be seen as average over all years for the four seasons in Fig. 3.

Highest AoA values occur in the polar stratosphere in hemispheric winter to spring being particularly high in the Southern Hemisphere. This again can be explained by intrusion and subsidence of old upper stratospheric and mesospheric air into the polar vortex. Due to the mesospheric SF₆ sink, this mesospheric air appears even older than it actually is.

The differences in the zonal monthly means of AoA to the previous data set, averaged over all years for the four seasons, are presented in Fig. 4. The main difference to the old data set is that the local minimum of AoA in the tropics around 36 km is no longer present in the new data set. This feature of the old data set has been proven to be a retrieval artefact, which was eliminated by a refined treatment of continuum radiation (see Sect. 3). This artefact triggered an oscillation in lower layers which are no longer present in the new data set. Above 40 km, the air is now found to be younger at almost all latitudes, which appears to be more realistic. The old data version was reported to have a possible high bias of up to 2 years above 35 km, most pronounced at the summer pole due to the simplified approach concerning the non-LTE treatment of interfering CO₂ lines (Stiller et al., 2008). The full non-LTE treatment used for the new data set has removed this systematic uncertainty. In addition, part of the lower AoA in

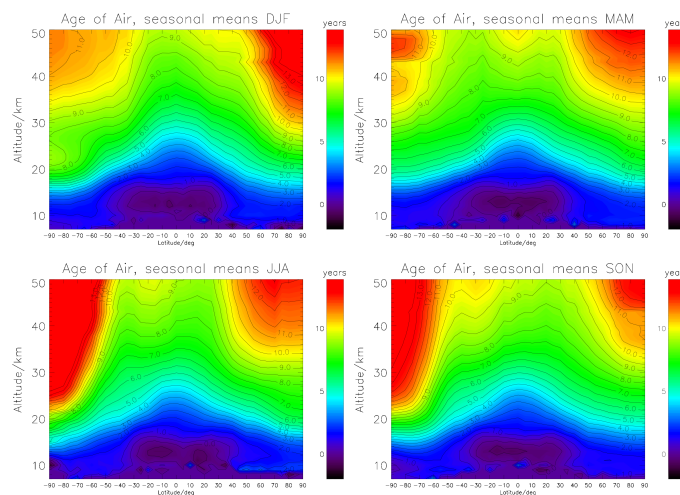


Figure 3. Zonal mean distribution of mean age of stratospheric air for the four seasons, derived by averaging MIPAS AoA data of all available years for the respective season.

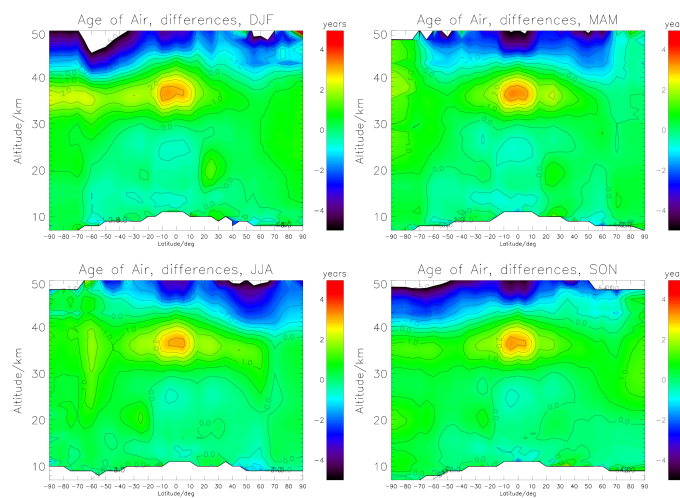


Figure 4. Differences of zonal seasonal mean distribution of mean age of stratospheric air to the previous data version averaged for the four seasons.

the upper stratosphere is attributed to the revised regularization of the retrieval.

Among studies of AoA (e.g. Stiller et al., 2012; Diallo et al., 2012; SPARC CCMVal, 2010) it became a standard for validation of measured or modelled AoA to compare with

earlier airborne measurements from the 1990s as published by Waugh and Hall (2002) and Hall et al. (1999). Overall this comparison on a latitudinal cross-section at 20 km turns out to be quite similar to the one in Fig. 4 in Stiller et al. (2012): the agreement of MIPAS AoA with the earlier air-

13168

F. J. Haenel et al.: Reassessment of MIPAS age of air trends and variability

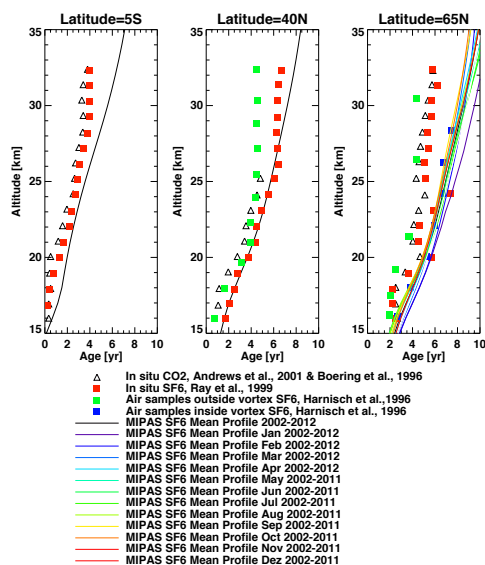


Figure 5. Comparison of MIPAS AoA profiles with airborne profiles of the 1990s for the tropics (5° S), the northern midlatitudes (40° N) and the northern high latitudes (65° N).

borne measurements is excellent in the northern and southern midlatitudes, whereas in the tropics and high latitudes MIPAS exhibits higher age. There are only small differences to the comparison with the previous MIPAS AoA version, like the spread of MIPAS AoA in the tropics is lower and the negative peak of low MIPAS AoA at about 30° N is no longer present in the new version. The respective figure is attached in the Supplement.

In Fig. 5 MIPAS AoA profiles are compared to airborne AoA profiles (in situ CO₂ measurements by Boering et al., 1996; Andrews et al., 2001; in situ SF₆ measurements by Ray et al., 1999; air sample measurements by Harnisch et al., 1996) for the tropics (5° S), the northern midlatitudes (40° N) and the northern high latitudes (65° N). In the tropics MIPAS AoA is older than in situ CO₂ and SF₆ measurements at all altitudes. In the northern midlatitudes the MIPAS profile fits excellently to the SF₆ in situ data up to an altitude of 27 km and is older higher up. As expected, in situ CO₂ measurements provide lower ages, and the AoA from SF₆ air samples by Harnisch et al. (1996) is younger, too. At northern high latitudes, MIPAS age profiles only fit well to the SF₆ air samples taken from polar vortex air. To illustrate the high seasonality, monthly averaged MIPAS profiles are additionally shown with oldest ages found for January.

$$2.45 / 4.5$$

5 Observed temporal variability for the period July 2002 to April 2012

For the analysis of the temporal variability of the new AoA data set the same methods were applied as in Stiller et al. (2012), i.e. the following regression function was fitted to the data:

$$\text{age}(t) = a + bt + c_1 \text{qbo}_1(t) + d_1 \text{qbo}_2(t) + \sum_{n=2}^9 \left(c_n \sin \frac{2\pi t}{l_n} + d_n \cos \frac{2\pi t}{l_n} \right) \quad (1)$$

where t is time, qbo_1 and qbo_2 are the quasi-biennial oscillation (QBO) indices and the sum represents eight sine and eight cosine functions of the period length l_n . The period of the first two sine and cosine functions is 12 and 6 months respectively, representing the seasonal and the semiannual cycle. The other six terms have period lengths of 3, 4, 8, 9, 18 and 24 months and describe deviations of the temporal variation from a pure sine or cosine wave. Fitting sine and cosine of the same period length accounts for a possible phase shift of the oscillation. The terms qbo_1 and qbo_2 are the normalized Singapore winds at 30 and 50 hPa as provided by the Free University of Berlin via <http://www.geo.fu-berlin.de/met/ag/strat/produkte/qbo/index.html>. These QBO proxies are approximately orthogonal such that their combination can emulate any QBO phase shift (Kyrölä et al., 2010). For the fit of the coefficients $a, b, c_1, \dots, c_9, d_1, \dots, d_9$ to the data, the method of von Clarmann et al. (2010) is used, which considers the full error covariance matrix of mean age data \mathbf{S}_m with the squared standard errors of the means of the monthly zonal means as the diagonal terms (Stiller et al., 2012).

An example of the fit of our regression model to MIPAS monthly zonal mean data can be seen in the Supplement. The fit considers a potential bias of the two MIPAS measurement periods (dashed orange line) as described in von Clarmann et al. (2010). Such a fit is done for every 10°/1–2 km latitude–altitude bin.

5.1 Age of air trends

In Stiller et al. (2012) the time series analysis was first discussed within the framework of descriptive statistics, i.e. without consideration of the autocorrelations in the residuals of the trend analysis. As a second step, the analysis was repeated within the framework of inductive statistics, where autocorrelated model errors have to be considered. In this study we focus on the trend analysis which is referred to as “model-error corrected linear increase” in Stiller et al. (2012), because the analysis without consideration of the au-

torrelated model errors leads to very similar trends whose significances, however, are considerably overestimated.

As described in Stiller et al. (2012) our regression model only accounts for the linear trend, several periodics and the QBO terms. Other atmospheric variability, especially from non-periodic events, is not included in this model. This results in fit residuals which are considerably larger than the data errors represented by the covariance matrix \mathbf{S}_m , which includes only the standard errors of the monthly means and the correlated terms to account for the possible bias between the MIPAS data subsets (von Clarmann et al., 2010). Therefore the χ_{reduced}^2 of the fit with

$$\chi_{\text{reduced}}^2 = \frac{(\mathbf{age}_{\text{MIPAS}} - \mathbf{age}_{\text{modelled}})^T \mathbf{S}_m^{-1} (\mathbf{age}_{\text{MIPAS}} - \mathbf{age}_{\text{modelled}})}{m - n} \quad (2)$$

exceeds the value of unity in most cases, where $\mathbf{age}_{\text{MIPAS}}$ and $\mathbf{age}_{\text{modelled}}$ are the data vectors containing the measured and modelled age values respectively and where m and n are the number of data pairs and the number of fitted coefficients respectively (Stiller et al., 2012). In order to consider the model errors of the regression model, the autocorrelation of two adjacent data points was estimated in a first step. In a second step the fit was rerun with the autocorrelation and a constant error term added to the covariance matrices. These additional terms in the covariance matrices were scaled within an iterative procedure, such that the resulting χ_{reduced}^2 of the trend fit was close to unity. This iterative procedure is necessary because the additional autocorrelated error term changes the weight between the data points in the fit.

The linear increase of AoA over the whole MIPAS period derived from our regression analysis varies with altitude and latitude. The global view can be seen in Fig. 6 top panel. Red areas indicate increasing AoA, while blue regions indicate decreasing AoA. Hatched areas indicate where the trend is not significant, i.e. it is smaller in absolute terms than its 2σ uncertainty.

The overall pattern of linear increase/decrease is in good agreement with the respective picture of the trend fit without consideration of autocorrelation and empirical errors (see respective figure in the Supplement), which confirms that our method is robust. The significance of most data bins is lower, as expected, due to the additional error terms.

The distribution of trends in the latitude–altitude plane roughly confirms the mean trends of those obtained by Stiller et al. (2012) and their general morphology but looks more coherent and less patchy, meaning that regions of linear increase and decrease respectively are more contiguous. There are basically two regions of linear decrease: a large one consisting of the tropics and southern subtropics between about 19 to 30 km and extending to the lowermost midlatitudinal southern stratosphere and a smaller one consisting of the upper tropical troposphere extending to the lowermost stratosphere (LMS) of midlatitudes. These regions are surrounded

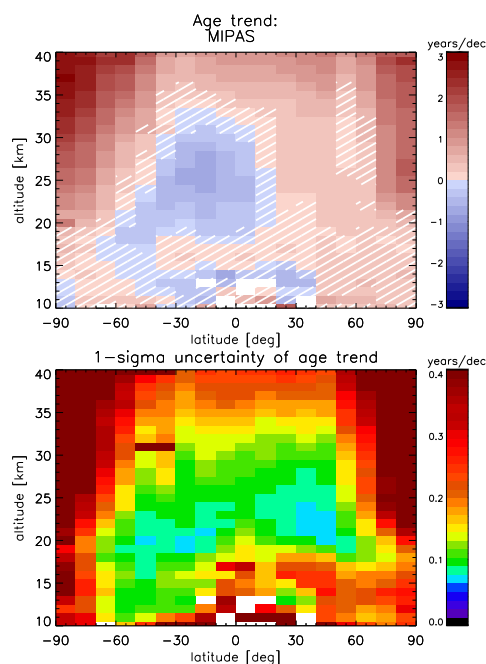


Figure 6. Top: Altitude–latitude cross-section of the model-error corrected linear increase of MIPAS AoA over the years 2002 to 2012, i.e. after including the model error and autocorrelations between the data points in the fit. Hatched areas indicate where the trend is not significant, i.e. it is smaller (in absolute terms) than its 2σ uncertainty. Bottom: 1σ uncertainty of the trend in terms of years/decade.

by regions of AoA linear increase. Largest positive linear trends were observed in the polar regions. Compared to findings of Stiller et al. (2012) a positive linear increase of mean age is confirmed for the northern midlatitudes and southern upper polar stratosphere. Negative age of air trends of Stiller et al. (2012) in the lowermost tropical stratosphere and lower southern midlatitudinal stratosphere are also confirmed. Differences are found in the northern polar stratosphere, where the mean age is now increasing as well. In the tropical stratosphere the picture is now almost opposite to the previous data of Stiller et al. (2012), meaning that AoA is increasing where it used to be decreasing and vice versa. These changes are attributed to the more adequate treatment of the background continuum emission in the retrieval and the associated removal of the spurious SF_6 maximum and subsequent errors. A clear asymmetry between the hemispheres is visible.

The uncertainties (see Fig. 6, bottom panel) are now more realistic, since now an additional model error has been added;

13170

F. J. Haenel et al.: Reassessment of MIPAS age of air trends and variability

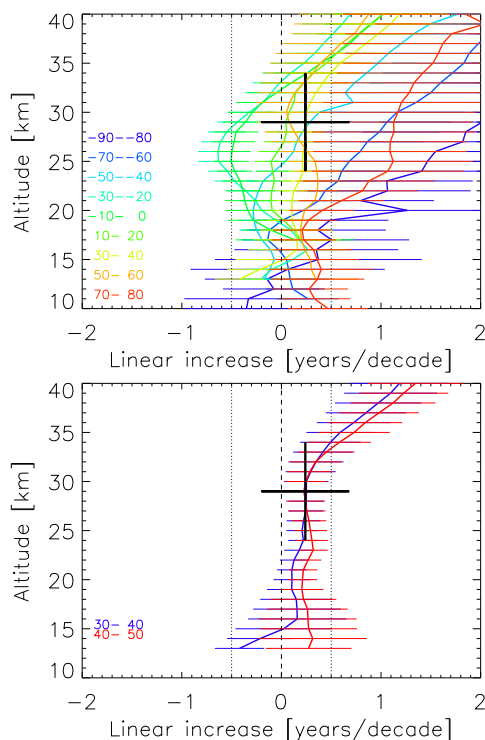


Figure 7. Vertical profiles of the age of air linear increase/decrease over the years 2002 to 2012 for example latitudes. Horizontal bars give the 2σ uncertainties of the linear variations. The 30-year trend as derived by Engel et al. (2009) for the northern midlatitudes is also shown for comparison as a black cross indicating its valid altitude range and its 2σ uncertainty.

however, they are smaller than the ones derived by Stiller et al. (2012), which is attributed to the longer time series, covering now the full MIPAS period, and the fact that the new AoA data set is less noisy than the previous one.

The vertical profiles of AoA linear trends for every other latitude bin are shown in Fig. 7, top panel. Engel et al. (2009) derived a trend of AoA for 30 to 50° N of $+0.24 \pm 0.22$ year per decade (1σ uncertainty level) for the 24 to 35 km altitude range for 1975–2005. This trend together with its valid altitude range and its 2σ uncertainty is marked as big black cross in Fig. 7. For better illustration the same picture with the MIPAS linear trend profiles for the two relevant latitude bins is shown in Fig. 7, bottom panel. The MIPAS AoA trends of 30 to 40 and 40 to 50° N are slightly lower than in the previous version and match now impressively well with the trend

estimated by Engel et al. (2009) in the 24 to 35 km altitude region. One has to keep in mind that the trend derived by Engel et al. (2009) represents the time period 1975–2005, while MIPAS measured from 2002 to 2012. So there is only a small time overlap between the two trends. Still the agreement of both is remarkable. The MIPAS AoA trends for the latitude bins 30 to 40 and 40 to 50° N are significantly distinct from 0 for all altitudes above 22 km even on the 2σ uncertainty level.

5.2 Annual cycle and QBO influence

Figure 8 shows the amplitudes and phases of the seasonal cycle, i.e. the amplitudes and phases of terms with period length 1 year determined with the regression model described above. Compared to Fig. 9 in Stiller et al. (2012) there are no substantial differences in the new data set. Thus, their respective conclusions remain valid in the light of the new data. Here we want to highlight the few differences and continue with the discussion, in particular by comparing the results with findings of other studies.

Diallo et al. (2012) found polar stratospheric AoA above 25 km, with youngest air at the end of local winter to spring, to be in the opposite phase than in the lowermost extratropical stratosphere in their analysis of ERA-Interim data. In the model analysis of Li et al. (2012) the maximum of AoA in the polar region in spring is also bounded to the lower stratosphere, whereas the upper polar stratosphere exhibits younger age. In contrast the oldest air in northern polar regions is found in MIPAS data in spring in the lower stratosphere and in mid-winter in the higher stratosphere. This difference to MIPAS AoA can be explained by the different derivations of AoA in the respective studies: while in Diallo et al. (2012) AoA is explicitly calculated by backward trajectories of the air parcel, and in Li et al. (2012) the AoA is determined by the pulse tracer method, the MIPAS AoA is derived by SF_6 observations which exhibit an overaging when SF_6 -depleted mesospheric air subsides into the polar stratosphere during winter. This overaging in the polar stratosphere during winter shifts the phase in the MIPAS data towards oldest air in polar midwinter, when subsidence of mesospheric air is strongest.

Some discernible difference to the previous data set is that the band of high seasonal amplitudes in the northern midlatitudes is not visible anymore in the new distribution of amplitudes (Fig. 8, top panel). Instead there is a region in northern midlatitudes above 25 km, which also exhibits high amplitudes like the equivalent region in the Southern Hemisphere. A higher amplitude of the seasonal cycle is now also found in the extratropical southern LMS. Hence, now both hemispheres show enhanced seasonal amplitudes in the extratropical LMS, which are tentatively attributed to the seasonality of the permeability of the subtropical jet (Stiller et al., 2012) and flooding of this region with old vortex air after the vortex breakdown at the end of winter and spring.

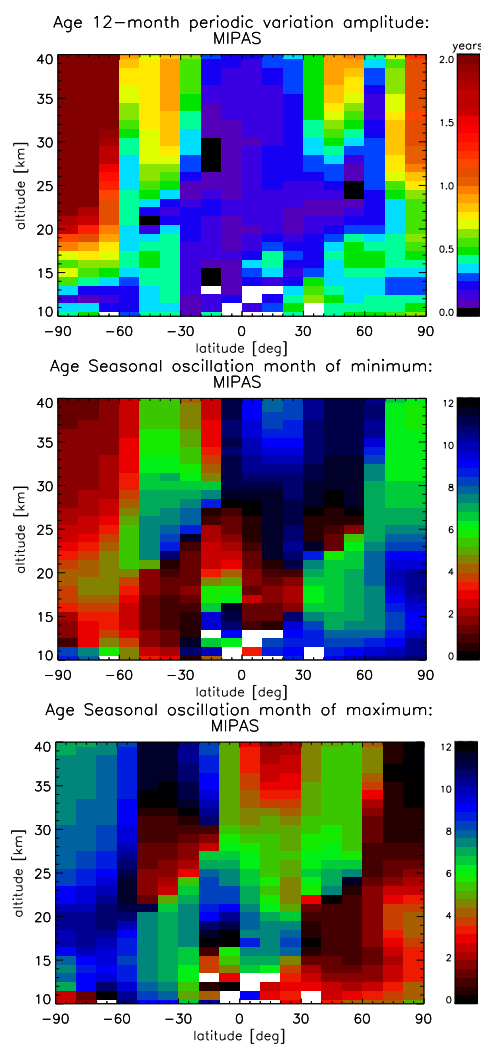


Figure 8. Altitude–latitude cross-sections of amplitudes (top) and month of the minimum (middle) and maximum (bottom) of the seasonal variation of the mean age of air.

Consistently Diallo et al. (2012) found high amplitudes of the seasonal cycle in the southern and northern extratropical LMS. Most parts of both the southern and northern extratropical LMS reach their maximum in AoA at the end of local winter to spring in the MIPAS data set as well as in the

analysis by Diallo et al. (2012). This hemispheric symmetry is a feature of the new MIPAS data set. Bönisch et al. (2009) found oldest AoA in the northern LMS in April and youngest in October with in situ measurements of SF₆ and CO₂ during the SPURT aircraft campaigns. MIPAS observed youngest air in hemispheric late summer to autumn when the mixing barrier in the subtropics is weakest and young air from the tropics is injected in this region, also referred to as “flushing” of the LMS (Hegglin and Shepherd, 2007). Also cross-tropopause isentropic mixing from the tropical troposphere in the extratropical LMS is enhanced during summer–early autumn when the subtropical jet is weak (Chen, 1995).

Model results of Li et al. (2012) of the seasonal variation of AoA also agree with MIPAS in the extratropical LMS.

In the northern subtropical lower stratosphere an abrupt meridional phase shift of almost half a year occurs, which means that these air masses are well isolated by the subtropical jet. Equatorwards the air is oldest in summer, when the subtropical mixing barrier and the BDC are weakest and older air from the extratropics is mixed in. This process is also indicated in the Southern Hemisphere and these opposite phases between the subtropics and the extratropics are also observed in the model results of Li et al. (2012).

In the midlatitudinal middle and upper stratosphere the air is youngest in local winter, when, according to the known seasonality of the Brewer–Dobson circulation, younger air is brought to higher latitudes more efficiently. The mixing barriers are partially visible by abrupt phase shifts in the month of minimum and maximum age respectively: air masses in the polar vortex are well isolated from the rest of the hemisphere. The subtropical mixing barrier is visible in the northern lower stratosphere at 30° N and is indicated in the upper stratosphere only in the plot of maximum age of Fig. 8. In the Southern Hemisphere the abrupt phase shifts seem to occur at 50–60° S and at 10–20° S.

In the tropics below approx. 28 km air is youngest in boreal winter, even in the Southern Hemisphere (except for altitude–latitude bins below 20 km). The hemispheric difference is lower than expected, which was also noticed by Stiller et al. (2012). However, this minimum in AoA in the southern tropics occurs approx. 2 months later in the new MIPAS data. In the Northern Hemisphere air is oldest in late summer, while it is oldest in austral spring to early summer in the Southern Hemisphere. Furthermore this maximum in AoA in the southern tropics occurs 2 months earlier in the new MIPAS data set compared to the previous one.

The amplitude of the QBO signal in AoA is shown in Fig. 9 for all latitudes and altitudes under assessment. High amplitudes are found not only in the tropics but also in the upper stratosphere at midlatitudes, whereas highest amplitudes were found in the upper polar stratosphere. We also find high amplitudes in the northern lowermost stratosphere.

13172

F. J. Haenel et al.: Reassessment of MIPAS age of air trends and variability

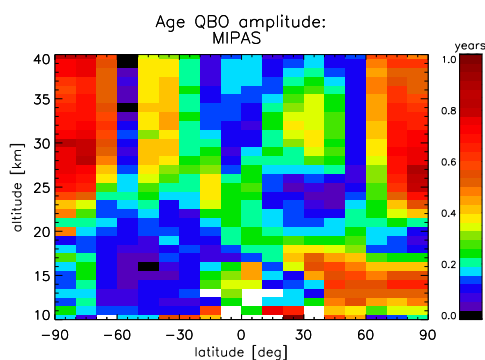


Figure 9. Altitude–latitude cross-sections of amplitudes of the QBO variation of mean age of air.

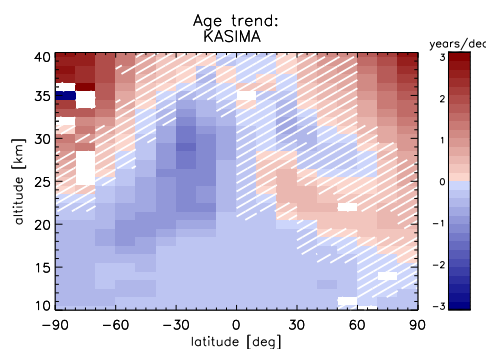


Figure 10. Calculated AoA trends for 2002–2012 from the KASIMA model with consideration of empirical errors and autocorrelation. Hatched areas indicate where the trend is not significant.

6 Comparison with model simulation

The MIPAS SF₆-based AoA trends for 2002–2012 are compared with trends derived from SF₆ distributions calculated with the KASIMA (see Kouker et al. (1999); Ruhnke et al. (1999); Reddman et al. (2001, 2010) for a description of the model and some applications). Here we used the model in the configuration as described in Reddman et al. (2001) but with a T42/L63 configuration corresponding to about 2.84° × 2.84° horizontal resolution and 63 vertical levels between 7 and 120 km. In addition, the model is nudged to ERA-Interim analyses below 1 hPa. SF₆ mixing ratio values were set at the lower boundary of the model in the troposphere using NOAA/ESRL data. Note that the model includes the mesospheric loss of SF₆, which is implemented in the model according to Reddman et al. (2001). Previously, Stiller et al. (2008) showed that the apparent high mean age values in late polar stratospheric winter observed in MIPAS observations can only be reproduced by the model simulations when including mesospheric loss.

For the determination of the trend of SF₆-derived mean age of air in the model calculation, the SF₆ distributions were calculated on a pressure–latitude grid using 64 latitude bins. In each pressure–latitude bin monthly zonal averages of SF₆ were calculated together with their standard error of the mean. The vertical pressure coordinates have been converted to geometrical altitudes assuming an isothermal atmosphere with a scale height H of 7 km ($z = -H \ln(p/p_0)$). Afterwards the monthly zonal means have been interpolated on the MIPAS altitude grid and binned in the MIPAS latitude bins. These regridded zonal SF₆ monthly means were sampled and converted to AoA in the same manner as it was done for the measured SF₆ values (see Sect. 4.1).

Figure 10 shows the distribution of age trends calculated with simulated SF₆ values from the KASIMA model in

a latitude–altitude plane with consideration of empirical errors and autocorrelations.

The model results agree remarkably well with the empirical AoA trends: positive decadal trends are found in the upper polar stratosphere in both hemispheres and at northern midlatitudes around 20 to 25 km while negative trends are found in the tropics and southern subtropics as well as in the southern lower and lowermost stratosphere at midlatitudes and southern polar region. The most pronounced negative trend is detected in the southern tropics and subtropics around 25 to 30 km, whereas it is found around 25 km in the MIPAS measurements. At northern midlatitudes at about 25 to 30 km altitude a tongue of negative trend is modelled. While MIPAS detected still positive trends there, there is at least a local age trend minimum in this region in the MIPAS data. At first glance there seems to be no disagreement between MIPAS and KASIMA in this region, because negative trends in KASIMA are not significant there. However, one has to be careful with the significances when comparing MIPAS and KASIMA: KASIMA is a nudged model, i.e. in wide parts of the atmosphere it represents the real atmosphere. This implies that the atmospheric variability patterns of KASIMA and MIPAS which are responsible for the error of the multilinear model share certain components and therefore cannot be assumed as fully uncorrelated. Thus, this error characterizes the expected difference between the regression function and truth; however, it cannot necessarily account for the differences between MIPAS and KASIMA. For this comparison the trends without consideration of the model errors may be more adequate. These figures are attached in the Supplement and show that the region of the “negative tongue” is significant in KASIMA, whereas it is significantly positive in MIPAS.

F. J. Haenel et al.: Reassessment of MIPAS age of air trends and variability

13173

At high latitudes lower stratospheric trends are positive in the MIPAS but negative in the KASIMA data set. These trends are not significant for MIPAS; however, they are significant when comparing the respective figures of trends without consideration of the model error (see figures in the Supplement). So there is indeed a contradiction in this region, which is most likely due to the “overaging” effect, which is more pronounced in the measured data because KASIMA underestimates polar winter subsidence.

What is striking in Fig. 10 is the hemispheric asymmetry between significant negative trends in the Southern Hemisphere and significant positive trends in the Northern Hemisphere, which was also found in the MIPAS data. This hemispheric asymmetry was also noticed by Monge-Sanz et al. (2013) with the TOMCAT model and by Mahieu et al. (2014) with the SLIMCAT model and was later also confirmed by Ploeger et al. (2015) with the CLaMS model.

7 Summary and conclusions

In this work the SF₆ retrieval setup for MIPAS ENVISAT spectra has been improved over the one developed by Stiller et al. (2012) and a newer version of spectra provided by ESA (level 1b data, version 5.02/5.06) was used to retrieve global profiles of the trace gas SF₆. Monthly zonal means were converted in AoA using a tropospheric reference curve. The new AoA data set resembles roughly that of Stiller et al. (2012) but shows differences with respect to several details. Some spurious features of the old data set no longer appear in the new data set. In particular, the new data set does not show the local AoA minimum at 36 km in the tropics, which was believed to be a retrieval artefact of the previous version and could be eliminated by a refined consideration of continuum radiation. A possible high bias of the old AoA data set above 40 km is removed as the air is considerably younger in this altitude region in the new data version.

The latitudinal cross-section of AoA at 20 km was compared to airborne observations from the 1990s and no substantial differences to the previous version of Stiller et al. (2012) were found. The comparison of AoA profiles with airborne measurements shows that in the tropics MIPAS AoA is older at all altitudes. At northern midlatitudes MIPAS agrees with most of SF₆ in situ data whereas at high northern latitudes MIPAS is again older, and only the SF₆ air samples inside the polar vortex match with the MIPAS data.

The temporal variability of AoA over the 10 years of MIPAS measurements (2002–2012) was analysed by fitting a regression model to the AoA time series. The annual cycle in AoA of particular regions in the stratosphere was investigated and found to be in good agreement with other studies.

The derived AoA decadal trends show a pronounced hemispheric asymmetry above the lowermost stratosphere. The results of Stiller et al. (2012) were confirmed with respect to the typical values and the general morphology. The over-

all picture of linear increase/decrease in the latitude–altitude plane, however, is more contiguous and less patchy with the new data. Positive linear trends were confirmed for the northern midlatitudes and southern polar middle stratosphere whereas negative trends were confirmed for the lowermost tropical stratosphere and lowermost southern midlatitudinal stratosphere. Differences to the previous data set occur in the northern polar upper stratosphere, where trends are now positive, and in the middle tropical stratosphere, where trends are now negative. The latter might be explained by the removal of the retrieval artefact which changed the shape of the AoA profile in the tropics considerably. The linear increase in the southern and northern polar stratosphere and in the northern midlatitudes can be considered as robust results. The significant positive trend in the northern midlatitudes supports the findings of Engel et al. (2009) and the inferred trends match impressively well with the estimated trend by Engel et al. (2009).

The refined MIPAS observations on AoA in this study do not corroborate the results of various model studies, which consistently predict a decreasing AoA for the whole stratosphere. However, our decadal trends cannot be compared to results from long-term model studies. Our comparison with the KASIMA model for the period 2002–2012 shows that the linear increase in the upper polar stratosphere and in the northern midlatitudes can be reproduced in the model at least when data are sampled and analysed in the same manner as the MIPAS data. It also demonstrates that the ERA-Interim data, used to nudge KASIMA, apparently are able to reproduce the observed transport trend, which shows that they are suitable for studies of the BDC and its trends.

Nevertheless this study finds a decreasing AoA trend in the tropics and in the lower and lowermost midlatitudinal southern stratosphere in agreement with long-term model studies and hence supports the idea of an increasing shallow branch of the BDC, which was also proposed by Bönisch et al. (2011) and supported by Diallo et al. (2012), at least in the Southern Hemisphere.

The Supplement related to this article is available online at doi:10.5194/acp-15-13161-2015-supplement.

Acknowledgements. This work was funded by the “CAWSES” priority programme of the German Research Foundation (DFG) under project STI 210/5-3 and by the German Federal Ministry of Education and Research (BMBF) within the “ROMIC” programme under project 01LG1221B.

E. Eckert was funded by the DFG project CL 319/2-1 (COLIBRI). We would like to acknowledge provision of MIPAS level 1b data by ESA and the SF₆ data from the NOAA/ESRL halocarbons in situ programme. The authors also acknowledge support by the Deutsche Forschungsgemeinschaft and Open Access Publishing

13174

F. J. Haenel et al.: Reassessment of MIPAS age of air trends and variability

Fund of Karlsruhe Institute of Technology. The authors like to thank the reviewers for their constructive comments.

The article processing charges for this open-access publication were covered by a Research Centre of the Helmholtz Association.

Edited by: M. Dameris

References

- Andrews, A. E., Boering, K. A., Daube, B. C., Wofsy, S. C., Loewenstein, M., Jost, H., Podolske, J. R., Webster, C. R., Herman, R. L., Scott, D. C., Flesch, G. J., Moyer, E. J., Elkins, J. W., Dutton, G. S., Hurst, D. F., Moore, F. L., Ray, E. A., Romashkin, P. A., and Strahan, S. E.: Mean ages of stratospheric air derived from in situ observations of CO₂, CH₄, and N₂O, *J. Geophys. Res.*, 106, 32295–32314, doi:10.1029/2001JD000465, 2001.
- Austin, J. and Li, F.: On the relationship between the strength of the Brewer–Dobson circulation and the age of stratospheric air, *Geophys. Res. Lett.*, 33, L17807, doi:10.1029/2006GL026867, 2006.
- Boering, K. A., Wofsy, S. C., Daube, B. C., Schneider, H. R., Loewenstein, M., Podolske, J. R., and Conway, T. J.: Stratospheric mean ages and transport rates from observations of carbon dioxide and nitrous oxide, *Science*, 274, 1340–1343, doi:10.1126/science.274.5291.1340, 1996.
- Bönisch, H., Engel, A., Curtius, J., Birner, Th., and Hoor, P.: Quantifying transport into the lowermost stratosphere using simultaneous in-situ measurements of SF₆ and CO₂, *Atmos. Chem. Phys.*, 9, 5905–5919, doi:10.5194/acp-9-5905-2009, 2009.
- Bönisch, H., Engel, A., Birner, Th., Hoor, P., Tarasick, D. W., and Ray, E. A.: On the structural changes in the Brewer–Dobson circulation after 2000, *Atmos. Chem. Phys.*, 11, 3937–3948, doi:10.5194/acp-11-3937-2011, 2011.
- Bunzel, F. and Schmidt, H.: The brewer–dobson circulation in a changing climate: impact of the model configuration, *J. Atmos. Sci.*, 70, 1437–1455, 2013.
- Butchart, N.: The Brewer–Dobson Circulation, *Rev. Geophys.*, 52, 157–184, doi:10.1002/2013RG000448, 2014.
- Butchart, N. and Scaife, A. A.: Removal of chlorofluorocarbons by increased mass exchange between the stratosphere and troposphere in a changing climate, *Nature*, 410, 799–802, doi:10.1038/35071047, 2001.
- Butchart, N., Scaife, A. A., Bourqui, M., de Grandpre, J., Hare, S. H. E., Kettleborough, J., Langematz, U., Manzini, E., Sassi, F., Shibata, K., Shindell, D., and Sigmond, M.: Simulations of anthropogenic change in the strength of the Brewer–Dobson circulation, *Clim. Dynam.*, 27, 727–741, doi:10.1007/s00382-006-0162-4, 2006.
- Butchart, N., Cionni, I., Eyring, V., Shepherd, T. G., Waugh, D. W., Akiyoshi, H., Austin, J., Brühl, C., Chipperfield, M. P., Cordero, E., Dameris, M., Deckert, R., Dhomse, S., Frith, S. M., Garcia, R. R., Gettelman, A., Giorgetta, M. A., Kinnison, D. E., Li, F., Mancini, E., McLandress, C., Pawson, S., Pitari, G., Plummer, D. A., Rozanov, E., Sassi, F., Scinocca, J. F., Shibata, K., Steil, B., and Tian, W.: Chemistry–climate model simulations of twenty-first century stratospheric climate and circulation changes, *J. Climate*, 23, 5349–5374, 2010.
- Calvo, N. and Garcia, R. R.: Wave forcing of the tropical upwelling in the lower stratosphere under increasing concentrations of greenhouse gases, *J. Atmos. Sci.*, 66, 3184–3196, 2009.
- Chen, P.: Isentropic cross-tropopause mass exchange in the extratropics, *J. Geophys. Res.-Atmos.*, 100, 16661–16673, doi:10.1029/95JD01264, 1995.
- Diallo, M., Legras, B., and Chédin, A.: Age of stratospheric air in the ERA-Interim, *Atmos. Chem. Phys.*, 12, 12133–12154, doi:10.5194/acp-12-12133-2012, 2012.
- Douglass, A. R., Stolarski, R. S., Schoeberl, M. R., Jackman, C. H., Gupta, M. L., Newman, P. A., Nielsen, J. E., and Fleming, E. L.: Relationship of loss, mean age of air and the distribution of CFCs to stratospheric circulation and implications for atmospheric lifetimes, *J. Geophys. Res.*, 113, D14309, doi:10.1029/2007JD009575, 2008.
- Engel, A., Möbius, T., Bönisch, H., Schmidt, U., Heinz, R., Levin, I., Atlas, E., Aoki, S., Nakazawa, T., Sugawara, S., Moore, F., Hurst, D., Elkins, J., Schauffler, S., Andrews, A., and Boering, K.: Age of stratospheric air unchanged within uncertainties over the past 30 years, *Nature Geosci.*, 2, 28–31, doi:10.1038/ngeo388, 2009.
- Fischer, H., Blom, C., Oelhaf, H., Carli, B., Carlotti, M., Delbouille, L., Ehalt, D., Flaud, J.-M., Isaksen, I., López-Puertas, M., McElroy, C. T., and Zander, R.: Envisat-MIPAS, an instrument for atmospheric chemistry and climate research, European Space Agency-Report SP-1229, edited by: Readings C. and Harris R. A., ESA Publications Division, ESTEC, P.O. Box 299, 2200 AG Noordwijk, the Netherlands, 2000.
- Fischer, H., Birk, M., Blom, C., Carli, B., Carlotti, M., von Clarmann, T., Delbouille, L., Dudhia, A., Ehalt, D., Endemann, M., Flaud, J. M., Gessner, R., Kleinert, A., Koopman, R., Langen, J., López-Puertas, M., Mosner, P., Nett, H., Oelhaf, H., Perron, G., Remedios, J., Ridolfi, M., Stiller, G., and Zander, R.: MIPAS: an instrument for atmospheric and climate research, *Atmos. Chem. Phys.*, 8, 2151–2188, doi:10.5194/acp-8-2151-2008, 2008.
- Flaud, J.-M., Piccolo, C., Carli, B., Perrin, A., Coudert, L. H., Teffo, J.-L., and Brown, L. R.: Molecular line parameters for the MIPAS (Michelson Interferometer for Passive Atmospheric Sounding) experiment, *Atmos. Oceanic Opt.*, 16, 172–182, 2003.
- Funke, B. and Höpfner, M.: Non-LTE and radiative transfer, in: The Karlsruhe Optimized and Precise Radiative Transfer Algorithm (KOPRA), edited by: Stiller, G. P., Wissenschaftliche Berichte FZKA 6487, Forschungszentrum Karlsruhe, Karlsruhe, 101–106, 2000.
- Funke, B., López-Puertas, M., Bermejo-Pantaleón, D., von Clarmann, T., Stiller, G. P., Höpfner, M., Grabowski, U., and Kaufmann, M.: Analysis of nonlocal thermodynamic equilibrium CO 4.7 μ m fundamental, isotopic and hot band emissions measured by the Michelson Interferometer for Passive Atmospheric Sounding on Envisat, *J. Geophys. Res.*, 112, D11305, doi:10.1029/2006JD007933, 2007.
- Garcia, R. R. and Randel, W. J.: Acceleration of the Brewer–Dobson circulation due to increases in greenhouse gases, *J. Atmos. Sci.*, 65, 2731–2739, doi:10.1175/2008JAS2712.1, 2008.
- Hall, B. D., Dutton, G. S., Mondeel, D. J., Nance, J. D., Rigby, M., Butler, J. H., Moore, F. L., Hurst, D. F., and Elkins, J. W.: Improving measurements of SF₆ for the study of atmospheric

F. J. Haenel et al.: Reassessment of MIPAS age of air trends and variability

13175

- transport and emissions, *Atmos. Meas. Tech.*, 4, 2441–2451, doi:10.5194/amt-4-2441-2011, 2011.
- Hall, T. M. and Plumb, R. A.: Age as a diagnostic of stratospheric transport, *J. Geophys. Res.*, 99, 1059–1070, 1994.
- Hall, T. M., Waugh, D. W., Boering, K. A., and Plumb, R. A.: Evaluation of transport in stratospheric models, *J. Geophys. Res.*, 104, 18815–18839, 1999.
- Harnisch, J., Borchers, R., Fabian, P., and Maiss, M.: Tropospheric trends for CF₄ and C₂F₆ since 1982 derived from SF₆ dated stratospheric air, *Geophys. Res. Lett.*, 23, 1099–1102, 1996.
- Heggin, M. I. and Shepherd, T. G.: O₃–N₂O correlations from the atmospheric chemistry experiment: revisiting a diagnostic of transport and chemistry in the stratosphere, *J. Geophys. Res.*, 112, D19301, doi:10.1029/2006JD008281, 2007.
- Kouker, W., Offermann, D., Küll, V., Reddmann, T., Ruhnke, R., and Franzen, A.: Streamers observed by the CRISTA experiment and simulated in the KASIMA model, *J. Geophys. Res.*, 104, 16405–16418, 1999.
- Kyrölä, E., Tamminen, J., Sofieva, V., Bertaux, J. L., Hauchecorne, A., Dalaudier, F., Fussen, D., Vanhellemont, F., Fanton d’Andon, O., Barrot, G., Guirlet, M., Fehr, T., and Saavedra de Miguel, L.: GOMOS O₃, NO₂, and NO₃ observations in 2002–2008, *Atmos. Chem. Phys.*, 10, 7723–7738, doi:10.5194/acp-10-7723-2010, 2010.
- Li, F., Austin, J., and Wilson, J.: The strength of the brewer–dobson circulation in a changing climate: coupled chemistry–climate model simulations, *J. Climate*, 21, 40–57, 2008.
- Li, F., Stolarski, R. S., and Newman, P. A.: Stratospheric ozone in the post-CFC era, *Atmos. Chem. Phys.*, 9, 2207–2213, doi:10.5194/acp-9-2207-2009, 2009.
- Li, F., Waugh, D. W., Douglass, A. R., Newman, P. A., Pawson, S., Stolarski, R. S., Strahan, S. E., and Nielsen, J. E.: Seasonal variations of stratospheric age spectra in the Goddard Earth Observing System Chemistry Climate Model (GEOSCCM), *J. Geophys. Res.-Atmos.*, 117, D05134, doi:10.1029/2011JD016877, 2012.
- Mahieu, E., Chipperfield, M. P., Notholt, J., Reddmann, T., Anderson, J., Bernath, P. F., Blumenstock, T., Coffey, M. T., Dhomse, S. S., Feng, W., Franco, B., Froidevaux, L., Griffith, D. W. T., Hannigan, J. W., Hase, F., Hossaini, R., Jones, N. B., Morino, I., Murata, I., Nakajima, H., Palm, M., Paton-Walsh, C., Russell III, J. M., Schneider, M., Servais, C., Smale, D., and Walker, K. A.: Recent Northern Hemisphere stratospheric HCl increase due to atmospheric circulation changes, *Nature*, 515, 104–107, 2014.
- McLanress, C. and Shepherd, T. G.: Simulated anthropogenic changes in the Brewer–Dobson circulation, including its extension to high latitudes, *J. Climate*, 22, 1516–1540, doi:10.1175/2008JCLI2679.1, 2009.
- Monge-Sanz, B. M., Chipperfield, M. P., Dee, D. P., Simmons, A. J., and Uppala, S. M.: Improvements in the stratospheric transport achieved by a chemistry transport model with ECMWF (re)analyses: identifying effects and remaining challenges, *Q. J. Roy. Meteor. Soc.*, 139, 654–673, doi:10.1002/qj.1996, 2013.
- Neely III, R. R., English, J. M., Toon, O. B., Solomon, S., Mills, M., and Thayer, J. P.: Implications of extinction due to meteoritic smoke in the upper stratosphere, *Geophys. Res. Lett.*, 38, L24808, doi:10.1029/2011GL049865, 2011.
- Oberländer, S., Langematz, U., and Meul, S.: Unraveling impact factors for future changes in the Brewer–Dobson circulation, *J. Geophys. Res.-Atmos.*, 118, 10296–10312, doi:10.1002/jgrd.50775, 2013.
- Okamoto, K., Sato, K., and Akiyoshi, H.: A study on the formation and trend of the Brewer–Dobson circulation, *J. Geophys. Res.-Atmos.*, 116, D10117, doi:10.1029/2010JD014953, 2011.
- Ploeger, F., Riese, M., Haenel, F., Konopka, P., Müller, R., and Stiller, G.: Variability of stratospheric mean age of air and of the local effects of residual circulation and eddy mixing, *J. Geophys. Res. Atmos.*, 120, 716–733, doi:10.1002/2014JD022468, 2015.
- Ray, E. A., Moore, F. L., Elkins, J. W., Dutton, G. S., Fahey, D. W., Vömel, H., Oltmans, S. J., and Rosenlof, K. H.: Transport into the Northern Hemisphere lowermost stratosphere revealed by in situ tracer measurements, *J. Geophys. Res.*, 104, 26565–26580, doi:10.1029/1999JD900323, 1999.
- Reddmann, T., Ruhnke, R., and Kouker, W.: Three-dimensional model simulations of SF₆ with mesospheric chemistry, *J. Geophys. Res.*, 106, 14525–14537, doi:10.1029/2000JD900700, 2001.
- Reddmann, T., Ruhnke, R., Versick, S., and Kouker, W.: Modeling disturbed stratospheric chemistry during solar-induced NO_x enhancements observed with MIPAS/ENVISAT, *J. Geophys. Res.-Atmos.*, 115, D00111, doi:10.1029/2009JD012569, 2010.
- Remedios, J. J., Leigh, R. J., Waterfall, A. M., Moore, D. P., Sembhi, H., Parkes, L., Greenhough, J., Chipperfield, M. P., and Hauglustaine, D.: MIPAS reference atmospheres and comparisons to V4.61/V4.62 MIPAS level 2 geophysical data sets, *Atmos. Chem. Phys. Discuss.*, 7, 9973–10017, doi:10.5194/acpd-7-9973-2007, 2007.
- Rind, D., Suozzo, R., Balachandran, N. K., and Prather, M. J.: Climate change and the middle atmosphere. part I: the doubled CO₂ climate, *J. Atmos. Sci.*, 47, 465–494, 1990.
- Rothman, L. S., Barbe, A., Benner, D. C., Brown, L. R., Camy-Peyret, C., Carleer, M. R., Chance, K., Clerbaux, C., Dana, V., Devi, V. M., Fayt, A., Flaud, J.-M., Gamache, R. R., Goldman, A., Jacquemart, D., Jucks, K. W., Lafferty, W. J., Mandin, J.-Y., Massie, S. T., Nemtchinov, V., Newnham, D. A., Perrin, A., Rinsland, C. P., Schroeder, J., Smith, K. M., Smith, M. A. H., Tang, K., Toth, R. A., Vander Auwera, J., Varanasi, P., and Yoshino, K.: The HITRAN molecular spectroscopic database: edition of 2000 including updates through 2001, *J. Quant. Spectrosc. Ra.*, 82, 5–44, doi:10.1016/S0022-4073(03)00146-8, 2003.
- Ruhnke, R., Kouker, W., and Reddmann, T.: The influence of the OH + NO₂ + M reaction on the NO_y partitioning in the late Arctic winter 1992/1993 as studied with KASIMA, *J. Geophys. Res.*, 104, 3755–3772, 1999.
- Shepherd, T. G.: Dynamics, stratospheric ozone, and climate change, *Atmos. Ocean*, 46, 117–138, doi:10.3137/ao.460106, 2008.
- SPARC CCMVal: Neu, J. and Strahan, S., Chapter 5. Transport, in: *SPARC Report on the Evaluation of Chemistry–Climate Models*, edited by: Eyring, V., Shepherd, T. G., and Waugh, D. W., SPARC Report No. 5, WCRP-132, WMO/TD-No. 1526, available at: http://www.atmos.physics.utoronto.ca/SPARC_SPARC/WMO_Zurich, 2010.
- Stiller, G. P. (Ed.): *The Karlsruhe Optimized and Precise Radiative Transfer Algorithm (KOPRA)*, vol. FZKA 6487 of Wissenschaftliche Berichte, Forschungszentrum Karlsruhe, 2000.
- Stiller, G. P., von Clarmann, T., Funke, B., Glatthor, N., Hase, F., Höpfner, M., and Linden, A.: Sensitivity of trace gas abundances

13176

F. J. Haenel et al.: Reassessment of MIPAS age of air trends and variability

- retrievals from infrared limb emission spectra to simplifying approximations in radiative transfer modelling, *J. Quant. Spectrosc. Ra.*, 72, 249–280, 2002.
- Stiller, G. P., von Clarmann, T., Höpfner, M., Glatthor, N., Grabowski, U., Kellmann, S., Kleinert, A., Linden, A., Milz, M., Reddmann, T., Steck, T., Fischer, H., Funke, B., López-Puertas, M., and Engel, A.: Global distribution of mean age of stratospheric air from MIPAS SF₆ measurements, *Atmos. Chem. Phys.*, 8, 677–695, doi:10.5194/acp-8-677-2008, 2008.
- Stiller, G. P., von Clarmann, T., Haenel, F., Funke, B., Glatthor, N., Grabowski, U., Kellmann, S., Kiefer, M., Linden, A., Lossow, S., and López-Puertas, M.: Observed temporal evolution of global mean age of stratospheric air for the 2002 to 2010 period, *Atmos. Chem. Phys.*, 12, 3311–3331, doi:10.5194/acp-12-3311-2012, 2012.
- Tikhonov, A.: On the solution of incorrectly stated problems and method of regularization, *Dokl. Akad. Nauk. SSSR+*, 151, 501–504, 1963.
- von Clarmann, T., Glatthor, N., Grabowski, U., Höpfner, M., Kellmann, S., Kiefer, M., Linden, A., Mengistu Tsidu, G., Milz, M., Steck, T., Stiller, G. P., Wang, D. Y., Fischer, H., Funke, B., Gil-López, S., and López-Puertas, M.: Retrieval of temperature and tangent altitude pointing from limb emission spectra recorded from space by the Michelson Interferometer for Passive Atmospheric Sounding (MIPAS), *J. Geophys. Res.*, 108, 4736, doi:10.1029/2003JD003602, 2003.
- von Clarmann, T., Höpfner, M., Kellmann, S., Linden, A., Chauhan, S., Funke, B., Grabowski, U., Glatthor, N., Kiefer, M., Schieferdecker, T., Stiller, G. P., and Versick, S.: Retrieval of temperature, H₂O, O₃, HNO₃, CH₄, N₂O, ClONO₂ and ClO from MIPAS reduced resolution nominal mode limb emission measurements, *Atmos. Meas. Tech.*, 2, 159–175, doi:10.5194/amt-2-159-2009, 2009.
- von Clarmann, T., Stiller, G., Grabowski, U., Eckert, E., and Orphal, J.: Technical Note: Trend estimation from irregularly sampled, correlated data, *Atmos. Chem. Phys.*, 10, 6737–6747, doi:10.5194/acp-10-6737-2010, 2010.
- Waugh, D. W. and Hall, T. M.: Age of stratospheric air: theory, observations, and models, *Rev. Geophys.*, 40, 1010, doi:10.1029/2000RG000101, 2002.

C. List of other Co-Authored Publications

Stiller, G. P., Kiefer, M., Eckert, E., von Clarmann, T., Kellmann, S., García-Comas, M., Funke, B., Leblanc, T., Fetzer, E., Froidevaux, L., Gomez, M., Hall, E., Hurst, D., Jordan, A., Kämpfer, N., Lambert, A., McDermid, I. S., McGee, T., Miloshevich, L., Nedoluha, G., Read, W., Schneider, M., Schwartz, M., Straub, C., Toon, G., Twigg, L. W., Walker, K., and Whiteman, D. N.: *Validation of MIPAS IMK/IAA temperature, water vapor, and ozone profiles with MOHAVE-2009 campaign measurements*, Atmos. Meas. Tech., 5, 289-320, doi:10.5194/amt-5-289-2012, 2012.

Fadnavis, S., Schultz, M. G., Semeniuk, K., Mahajan, A. S., Pozzoli, L., Sonbawne, S., Ghude, S. D., Kiefer, M., and Eckert, E.: *Trends in peroxyacetyl nitrate (PAN) in the upper troposphere and lower stratosphere over southern Asia during the summer monsoon season: regional impacts*, Atmos. Chem. Phys., 14, 12725-12743, doi:10.5194/acp-14-12725-2014, 2014.

Glatthor, N., Höpfner, M., Stiller, G. P., von Clarmann, T., Funke, B., Lossow, S., Eckert, E., Grabowski, U., Kellmann, S., Linden, A., Walker, K., and Wiegele, A.: *Seasonal and interannual variations in HCN amounts in the upper troposphere and lower stratosphere observed by MIPAS*, Atmos. Chem. Phys., 15, 563-582, doi:10.5194/acp-15-563-2015, 2015.

Laeng, A., Plieninger, J., von Clarmann, T., Grabowski, U., Stiller, G., Eckert, E., Glatthor, N., Haenel, F., Kellmann, S., Kiefer, M., Linden, A., Lossow, S., Deaver, L., Engel, A., Hervig, M., Levin, I., McHugh, M., Noël, S., Toon, G., and Walker, K.: *Validation of MIPAS IMK/IAA methane profiles*, Atmos. Meas. Tech., 8, 5251-5261, doi:10.5194/amt-8-5251-2015, 2015.

Moreira, L., Hocke, K., Eckert, E., von Clarmann, T., and Kämpfer, N.: *Trend analysis of the 20-year time series of stratospheric ozone profiles observed by the GROMOS microwave radiometer at Bern*, Atmos. Chem. Phys., 15, 10999-11009, doi:10.5194/acp-15-10999-2015, 2015.

Moreira, L., Hocke, K., Navas-Guzmán, F., Eckert, E., von Clarmann, T., and Kämpfer, N.: *The natural oscillations in stratospheric ozone observed by the GROMOS microwave radiometer at the NDACC station Bern*, Atmos. Chem. Phys., 16, 10455-10467, doi:10.5194/acp-16-10455-2016, 2016.

C. Bibliography

- Andrews, D. G. and M. E. McIntyre (1976). “Planetary Waves in Horizontal and Vertical Shear: The Generalized Eliassen-Palm Relation and the Mean Zonal Acceleration.” In: *Journal of Atmospheric Sciences* 33, pp. 2031–2048. DOI: [10.1175/1520-0469\(1976\)033<2031:PWIHAV>2.0.CO;2](https://doi.org/10.1175/1520-0469(1976)033<2031:PWIHAV>2.0.CO;2).
- (1978). “Generalized Eliassen-Palm and Charney-Drazin Theorems for Waves on Axisymmetric Mean Flows in Compressible Atmospheres”. In: *Journal of the Atmospheric Sciences* 35.2, pp. 175–185. DOI: [10.1175/1520-0469\(1978\)035<0175:GEPACD>2.0.CO;2](https://doi.org/10.1175/1520-0469(1978)035<0175:GEPACD>2.0.CO;2).
- Austin, John, J. Scinocca, D. Plummer, L. Oman, D. Waugh, H. Akiyoshi, S. Bekki, P. Braesicke, N. Butchart, M. Chipperfield, D. Cugnet, M. Dameris, S. Dhomse, V. Eyring, S. Frith, R. R. Garcia, H. Garny, A. Gettelman, S. C. Hardiman, D. Kinnison, J. F. Lamarque, E. Mancini, M. Marchand, M. Michou, O. Morgenstern, T. Nakamura, S. Pawson, G. Pitari, J. Pyle, E. Rozanov, T. G. Shepherd, K. Shibata, H. Teyssède, R. J. Wilson, and Y. Yamashita (2010). “Decline and recovery of total column ozone using a multimodel time series analysis”. In: *Journal of Geophysical Research: Atmospheres* 115.D3. D00M10, n/a–n/a. ISSN: 2156-2202. DOI: [10.1029/2010JD013857](https://doi.org/10.1029/2010JD013857). URL: <http://dx.doi.org/10.1029/2010JD013857>.
- Bayes, M. and M. Price (1763). “An Essay towards Solving a Problem in the Doctrine of Chances. By the Late Rev. Mr. Bayes, F. R. S. Communicated by Mr. Price, in a Letter to John Canton, A. M. F. R. S.” In: *Philosophical Transactions of the Royal Society of London Series I* 53, pp. 370–418.
- Bönisch, H., A. Engel, T. Birner, P. Hoor, D. W. Tarasick, and E. A. Ray (2011). “On the structural changes in the Brewer-Dobson circulation after 2000”. In: *Atmos. Chem. Phys.* 11.8, pp. 3937–3948. DOI: [10.5194/acp-11-3937-2011](https://doi.org/10.5194/acp-11-3937-2011).
- Brasseur, G. and S. Solomon (2005). *Aeronomy of the Middle Atmosphere—Chemistry and Physics of the Stratosphere and Mesosphere*. third. Atmospheric and Oceanographic Sciences Library 32. Springer, P. O. Box 17, 3300 AA Dordrecht, The Netherlands.
- Butchart, N. (2014). “The Brewer-Dobson circulation”. In: *Reviews of Geophysics* 52.2, pp. 157–184. ISSN: 1944-9208. DOI: [10.1002/2013RG000448](https://doi.org/10.1002/2013RG000448).
- Butchart, N. and A. A. Scaife (2001). “Removal of chlorofluorocarbons by increased mass exchange between the stratosphere and troposphere in a changing climate”. In: *Nature* 410, pp. 799–802. DOI: [doi:10.1038/35071047](https://doi.org/10.1038/35071047).
- Chandrasekhar, S. (1960). *Radiative Transfer*. Dover Publ., New York.
- Chapman, S. (1930). “XXXV. On ozone and atomic oxygen in the upper atmosphere”. In: *The London, Edinburgh, and Dublin Philosophical Magazine and Journal of Science* 10.64, pp. 369–383. DOI: [10.1080/14786443009461588](https://doi.org/10.1080/14786443009461588).

- Chirkov, M., G. P. Stiller, A. Laeng, S. Kellmann, T. von Clarmann, C. Boone, J. W. Elkins, A. Engel, N. Glatthor, U. Grabowski, C. M. Harth, M. Kiefer, F. Kolonjari, P. B. Krummel, A. Linden, C. R. Lunder, B. R. Miller, S. A. Montzka, J. Mühle, S. O'Doherty, J. Orphal, R. G. Prinn, G. Toon, M. K. Vollmer, K. A. Walker, R. F. Weiss, A. Wiegele, and D. Young (2016). "Global HCFC-22 measurements with MIPAS: retrieval, validation, global distribution and its evolution over 2005–2012". In: *Atmos. Chem. Phys.* 16.5, pp. 3345–3368. DOI: [10.5194/acp-16-3345-2016](https://doi.org/10.5194/acp-16-3345-2016).
- Chubachi, S. (1985). "A Special Ozone Observation at Syowa Station, Antarctica from February 1982 to January 1983". In: *Atmospheric Ozone: Proceedings of the Quadrennial Ozone Symposium held in Halkidiki, Greece 3–7 September 1984*. Ed. by C. S. Zerefos and A. Ghazi. Dordrecht: Springer Netherlands, pp. 285–289. ISBN: 978-94-009-5313-0. DOI: [10.1007/978-94-009-5313-0_58](https://doi.org/10.1007/978-94-009-5313-0_58).
- Dinelli, B. M., E. Arnone, G. Brizzi, M. Carlotti, E. Castelli, L. Magnani, E. Papandrea, M. Prevedelli, and M. Ridolfi (2010). "The MIPAS2D database of MIPAS/ENVISAT measurements retrieved with a multi-target 2-dimensional tomographic approach". In: *Atmospheric Measurement Techniques* 3.2, pp. 355–374. DOI: [10.5194/amt-3-355-2010](https://doi.org/10.5194/amt-3-355-2010). URL: <http://www.atmos-meas-tech.net/3/355/2010/>.
- Dobson, G. M. B. (1931). "Ozone in the Upper Atmosphere and its Relation to Meteorology." In: *Nature* 127, pp. 668–672. DOI: [10.1038/127668a0](https://doi.org/10.1038/127668a0).
- (1968). "Forty years' research on atmospheric ozone at Oxford: a history". In: *Applied Optics* 7, p. 387. DOI: [10.1364/AO.7.000387](https://doi.org/10.1364/AO.7.000387).
- Dobson, G. M. B., D. N. Harrison, and J. Lawrence (1929). "Measurements of the Amount of Ozone in the Earth's Atmosphere and Its Relation to Other Geophysical Conditions. Part III". In: *Proceedings of the Royal Society of London Series A* 122, pp. 456–486. DOI: [10.1098/rspa.1929.0034](https://doi.org/10.1098/rspa.1929.0034).
- Douglass, A. R., R. S. Stolarski, M. R. Schoeberl, C. H. Jackman, M. L. Gupta, P. A. Newman, J. E. Nielsen, and E. L. Fleming (2008). "Relationship of loss, mean age of air and the distribution of CFCs to stratospheric circulation and implications for atmospheric lifetimes". In: *J. Geophys. Res.* 113, D14309. DOI: [10.1029/2007JD009575](https://doi.org/10.1029/2007JD009575).
- Eckert, E., T. von Clarmann, M. Kiefer, G. P. Stiller, S. Lossow, N. Glatthor, D. A. Degenstein, L. Froidevaux, S. Godin-Beekmann, T. Leblanc, S. McDermid, M. Pastel, W. Steinbrecht, D. P. J. Swart, K. A. Walker, and P. F. Bernath (2014). "Drift-corrected trends and periodic variations in MIPAS IMK/IAA ozone measurements". In: *Atmospheric Chemistry and Physics* 14.5, pp. 2571–2589. DOI: [10.5194/acp-14-2571-2014](https://doi.org/10.5194/acp-14-2571-2014). URL: <http://www.atmos-chem-phys.net/14/2571/2014/>.
- Eckert, E., A. Laeng, S. Lossow, S. Kellmann, G. Stiller, T. von Clarmann, N. Glatthor, M. Höpfner, M. Kiefer, H. Oelhaf, J. Orphal, B. Funke, U. Grabowski, F. Haenel, A. Linden, G. Wetzela, W. Woiwode, P. F. Bernath, C. Boone, G. S. Dutton, J. W. Elkins, A. Engel, J. C. Gille, F. Kolonjari, T. Sugita, G. C. Toon, and K.

- A. Walker (2016). “MIPAS IMK/IAA CFC-11 (CCl_3F) and CFC-12 (CCl_2F_2) measurements: accuracy, precision and long-term stability”. In: *Atmospheric Measurement Techniques* 9.7, pp. 3355–3389. DOI: [10.5194/amt-9-3355-2016](https://doi.org/10.5194/amt-9-3355-2016). URL: <http://www.atmos-meas-tech.net/9/3355/2016/>.
- Eckert, E., T. von Clarmann, A. Laeng, G. P. Stiller, B. Funke, N. Glatthor, U. Grabowski, S. Kellmann, M. Kiefer, A. Linden, A. Babenhauserheide, G. Wetzel, C. Boone, A. Engel, J. J. Harrison, P. E. Sheese, K. A. Walker, and P. F. Bernath (2017). “MIPAS IMK/IAA carbon tetrachloride (CCl_4) retrieval and first comparison with other instruments”. In: *Atmospheric Measurement Techniques* 10.7, pp. 2727–2743. DOI: [10.5194/amt-10-2727-2017](https://doi.org/10.5194/amt-10-2727-2017). URL: <https://www.atmos-meas-tech.net/10/2727/2017/>.
- Engel, A., T. Möbius, H. Bönisch, U. Schmidt, R. Heinz, I. Levin, E. Atlas, S. Aoki, T. Nakazawa, S. Sugawara, F. Moore, D. Hurst, J. Elkins, S. Schauffler, A. Andrews, and K. Boering (2009). “Age of stratospheric air unchanged within uncertainties over the past 30 years”. In: *Nature Geosci.* 2, pp. 28–31. DOI: [10.1038/ngeo388](https://doi.org/10.1038/ngeo388).
- SPARC CCMVal Report on the Evaluation of Chemistry-Climate Models* (2010). Tech. rep. SPARC, 426 pp.
- Fabry, Ch. and H. Buisson (1921). “Étude de l’extrémité ultra-violette du spectre solaire”. In: *J. Phys. Radium*, 2 7, pp. 197–226. DOI: <https://doi.org/10.1051/jphysrad:0192100207019700>.
- Farman, J. C., B. G. Gardiner, and J. D. Shanklin (1985). “Large losses of total ozone in Antarctica reveal seasonal ClO_x/NO_x interaction”. In: *Nature* 315, pp. 207–210.
- Fischer, H., M. Birk, C. Blom, B. Carli, M. Carlotti, T. von Clarmann, L. Delbouille, A. Dudhia, D. Ehhalt, M. Endemann, J. M. Flaud, R. Gessner, A. Kleinert, R. Koopman, J. Langen, M. López-Puertas, P. Mosner, H. Nett, H. Oelhaf, G. Perron, J. Remedios, M. Ridolfi, G. Stiller, and R. Zander (2008). “MIPAS: an instrument for atmospheric and climate research”. In: *Atmospheric Chemistry & Physics* 8, pp. 2151–2188.
- Fischer, H., M. Birk, C. Blom, B. Carli, M. Carlotti, T. von Clarmann, L. Delbouille, A. Dudhia, D. Ehhalt, M. Endemann, J. M. Flaud, R. Gessner, A. Kleinert, R. Koopmann, J. Langen, M. López-Puertas, P. Mosner, H. Nett, H. Oelhaf, G. Perron, J. Remedios, M. Ridolfi, G. Stiller, and R. Zander (2008). “MIPAS: an instrument for atmospheric and climate research”. In: *Atmos. Chem. Phys.* 8, pp. 2151–2188.
- Funke, B. (2000). “Line mixing”. In: *The Karlsruhe Optimized and Precise Radiative transfer Algorithm (KOPRA)*. Ed. by G. P. Stiller. Wissenschaftliche Berichte FZKA 6487. Forschungszentrum Karlsruhe, pp. 69–75.
- Funke, B. and M. Höpfner (2000). “Non-LTE and radiative transfer”. In: *The Karlsruhe Optimized and Precise Radiative transfer Algorithm (KOPRA)*. Ed. by G. P. Stiller. Wissenschaftliche Berichte FZKA 6487. Forschungszentrum Karlsruhe, pp. 101–106.

- Gil-López, S., M. López-Puertas, M. Kaufmann, B. Funke, M. García-Comas, M. E. Koukouli, N. Glatthor, U. Grabowski, Höpfner, G. P. Stiller, and T. von Clarmann (2005). “Retrieval of stratospheric and mesospheric O₃ from high resolution MIPAS spectra at 15 and 10 μm”. In: *Adv. Space Res.* 36.5, pp. 943–951. DOI: [10.1016/j.asr.2005.05.123](https://doi.org/10.1016/j.asr.2005.05.123)
- Glatthor, N., T. von Clarmann, H. Fischer, U. Grabowski, M. Höpfner, S. Kellmann, M. Kiefer, A. Linden, M. Milz, T. Steck, G. P. Stiller, G. Mengistu Tsidu, D. Y. Wang, and B. Funke (2004). “Spaceborne ClO observations by the Michelson Interferometer for Passive Atmospheric Sounding (MIPAS) before and during the Antarctic major warming in September/October 2002”. In: *J. Geophys. Res.* 109, D11307. DOI: [10.1029/2003JD004440](https://doi.org/10.1029/2003JD004440)
- Glatthor, N., T. von Clarmann, H. Fischer, B. Funke, U. Grabowski, M. Höpfner, S. Kellmann, M. Kiefer, A. Linden, M. Milz, T. Steck, G. P. Stiller, G. Mengistu Tsidu, and D. Y. Wang (2005). “Mixing processes during the Antarctic vortex split in September/October 2002 as inferred from source gas and ozone distributions from ENVISAT-MIPAS”. In: *J. Atmos. Sci.* 62.3, pp. 787–800.
- Glatthor, N., T. von Clarmann, H. Fischer, B. Funke, S. Gil-López, U. Grabowski, M. Höpfner, S. Kellmann, A. Linden, M. López-Puertas, G. Mengistu Tsidu, M. Milz, T. Steck, G. P. Stiller, and D.-Y. Wang (2006). “Retrieval of stratospheric ozone profiles from MIPAS/ENVISAT limb emission spectra: a sensitivity study”. In: *Atmos. Chem. Phys.* 6, pp. 2767–2781.
- Glatthor, N., T. von Clarmann, G. P. Stiller, B. Funke, M. E. Koukouli, H. Fischer, U. Grabowski, M. Höpfner, S. Kellmann, and A. Linden (2009). “Large-scale upper tropospheric pollution observed by MIPAS HCN and C₂H₆ global distributions”. In: *Atmos. Chem. Phys.* 9, pp. 9619–9634.
- Glatthor, N., M. Höpfner, A. Leyser, G. P. Stiller, T. von Clarmann, U. Grabowski, S. Kellmann, A. Linden, B.-M. Sinnhuber, G. Krysztofiak, and K. A. Walker (2017). “Global carbonyl sulfide (OCS) measured by MIPAS/Envisat during 2002–2012”. In: *Atmospheric Chemistry and Physics* 17.4, pp. 2631–2652. DOI: [10.5194/acp-17-2631-2017](https://doi.org/10.5194/acp-17-2631-2017). URL: <https://www.atmos-chem-phys.net/17/2631/2017/>
- Götz, F. W. P., A. R. Meetham, and G. M. B. Dobson (1934). “The Vertical Distribution of Ozone in the Atmosphere”. In: *Royal Society of London Proceedings Series A* 145, pp. 416–446. DOI: [10.1098/rspa.1934.0109](https://doi.org/10.1098/rspa.1934.0109).
- Haenel, F. J., G. P. Stiller, T. von Clarmann, B. Funke, E. Eckert, N. Glatthor, U. Grabowski, S. Kellmann, M. Kiefer, A. Linden, and T. Reddmann (2015). “Reassessment of MIPAS age of air trends and variability”. In: *Atmos. Chem. Phys.* 15.22, pp. 13161–13176. DOI: [10.5194/acp-15-13161-2015](https://doi.org/10.5194/acp-15-13161-2015).
- Hall, T. M. and R. A. Plumb (1994). “Age as a diagnostic of stratospheric transport,” in: *J. Geophys. Res.* 99.D1, pp. 1059–1070.
- Hardiman, Steven C., Neal Butchart, and Natalia Calvo (2013). “The morphology of the Brewer–Dobson circulation and its response to climate change in CMIP5 simulations”. In: *Quarterly Journal of the Royal Meteorological Society* 140.683,

- pp. 1958–1965. ISSN: 1477-870X. DOI: [10.1002/qj.2258](https://doi.org/10.1002/qj.2258), URL: <http://dx.doi.org/10.1002/qj.2258>.
- Hase, F. and M. Höpfner (2000). “Atmospheric raypath modeling for radiative transfer algorithms”. In: *The Karlsruhe Optimized and Precise Radiative transfer Algorithm (KOPRA)*. Ed. by G. P. Stiller. Wissenschaftliche Berichte FZKA 6487. Forschungszentrum Karlsruhe, pp. 35–42.
- Haynes, P. H., M. E. McIntyre, T. G. Shepherd, C. J. Marks, and K. P. Shine (1991). “On the ‘Downward Control’ of Extratropical Diabatic Circulations by Eddy-Induced Mean Zonal Forces.” In: *Journal of Atmospheric Sciences* 48, pp. 651–680. DOI: [10.1175/1520-0469\(1991\)048<0651:OTCOED>2.0.CO;2](https://doi.org/10.1175/1520-0469(1991)048<0651:OTCOED>2.0.CO;2).
- Hegglin, M. I., D. W. Fahey, M. McFarland, S. A. Montzka, and E. R. Nash (2015). *Twenty Questions and Answers About the Ozone Layer: 2014 Update, Scientific Assessment of Ozone Depletion: 2014*. 84 pp., World Meteorological Organization, Geneva, Switzerland.
- Höpfner, M. (2000). “Derivatives and interface to the retrieval”. In: *The Karlsruhe Optimized and Precise Radiative transfer Algorithm (KOPRA)*. Ed. by G. P. Stiller. Wissenschaftliche Berichte FZKA 6487. Forschungszentrum Karlsruhe, pp. 133–144.
- Höpfner, M., T. von Clarmann, H. Fischer, N. Glatthor, U. Grabowski, S. Kellmann, M. Kiefer, A. Linden, G. Mengistu Tsidu, M. Milz, T. Steck, G. P. Stiller, D.-Y. Wang, and B. Funke (2004). “First spaceborne observations of Antarctic stratospheric ClONO₂ recovery: Austral spring 2002”. In: *J. Geophys. Res.* 109, D11308. DOI: [10.1029/2004JD004609](https://doi.org/10.1029/2004JD004609).
- Kellmann, S., T. von Clarmann, G. P. Stiller, E. Eckert, N. Glatthor, M. Höpfner, M. Kiefer, J. Orphal, B. Funke, U. Grabowski, A. Linden, G. S. Dutton, and J. W. Elkins (2012). “Global CFC-11 (CCl₃F) and CFC-12 (CCl₂F₂) Measurements with the Michelson Interferometer for Passive Atmospheric Sounding (MIPAS): retrieval, climatologies and trends”. In: *Atmos. Chem. Phys.* 12.24, pp. 11857–11875. DOI: [10.5194/acp-12-11857-2012](https://doi.org/10.5194/acp-12-11857-2012).
- Kleinert, A., G. Aubertin, G. Perron, M. Birk, G. Wagner, F. Hase, H. Nett, and R. Poulin (2007). “MIPAS Level 1B algorithms overview: operational processing and characterization”. In: *Atmos. Chem. Phys.* 7, pp. 1395–1406.
- SPARC Report on Lifetimes of Stratospheric Ozone-Depleting Substances, Their Replacements, and Related Species* (2013). Tech. rep. SPARC, 256 pp.
- Li, F., R. S. Stolarski, and P. A. Newman (2009). “Stratospheric ozone in the post-CFC era”. In: *Atmos. Chem. Phys.* 9.6, pp. 2207–2213.
- Liang, Q., P.A. Newman, and Reimann S. (2016). *SPARC Report on the Mystery of Carbon tetrachloride*. SPARC Report No. 7, WCRP-13/2016. SPARC.
- Liou, Kuo-Nan (1980). *An Introduction to Atmospheric Radiation*. International geophysics series - Volume 26, New York: Academic Press, Inc.

- López-Puertas, M., T. von Clarmann, A. Dudhia, J.-M. Flaud, B. Funke, M. García-Comas, S. Gil-López, N. Glatthor, U. Grabowski, V. Jay, M. Kiefer, M. Á. López-Valverde, G. Perron, and G. P. Stiller (2003). “Non-LTE studies for the validation of MIPAS/ENVISAT L2 products”. In: *Proc. ENVISAT Validation Workshop, 9–13 December, 2002, ESRIN, Frascati, Italy, CD-ROM*. Vol. SP-531. ESA Publications Division, ESTEC, Postbus 299, 2200 AG Noordwijk, The Netherlands.
- Mahfouf, J. F., D. Cariolle, J. F. Royer, J. F. Geleyn, and B. Timbal (1994). “Response of the Météo-France climate model to changes in CO₂ and sea surface temperature”. In: *Climate Dynamics* 9, pp. 345–362. DOI: [10.1007/BF00223447](https://doi.org/10.1007/BF00223447).
- Molina, M. J. and F. S. Rowland (1974). “Stratospheric sink for chlorofluoromethanes: Chlorine atom-catalysed destruction of ozone”. In: *Nature* 249, pp. 810–812.
- Norton, H. and R. Beer (1976). “New apodizing functions for Fourier spectrometry”. In: *J. Opt. Soc. Am* 66.3. (Errata *J. Opt. Soc. Am.*, 67, 419, 1977), pp. 259–264.
- Oman, L. D., D. A. Plummer, D. W. Waugh, J. Austin, J. F. Scinocca, A. R. Douglass, R. J. Salawitch, T. Canty, H. Akiyoshi, S. Bekki, P. Braesicke, N. Butchart, M. P. Chipperfield, D. Cugnet, S. Dhomse, V. Eyring, S. Frith, S. C. Hardiman, D. E. Kinnison, J.-F. Lamarque, E. Mancini, M. Marchand, M. Michou, O. Morgenstern, T. Nakamura, J. E. Nielsen, D. Olivie, G. Pitari, J. Pyle, E. Rozanov, T. G. Shepherd, K. Shibata, R. S. Stolarski, H. Teyssèdre, W. Tian, Y. Yamashita, and J. R. Ziemke (2010). “Multimodel assessment of the factors driving stratospheric ozone evolution over the 21st century”. In: *Journal of Geophysical Research: Atmospheres* 115.D24. D24306, n/a–n/a. ISSN: 2156-2202. DOI: [10.1029/2010JD014362](https://doi.org/10.1029/2010JD014362). URL: <http://dx.doi.org/10.1029/2010JD014362>.
- Petty, G. W. (2006). *A First Course in Atmospheric Radiation*. Second Edition. ISBN-13: 978-0-9279033-5-6: Sundog Publishing.
- Plumb, R. Alan (2002). “Stratospheric Transport”. In: *Journal of the Meteorological Society of Japan. Ser. II* 80.4B, pp. 793–809. DOI: [10.2151/jmsj.80.793](https://doi.org/10.2151/jmsj.80.793).
- Raspollini, P., B. Carli, M. Carlotti, S. Ceccherini, A. Dehn, B. M. Dinelli, A. Dudhia, J.-M. Flaud, M. López-Puertas, F. Niro, J. J. Remedios, M. Ridolfi, H. Sembhi, L. Sgheri, and T. von Clarmann (2013). “Ten years of MIPAS measurements with ESA Level 2 processor V6 – Part I: retrieval algorithm and diagnostics of the products”. In: *Atmos. Meas. Tech.* 6.9, pp. 2419–2439. DOI: [10.5194/amt-6-2419-2013](https://doi.org/10.5194/amt-6-2419-2013).
- Rind, D., R. Suozzo, N. K. Balachandran, and M. J. Prather (1990). “Climate Change and the Middle Atmosphere. Part I: The Doubled CO₂ Climate”. In: *Journal of the Atmospheric Sciences* 47.4, pp. 475–494. DOI: [10.1175/1520-0469\(1990\)047<0475:CCATMA>2.0.CO;2](https://doi.org/10.1175/1520-0469(1990)047<0475:CCATMA>2.0.CO;2).
- Rodgers, C. D. (2000). *Inverse Methods for Atmospheric Sounding: Theory and Practice*. Vol. 2. Series on Atmospheric, Oceanic and Planetary Physics, F. W. Taylor, ed. Singapore, New Jersey, London, Hong Kong: World Scientific.

- Schönbein, C. F. (1840). “Beobachtungen über den bei der Elektrolyse des Wassers und dem Ausströmen der gewöhnlichen Elektrizität aus Spitzen sich entwickelnden Geruch”. In: *Annalen der Physik* 126, pp. 616–635. DOI: [10.1002/andp.18401260804](https://doi.org/10.1002/andp.18401260804).
- Shepherd, T. G. (2008). “Dynamics, Stratospheric Ozone, and Climate Change”. In: *Atmosphere-Ocean* 46.1, pp. 117–138. DOI: [10.3137/ao.460106](https://doi.org/10.3137/ao.460106).
- Sinnhuber, B.-M., G. Stiller, R. Ruhnke, T. von Clarmann, S. Kellmann, and J. Aschmann (2011). “Arctic winter 2010/2011 at the brink of an ozone hole”. In: *Geophys. Res. Lett.* 38, L24814. DOI: [10.1029/2011GL049784](https://doi.org/10.1029/2011GL049784).
- Solomon, S. (1999). “Stratospheric Ozone Depletion: A Review of Concepts and History”. In: *Rev. Geophys.* 37.23, pp. 275–315.
- Solomon, S., R. R. Garcia, F. S. Rowland, and D. J. Wuebbles (1986). “On the depletion of Antarctic ozone”. In: *Nature* 321, pp. 755–758.
- Stiller, G. P., ed. (2000). *The Karlsruhe Optimized and Precise Radiative Transfer Algorithm (KOPRA)*. Vol. FZKA 6487. Wissenschaftliche Berichte. Karlsruhe: Forschungszentrum Karlsruhe.
- Stiller, G. P., G. Mengistu Tsidu, T. von Clarmann, N. Glatthor, M. Höpfner, S. Kellmann, A. Linden, R. Ruhnke, H. Fischer, M. López-Puertas, B. Funke, and S. Gil-López (2005). “An enhanced HNO₃ second maximum in the Antarctic mid-winter upper stratosphere 2003”. In: *J. Geophys. Res.* 110.D20, D20303. DOI: [10.1029/2005JD006011](https://doi.org/10.1029/2005JD006011).
- Stiller, G. P., T. von Clarmann, C. Brühl, H. Fischer, B. Funke, N. Glatthor, U. Grabowski, M. Höpfner, P. Jöckel, S. Kellmann, M. Kiefer, A. Linden, M. López-Puertas, G. Mengistu Tsidu, M. Milz, T. Steck, and B. Steil (2007). “Global distributions of HO₂NO₂ as observed by the Michelson Interferometer for Passive Atmospheric Sounding (MIPAS)”. In: *J. Geophys. Res.* 112, D09314. DOI: [10.1029/2006JD007212](https://doi.org/10.1029/2006JD007212).
- Stiller, G. P., T. von Clarmann, F. Haenel, B. Funke, N. Glatthor, U. Grabowski, S. Kellmann, M. Kiefer, A. Linden, S. Lossow, and M. López-Puertas (2012). “Observed temporal evolution of global mean age of stratospheric air for the 2002 to 2010 period”. In: *Atmospheric Chemistry & Physics* 12, pp. 3311–3331. DOI: [10.5194/acp-12-3311-2012](https://doi.org/10.5194/acp-12-3311-2012).
- Stiller, G. P., M. Kiefer, E. Eckert, T. von Clarmann, S. Kellmann, M. García-Comas, B. Funke, T. Leblanc, E. Fetzer, L. Froidevaux, M. Gomez, E. Hall, D. Hurst, A. Jordan, N. Kämpfer, A. Lambert, I. S. McDermid, T. McGee, L. Miloshevich, G. Nedoluha, W. Read, M. Schneider, M. Schwartz, C. Straub, G. Toon, L. W. Twigg, K. Walker, and D. N. Whiteman (2012). “Validation of MIPAS IMK/IAA temperature, water vapor, and ozone profiles with MOHAVE-2009 campaign measurements”. In: *Atmos. Meas. Tech.* 5.2, pp. 289–320. DOI: [10.5194/amt-5-289-2012](https://doi.org/10.5194/amt-5-289-2012).

- Stiller, G. P., F. Fierli, T. von Clarmann, B. Funke, and T. Reddmann (2013). “Can the MIPAS-Observed Pattern of Mean age of air Trends be Explained by Shifts of the Subtropical Mixing Barriers?” In: *AGU Fall Meeting Abstracts*.
- Stiller, G. P., F. Fierli, F. Ploeger, C. Cagnazzo, B. Funke, F. J. Haenel, T. Reddmann, M. Riese, and T. von Clarmann (2017). “Shift of subtropical transport barriers explains observed hemispheric asymmetry of decadal trends of age of air”. In: *Atmospheric Chemistry and Physics* 17.18, pp. 11177–11192. DOI: [10.5194/acp-17-11177-2017](https://doi.org/10.5194/acp-17-11177-2017). URL: <https://www.atmos-chem-phys.net/17/11177/2017/>.
- The University of Oxford Physics Department (2008). *Michelson Interferometer for Passive Atmospheric Sounding (MIPAS)*. <http://www.atm.ox.ac.uk/group/mipas/>. [Accessed: @06-Apr-2016].
- Tikhonov, A. (1963). “On the solution of incorrectly stated problems and method of regularization”. In: *Dokl. Akad. Nauk. SSSR* 151.3, pp. 501–504.
- von Clarmann, T. (2014). “Smoothing error pitfalls”. In: *Atmos. Meas. Tech.* 7, pp. 3023–3034. DOI: [10.5194/amtd-7-3023-2014](https://doi.org/10.5194/amtd-7-3023-2014).
- von Clarmann, T. and U. Grabowski (2016). “Direct inversion of circulation and mixing from tracer measurements – Part 1: Method”. In: *Atmospheric Chemistry and Physics* 16.22, pp. 14563–14584. DOI: [10.5194/acp-16-14563-2016](https://doi.org/10.5194/acp-16-14563-2016). URL: <https://www.atmos-chem-phys.net/16/14563/2016/>.
- von Clarmann, T., N. Glatthor, U. Grabowski, M. Höpfner, S. Kellmann, M. Kiefer, A. Linden, G. Mengistu Tsidu, M. Milz, T. Steck, G. P. Stiller, D. Y. Wang, H. Fischer, B. Funke, S. Gil-López, and M. López-Puertas (2003). “Retrieval of temperature and tangent altitude pointing from limb emission spectra recorded from space by the Michelson Interferometer for Passive Atmospheric Sounding (MIPAS)”. In: *J. Geophys. Res.* 108.D23, 4736. DOI: [10.1029/2003JD003602](https://doi.org/10.1029/2003JD003602).
- von Clarmann, T., N. Glatthor, M. E. Koukouli, G. P. Stiller, B. Funke, U. Grabowski, M. Höpfner, S. Kellmann, A. Linden, M. Milz, T. Steck, and H. Fischer (2007). “MIPAS measurements of upper tropospheric C₂H₆ and O₃ during the Southern hemispheric biomass burning season in 2003”. In: *Atmos. Chem. Phys.* 7, pp. 5861–5872.
- von Clarmann, T., M. Höpfner, S. Kellmann, A. Linden, S. Chauhan, B. Funke, U. Grabowski, N. Glatthor, M. Kiefer, T. Schieferdecker, G. P. Stiller, and S. Versick (2009). “Retrieval of temperature, H₂O, O₃, HNO₃, CH₄, N₂O, ClONO₂ and ClO from MIPAS reduced resolution nominal mode limb emission measurements”. In: *Atmos. Meas. Techn.* 2.1, pp. 159–175.
- von Clarmann, T., G. Stiller, U. Grabowski, E. Eckert, and J. Orphal (2010). “Technical Note: Trend estimation from irregularly sampled, correlated data”. In: *Atmospheric Chemistry & Physics* 10, pp. 6737–6747.
- World Meteorological Organization (2011). *Scientific Assessment of Ozone Depletion: 2010*. Global Ozone Research and Monitoring Project – Report No. 52, 516 pp., Geneva, Switzerland.

-
- Zander, R., E. Mahieu, M. R. Gunson, M. C. Abrams, A. Y. Chang, M. M. Abbas, C. Aelig, A. Engel, A. Goldman, F. W. Irion, N. Kämpfer, H. A. Michelson, M. J. Newchurch, C. P. Rinsland, R. J. Salawitch, G. P. Stiller, and G. C. Toon (1996). "The 1994 northern midlatitude budget of stratospheric chlorine derived from ATMOS/ATLAS-3 observations". In: *Geophys. Res. Lett.* 23.17, pp. 2357–2360.

C. Acknowledgements

This work was funded by Deutsche Forschungsgemeinschaft (DFG) through the "Consideration of Lifetimes of Tracers for the Determination of Stratospheric Age Spectra and the Brewer Dobson Circulation" (CoLiBri) project under the project number: 232327523. The retrievals of IMK/IAA were partly performed on the HP XC4000 of the Scientific Supercomputing Center (SSC) Karlsruhe under project grant MIPAS. IMK data analysis was supported by DLR under contract number 50EE0901. MIPAS level 1B data were provided by ESA. I would like to acknowledge support by Open Access Publishing Fund of Karlsruhe Institute of Technology. The Atmospheric Chemistry Experiment (ACE), also known as SCISAT, is a Canadian-led mission mainly supported by the Canadian Space Agency and the Natural Sciences and Engineering Research Council of Canada. Work at the Jet Propulsion Laboratory, California Institute of Technology, was carried out under contract with the National Aeronautics and Space Administration. Data collection and analysis of MIPAS-STR data used here were supported by the EU-project RECONCILE (grant No. 15 226365-FP7-ENV-2008-1) and the BMBF-project ENVIVAL-Life (DLR grant no. 50EE0841). Balloon flights and data analysis of MIPAS-B data used here were supported by the European Space Agency (ESA), the German Aerospace Center (DLR), CNRS (Centre National de la Recherche Scientifique), and CNES (Centre National d'Etudes Spatiales). The ILAS-II project was funded by Ministry of the Environment of Japan.

I would like to thank:

- Prof. Stefan Hinz for the opportunity to do my PhD at the BGU faculty, for his support and help with organizational questions and his interest in my work.
- PD Dr. Thomas von Clarmann for being an outstanding supervisor, for his willingness and joy to discuss tricky questions to the tiniest detail, his honest advice and enthusiastic support, his continuous reassurance and the motivation he gave me all these years and, finally, for thoroughly proofreading my thesis and my scientific publications.
- Dr. Gabriele Stiller for her support through all these years, her excellent input on scientific questions and critical proofreading of my scientific publications, and always keeping me up to date on everything.
- Prof. Kaley Walker for her support and encouragement to try out new things, as well as finding my own way, for the welcoming atmosphere during my stay at University of Toronto and for putting a lot of effort into making my stay in Toronto possible in the first place.

- The three reviewers of my thesis: PD Dr. Thomas von Clarmann, Prof. Stefan Hinz and André Butz.
- Dr. Michael Kiefer for his help with MIPAS data, assessing and handling MIPAS averaging kernels and his continuous support.
- Dr. Norbert Glatthor for his help, particularly in my work on the MIPAS CCl₄ retrieval.
- Dr. Udo Grabowski for his introduction to and continuous help with the ANCISTRUS-SPEC invers model.
- Dr. Alexandra Laeng for providing routines for MIPAS data validation and her contributions to my scientific publications on MIPAS CFCs and CCl₄.
- Dr. Patrick Sheese for his help with comparisons of MIPAS and ACE-FTS.
- Dr. Arne Babenhauserheide for his help with comparing the MIPAS CCl₄ product with historic data from ATMOS.
- Dr. Christopher Boone for his ideas on how to further improve the MIPAS CCl₄ retrieval.
- Prof. John Gille for the numerous, intriguing discussions about HIRDLS and the related CFC validation, and for his always accomodating and welcoming attitude.
- Felicia Kolonjari for our intense conversations on ACE-FTS versus MIPAS CFCs and the great time Toronto.
- Dr. Florian Haenel for his help, particularly for providing educational material during the last weeks before my defense.
- Andrea Linden and Sylvia Kellmann for their help and practical advice regarding the MIPAS retrieval processor.
- Dr. Udo Grabowski, Dr. Johannes Plieninger, Dr. Arne Babenhauserheide and Johann Seemayer for their technical support.
- The entire IMK-ASF-SAT group for the great working environment and their support, as well as the great Christmas jam sessions.
- Mrs. Astrud Wiessner, Derya Cayiroglu and Sandra Leist for their administrative help and organization.
- My brother Kevin Eckert for enthusiastically discussing physics, living through being a PhD candidate and going through my thesis with me.
- My parents for their continuous support and understanding.

- Dr. Stefan Haaß for his encouragement and uplifting spirit.
- Andrea Vargas and Padmashree Badarinat for being my inspiration.
- My best friends Melanie Hankemeier and Michael Frank for their unlimited support and for always believing in me.